Title
Applications of the uranium decay systems in deep time and the Quaternary: chronologic insights within planetary interiors and beneath glaciers

Author
Edwards, Graham Harper

Publication Date
2021

UNIVERSITY OF CALIFORNIA
SANTA CRUZ

APPLICATIONS OF THE URANIUM DECAY SYSTEMS IN DEEP TIME AND THE QUATERNARY: CHRONOLOGIC INSIGHTS WITHIN PLANETARY INTERIORS AND BENEATH GLACIERS

A dissertation submitted in partial satisfaction of the
requirements for the degree of

DOCTOR OF PHILOSOPHY

in

EARTH SCIENCES

by

Graham Harper Edwards

September 2021

The Dissertation of Graham Harper Edwards is approved:

Terrence Blackburn, Chair

Slawek Tulaczyk

Myriam Telus

Peter Biehl
Vice Provost and Dean of Graduate Studies

Table of Contents

List of Figures

List of Tables

Abstract

Applications of the uranium decay systems in deep time and the Quaternary: chronologic insights within planetary interiors and beneath glaciers

by

Graham Harper Edwards

Isotopes of uranium and their radioactive decay products are important timekeepers for geologic and planetary processes, capable of recording precise dates across an enormous range of timescales and environments. This dissertation encompasses four distinct studies that employ the U decay systems to explore both time and physical processes in various geologic and planetary systems. While the focus of the chapters vary in both geologic and temporal setting, the studies fall under a unifying theme of pairing geochronologic methods with models that relate chronologies to Earth system and asteroidal processes.

The first two chapters use U-Pb thermochronology to measure high-temperature cooling processes in deep time (million-to-billion-year timescales). The first chapter interprets the cooling dates of U-Pb thermochronometers from middle-to-lower crustal xenoliths with thermal models to reconstruct the thermal history of the Superior craton, constraining the timing, temperature, and lithospheric response of the region to mantle plume heating 1.1 billion years ago. The second chapter interprets Pb-Pb cooling dates of phosphate minerals in LL ordinary chondrites with thermal models to reconstruct the size and timeframes of accretion of the LL parent planetesimal, revealing a large (>150 km diameter) asteroidal body that accreted rapidly after the formation of its constituent chondrule particles.

The latter chapters use intermediate decay products of the ^{238}U-series to explore subglacial conditions over the Pleistocene. The third chapter explores physical and chemical weathering processes in the hyperarid polar environment of

Taylor Valley, Antarctica and confirms that Taylor Glacier actively comminutes sediment at its base, challenging canonical assumptions that glaciers in the McMurdo Dry Valleys are non-erosive. The fourth chapter dates subglacial melting events beneath the northern Laurentide Ice Sheet and reveals their coincidence with Heinrich events, recurring episodes of voluminous iceberg discharge into the North Atlantic during the last glacial period. This terrestrial record of basal ice sheet processes corroborates subsurface ocean warming as the primary stimulus for Heinrich events and identifies subglacial aquifers and permafrost as important reservoirs involved in deglacial perturbations of the Atlantic Ocean uranium budget.

Collectively, the studies herein span timeframes that exceed the age of the Earth and peer into deep planetary interiors as well as the geosphere-cryosphere interface, each applying U decay systems in distinct ways to explore both geologic time and process.

To my mother, Sara, and our walks in the woods that started it all.

* * *

To Gavin, for the last five years of collaboration and the many more to come.

Acknowledgments

I could fill a second dissertation acknowledging and thanking all the people whose kindness, generosity, and support made this possible. I will spare the reader that treatise, but I hope they will indulge my best effort to acknowledge those individuals and groups whose contributions I refuse to overlook...

Many thanks to my advisor Terry Blackburn, for your support and mentorship. Thank you for sharing your knowledge and ideas and providing a supportive space for me to grow intellectually. I will fondly recall days sat in front of the TIMS or a chalkboard working our way through juicy problems, both analytical and geologic, alike. Thank you to Slawek Tulaczyk for sharing your expansive glaciological knowledge and patiently guiding me to resolutions of seemingly unresolvable problems. Thank you to Myriam Telus for sharing your extraterrestrial insights and introducing me to the complexity and magnificence of the solar system. Thank you to Kurt Cuffey for thoughtful conversations about glaciers, sediments, and how the two interact. Thank you all for tolerating and indulging my relentless questions, those conversations are now the core of my scientific knowledge.

I am profoundly grateful for the collaboration, camaraderie, and friendship of Gavin Piccione. There are not words that adequately describe how vital Gavin has been to my academic and personal growth over these last 5 years. I look forward to all of the science and boondoggles ahead of us.

Thank you to Maria Solis Kennedy, for your patience and support through this process and your aesthetic advice in the preparation of this document.

Thank you to my mother, Sara D. Edwards, for your unwavering confidence in me and for sending me snacks and support when I needed them most. Thank you to my brothers Brent and Landon for all the adventures and for simply being awesome.

I am immeasurably grateful for my therapist Michael Arthur. Successfully navigating (more or less) the emotional gauntlet of graduate school would not have been possible for me without our work together.

Thank you to Brian Dreyer for the invaluable mentorship and the many great conversations. I will always be indebted to you for all of the (geo)chemical and analytical insights you shared with me. Our many long conversations about chemistry and mass spectrometry that drifted into the philosophical will remain some of my fondest memories of graduate school. Many thanks to Shaun Yardley of Isotopx for his patience and assistance through innumerable emails and phone calls while working on the TIMS and for still seeming excited to see me at conferences after all the trouble I've put him through. Thank you to Brandon Cheney for always coming through when I needed help and having a creative solution to my most obnoxious problems. Thank you to Dan Sampson for sharing his arcane knowledge of electricity to keep the lab and instruments running. A very special thank you to Jennifer Fish who has routinely deciphered the impenetrable bureaucracy of the university for me, all the while maintaining your unwavering kindness and warm presence. Your detailed attention for each graduate student in this department is singular. And innumerable thank you's to Amy Kornberg for all the help and for brightening my day whenever I roamed through A232.

Thanks to the many UCSC students whom I have known through coursework and research. Special thanks to Dylan Tasker for teaching me chemistry methods and making my first year of graduate school especially memorable. Paul Colosi possesses a rare combination of amicability and impeccable attention to detail. I will always look back on our work together happily. Stefani Himes is an exemplary isotope geochemist. She balances her profound interests in geology and isotope chemistry with an infectious dedication to always growing intellectually.

It is a pleasure to call you a colleague. I am grateful to Cosmo Varah-Sikes for his commitment to Type 7 chondrites. Congratulations on your thesis, Cosmo! Thank you Linh Phan for inspiring me with your excitement for isotope geochemistry. Thanks to Sam Ferdman, Clara Stanbury, Sydney Ganem, Franny O'Byrne, Michael Scudder, and Xander Levinson for your assistance around the lab!

Lastly, thank you to everyone who has been there for me during and before graduate school. I apologize for not mentioning you by name, but you know who you are and please know how grateful I am for all you are and have done.

◆ ◆ ◆

I acknowledge the following funding sources: Aaron & Elizabeth Waters Award, University of California Santa Cruz Chancellor Fellowship, National Science Foundation (Award 1644171), and ARCS Foundation.

◆ ◆ ◆

The text of this dissertation includes reprints of the following previously published material:

Edwards, G.H. & Blackburn, T., 2018. "Detecting the extent of ca. 1.1 Ga Midcontinent Rift plume heating using U-Pb thermochronology of the lower crust," *Geology* 46, 911–914. DOI: 10.1130/G45150.1

Edwards, G.H. & Blackburn, T., 2020. "Accretion of a large LL parent planetesimal from a recently formed chondrule population," *Science Advances* 6, eaay8641. DOI: 10.1126/sciadv.aay8641

Terrence Blackburn, the coauthor of both publications, directed and supervised the research which forms the basis for this dissertation.

Introduction

The geochronometric utility of the element uranium (U) was realized (Rutherford, 1906; Strutt, 1908; Holmes, 1911) not long after the discovery of its radioactivity (Becquerel, 1896). When Soddy (1913) summarized the concept of isotopes, the foundation of modern radiometric geochronology, his insight was gained from studies of the early intermediate daughter products of the ^{238}U decay chain. In the ensuing century, the chronometric capacity of the U decay systems have expanded with developments in analytical capabilities, which currently enable determination of U-series, U-Pb, and Pb-Pb dates with single to sub-per mille confidence intervals (Cheng et al., 2013; Schoene, 2013). Contemporary high-precision measurements of isotopes from the uranium decay systems provide indispensable chronologic constraints within numerous fields, including planetary sciences (Barboni et al., 2017), geology (Burgess et al., 2017), climate science (Wang et al., 2001), and archaeology (Holen et al., 2017).

This dissertation attempts to build on this precedent and uses well-established geochemical techniques to explore novel applications of U radioisotopes and daughter nuclides as chronometers in terrestrial and asteroidal systems. The systems studied herein range among planetesimals formed during our solar system's infancy, the deep crust of Precambrian Earth, and subglacial systems in Antarctica and North America. Yet, these studies are related not only under a theme of radiogenic isotope geochemistry of the U decay systems but by a general scientific approach. In each study, high-precision isotopic measurements are interpreted in the context of mathematical and geochemical models that simulate both isotopic systems as well as physical processes in corresponding natural systems. Each chapter of this dissertation strives not only to measure time but to resolve process.

Chapters 1 and 2 focus on the application of high-temperature U-Pb thermochronology to assess timescales of heating and cooling in planetary interiors in deep time. In these studies, I applied well-established laboratory and analytical techniques to measure U-Pb isotopic compositions that I interpreted in novel ways with thermochronologic models.

In Chapter 1, we discerned a reheating signal from U-Pb thermochronometers in middle-to-lower crustal xenoliths from northern Ontario that reflect the thermal impact of 1.1 Ga plume heating. By pairing U-Pb data of thermochronologic accessory mineral phases (rutile, apatite) with coupled lithosphere thermal and thermochronometric Pb-production-diffusion models, we statistically identified the most probable conditions of plume temperature and lithospheric thinning due to plume impingement near Attawapiskat, Canada. This study, published in the journal *Geology*, emphasizes the massive size and thermal fingerprint of the Keweenawan mantle plume that fueled 1.1 Ga volcanism at the Midcontinent Rift.

In Chapter 2, we reported ^{207}Pb-^{206}Pb dates of phosphate minerals from LL chondrites, and verified the accuracy and primacy of these dates with paired U-Pb systematics. We interpreted the Pb-phosphate cooling dates in the context of coupled planetesimal thermal models and Pb-production-difussion in phosphate models, revealing that these cooling dates require not only a large ($\geq$150 km radius) parent planetesimal radius but also that the timing of LL chondrite parent planetesimal accretion closely overlapped with the formation of its constituent chondrules. Published in *Science Advances*, these findings add to a growing body of scholarship that support the rapid accretion of large (>100 km diameter) protoplanetary bodies in the early solar system, a process that may circumvent the so-called "meter-size barrier" that has long obstructed the accretion of planetary bodies under canonical accretion models.

Chapters 3 and 4 shift in setting and time from ancient planetary interiors to subglacial environments during the Pleistocene. This shifted spatiotemporal frame requires a concomitant shift in geochronologic methods, and in these studies I replace U-Pb chronometry with U-series isotopes and U-Th chronometry, relying on the sub-million-year resolution of the ^{238}U decay series.

Chapter 3 explores physical and chemical weathering processes in the hyper-arid polar environment of Taylor Valley, Antarctica through the lens of ^{230}Th-^{234}U-^{238}U isotopes. These so-called U-series radioisotopes trace weathering processes in silicate sediments through chemical and physical fractionation processes. The elements U and Th fractionate chemically during detrital mineral dissolution and authigenic mineral precipitation. Intermediate daughter isotopes ^{230}Th and ^{234}U fractionate physically due to the energetic recoil of radionuclides across grain-boundaries during α-decay events. Since these physical fractionation processes depend on radioactive decay, they can record chronologic information about physical sediment production and chemical alteration. We explore these processes in a systematic study of glacigenic sediments that were deposited by Taylor Glacier over the course of the last >1.5 Ma, and explore the timescales of both chemical weathering processes as well as physical comminution of fine-grained particles. Our data show that silicate rock comminution has recently occurred beneath Taylor Glacier, challenging canonical models of limited physical weathering in the modern McMurdo Dry Valleys and, instead, supporting a growing body of evidence that Taylor Glacier boasts subsolidus waters at its base that promotes localized basal sliding and erosion. Following deposition, U-series isotopes record a complex suite of chemical weathering processes, the most prominent of which is ^{230}Th and ^{234}U implantation into silicate sediments from uraniferous authigenic phases, a process that may be relevant in other hyperarid soil environments, including Martian soils.

In Chapter 4 we date a suite of subglacially formed carbonate precipitates from central Baffin Island with ^{230}Th-^{234}U-^{238}U geochronology. Since carbonate minerals are aqueously precipitated from liquid waters, these dates record subglacial melting events beneath the northern Laurentide Ice Sheet (LIS), which overlap with the timing of Heinrich events, episodic ice loss events during the last glacial period that occurred at approximately 7000 year intervals when ice surged out of the Hudson Strait and released swarms of icebergs into the North Atlantic Ocean (Hemming, 2004). While Heinrich events have historically been studied through climate records and ocean sediment archives, our data provide a novel terrestrial perspective that shows ice stream acceleration on Baffin Island coincident with Hudson Strait ice streaming, implying a shared trigger by ocean subsurface warming. In addition, the precipitates record distinct chemical compositions reflected in isotopes of oxygen, carbon, strontium, and U that indicate mixture of local meltwaters with groundwaters substantially enriched in the isotope ^{234}U. We identify subglacial groundwaters and permafrosts as an important hydrologic reservoir that may regulate the ocean U budget over the course of Pleistocene glacial cycles (Esat and Yokoyama, 2006; Chen et al., 2016; Arendt et al., 2018).

The studies herein detail a subset of the far-reaching applications of the U decay systems as both geochronometers and geochemical tracers. The collective timeframes span all of geologic time, and the environments range from deep planetary interiors to the margins of glaciers. Building on over 100 years of geochronologic precedent with the U decay system, this work strives to unravel further nuance in Earth and planetary sciences by using chronologies to more carefully explore processes.

Chapter 1

Detecting the extent of ca. 1.1 Ga Midcontinent Rift plume heating using U-Pb thermochronology of the lower crust

Reprinted from:

Edwards, G.H. & Blackburn, T., 2018. “Detecting the extent of ca. 1.1 Ga Midcontinent Rift plume heating using U-Pb thermochronology of the lower crust,” *Geology* 46, 911–914. DOI: 10.1130/G45150.1

GEOLOGY | THE GEOLOGICAL SOCIETY OF AMERICA®

https://doi.org/10.1130/G45150.1

Manuscript received 13 May 2018
Revised manuscript received 6 August 2018
Manuscript accepted 8 August 2018

Detecting the extent of ca. 1.1 Ga Midcontinent Rift plume heating using U-Pb thermochronology of the lower crust

Graham Harper Edwards and Terrence Blackburn
Department of Earth and Planetary Sciences, University of California Santa Cruz, 1156 High Street, EMS A232, Santa Cruz, California 95064, USA

ABSTRACT

The occurrence of mantle plumes in the geologic past is hypothesized to be marked by voluminous basaltic volcanism and topographic and gravitational anomalies. Missing from these identifying characteristics is a direct measurement of the elevated mantle temperatures associated with an upwelling channel from the deep mantle. To assess the extent of plume heating in the 1.1 Ga Midcontinent Rift System (North America), we present U-Pb thermochronologic evidence for a ca. 1.1 Ga sublithosphere heat source near Attawapiskat, Canada, >600 km from the inferred plume center. Apatite and rutile U-Pb cooling dates from middle to lower crustal xenoliths exhumed in the Jurassic Victor kimberlite record a thermal history >2.5 b.y. in duration. Shallow amphibolite and gabbro yield Archean to Paleoproterozoic dates with high U-Pb discordance, consistent with middle crust cooling prior to 1.1 Ga. Deeper garnet-bearing samples yield younger dates with low U-Pb discordance. Replicating these data with models reveals a thermal history in which the extent of heating corresponds with sample depth, an observation consistent with heating from below. Thermochronologic data are best fit by model simulations in which the Attawapiskat lithosphere experienced a ca. 1.1 Ga heating event triggered by partial lithosphere removal and mantle temperatures >200 °C in excess of that of ambient mantle, consistent with a model of ~100 m.y. plume head residence beneath the Attawapiskat region.

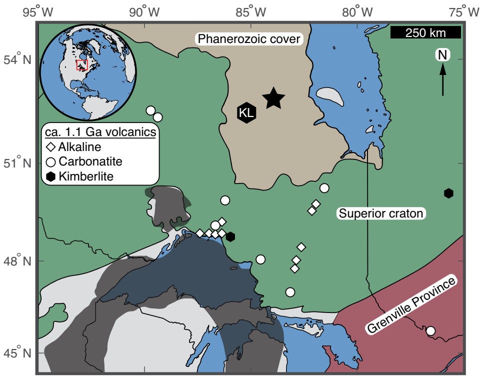

Figure 1. Map of Midcontinent Rift (shaded) and nearby volcanics dated within 100 m.y. of Midcontinent Rift volcanism (adapted from Heaman et al., 2004; Ernst and Bell, 2010; Smit et al., 2014b). Jurassic Attawapiskat kimberlite field (star) includes Victor kimberlite (52.82°N, 83.88°W), and Kyle Lake kimberlite field is labeled "KL".

INTRODUCTION

The Midcontinent Rift (MCR), or Keweenawan Rift, of North America is an ~2000-km-long failed continental rift structure centered at the southern extent of the Superior Province (Fig. 1). MCR flood basalts erupted over a span of 24 m.y. between 1108 and 1084 Ma (Davis and Green, 1997; Fairchild et al., 2017). Mantle plume heating has been invoked as the driver of the MCR and Keweenawan large igneous province for a variety of reasons. The large volume of igneous rock and isotopic signatures of MCR volcanics support an enriched mantle source (Nicholson and Shirey, 1990). Geophysical and geochemical models indicate elevated mantle potential temperatures of >1500 °C (Hutchinson et al., 1990). The coincidence of a radial drainage pattern and a negative gravitational anomaly centered about the Lake Superior Basin has been interpreted as the result of magmatic addition and underplating related to a mantle plume (Allen et al., 1992). Away from the inferred plume center, ca. 1.1 Ga alkali basalts and carbonatite eruptions are proposed to be small partial melts triggered by plume heating (Fig. 1; Ernst and Bell, 2010). Seismic tomography of the surrounding region combined with mantle xenolith geochemistry place the chemically depleted Archean chemical boundary layer to a contemporary depth of ~125 km, underlain by a thermal boundary layer consisting of conductively cooled, though less depleted and possibly younger, lithospheric mantle reaching ~200 km in depth (Yuan and Romanowicz, 2010). Such a mantle lithosphere structure is consistent with the regrowth of a thermal boundary layer following basal lithosphere erosion by a plume head.

The aforementioned lines of evidence support a plume heat source for MCR volcanism, yet the nature of the plume-lithosphere interaction is not well understood. Swanson-Hysell et al. (2014) reconciled plate velocities >20 cm/yr with 24 m.y. of MCR volcanism by invoking an upside-down drainage model (Sleep, 1997) whereby crustal thinning drives pooling and protracted residence of hot plume material beneath the Midcontinent Rift. We present evidence for heating of the basal lithosphere, a predicted hallmark of plume impingement, at ca. 1.1 Ga beneath the Attawapiskat region, 600 km north of the Midcontinent Rift.

Kimberlites in the Attawapiskat region of northern Ontario, Canada, contain crustal (amphibolite, gabbro, granulite) and mantle xenoliths that provide a glimpse into the ancient lithosphere conditions at this location

---

CITATION: Edwards, G.H., and Blackburn, T., 2018, Detecting the extent of ca. 1.1 Ga Midcontinent Rift plume heating using U-Pb thermochronology of the lower crust: Geology, v. 46, p. 911–914, https://doi.org/10.1130/G45150.1

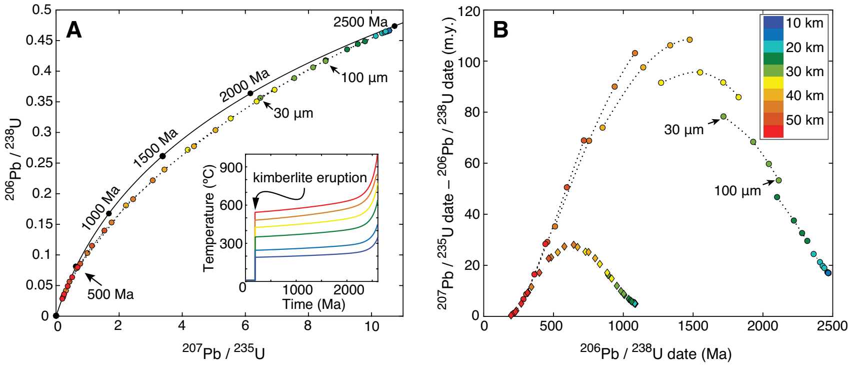

Figure 2. Model rutile U-Pb data for simulated time-temperature histories of unperturbed crustal column. A: Concordia plot presents results for thermal history of continuous cooling from 2500 Ma to a 170 Ma kimberlite eruption. Inset shows corresponding time-temperature histories. Colors denote crustal depth. Dotted curves represent interpolations among multiple crystal sizes, shown in microns, from each depth. B: Difference between ^{207}Pb/^{235}U and ^{206}Pb/^{238}U dates against ^{206}Pb/^{238}U date for model results of continuous cooling since 2.5 Ga (circles) and 1.1 Ga (diamonds).

(Fig. 1). The Kyle Lake kimberlites erupted coincidently with rifting (ca. 1075 Ma), while the Attawapiskat kimberlites, including the Victor kimberlite, are Jurassic in age (ca. 170 Ma; U-Pb perovskite; Heaman et al., 2004; Fig. 1). The thermal conditions of the Superior Province mantle lithosphere are recorded by the pressure and temperature conditions of silicate minerals and the nitrogen aggregation states of diamonds entrained within both kimberlite families. The observation that thermally mature diamonds exhumed in the Proterozoic were replaced by a less-heated diamond population in the Jurassic suggests that the region experienced a major regional heating event that raised the geothermal gradient of the entire lithosphere, exceeding the temperature of the diamond stability field, and then resumed cooling and diamond growth prior to Jurassic kimberlite eruption (Smit et al., 2014b), with diamond stability reestablished by ca. 720 Ma (Aulbach et al., 2017). These data, however, neither constrain the time scales of reheating more precisely than between ca. 720 and ca. 1100 Ma nor permit testing of possible sublithosphere heat sources.

Uranium-lead (U-Pb) thermochronometers record thermal histories between 400 and 800 °C due to the temperature-dependent diffusion of radiogenic Pb in U-bearing accessory phases like apatite and rutile. However, the production of radiogenic ^{206}Pb relative to ^{207}Pb varies with time as a result of the difference in the half-lives of ^{238}U and ^{235}U. The resulting Pb-isotopic evolution can be captured by U-Pb thermochronometers and is unique to the time scales of cooling. The effects of Pb production and loss on the U-Pb isotopic evolution of U-bearing accessory phases have been described with a lithosphere-scale thermal model coupled to a model that forward calculates U-Pb cooling dates for a tested thermal history (Blackburn et al., 2012). For a generalized crustal section beginning cooling at 2.5 Ga, model rutile U-Pb dates span from 2.5 Ga, recorded by the shallowest samples, to the time of kimberlite eruption, recorded by the deepest samples which were too hot to retain radiogenic Pb prior to cooling at the surface (Fig. 2A). Superimposed on this depth-age relationship is the length-scale effect of diffusion, whereby the age difference between large and small crystals inversely relates to cooling rate (Fig. 2). Middle to lower crustal samples may experience a long duration within a mineral's Pb partial retention zone (PRZ), resulting in U-Pb discordance that scales with the time and duration of PRZ residence (Blackburn et al., 2011, 2012). The degree of discordance may be characterized by plotting the difference between ^{207}Pb/^{235}U and ^{206}Pb/^{238}U dates (hereafter referred to as ΔU-Pb) against the more precise ^{206}Pb/^{238}U date (Fig. 2B). Two crustal sections that cool following initially high geothermal gradients at 1.1 Ga and 2.5 Ga yield thermochronologic U-Pb data that occupy distinct areas in ΔU-Pb versus ^{206}Pb/^{238}U date space due to the retention of Pb isotopic compositions produced at different time scales (Fig. 2B). In general, high ΔU-Pb values are a hallmark of ancient prolonged cooling histories.

We apply U-Pb thermochronology to xenoliths from the Victor kimberlite (North pipe) to assess the thermal history of the lower crust in the Attawapiskat region. We utilize the existing model framework to explore how forward-modeled U-Pb data respond to simulations of single end-member scenarios of basal lithosphere heating and thinning as well as scenarios that hybridize the end-member conditions. Comparing modeled and measured data, we show that Attawapiskat xenoliths record conductive heating from below, as predicted by a plume model, and thus map a minimum northward extent of heating associated with the MCR and suspected plume head. Notably these U-Pb thermochronologic data provide a direct measurement of plume heating without relying on mantle chemical models. Such a measurement has hitherto been lacking and that lack has consequently been utilized by detractors of the plume hypothesis (e.g., Anderson and Natland, 2005).

METHODS AND RESULTS

Measured Thermochronologic Data

Crustal xenoliths of various lithologies from the Victor North kimberlite (Fig. 1) were selected in order to examine material from a range of possible depths. The xenoliths studied here exhibit lithologies corresponding to depths between 20 and 50 km for a generalized crustal section, where garnet may be used as a mineral stratigraphic marker associated with depths >30 km (Jagoutz and Schmidt, 2012). Measurements of single- and multi-crystal rutile and apatite U-Pb isotope dilution–thermal ionization mass spectrometry (ID-TIMS) dates were conducted following the methods summarized in Appendix DR1 of the GSA Data Repository[1].

---

[1] GSA Data Repository item 2018333, expanded laboratory, numerical, and statistical methodologies, and results of model sensitivity tests, is available online at http://www.geosociety.org/datarepository/2018/ or on request from editing@geosociety.org.

Rutile and apatite U-Pb data for nine Victor xenoliths of a range of lithologies are presented in Figure 3. Combined rutile and apatite U-Pb data in ΔU-Pb space reveal a bifurcated topology spanning intercepts (ΔU-Pb = 0 m.y.) of >2500 Ma and 160 Ma. Rutile from four of five garnet-bearing samples (likely from depths >30 km) exhibit $^{206}Pb/^{238}U$ dates from ca. 160 to ca. 1100 Ma and relatively low degrees of discordance (ΔU-Pb < 20 m.y.) for higher-precision (high radiogenic Pb) measurements. Rutile from gabbros and biotite-bearing granulites reveal older cooling dates (1150–1350 Ma) and values of ΔU-Pb >75 m.y. Apatite analyses from non–garnet-bearing amphibolite and gabbro xenoliths (likely from depths <30 km) exhibit $^{206}Pb/^{238}U$ ages ranging from ca. 1270 to 2500 Ma with an arcing array of ΔU-Pb values.

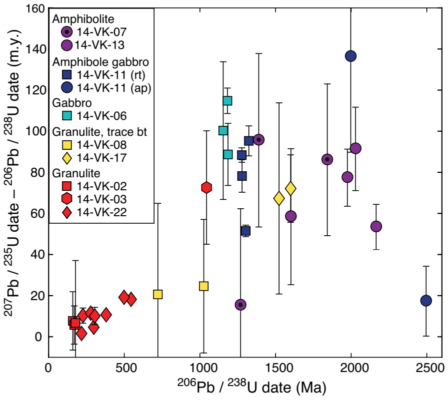

Figure 3. Measured U-Pb data plotted as difference between $^{207}Pb/^{235}U$ and $^{206}Pb/^{238}U$ dates versus $^{206}Pb/^{238}U$ date (±2σ) for single- and multi-grain rutile (rt; polygons) and apatite (ap; circles) fractions from Victor kimberlite xenoliths (North America). bt—biotite.

Modeled Thermochronologic Data

Numerical models predict how U-Pb thermochronometers in a crustal column respond to 1.1 Ga heating (Fig. 4). The unperturbed history (black curve in Fig. 4) is characterized by a single arc through ΔU-Pb space. An increasingly pronounced bifurcated topology develops with heating intensity and associated Pb loss. Shallow samples yield older dates and high ΔU-Pb values, the latter of which correlate with reheating intensity (peaks to the right, Fig. 4). Deeper samples are fully reset and contain little to no Pb produced prior to 1.1 Ga, resulting in ΔU-Pb curves that are nearly identical to the data predicted for unperturbed cooling beginning at 1.1 Ga (Figs. 2B, 4). Numerical modeling methods and sensitivity tests are available in Appendices DR2 and DR3.

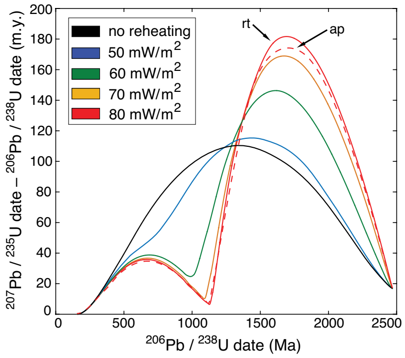

Figure 4. Model rutile (rt) and apatite (ap) U-Pb data plotted as difference between $^{207}Pb/^{235}U$ and $^{206}Pb/^{238}U$ dates versus $^{206}Pb/^{238}U$ date from simulated time-temperature histories of cooling since 2.5 Ga and reheating at 1.1 Ga for a single grain size (50 μm radius) at closely spaced depths. Reheating is accomplished by raising geotherm to designated surface flux (color) and holding for 10 m.y.

DATA INTERPRETATION AND CONCLUSIONS

The topology of measured U-Pb thermochronologic data for rutile and apatite from Victor kimberlite xenoliths preclude a history of continuous cooling (Fig. 3). Rather, the bifurcated topology describes a history of cooling and reheating, most consistent with a scenario of cooling beginning prior to 2500 Ma, a 1100 Ma reheating event characterized by a substantial increase in the geothermal gradient (>50 mW/m^2; Fig. 4), and the ≥160 Ma eruption of the Victor kimberlite. This sequence agrees with models of Superior Province amalgamation (e.g., Langford and Morin, 1976), the timing of MCR magmatism (Davis and Green, 1997), and ca. 170 Ma Attawapiskat kimberlite eruptions (Heaman et al., 2004).

Local magmatism at sub- or intracrustal depths does not offer a compelling explanation for the heating experienced by the Victor xenoliths. Despite widespread magmatism occurring 600 km to the south in the Midcontinent Rift, there is no evidence for Mesoproterozoic magmatism of significant magnitude or duration occurring in the Attawapiskat region related to the rift (Fig. 1) nor Grenvillian convergence (e.g., Rivers, 1997). Simulations of crustal igneous sources of variable size and temperature require intrusion sizes >25 km and temperatures >1200 °C to reproduce measured data (Appendix DR4). Although the scenario cannot be ruled out absolutely, the presence of a >25-km-thick intrusion beneath the Attawapiskat region is contradicted by independent geologic and geophysical evidence: zircon U-Pb dates from Victor xenoliths limit crustal igneous activity to before 2.2 Ga (Landis, 2016), Pb compositions of sample 14-VK-02 support an Archean origin for this deepest-residing xenolith (Appendix DR1), and combined seismic and gravity data limit the extent of significant magmatic underplating to within <100 km of the MCR center (Hutchinson et al., 1990). The only contemporaneous magmatism in the Attawapiskat region is the Kyle Lake kimberlites (Fig. 1; Heaman et al., 2004), yet kimberlites are associated with crustal transit times that, even at mantle temperatures (1400 °C), are predicted to remove negligible Pb (<0.1%) from rutile or apatite (Blackburn et al., 2011).

The lower crustal thermochronologic results require a significant heat source: at a maximum lower crustal temperature of 1100 °C (solidus), a 250 k.y. holding time is required to match data trends. Yet, the presence of thermally immature diamonds in Jurassic kimberlites indicates that the entirety of the Attawapiskat lithosphere, not just the crust, was heated (Smit et al., 2014b). Further, the measured data suggest a correlation between sample depth and degree of reheating, whereby deeper-residing samples of higher metamorphic grade exhibit younger dates, reflecting more pronounced resetting of the Pb isotopic system. The correlation is consistent with a scenario of long-term heating from below, through intact lithosphere mapped by mantle xenolith pressure-temperature data to a depth of 180 km at ca. 1.1 Ga (Smit et al., 2014a).

Possible end-member sublithosphere heat sources include (1) increased asthenosphere temperature or (2) removal of mantle lithosphere and replacement by asthenosphere at ambient mantle temperatures (1400 °C). Our numerical thermal model simulates both end members and their hybridized conditions for a 100 m.y. heating event starting at 1135 Ma.

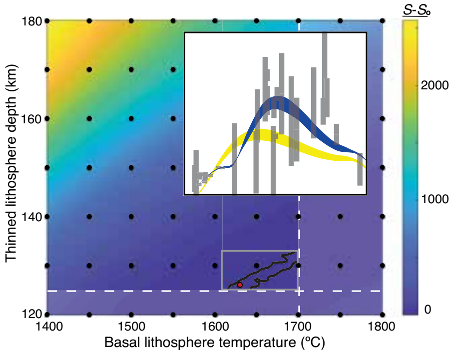

Figure 5. Results of Pearson chi-squared (χ^2) tests comparing measured and modeled data for range of simulated conditions of lithosphere thinning depth and basal temperature. Colored contour values are calculated from simulated model conditions (black dots) and represent difference between sum of χ^2 values for given model condition (*S*) and the minimum χ^2 summation (S_o, red circle). Black contours demarcate conditions producing *S* values within 1σ of S_o from higher-resolution suite of simulations (bounded by gray box). Dashed white lines indicate permissible minimum depth and maximum temperature. Inset shows measured U-Pb data (gray) with model rutile U-Pb data ranges (25–150 µm grain radii) for the best-fit model (blue) and unperturbed condition (1400 °C, 180 km; yellow). Inset axes are the same as those in Figure 3.

Similar results are found for heating onsets between 1000 and 1200 Ma, while heating events beyond this time frame yield poor agreement between measured and model data (Appendix DR3). Model U-Pb results for each scenario compared to measured data with a Pearson χ^2 test are presented in Figure 5 as the deviation from the best-fit scenario. Simulations of lithosphere thinning with no increase in mantle temperature require removal to <125 km depths to reproduce measured data. This scenario conflicts with depleted compositions and Re-Os dates of mantle xenoliths that place Archean lithosphere to depths of at least 125 km through the Jurassic (Smit et al., 2014a). A model of only mantle reheating with intact lithosphere to 180 km requires basal temperatures ≥600 °C in excess of that of the ambient mantle, vastly exceeding projected temperatures for plumes sourced from the core-mantle boundary (e.g., Albers and Christensen, 1996). The black contours in Figure 5 identify a suite of hybrid model conditions that best replicate the measured U-Pb data within the known lithosphere architecture. The conditions are characterized by mantle temperatures >1600 °C and lithosphere removal to depths <135 km. Collectively, the model and measured data evidence that the Superior Province crust was heated at 1.1 Ga, triggered by partial lithosphere removal and mantle temperatures >200 °C in excess of that of ambient mantle. Such a heating history is consistent with a spatially extensive plume head extending at least as far north as the Attawapiskat region and residing on time scales of ~100 m.y. Plume impingement was accompanied by widespread shallowing of the lithosphere thermal boundary layer beneath the Superior Province (Yuan and Romanowicz, 2010) that rethickened by conductive cooling to ~200 km at the time of Victor kimberlite eruption in the Jurassic (Smit et al., 2014b).

ACKNOWLEDGMENTS

We thank Karen Smit, Noah McLean, and Kevin Mahan for insightful discussions. This manuscript was improved by constructive comments from Nick Swanson-Hysell, Mark Schmitz, Ian Campbell, and two anonymous reviewers. We thank De Beers Canada, Inc., and Karen Smit for providing sample access. Funding support includes National Science Foundation grant 1532276 and the University of California Santa Cruz Chancellor fellowship to Edwards.

REFERENCES CITED

Albers, M., and Christensen, U.R., 1996, The excess temperature of plumes rising from the core-mantle boundary: Geophysical Research Letters, v. 23, p. 3567–3570, https://doi.org/10.1029/96GL03311.

Allen, D.J., Hinze, W.J., and Cannon, W.F., 1992, Drainage, topographic, and gravity anomalies in the Lake Superior region: Evidence for a 1100 Ma mantle plume: Geophysical Research Letters, v. 19, p. 2119–2122, https://doi.org/10.1029/92GL02285.

Anderson, D.L., and Natland, J.H., 2005, A brief history of the plume hypothesis and its competitors: Concept and controversy, *in* Foulger, G.R., et al., eds., Plates, Plumes, and Paradigms: Geological Society of America Special Paper 388, p. 119–145, https://doi.org/10.1130/0-8137-2388-4.119.

Aulbach, S., Creaser, R.A., Stachel, T., Chinn, I., and Kong, J., 2017, Re-Os isotope systematics of sulphide inclusions in diamonds from Victor (Superior craton) document mobilisation of volatiles and Os during Rodinia break-up: Abstract 4573 presented at 11th International Kimberlite Conference, Gaborone, Botswana, 18–22 September, 3 p.

Blackburn, T., Bowring, S.A., Schoene, B., Mahan, K., and Dudas, F., 2011, U-Pb thermochronology: Creating a temporal record of lithosphere thermal evolution: Contributions to Mineralogy and Petrology, v. 162, p. 479–500, https://doi.org/10.1007/s00410-011-0607-6.

Blackburn, T.J., Bowring, S.A., Perron, J.T., Mahan, K.H., Dudas, F.O., and Barnhart, K.R., 2012, An exhumation history of continents over billion-year time scales: Science, v. 335, p. 73–76, https://doi.org/10.1126/science.1213496.

Davis, D.W., and Green, J.C., 1997, Geochronology of the North American Midcontinent Rift in western Lake Superior and implications for its geodynamic evolution: Canadian Journal of Earth Sciences, v. 34, p. 476–488, https://doi.org/10.1139/e17-039.

Ernst, R.E., and Bell, K., 2010, Large igneous provinces (LIPs) and carbonatites: Mineralogy and Petrology, v. 98, p. 55–76, https://doi.org/10.1007/s00710-009-0074-1.

Fairchild, L.M., Swanson-Hysell, N.L., Ramezani, J., Sprain, C.J., and Bowring, S.A., 2017, The end of Midcontinent Rift magmatism and the paleogeography of Laurentia: Lithosphere, v. 9, p. 117–133, https://doi.org/10.1130/L580.1.

Heaman, L.M., Kjarsgaard, B.A., and Creaser, R.A., 2004, The temporal evolution of North American kimberlites: Lithos, v. 76, p. 377–397, https://doi.org/10.1016/j.lithos.2004.03.047.

Hutchinson, D.R., White, R.S., Cannon, W.F., and Schulz, K.J., 1990, Keweenaw hot spot: Geophysical evidence for a 1.1 Ga mantle plume beneath the Midcontinent Rift System: Journal of Geophysical Research, v. 95, p. 10,869–10,884, https://doi.org/10.1029/JB095iB07p10869.

Jagoutz, O., and Schmidt, M.W., 2012, The formation and bulk composition of modern juvenile continental crust: The Kohistan arc: Chemical Geology, v. 298–299, p. 79–96, https://doi.org/10.1016/j.chemgeo.2011.10.022.

Landis, S.T., 2016, Thermal evolution of the Superior craton: Accessory phase U-Pb thermochronometry constraints on a diamond-forming event younger than 1.1 Ga near Attawapiskat, Ontario [M.S. thesis]: Santa Cruz, University of California Santa Cruz, 20 p.

Langford, F.F., and Morin, J.A., 1976, The development of the Superior Province of northwestern Ontario by merging island arcs: American Journal of Science, v. 276, p. 1023–1034, https://doi.org/10.2475/ajs.276.9.1023.

Nicholson, S.W., and Shirey, S.B., 1990, Midcontinent Rift volcanism in the Lake Superior region: Sr, Nd, and Pb isotopic evidence for a mantle plume origin: Journal of Geophysical Research, v. 95, p. 10,851–10,868, https://doi.org/10.1029/JB095iB07p10851.

Rivers, T., 1997, Lithotectonic elements of the Grenville Province: Review and tectonic implications: Precambrian Research, v. 86, p. 117–154, https://doi.org/10.1016/S0301-9268(97)00038-7.

Sleep, N.H., 1997, Lateral flow and ponding of starting plume material: Journal of Geophysical Research, v. 102, p. 10,001–10,012, https://doi.org/10.1029/97JB00551.

Smit, K.V., Pearson, D.G., Stachel, T., and Seller, M., 2014a, Peridotites from Attawapiskat, Canada: Mesoproterozoic reworking of Palaeoarchaean lithospheric mantle beneath the Northern Superior superterrane: Journal of Petrology, v. 55, p. 1829–1863, https://doi.org/10.1093/petrology/egu043.

Smit, K.V., Stachel, T., and Stern, R.A., 2014b, Diamonds in the Attawapiskat area of the Superior craton (Canada): Evidence for a major diamond-forming event younger than 1.1 Ga: Contributions to Mineralogy and Petrology, v. 167, p. 962, https://doi.org/10.1007/s00410-013-0962-6.

Swanson-Hysell, N.L., Vaughan, A.A., Mustain, M.R., and Asp, K.E., 2014, Confirmation of progressive plate motion during the Midcontinent Rift's early magmatic stage from the Osler Volcanic Group, Ontario, Canada: Geochemistry Geophysics Geosystems, v. 15, p. 2039–2047, https://doi.org/10.1002/2013GC005180.

Yuan, H., and Romanowicz, B., 2010, Lithospheric layering in the North American craton: Nature, v. 466, p. 1063–1068, https://doi.org/10.1038/nature09332.

Printed in USA

Chapter 2

Accretion of a large LL parent planetesimal from a recently formed chondrule population

Reprinted from:

Edwards, G.H. & Blackburn, T., 2020. "Accretion of a large LL parent planetesimal from a recently formed chondrule population," *Science Advances* 6, eaay8641. DOI: 10.1126/sciadv.aay8641

SCIENCE ADVANCES | RESEARCH ARTICLE

ASTRONOMY

Accretion of a large LL parent planetesimal from a recently formed chondrule population

Graham H. Edwards* **and Terrence Blackburn**

Chondritic meteorites, derived from asteroidal parent bodies and composed of millimeter-sized chondrules, record the early stages of planetary assembly. Yet, the initial planetesimal size distribution and the duration of delay, if any, between chondrule formation and chondrite parent body accretion remain disputed. We use Pb-phosphate thermochronology with planetesimal-scale thermal models to constrain the minimum size of the LL ordinary chondrite parent body and its initial allotment of heat-producing ^{26}Al. Bulk phosphate ^{207}Pb/^{206}Pb dates of LL chondrites record a total duration of cooling ≥75 Ma, with an isothermal interior that cools over ≥30 Ma. Since the duration of conductive cooling scales with parent body size, these data require a ≥150-km radius parent body and a range of bulk initial ^{26}Al/^{27}Al consistent with the initial ^{26}Al/^{27}Al ratios of constituent LL chondrules. The concordance suggests that rapid accretion of a large LL parent asteroid occurred shortly after a major chondrule-forming episode.

INTRODUCTION

The ordinary chondrites (OCs) include the H, L, and LL chondrites, which derive from undifferentiated parent asteroids, or families of parent asteroids, that formed interior to Jupiter's orbit during the accretionary stages of the early Solar System (*1*). Dynamical and thermal models support rapid ($\lesssim$0.1 Ma) accretion time scales for these OC parent bodies within the first 3 Ma of the Solar System's first-forming solids, calcium- and aluminum-rich inclusions (CAIs) (*2*–*6*). After accretion, internal radiogenic heating coupled with conductive cooling produced a metamorphic gradient across planetesimal radii (*7*) that resulted in the observed range of OC petrologic types 3 to 7 (Fig. 1A). The dominant radiogenic heat source in these and other asteroidal bodies was decay of the short-lived radionuclide ^{26}Al (*8*). The initial solar nebula allotment of ^{26}Al relative to stable ^{27}Al, hereafter denoted $(^{26}\mathrm{Al}/^{27}\mathrm{Al})_0$, is inferred from CAIs at a value of $(^{26}\mathrm{Al}/^{27}\mathrm{Al})_0 \sim 5 \times 10^{-5}$ (*9*). The homogenous evolution of ^{26}Al/^{27}Al in the solar nebula is supported by several lines of evidence, including chondrule Al-Mg systematics (*6*, *10*), corroboration of ^{26}Al chronometry with the Hf-W system (*11*), and the modeled efficiency of nebular mixing (*12*). On the basis of this evidence of homogeneity, the extinct radionuclide has also served as a precise chronometer for chondrule formation. Al-Mg dates of OC chondrules indicate production at least 1 Ma after the formation of CAIs with the bulk of production at or after ~2 Ma (*6*), preceding the modeled time frames of OC body accretion by 10^4- to 10^5-year time scales (*4*, *5*). Hf-W system closure in type 4 OCs at ~4 Ma after CAIs constrains the latest time of accretion (*13*). However, ^{207}Pb-^{206}Pb dates determined from sequential leaching experiments of some L group chondrules indicate protracted chondrule formation spanning 0 to 4 Ma after CAIs (*14*, *15*), contradicting the delayed onset and short duration of chondrule formation episodes implied by Al-Mg systematics as well as the assumed homogenous nebular distribution of ^{26}Al relative to CAIs. These two chondrule production time lines predict contrasting relationships between chondrule formation and OC parent body accretion. Al-Mg systematics support a model in which chondrule formation and planetesimal accretion are closely linked temporally and, perhaps, even causally (*16*, *17*), requiring a chondrule-forming environment that accommodates nearly contemporaneous accretion and does not need substantial chondrule transport before accretion. In contrast, chondrule ^{207}Pb-^{206}Pb systematics suggest that OC bodies accreted from a long-lived chondrule population that experienced protracted production and recycling events, requiring numerous chondrule-forming mechanisms active over the course of the first ~5 Ma of the Solar System and substantial chondrule transport before accretion (*15*).

The temporal relationship between chondrule production and accretion may be evaluated by comparing the time-dependent Al-Mg systematics of chondrules with the accretion time frame of their corresponding chondritic parent body. Most of Al-Mg studies of OC chondrules have focused on the rare LL chondrites (*6*), for which the most reliable ^{26}Al ages for OC chondrules come from the very primitive and minimally altered LL3.00 Semarkona. And while ^{26}Al chondrule dates provide minima for the timing of accretion, the OC accretionary time frames have been more precisely inferred from models constrained by the body-scale thermal histories recorded in OCs of various petrologic types (*4*, *5*, *18*). These longer duration (10 to 100 Ma) cooling histories of the OC parent bodies have been directly measured by temperature-sensitive radiometric systems that record the time scales of cooling, as opposed to formation, via the high-temperature diffusive loss and low-temperature retention of radiogenic daughter nuclides. These thermochronologic dates broadly exhibit an inverse correlation between petrologic type and the time scales of cooling that supports an "onion shell" model of planetesimals (*13*, *18*–*20*). The onion shell model invokes gradual conductive cooling of the planetesimal over 10 to 100 Ma time scales from peak metamorphic temperatures through thermochronologic closure temperatures, resulting in cooling dates that scale with depth of residence in the planetesimal. Samples of low petrologic type cooled rapidly near the planetesimal surface and yield old cooling dates, while samples of higher petrologic type cooled slowly at depth and yield young dates (Fig. 1, A and B). Deviation from the onion shell model may occur in the case of type 7 chondrites, which are generally interpreted to reflect impact-induced heating of shallow type 5 to 6 material to the point of incipient melting (*21*, *22*). Thus, type 7 chondrites may be expected to record early cooling consistent with shallow residence or rapid quenching after impact exhumation (Fig. 1).

Arguably, the most important thermochronologic evidence for reconstructing the parent body size and accretionary time frames from >>10-Ma cooling histories in the H and L chondrites has come

---

Department of Earth and Planetary Sciences, University of California Santa Cruz, Santa Cruz, CA 95064, USA.
*Corresponding author. Email: ghedwards@ucsc.edu

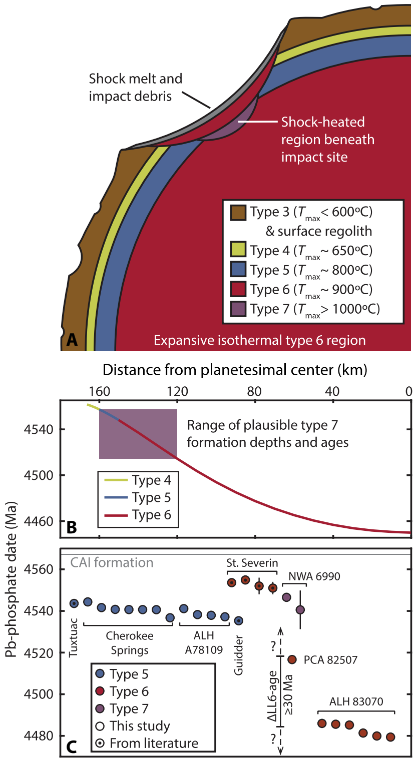

Fig. 1. Model chondrite parent body thermal structure, corresponding model Pb-phosphate cooling dates, and measured LL chondrite Pb-phosphate dates. (**A**) Schematic diagram of the distribution and peak metamorphic temperatures (T_{max}) of chondrite petrologic types in a concentrically zoned onion shell planetesimal. Type 3.0 samples are unmetamorphosed, type 6 samples experienced considerable metamorphism at silicate and FeS subsolidus conditions, and type 7 chondrites reflect heating to suprasolidus temperatures (*21*, *22*, *32*, *51*). Depth ranges of petrologic types 4 to 6 are identified on the basis of peak metamorphic temperature ranges summarized in (*44*). We identify the depth range of type 7 formation following relationships between body size and maximum crater depths permitting planetesimal survival (*49*), assuming a 180-km radius body. (**B**) Pb-phosphate cooling dates simulated by coupled planetesimal thermal and Pb production-diffusion in phosphate models at depths corresponding to petrologic types 4 to 7 in (A). (**C**) Summary of measured LL chondrite Pb-phosphate model cooling dates from this and previous studies (*19*, *23*, *24*). Pb-phosphate dates are calculated using the revised bulk chondritic $^{238}U/^{235}U$ of (*14*). St. Severin and NWA 6990 reflect shallow samples affected by an early impact event and, thus, deviate from onion shell model behavior.

from high-precision ^{207}Pb-^{206}Pb dates of bulk phosphate mineral fractions (hereafter Pb-phosphate dates). The utility of the Pb-phosphate system stems from two key characteristics: (i) Its temporal resolution can resolve protracted conductive cooling histories in excess of 100 Ma that short-lived thermochronologic systems (e.g., Al-Mg and Hf-W) cannot and (ii) its capacity to internally verify closed-system behavior with paired ^{238}U-^{206}Pb and ^{235}U-^{207}Pb systematics (see Results) that is not shared by other long-lived thermochronologic systems (e.g., Ar-Ar and apatite/merrillite fission track). Yet, to date, the Pb-phosphate measurements of LL chondrites were limited and apparently inconsistent with onion shell cooling (*18*, *19*, *23*, *24*). This study resolves these deficits and inconsistencies using Pb-phosphate measurements of five additional LL chondrites coupled with thermal simulations that reveal the thermal history, size, and accretionary time frame of the LL parent planetesimal.

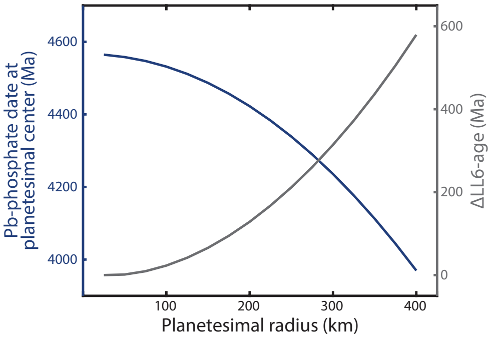

Fig. 2. Relationship between parent body radius and Pb-phosphate dates in a conductively cooling planetesimal. Coupled thermal and Pb production-diffusion in phosphate models predict the Pb-phosphate cooling dates at the center of the simulated planetesimal and the type 5–type 6 boundary as identified by the depth at which the average LL6 temperature (~900°C) (*51*) is reached. The Pb-phosphate date in the center of the body (blue) becomes increasingly younger for larger planetesimal radii, while increasing radius results in larger differences between this youngest LL6 age and the oldest LL6 chondrite at the LL5-LL6 boundary (ΔLL6-age, gray). This simulation assumes a 50-μm phosphate grain radius and instantaneous accretion 2.1 Ma after CAIs for $(^{26}Al/^{27}Al)_0 = 5.23 \times 10^{-5}$.

The thermal evolution of the OC parent planetesimals has been predicted by numerical models that simulate internal radiogenic heating and conductive cooling of a spherical body (*4*, *7*). Here, we compare simulated planetesimal thermal histories with measured Pb-phosphate data by using the output from model thermal histories as inputs to a model simulating Pb production and temperature-dependent diffusion in apatite (*18*, *25*). The onion shell cooling scenario predicts that if a body conductively cooled unperturbed to body-wide closure of the Pb-phosphate system (the nominal closure temperature of Pb diffusion in apatite is ~500°C), the planetesimal center would record the youngest Pb-phosphate date (Fig. 1). Thus, the youngest undisturbed type 6 Pb-phosphate date measured among an OC group provides a minimum estimate of the parent body size. If any unmeasured younger type 6 samples exist and are subsequently measured, the new youngest type 6 date would imply an even larger body (Fig. 2). Further, in thermal models of large undifferentiated bodies, rapid radiogenic heating establishes an expansive isothermal interior at type 6 temperatures (*4*, *7*, *21*) that cools gradually over >>10 Ma (Fig. 1). Since the radius of this isothermal type 6 region will scale with planetesimal size, so too will the duration of its cooling (Fig. 2). Unlike prior studies, we neither assume the size of the simulated planetesimal (*7*) nor fix meteorite samples to particular depths of residence in the parent planetesimal to assess thermochronologic records (*4*), both of which are unknown parameters. Rather, this study interrogates the youngest measured Pb-phosphate age and the measured duration of LL6 Pb-phosphate cooling with the abovementioned model framework to infer the minimum size of the LL parent planetesimal and the corresponding time frame of planetesimal accretion.

RESULTS

Pb-phosphate dates and the LL parent planetesimal thermal structure

Model Pb-phosphate dates from five previously unmeasured LL chondrites are reported in Fig. 1C (tables S1 and S2). The phosphate phases measured here are primarily apatite with minor amounts of merrillite (table S3). These two phases are not readily separated by standard mineral separation methods and represent variable contributions to each measured fraction. However, in the context of the present study, this variability is inconsequential since the similar ionic porosities of apatite and merrillite predict indiscernible Pb closure temperatures (*18*). Grain sizes of phosphate fractions ranged from 10 to 150 μm, with apparent mean effective radii of ~50 μm (fig. S1). We only report dates for phosphate fractions exhibiting ratios of radiogenic Pb (Pb*) to common Pb (Pb_c) >2 (table S1). Relying solely on high Pb*/Pb_c measurements mitigates errors that may result from terrestrial Pb contamination and the treatment of this more radiogenic Pb_c as a primitive initial Solar System composition in model age calculations (fig. S2).

We identify Cherokee Springs as an LL5 following the recommendation of (*26*) on the basis of prominent chondrules and a degree of recrystallization most consistent with a type 5 designation. Such an identification is further supported by its thermochronologic coincidence with other LL5 samples (Fig. 1C). The type 7 classification of Northwest Africa 6990 (NWA 6990) is supported by its granoblastic texture, absence of observable chondrules, and the coarse vein-like texture of some of its phosphates (fig. S3), analogous to those observed in the partly melted H7 Portales Valley (*21*, *27*). The early Pb-phosphate cooling dates of NWA 6990 (LL7) and St. Severin (LL6) suggest a history of shallow residence or impact-induced exhumation to near-surface locations that resulted in early quenching (Fig. 1), consistent with the incipient-melt texture of NWA 6990 and the clastic brecciated texture of St. Severin (*28*). We, thus, ignore St. Severin and NWA 6990 in our assessment of an onion shell cooling history of the LL chondrite parent body. These samples reflect heating and exhumation occurring from one or more >4540 Ma impacts on the LL parent planetesimal surface that did not disrupt the entire LL parent body. Any impact powerful enough to excavate all of the other, onion shell–recording samples must have occurred no sooner than the Pb-phosphate cooling age of ALH 83070 (~4485 Ma; Fig. 1). Excluding the St. Severin breccia, the inverse correlation between LL5-LL6 petrologic types and Pb-phosphate dates indicates an onion shell structure for the LL parent body (Fig. 1C), consistent with the Hf-W systematics of LL chondrites (*13*).

Evaluating Pb-phosphate dates with U-Pb systematics

The radiogenic $^{207}Pb/^{206}Pb$ compositions of OC phosphates permit calculation of Pb-phosphate dates with sub-million-year resolution that precisely record the 10- to 100-Ma cooling histories of OC bodies. Yet, the temperature dependence of diffusive Pb loss from phosphate minerals can leave this system susceptible to perturbation by secondary reheating events from impact-induced shock heating, as observed in the highly shocked L chondrite Sixiangkou (*29*). Thermal conditions associated with shock stages ≥S5 are predicted to be requisite for Pb-phosphate system partial resetting (*18*). The shock stages of the sub–type 7 samples studied here reflect shock stages below S4 based on visual petrographic inspection: Undulatory extinction, planar fractures, and minor opaque shock veins are present, but no pervasive melt veins were observed. Thus, we conclude Pb-phosphate system disruption is unlikely. However, any duration of open-system behavior of Pb in phosphate may be identified by evaluating the concordance between the ^{238}U-^{206}Pb and ^{235}U-^{207}Pb systems in the corresponding phosphate minerals (*19*, *29*). Ancient reheating events may have induced the partial loss of older Pb compositions, resulting in a younger $^{207}Pb/^{206}Pb$ composition and corresponding Pb-phosphate date. In such instances of partial resetting, some Pb* is retained, resulting in Pb compositions that are more radiogenic than would be predicted by Pb*/U ratios alone. The resultant discordance between the ^{238}U-^{206}Pb and ^{235}U-^{207}Pb systems may be used as a sensitive monitor of Pb loss induced by open-system behavior. Pb loss and U gain drive "positive" discordance below U-Pb Concordia, while Pb gain or U loss produce "negative" discordance above U-Pb Concordia. Individual phosphate U-Pb compositions array along a mixing line between the primary cooling age and the age of the open-system event.

Pb_c-corrected U-Pb compositions of LL chondrite phosphate fractions are plotted in Fig. 3 with linear regressions. The model U-Pb compositions plotted in each of these Concordia plots are primarily controlled by the thermal history as described above, yet superimposed on this record are effects resulting from contemporary alteration (discussed below) as well as variation in grain size and μ ($^{238}U/^{204}Pb$). Given the length scale dependence of diffusion, larger phosphate crystals will record older Pb and U-Pb compositions for the same cooling histories as smaller grains. Such behavior is detrimental to linear regression of discordant fractions supposedly recording concurrent cooling ages. In addition, the Pb*/Pb_c ratios of fractions of similar age scale with the μ of those fractions. Given the sensitivity of Pb* compositions to assumed Pb_c for low Pb*/Pb_c fractions (fig. S2), it is imperative that only grains of similar μ are regressed so that apparent patterns do not result from errors in Pb_c corrections. We, thus, reject fractions that show evidence of deviation from other fractions in terms of grain size or μ (Fig. 3). In the case of ALH 83070, we have enough data to regress two separate chords showing highly similar, yet distinct, U-Pb systematics.

The OC phosphate fractions measured in this study all exhibit U-Pb discordance, particularly negative discordance (Fig. 3 and tables S1 and S2). Observations of negative discordance are common among U-Pb studies of OC phosphates (*19*, *30*). However, in all four cases, the discordant measurements define chords that extrapolate lower intercepts nearly within 2σ of 0 Ma (Fig. 3). This is to say, the discordant arrays define mixing lines between the primary cooling ages and contemporary open-system events, which would not alter the composition of the retained Pb. Thus, the Pb* compositions of these phosphate fractions are a pristine record of the original Pb-phosphate cooling ages. Even if the nonzero intercepts reflect ancient shock heating–induced perturbations, the Pb-phosphate system is drastically less sensitive to resetting than the U-Pb system: for short-duration reheating events consistent with the minor level of offset from a nil intercept observed here, the Pb-phosphate date changes by <4% of the respective change in the $^{206}Pb/^{238}U$ date (fig. S4). Thus, if a nonzero intercept reflects a minor perturbation in the U-Pb system due to reheating, the effect on the Pb-phosphate system is likely negligible, confirming that the Pb-phosphate dates record the time scales of primary cooling.

The cause of the observed U-Pb discordance is U or Pb loss from phosphate weathering during terrestrial residence, a model supported

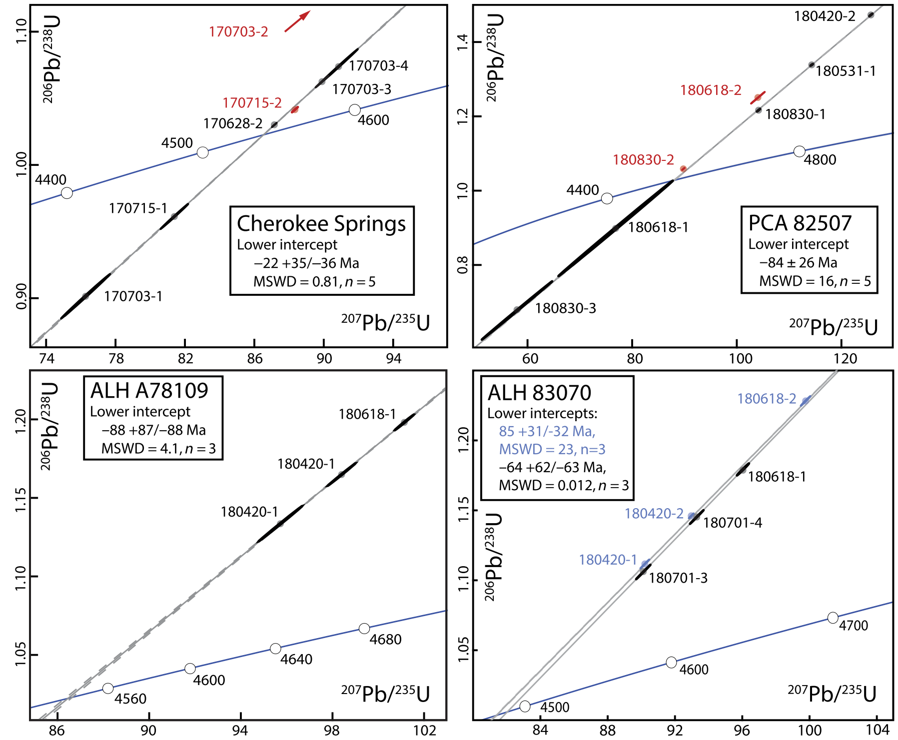

Fig. 3. Concordia diagrams of LL chondrite phosphate U-Pb compositions. Individual phosphate fractions are plotted with gray points and 2σ uncertainty ellipses traced in black. U-Pb Concordia is traced in blue with concordant ages (in Ma) identified by white circles. Fractions exhibit pervasive discordance, especially negative discordance. In all cases, U-Pb measurements plot on chords that project lower intercepts nearly within uncertainty (2σ) of a nil age. Regressions are plotted with light gray lines (uncertainty envelopes dashed). Excluded measurements (red) are rejected following criteria discussed in the text. Regressions are calculated for two groups of phosphate fractions from ALH 83070 (light blue and black). NWA 6990 is excluded because the two phosphate fractions exhibit overlapping U-Pb compositions and a chord cannot be regressed. Linear regressions are calculated (MSWD: Mean squared weighted deviation) and plotted using the algorithms of U-Pb Redux (*42*).

by two observations: (i) Cherokee Springs, the only studied "fall," exhibits the lowest discordance (Fig. 3), and (ii) meteorite phosphates are among the most susceptible phases to dissolution by terrestrial waters (*31*). Any significant U or Pb gain is precluded by the intensive cleaning procedures used in this study (see Supplementary Text). We emphasize here that although we report and interpret regressions of LL phosphate U-Pb data, the modern U and Pb loss renders the apparent U-Pb dates individually meaningless. Rather, the calculated lower intercepts simply provide a test of closed-system behavior. Because the U and Pb loss is all modern, the apparent Pb-phosphate dates accurately reflect primary cooling within the LL chondrite parent planetesimal. Only the ^{207}Pb-^{206}Pb–derived Pb-phosphate dates have adequate temporal resolution of primary cooling and are here interpreted to discern the undisturbed onion shell thermal history of the LL planetesimal.

Interpreting the LL parent planetesimal thermal history

The LL chondrites record a ≥75-Ma Pb-phosphate cooling history and, in contrast to the relatively brief Pb-phosphate cooling time frames of H6 and L6 chondrites (*18*), a >30-Ma LL6 Pb-phosphate cooling period (hereafter ΔLL6-age) defined by the difference in the Pb-phosphate dates in the LL6 chondrites PCA 82507 and ALH 83070 (Fig. 1). Since both of these chondrites record the protracted onion shell cooling of the LL planetesimal, their ΔLL6-age describes the minimum duration of Pb-phosphate cooling for the interior isothermal LL6 region (Fig. 2). The coupled models described above permit simulation of undifferentiated LL planetesimals for a range of sizes and bulk initial ^{26}Al/^{27}Al compositions to characterize the relationship between ΔLL6-age and these two accretionary parameters (Fig. 4). Larger bodies and higher ^{26}Al abundances correspond to longer onion shell cooling durations and large ΔLL6-age values. In contrast, the type 6 region of bodies of both smaller size and lower ^{26}Al allocations cool through Pb-phosphate system closure earlier and more rapidly, thus recording relatively lower ΔLL6-age values. In Fig. 4, the contour consistent with the observed Pb-phosphate date range of the LL6 region (ΔLL6-age = 30 Ma) is traced in gray. Additional parameters are superimposed onto the parameter space in Fig. 4: the minimum planetesimal size constrained by the youngest LL6 (ALH

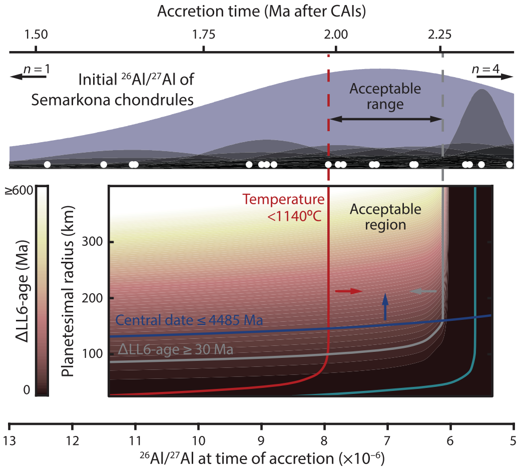

Fig. 4. Pb-phosphate thermochronologic and petrologic constraints on LL parent planetesimal size and ^{26}Al/^{27}Al at the time of accretion. Contours identify the date range of the modeled type 6 region (ΔLL6-age). The measured minimum ΔLL6-age of 30 Ma is traced in gray (see Supplementary Methods). The blue curve traces conditions that yield a date of 4485 Ma (ALH 83070) at the planetesimal center (labeled "Central date"), although younger dates are permissible (blue arrow, Fig. 2). The red curve traces the maximum solidus temperature (1140°C) for LL chondrite compositions (*32*). The teal curve traces the minimum possible metamorphic temperature (800°C) recorded by any LL6 chondrite (*51*). The purple kernel density estimation reflects the initial ^{26}Al/^{27}Al composition of Semarkona chondrules ($n = 24$) with individual chondrule (^{26}Al/^{27}Al)$_o$ means denoted by white dots and corresponding uncertainties plotted as overlying gray Gaussian bells, whereby taller bells reflect lower uncertainty measurements (*10*, *52*–*54*). One chondrule (^{26}Al/^{27}Al)$_o$ ratio ("$n = 1$") exceeds the upper bound of the plotted ^{26}Al/^{27}Al range, and four ("$n = 4$") are below the lower bound. Time line is calculated from (^{26}Al/^{27}Al)$_o$ = 5.23 × 10^{-5}.

83070, ~4485 Ma) and the maximum planetesimal temperature defined by the silicate solidus (*32*). The absence of any achondritic or metallic meteorites that are closely affiliated with the LL chondrite group supports the assumption that bulk silicate melting did not occur in the LL parent body. Further, the early cooling date of NWA 6990 contradicts residence of at least this LL7 in the deep interior of a partially differentiated body. Collectively, the silicate solidus, youngest LL6 Pb-phosphate date, and minimum ΔLL6-age constrain both the minimum planetesimal size and the radiogenic heating budget of the LL parent body. The body must have been large enough and heated sufficiently to yield a central cooling date ≤4485 Ma, and an LL6 Pb-phosphate date range of ≥30 Ma yet remained below the silicate solidus even at its center. These requirements define a parameter space of permissible planetesimal sizes and initial ^{26}Al abundances indicated by the color-coded arrows in Fig. 4.

Minimum size of the LL parent planetesimal

Pb-phosphate and petrologic constraints require a minimum LL chondrite parent body radius of ~150 km (Fig. 4). The initial planetesimal size distribution of the nascent Solar System is a key parameter for N-body simulations of Solar System evolution and is used to both seed initial conditions and evaluate simulation outcomes (*33*, *34*). The canonical model of the early planetesimal size distribution describes a preponderance of bodies ≤50 km in radius produced by a coagulative process of accretion (*3*, *35*). However, the minimum LL parent body radius constrained here exceeds this canonical planetesimal size by a factor of 3. The ≥150-km LL planetesimal minimum size, combined with similar size constraints for the H and L bodies (*18*), supports alternative dynamical models that predict primary planetesimal populations characterized by numerous bodies reaching hundreds of kilometers in radius and formed by turbulent accretion processes (*2*, *34*, *36*). To accommodate a canonical planetesimal size (≤50-km radius) using the thermochronologic data constraints presented herein, our simulations require an unrealistic order of magnitude reduction in the modeled thermal diffusivity of the LL parent body (fig. S5).

Requisite ^{26}Al/^{27}Al at the time of LL parent planetesimal accretion

Large planetesimals require an internal radiogenic heat source to account for the observed metamorphism of all but the shallowest, potentially impact-heated, materials (*37*), and the energy available from ^{26}Al-decay stands out as the dominant heat source by orders of magnitude (*8*). For the minimum planetesimal size required by Pb-phosphate data, the thermal limits in Fig. 4 constrained by the silicate solidus and measured ΔLL6-age identify a range of LL parent body initial ^{26}Al/^{27}Al ratios spanning 6.1 × 10^{-6} to 7.9 × 10^{-6}. This ^{26}Al/^{27}Al range reflects bulk planetesimal ^{26}Al/^{27}Al compositions necessary to satisfy body-scale thermal requirements and is not sensitive to the inherent variability expected in the measurements of discrete particles (e.g., chondrules) that may have experienced complex thermal histories prior to and following accretion. Therefore, if we assume the body accreted in an environment of locally homogenized ^{26}Al/^{27}Al and that accretion was rapid (≲0.1 Ma) as supported by dynamical and thermal models (*2*–*4*), this range defines a 270-ka time frame in which accretion occurred (Fig. 4), independent of assumed (^{26}Al/^{27}Al)$_o$. If the process of accretion was more protracted than dynamic models predict, then a broader time window for accretion could be accommodated, although these conditions are not explored here. The measured and model data presented in Fig. 4 constrain an initial ^{26}Al/^{27}Al range that is insensitive to extreme variations in both body radius and thermal diffusivity for modeled planetesimals that meet the requirements of measured Pb-phosphate cooling dates (Fig. 4 and fig. S5). In summary, the initial ^{26}Al budget defined here provides an estimate for the bulk parent body ^{26}Al/^{27}Al ratio at the time of LL planetesimal accretion that is independent of assumptions of parent body size, thermal diffusivity, accretion time, and (^{26}Al/^{27}Al)$_o$. In contrast, the initial ^{26}Al/^{27}Al determined here is dependent on the assumed temperature limits of the silicate solidus and minimum LL6 peak metamorphic temperature, the assumed bulk LL chondrite Al content, and the assumed heat produced from ^{26}Al decay. Each of these parameters is well constrained (see Materials and Methods). However, changes in the modeled temperature limits expand or contract the constrained bulk planetesimal ^{26}Al/^{27}Al range (fig. S5), while the latter two parameters directly scale the amount of heat available for a given initial ^{26}Al/^{27}Al. Thus, higher bulk Al and heat production values accommodate lower absolute initial ^{26}Al/^{27}Al ratios but do not affect the range of permissible ratios that define the window of accretion times.

DISCUSSION

Thermal limits and Pb-phosphate data define an initial ^{26}Al/^{27}Al composition for the bulk LL parent planetesimal that overlaps with the initial $^{26}Al/^{27}Al$ compositions of >60% of Semarkona ferromagnesian chondrules (Fig. 4). Twenty of the 24 measured ferromagnesian Semarkona chondrules (>80%) record initial $^{26}Al/^{27}Al$ ratios that do not significantly exceed the maximum bulk planetesimal $^{26}Al/^{27}Al$ of 7.9×10^{-6} (Fig. 4). The observed agreement indicates that the bulk LL planetesimal $^{26}Al/^{27}Al$ ratio at the time of its accretion matched most of its constituent chondrules at their respective time of formation, supporting models in which chondrule production is closely followed by, and perhaps even plays a causal role in, chondrite parent body accretion (*16*, *17*). This model is furthermore consistent with evidence from cosmogenic nuclides in chondrules that indicate rapid accretion following chondrule formation (*38*). These results do not rely on assumptions of $^{26}Al/^{27}Al$ homogeneity in the early nebula as has been challenged by (*15*). Our interpretations rely on the observation that the $^{26}Al/^{27}Al$ ratio of the LL planetesimal at the time of accretion matched the ratios of a majority of its constituent chondrules when they formed, implying concurrence of these processes under the parsimonious assumption that the chondrule-forming and accretion environments shared a $^{26}Al/^{27}Al$ reservoir. Rejecting this assumption requires the improbable alternative assumption that, despite forming in reservoirs of variable $^{26}Al/^{27}Al$, ~60 to 85% of the LL chondrules formed with initial $^{26}Al/^{27}Al$ ratios indistinguishable from that of the LL planetesimal to which they were subsequently transported and accreted.

Five of the Semarkona ferromagnesian chondrules exhibit initial $^{26}Al/^{27}Al$ compositions below the minimum initial body value of 6.1×10^{-6}, although three chondrules are within <5% of this minimum. Yet, this discordance is readily explained by evidence for postaccretion alteration of the Al-rich plagioclase and mesostasis that could have partially reset the Al-Mg system in some chondrules (*39*). While Semarkona reflects the least altered sample of the LL parent body, increasingly altered LL3 chondrites (type >3.00) have a greater proportion of chondrules with initial $^{26}Al/^{27}Al$ ratios lower than $\sim 6 \times 10^{-6}$ (e.g., 6). Alternatively, if protracted time frames of accretion and chondrule production overlapped, the shallowest LL3 material, including Semarkona, may reflect the latest materials accreted to the body after the majority of the body was assembled with a $^{26}Al/^{27}Al \geq 6.1 \times 10^{-6}$. In this case, some younger chondrules may have been incorporated along with chondrules that formed earlier. Under both scenarios, outlying low $^{26}Al/^{27}Al$ chondrules are likely not representative of the $^{26}Al/^{27}Al$ ratio during the primary phases of LL chondrule formation and planetesimal accretion. In contrast, the four measured chondrules with initial $^{26}Al/^{27}Al$ ratios significantly (2σ) in excess of 7.9×10^{-6} may reflect earlier generations incorporated into the family of newly formed chondrules that accreted onto the nascent LL parent body. However, the inherited chondrule population is a minority (~15%) of the total population, contradicting models of widespread protracted chondrule formation, storage, and recycling before planetesimal assembly (*14*, *15*).

In summary, the broad concurrence of chondrule formation with the onset of accretion to the LL parent body supports chondrule production mechanisms that may occur several million years after CAIs and without considerable chondrule transport before accretion. Chondrule production models satisfying these requirements include planetesimal bow shocks, molten planetesimals, and high-energy collisions. The evidence we present above for the prevalence of large bodies in the nascent Solar System lends credence to bow shock models that require large planetesimals for efficient chondrule production (*40*). Whatever the mechanism may be, our findings imply that chondrule-forming processes also lead to the rapid accretion of >100-km bodies from subcentimeter particles, thereby leaping the so-called "meter-size barrier" of planetary accretion (*36*) that dynamic models have historically failed to overcome.

MATERIALS AND METHODS

Phosphate extraction and preparation for U and Pb isotopic analysis

Samples of five LL and one L chondrite were provided by the Smithsonian and Antarctic Meteorite collections (tables S1 and S2). NWA 6990 (LL7) was purchased from M. Ouzillou of Skyfall Meteorites. Samples were selected on the basis of available sample size (>5 g of bulk material) and low grades of weathering—Cherokee Springs is a fall, and all Antarctic collection samples are weathering grade A or A/B. The Cherokee Springs, Ladder Creek, and NWA 6990 samples were crushed by hand with an agate mortar and pestle. All other samples were comminuted by electric pulse disaggregation, performed by Zirchron LLC. Crushed and fragmented samples were sieved to <500 μm, and phosphates were purified from bulk rock by magnetic and heavy liquid separations. The purified phosphate mineral separates were recovered from nonmagnetic fractions (1.4 A magnetic field, 15° slope) that sank in LST heavy liquid (2.85 g/cm^3). Given the slight acidity of LST (pH ~ 4), care was taken to promptly remove phosphate fractions from LST, minimizing exposure to <60 min. Multigrain phosphate mineral fractions were selected for isotopic analysis by optical microscopy, whereby phosphate grains were included on the basis of the absence of apparent inclusions and minimal apparent alteration or mechanical damage (fig. S1).

In an effort to minimize contributions of laboratory Pb blank and labile Pb on grain surfaces, special effort was taken to clean fractions before addition of tracer and dissolution. Selected grains were loaded into 3-ml Savillex PFA vials and rinsed two times with 18 megohm·cm deionized ultrapure water before sonication for 30 min in 500 μl of 5% ultrapure acetic acid at room temperature (Ladder Creek fractions 170608-1 and 170608-3 were sonicated for only 15 min). The acetic acid leachate was pipetted off, and leached grains were rinsed a minimum of five times with ultrapure water to dilute and remove dissolved Pb before the grains were transferred to clean 3-ml PFA vials. These "cleaned" fractions were then spiked with EARTHTIME mixed ^{202}Pb-^{205}Pb-^{233}U-^{235}U tracer (*41*) and dissolved in 450 to 600 μl of 6N HCl for 12 hours on a 130°C hotplate. Dissolved samples were converted to 1.1 N HBr for column introduction, and U and Pb were separated from other elements using an HBr/HCl anion exchange recipe in a 50-μl microcolumn. Pb was eluted in 6N HCl and ultrapure water, and Pb purity was improved by passing >500 μl of 1.1 N HBr over the column before eluting Pb.

To test the efficacy of the 5% acetic acid leaching procedure, fractions of ALH 83070 (180701-1 and 180701-2) were treated with an alternative cleaning method, identical to the above method with the exception that the grains were sonicated for 30 min in ultrapure water rather than 5% acetic acid. For these fractions and concurrently treated (acetic leached) fractions, the "leachates" were collected and spiked with an in-house calibrated ^{205}Pb-^{233}U-^{235}U tracer, converted to 3N HCl, and U and Pb were purified using a 50-μl microcolumn HCl-based anion-exchange chemistry. Results confirming the efficacy of the acetic acid leaching treatment are presented in the Supplementary Text.

U and Pb isotopic data were measured with isotope dilution–thermal ionization mass spectrometry (ID-TIMS) conducted on the

UCSC IsotopX X62 Thermal Ionization Mass Spectrometer. U and Pb separates were loaded onto zone-refined (99.999% purity) Re ribbon with a Si gel–0.035 M H_3PO_4 activator. Pb was measured with a peak jumping method on a Daly photomultiplier ion counting system. U was measured as an oxide by static collection on Faraday cup detectors connected to 10^{12} ohm resistance amplifier cards. Mass fractionations were calculated and corrected internally using tracer isotope pairs ^{202}Pb-^{205}Pb and ^{233}U-^{235}U. Isotopic measurements were corrected for contributions from blank, spike, and initial Pb_c (table S4), and model U-Pb and Pb-Pb dates were calculated with U-Pb Redux software (*42*). Total procedural blanks were measured throughout the duration of data acquisition and ranged from 0.3 to 1.0 pg for Pb and <0.2 pg for U. Ratios of ^{204}Pb/^{206}Pb and ^{207}Pb/^{206}Pb were calculated using calculations summarized in (*42*) to correct ID-TIMS isotopic measurements for blank and spike contributions and propagate uncertainties. We used the primordial Pb_c composition of Canyon Diablo troilite (*43*) to correct for initial Pb_c. We chose this composition over that suggested more recently by (*44*) given its long history of use in OC phosphate studies (*18*, *19*, *23*, *24*) and the fact that for measurements with $Pb^*/Pb_c > 2$ (the threshold at which we calculate Pb-phosphate dates), the effect on the calculated age is negligible (fig. S2).

Thermal and Pb production-diffusion in phosphate models

Coupled planetesimal-scale thermal and Pb production-diffusion in phosphate codes use the model framework of (*18*), for which the same discussions of model structure, inputs, and constants therein apply here. Simulations assume instantaneous accretion of bodies following dynamical model predictions of planetesimal accretion from subkilometer objects on 10^4- to 10^5-year time scales for models characterized by both turbulent and coagulative accretion (*2*, *3*, *34*). We assumed an updated ^{26}Al heat production of 0.355 W/kg (*45*).We adapted physical and thermal constants to better represent LL chondrite compositions: We used an Al content of 1.18 weight % (*46*), a bulk density of $\rho = 3210$ kg/m^3 (*47*), and a bulk specific heat capacity of $c_p = 950$ J kg^{-1} K^{-1}, scaled linearly on the basis of relative Fe-Ni metal abundance (*48*) from values calculated for H and L chondrites at 600 K (*49*). We used an H chondrite upper-bound thermal conductivity of $k = 4$ W m^{-1} K^{-1} after (*49*) since variation in this parameter is predominantly controlled by shock-induced porosity rather than compositional differences (*50*). Nonetheless, we explored the effects of varying thermal parameters by exploring variation in k (fig. S5). Given the relationship of thermal diffusivity (κ) to these parameters via $\kappa = k \cdot \rho^{-1} \cdot c_p^{-1}$, variations in any one variable also test the same proportional magnitude of variation in any other variable, since the κ term is ultimately used in thermal calculations.

SUPPLEMENTARY MATERIALS

Supplementary material for this article is available at http://advances.sciencemag.org/cgi/content/full/6/16/eaay8641/DC1

REFERENCES AND NOTES

1. P. Vernazza, B. Zanda, R. P. Binzel, T. Hiroi, F. E. DeMeo, M. Birlan, R. Hewins, L. Ricci, P. Barge, M. Lockhart, Multiple and fast: The accretion of ordinary chondrite parent bodies. *Astrophys. J.* **791**, 120 (2014).
2. A. Johansen, J. S. Oishi, M.-M. Mac Low, H. Klahr, T. Henning, A. Youdin, Rapid planetesimal formation in turbulent circumstellar disks. *Nature* **448**, 1022–1025 (2007).
3. S. J. Weidenschilling, Initial sizes of planetesimals and accretion of the asteroids. *Icarus* **214**, 671–684 (2011).
4. S. Henke, H.-P. Gail, M. Trieloff, W. H. Schwarz, Thermal evolution model for the H chondrite asteroid-instantaneous formation versus protracted accretion. *Icarus* **226**, 212–228 (2013).
5. N. Sugiura, W. Fujiya, Correlated accretion ages and ε^{54}Cr of meteorite parent bodies and the evolution of the solar nebula. *Meteorit. Planet. Sci.* **49**, 772–787 (2014).
6. J. Pape, K. Mezger, A.-S. Bouvier, L. P. Baumgartner, Time and duration of chondrule formation: Constraints from ^{26}Al-^{26}Mg ages of individual chondrules. *Geochim. Cosmochim. Acta* **244**, 416–436 (2019).
7. M. Miyamoto, N. Fujii, H. Takeda, Ordinary chondrite parent body: An internal heating model. *Lunar Planet. Sci. Conf.* **12B**, 1145–1152 (1981).
8. A. Ghosh, S. J. Weidenschilling, H. Y. McSween, A. Rubin, Asteroidal heating and thermal stratification of the asteriod belt, in *Meteorites and the Early Solar System II*, D. S. Lauretta, H. Y. McSween, Eds. (University of Arizona Press, 2006), pp. 555–566.
9. B. Jacobsen, Q.-z. Yin, F. Moynier, Y. Amelin, A. N. Krot, K. Nagashima, I. D. Hutcheon, H. Palme, ^{26}Al–^{26}Mg and ^{207}Pb–^{206}Pb systematics of Allende CAIs: Canonical solar initial ^{26}Al/^{27}Al ratio reinstated. *Earth Planet. Sci. Lett.* **272**, 353–364 (2008).
10. J. Villeneuve, M. Chaussidon, G. Libourel, Homogeneous distribution of ^{26}Al in the Solar System from the Mg isotopic composition of chondrules. *Science* **325**, 985–988 (2009).
11. G. Budde, T. S. Kruijer, T. Kleine, Hf-W chronology of CR chondrites: Implications for the timescales of chondrule formation and the distribution of ^{26}Al in the solar nebula. *Geochim. Cosmochim. Acta* **222**, 284–304 (2018).
12. A. P. Boss, Mixing in the solar nebula: Implications for isotopic heterogeneity and large-scale transport of refractory grains. *Earth Planet. Sci. Lett.* **268**, 102–109 (2008).
13. J. L. Hellmann, T. S. Kruijer, J. A. Van Orman, K. Metzler, T. Kleine, Hf-W chronology of ordinary chondrites. *Geochim. Cosmochim. Acta* **258**, 290–309 (2019).
14. J. N. Connelly, M. Bizzarro, A. N. Krot, Å. Nordlund, D. Wielandt, M. A. Ivanova, The absolute chronology and thermal processing of solids in the solar protoplanetary disk. *Science* **338**, 651–655 (2012).
15. J. Bollard, J. N. Connelly, M. J. Whitehouse, E. A. Pringle, L. Bonal, J. K. Jørgensen, Å. Nordlund, F. Moynier, M. Bizzarro, Early formation of planetary building blocks inferred from Pb isotopic ages of chondrules. *Sci. Adv.* **3**, e1700407 (2017).
16. G. Budde, T. Kleine, T. S. Kruijer, C. Burkhardt, K. Metzler, Tungsten isotopic constraints on the age and origin of chondrules. *Proc. Natl. Acad. Sci. U.S.A.* **113**, 2886–2891 (2016).
17. C. M. O. Alexander, J. N. Grossman, D. S. Ebel, F. J. Ciesla, The formation conditions of chondrules and chondrites. *Science* **320**, 1617–1619 (2008).
18. T. Blackburn, C. M. O. Alexander, R. Carlson, L. T. Elkins-Tanton, The accretion and impact history of the ordinary chondrite parent bodies. *Geochim. Cosmochim. Acta* **200**, 201–217 (2017).
19. C. Göpel, G. Manhès, C. J. Allègre, U-Pb systematics of phosphates from equilibrated ordinary chondrites. *Earth Planet. Sci. Lett.* **121**, 153–171 (1994).
20. M. Trieloff, E. K. Jessberger, I. Herrwerth, J. Hopp, C. Fiéni, M. Ghélis, M. Bourot-Denise, P. Pellas, Structure and thermal history of the H-chondrite parent asteroid revealed by thermochronometry. *Nature* **422**, 502–506 (2003).
21. A. W. Tait, A. G. Tomkins, B. M. Godel, S. A. Wilson, P. Hasalova, Investigation of the H7 ordinary chondrite, Watson 012: Implications for recognition and classification of Type 7 meteorites. *Geochim. Cosmochim. Acta* **134**, 175–196 (2014).
22. H. Takeda, T. J. Huston, M. E. Lipschutz, On the chondrite-achondrite transition: Mineralogy and chemistry of Yamato 74160 (LL7). *Earth Planet. Sci. Lett.* **71**, 329–339 (1984).
23. A. Bouvier, J. Blichert-Toft, F. Moynier, J. D. Vervoort, F. Albarède, Pb-Pb dating constraints on the accretion and cooling history of chondrites. *Geochim. Cosmochim. Acta* **71**, 1583–1604 (2007).
24. J. H. Chen, G. J. Wasserburg, The isotopic composition of uranium and lead in Allende inclusions and meteoritic phosphates. *Earth Planet. Sci. Lett.* **52**, 1–15 (1981).
25. D. J. Cherniak, Diffusion in accessory minerals: Zircon, titanite, apatite, monazite and xenotime. *Rev. Mineral. Geochemistry.* **72**, 827–869 (2010).
26. E. Jarosewich, M. Brian, Chemical analyses with notes on one mesosiderite and seven chondrites. *Geochim. Cosmochim. Acta* **33**, 411–416 (1969).
27. A. Ruzicka, M. Killgore, D. W. Mittlefehldt, M. D. Fries, Portales Valley: Petrology of a metallic-melt meteorite breccia. *Meteorit. Planet. Sci.* **40**, 261–295 (2005).
28. A. Ruzicka, J. M. Friedrich, R. Hugo, M. Hutson, Macro- and microstructures in ordinary chondrites: Implcations for impact deformation and annealing processes, in *46th Lunar and Planetary Science Conference*, Woodlands, Texas, 16 to 20 March 2015, pp. 1544.
29. S. Li, W. Hsu, The nature of the L chondrite parent body's disruption as deduced from high-pressure phases in the Sixiangkou L6 chondrite. *Meteorit. Planet. Sci.* **53**, 2107–2122 (2018).
30. A. Blinova, Y. Amelin, C. Samson, Constraints on the cooling history of the H-chondrite parent body from phosphate and chondrule Pb-isotopic dates from Estacado. *Meteorit. Planet. Sci.* **42**, 1337–1350 (2007).
31. G. Crozaz, C. Floss, M. Wadhwa, Chemical alteration and REE mobilization in meteorites from hot and cold deserts. *Geochim. Cosmochim. Acta* **67**, 4727–4741 (2003).

32. T. E. Johnson, G. K. Benedix, P. A. Bland, Metamorphism and partial melting of ordinary chondrites: Calculated phase equilibria. *Earth Planet. Sci. Lett.* **433**, 21–30 (2016).
33. K. J. Walsh, A. Morbidelli, S. N. Raymond, D. P. O'Brien, A. M. Mandell, A low mass for Mars from Jupiter's early gas-driven migration. *Nature* **475**, 206–209 (2011).
34. J. N. Cuzzi, R. C. Hogan, W. F. Bottke, Towards initial mass functions for asteroids and Kuiper belt objects. *Icarus* **208**, 518–538 (2010).
35. J. E. Chambers, Planetary accretion in the inner Solar System. *Earth Planet. Sci. Lett.* **223**, 241–252 (2004).
36. A. Morbidelli, W. F. Bottke, D. Nesvorný, H. F. Levison, Asteroids were born big. *Icarus* **204**, 558–573 (2009).
37. J. D. Gilmour, M. J. Filtness, Dissipation of the Solar System's debris disk recorded in primitive meteorites. *Nat. Astron.* **3**, 326–331 (2019).
38. A. S. G. Roth, K. Metzler, L. P. Baumgartner, I. Leya, Cosmic-ray exposure ages of chondrules. *Meteorit. Planet. Sci.* **51**, 1256–1267 (2016).
39. J. A. Lewis, R. H. Jones, Primary feldspar in the Semarkona LL3.00 chondrite: Constraints on chondrule formation and secondary alteration. *Meteorit. Planet. Sci.* **54**, 72–89 (2019).
40. M. A. Morris, A. C. Boley, in *Chondrules*, S. S. Russell, H. C. Connolly, A. N. Krot, Eds. (Cambridge Univ. Press, 2018), pp. 375–399.
41. D. J. Condon, B. Schoene, N. M. McLean, S. A. Bowring, R. R. Parrish, Metrology and traceability of U-Pb isotope dilution geochronology (EARTHTIME Tracer Calibration Part I). *Geochim. Cosmochim. Acta* **164**, 464–480 (2015).
42. N. M. McLean, J. F. Bowring, S. A. Bowring, An algorithm for U-Pb isotope dilution data reduction and uncertainty propagation. *Geochem. Geophys. Geosyst.* **12**, Q0AA18 (2011).
43. M. Tatsumoto, R. J. Knight, C. J. Allegre, Time differences in the formation of meteorites as determined from the ratio of lead-207 to lead-206. *Science* **180**, 1279–1283 (1973).
44. J. Blichert-Toft, B. Zanda, D. S. Ebel, F. Albaràde, The Solar System primordial lead. *Earth Planet. Sci. Lett.* **300**, 152–163 (2010).
45. J. Castillo-Rogez, T. V. Johnson, M. H. Lee, N. J. Turner, D. L. Matson, J. Lunine, ^{26}Al decay: Heat production and a revised age for Iapetus. *Icarus* **204**, 658–662 (2009).
46. K. Lodders, B. Fegley, in *Planetary Scientist's Companion* (Oxford Univ. Press, 1998), pp. 290–331.
47. D. T. Britt, S. J. G. J. Consolmagno, Stony meteorite porosities and densities: A review of the data through 2001. *Meteorit. Planet. Sci.* **38**, 1161–1180 (2003).
48. T. L. Dunn, G. Cressey, H. Y. McSween, T. J. McCoy, Analysis of ordinary chondrites using powder X-ray diffraction: 1. Modal mineral abundances. *Meteorit. Planet. Sci.* **45**, 123–134 (2010).
49. K. Yomogida, T. Matsui, Physical properties of ordinary chondrites. *J. Geophys. Res.* **88**, 9513–9533 (1983).
50. C. P. Opeil, G. J. Consolmagno, D. J. Safarik, D. T. Britt, Stony meteorite thermal properties and their relationship with meteorite chemical and physical states. *Meteorit. Planet. Sci.* **47**, 319–329 (2012).
51. V. Slater-Reynolds, H. Y. McSween Jr., Peak metamorphic temperatures in type 6 ordinary chondrites: An evaluation of pyroxene and plagioclase geothermometry. *Meteorit. Planet. Sci.* **40**, 745–754 (2005).
52. N. T. Kita, H. Nagahara, S. Togashi, Y. Morishita, A short duration of chondrule formation in the solar nebula: Evidence from ^{26}Al in Semarkona ferromagnesian chondrules. *Geochim. Cosmochim. Acta* **64**, 3913–3922 (2000).
53. N. G. Rudraswami, J. N. Goswami, B. Chattopadhyay, S. K. Sengupta, A. P. Thapliyal, ^{26}Al records in chondrules from unequilibrated ordinary chondrites: II. Duration of chondrule formation and parent body thermal metamorphism. *Earth Planet. Sci. Lett.* **274**, 93–102 (2008).
54. I. D. Hutcheon, R. Hutchison, Evidence from the Semarkona ordinary chondrite for ^{26}Al heating of small planets. *Nature* **337**, 238–241 (1989).
55. G. J. MacPherson, G. R. Huss, Petrogenesis of Al-rich chondrules: Evidence from bulk compositions and phase equilibria. *Geochim. Cosmochim. Acta* **69**, 3099–3127 (2005).
56. P. Vermeesch, On the visualisation of detrital age distributions. *Chem. Geol.* **312–313**, 190–194 (2012).
57. P. Vermeesch, IsoplotR: A free and open toolbox for geochronology. *Geosci. Front.* **9**, 1479–1493 (2018).
58. C. Y. Ho, M. W. Ackerman, K. Y. Wu, S. G. Oh, T. N. Havill, Thermal conductivity of ten selected binary alloy systems. *J. Phys. Chem. Ref. Data Monogr.* **7**, 959–1178 (1978).
59. A. H. Jaffey, K. F. Flynn, L. E. Glendenin, W. C. Bentley, A. M. Essling, Precision measurement of half-lives and specific activities of ^{235}U and ^{238}U. *Phys. Rev. C* **4**, 1889–1906 (1971).
60. J. Hiess, D. J. Condon, N. McLean, S. R. Noble, ^{238}U/^{235}U systematics in terrestrial uranium-bearing minerals. *Science* **335**, 1610–1614 (2012).

Acknowledgments: We thank L. Welzenbach, T. McCoy, and both the Smithsonian and Antarctic Meteorite collections for access to samples. We also thank C. Alexander, F. Nimmo, and M. Telus for feedback; S. Burgess and N. McLean for help in developing Pb reduction algorithms; and P. Colosi for laboratory assistance. The manuscript was improved by the reviews of K. Mezger and two anonymous reviewers. **Funding:** The University of California Santa Cruz Chancellor fellowship partly funded G.H.E. during this study. T.B. acknowledges funding from general startup funds at the University of California, Santa Cruz. **Author contributions:** G.H.E. conducted experiments with oversight and guidance from T.B. G.H.E. and T.B. analyzed the data and drafted and finalized the manuscript. **Competing interests:** All authors declare that they have no competing interests. **Data and materials availability:** All data needed to evaluate the conclusions in the paper are present in the paper and/or the Supplementary Materials. Additional data related to this paper may be requested from the authors.

Submitted 24 July 2019
Accepted 22 January 2020
Published 15 April 2020
10.1126/sciadv.aay8641

Citation: G. H. Edwards, T. Blackburn, Accretion of a large LL parent planetesimal from a recently formed chondrule population. *Sci. Adv.* **6**, eaay8641 (2020).

Chapter 3

Uranium-series isotopes as tracers of physical and chemical weathering in glacial sediments from Taylor Valley, Antarctica

3.1 Abstract

The McMurdo Dry Valleys of Antarctica reflect extensive glacial erosion, yet currently exhibit hyperarid polar conditions characterized by limited chemical and physical weathering. Yet, efficient chemical weathering occurs when moisture is available, and polythermal subglacial conditions may accommodate ongoing mechanical weathering and valley incision. Taylor Valley hosts several Pleistocene glacial drift deposits that record prior expansions of Taylor Glacier and sediment redistribution, if not production. We measure U-series isotopes in the fine-grained sediments of these drifts to assess the timescales of physical weathering and subsequent chemical alteration. The isotopes ^{238}U, ^{234}U, and ^{230}Th are sensitive to both chemical and physical fractionation processes in sedimentary systems, including the physical fractionation of daughter isotopes by energetic recoil following radioactive decay. By comparing mathematical models of U-series response to chemical weathering and physical fractionation processes with isotopic measurements, we show that Pleistocene drift sediments record histories of significant chemical alteration. However, fine-grained sediments entrained in the basal ice of Taylor Glacier record only brief chemical alteration and U-series fractionation, indicating comparatively recent sediment comminution and active incision of upper Taylor Valley by Taylor Glacier over the Pleistocene. In addition, the results of this study emphasize the utility of U-series isotopes as tracers of chemical and physical weathering in sedimentary and pedogenic systems, with particular sensitivity to radionuclide implantation by α-recoil from high-U authigenic phases into lower-U detrital phases. This process has occurred extensively in >200 ka drifts but to a lesser degree in younger deposits. U-series α-recoil implantation may be an important physicochemical process with chronometric implications in other hyperarid and saline sedimentary systems, including analogous Martian environments.

3.2 Introduction

The Antarctic McMurdo Dry Valleys (MDV) represent an extreme environment where hyperarid, polar conditions predict limited physical and chemical weathering processes seemingly at odds with other evidences for remarkably active weathering. Low temperatures and low moisture content of MDV soils predict extremely gradual chemical weathering rates that have preserved some soils for millions of years with minimal chemical alteration (Bockheim, 1997; Campbell and Claridge, 1981). Similarly, physical erosion is limited by low precipitation rates (<100 mm annually) that restrict fluvial erosion and low annual temperatures (< 14 °C, Doran et al., 2002) that predict frozen and non-erosive subglacial conditions. In contrast, vigorous aqueous chemical weathering is observed at sites where liquid water occurs (Lyons et al., 2021; Marra et al., 2017), and deeply incised glacial valleys with thick sedimentary fills indicate of a history of significant physical weathering.

The erosive capacities of glaciers are closely linked to climate (Hallet et al., 1996). Warm and wet climates accommodate basal temperatures at the pressure melting point of water that lubricate the "warm" glacier base, increase sliding velocities, and promote efficient comminution of bedrock and sediment transport. Cold and arid climates, such as those of the MDV, promote "cold-based" glaciers that remain frozen at their beds, resulting in relatively limited sediment production or transport (Cuffey et al., 2000). To reconcile the glacially erosive history of the MDVs with their contemporary climate, models of MDV evolution invoke post-Paleocene ($\lesssim$55 Ma) climates that facilitated warm-based glacial conditions and active denudation until ~15 Ma (Denton et al., 1993; Sugden and Denton, 2004), after which transition to a hyperarid polar climate induced widespread cold-based conditions among MDV glaciers. Under this model, contemporary advances of MDV glaciers only rearrange pre-Pliocene glacial deposits by cold-based processes.

This model of MDV glaciers, however, is not consistent with observations of Taylor Valley, where several lines of evidence imply at least partly wet-based, or polythermal, conditions beneath Taylor Glacier, an outlet of the East Antarctic Ice Sheet (EAIS; Fig 3.1). Extensive englacial debris observed in Taylor Glacier implies melt-freeze processes of sediment entrainment (e.g. Mager et al., 2007). A high reflectivity zone of liquid water has been detected by ice penetrating radar in an overdeepening beneath Lower Taylor Glacier (Hubbard et al., 2004). Despite predicted basal temperatures of ≤ -7 °C at this location, subsolidus conditions might be facilitated by high salinities, a scenario supported by the presence of Blood Falls, a subglacially fed hypersaline brine seep at the glacier's terminus (e.g. Badgeley et al., 2017). Such polythermal basal conditions would help to explain the extensive Pleistocene drift sheets deposited by Taylor Glacier (Section 3.2.1). To further explore and resolve these conflicting evidences of both active and restricted weathering, we use U-series isotopes to interrogate the combined physical and chemical weathering histories of glacial sediments from Taylor Valley.

3.2.1 Modern setting & depositional history of Taylor Valley

Taylor Glacier flows from the Taylor Dome of the EAIS into upper Taylor Valley, terminating in the saline proglacial Lake Bonney (Fig. 3.1). The Asgard Range and Kukri Hills border the valley to the North and South, respectively, and several alpine glaciers flow into Taylor Valley from these peaks (Fig. 3.1). In upper (western) Taylor Valley, Taylor Glacier sits atop Beacon Supergroup sedimentary rocks (primarily sandstones), and sills of Jurassic Ferrar dolerite and Quaternary mafic volcanics crop out at higher elevations (e.g. Hall et al., 2000). Taylor Glacier and the nearby alpine glaciers are currently at their maximum Holocene extents but no longer advancing (Denton et al., 1989; Hall et al., 2000; Fountain et al., 2006). At least four glacial drift sheets record prior Quaternary advances of Taylor Glacier (Denton et al., 1970), and Bockheim et al. (2008) summarized the distribution of these "Taylor" drifts, as shown in Figure 3.1. The most ancient drift deposits are identified as Taylor-IVb, younging to Taylor-I, which reflects the contemporary advancement of Taylor Glacier. For brevity, we adapt the nomenclature of Bockheim et al. (2008) such that we use Taylor-III to describe the combined Taylor-III / Taylor-IVa grouping and Taylor-IV to describe the older Taylor-IVb unit.

Multiple geochronometric techniques constrain the depositional ages of the Taylor drift sheets. Taylor-IV drifts reflect the earliest recorded Taylor Glacier advance at $\leq$2.7 Ma based on ^{40}Ar-^{39}Ar ages of underlying volcanics (Wilch et al., 1993). The minimum age of Taylor-IV advance is constrained by cosmogenic ^{10}Be dates from correlated moraines in nearby Arena Valley that require moraine emplacement before 1.5 Ma (Brook et al., 1993). Thus, Taylor-IV represents an ancient advance (or series of advances) of Taylor Glacier between 2.7 and 1.5 Ma, during which the ice margin reached elevations $>$800 m above the contemporary valley floor. The deposition ages of the younger Taylor-II and -III drifts are constrained by both cosmogenic exposure ages from Arena Valley moraines (Brook et al., 1993) and U-Th ages of lacustrine carbonates (Higgins et al., 2000; Hendy et al., 1979). The lacustrine carbonate U-Th dates formed when the Ross Ice Shelf dammed Taylor Valley during West Antarctic Ice Sheet expansion, forming a paleolake that flooded elevations up to $\sim$300 m in western Taylor Valley (Hall et al., 2000; Toner et al., 2013), which coincided with periods of reduced Taylor Glacier and EAIS extent (Higgins et al., 2000). In contrast, the cosmogenic exposure ages record boulder emplacement during Taylor Glacier expansion. Despite minor inconsistencies, these chronologies indicate deposition of Taylor-III between 450–250 ka and Taylor-II after 70 ka (Fig. 3.2).

These combined Taylor drift chronologies validate a correlation between drift depositional age and contemporary elevation (Fig. 3.2). While this relationship is typical of glacial systems, it has important implications for the ice volume and erosional histories of Taylor Glacier. Under the canonical model of near-nil Plio-Pleistocene MDV glacial erosion rates, the drift age-elevation relationship reflects a decreasing trend in Taylor Glacier ice volumes during periods of EAIS expansion over the course of the Pleistocene. An alternative endmember model invokes Pleistocene incision by Taylor Glacier, whereby the polythermal subglacial conditions of Taylor Glacier accommodated significant erosion of the valley floor over the course of the Pleistocene (Fig. 3.2). While permitting variability in ice volumes, this model relates the age-elevation relationship of Taylor drifts to more consistent high-stand ice volumes and a gradually deepening valley floor. Although the known timescales of drift emplacement do not offer the ability to resolve these two plausible scenarios, we use the radiometric properties of the U-series system in fine-particles to discern whether the fine sediments that comprise Taylor drifts record ancient (>1.5 Ma) or recent (<500 ka) incision.

3.2.2 The effects of physical and chemical weathering on U-Series systematics of fine particles

The weathering of fine particles may be generally divided into two components. A physical component of mechanical comminution from larger particles to finer particles and a chemical component of mineral dissolution and precipitation. Subglacial comminution processes tend to converge on sand-to-silt-sized particles (2000–5 µm diameters) that resist further physical comminution to smaller sizes (Haldorsen, 1981). Hence, in the context of this study we expect that physical weathering happens only early on in the history of most glacigenic sand-to-silt-sized sediments, after which chemical weathering takes on an enhanced role as primary detrital material is dissolved and replaced by authigenic mineral phases.

In closed geologic systems over >1.5 Ma durations, the ingrowth and out-growth of intermediate daughter products cause the relative amounts of isotopes in the ^{238}U decay series to converge on equilibrium values, nominally secular equilibrium (SE), which is represented by parent-daughter activity ratios of unity (e.g. (^{234}U/^{238}U)=1). After any perturbation that drives the system out of SE, a parent-daughter ratio converges within ~1 % of SE after 6 half-lives ($t_{1/2}$) of the shorter-lived isotope. In the present study, we consider the U-series isotopes ^{238}U, ^{234}U, and ^{230}Th. Although ^{238}U decays to ^{234}U via the short-lived isotopes ^{234}Th ($t_{1/2} \sim 24$ days) and ^{234}Pa ($t_{1/2} \sim 1.2$ minutes), their lifetimes are geologically negligible, and we treat ^{238}U as decaying directly to ^{234}U. The following sections consider how chemical and physical weathering processes affect the ^{230}Th-^{234}U-^{238}U systematics of fine-grained particles derived from ancient bedrock in SE.

The effects of physical weathering on the ^{238}U decay series

Following the reduction of material to silt-sized (<50 µm diameter) particles, the U-series system progresses into disequilibrium because of the physical fractionation of intermediate daughter products by energetic recoil of radiogenic nuclides during radioactive α-decay. Within mineral grains, as radionuclides (e.g. ^{238}U and ^{234}U) undergo α-decay, an α-particle (^{4}He nucleus) is ejected from the parent nucleus and the newly produced radiogenic daughter nuclide recoils in the opposite direction through the surrounding crystalline matrix in response to the energetic α-emission. In framework silicates (e.g. feldspars and quartz), this recoil distance is approximately ~35 nm, though it varies slightly among the different α-decay products (Semkow, 1991). If the decay occurs near the surface of the mineral grain, the daughter nuclide may be ejected from the grain and lost from the mineral system (Fig. 3.3). Thus, fine-grained particles (<50 µm diameter) exhibit a measurable reduction in (^{234}U/^{238}U) below SE due to α-recoil loss of ^{234}U after ^{238}U decay (Ku, 1965; DePaolo et al., 2006). Although α-recoil ejection of ^{234}U occurs in large crystals (Kigoshi, 1971), the disequilibrium only becomes detectable in grains with diameters <50 µm, where the particles have a sufficiently high surface-area-to-volume ratio to incur ^{234}U loss in amounts measurable by modern mass spectrometric methods (> 0.1 %). After 1.5 Ma (six half-lives of ^{234}U) the (^{234}U/^{238}U) reaches a new equilibrium controlled by the sediment grain size and surface morphologies (Fig. 3.3). Fine particles comminuted prior to 1.5 Ma maintain a low (^{234}U/^{238}U) that reflects this antiquity. Prior authors (e.g. Lee et al., 2010; Cogez et al., 2018) have speculated that the same principles apply to subsequent intermediate daughter nuclides with shorter half-lives, such as ^{230}Th, which would exhibit similar behavior to ^{234}U, differing only in that they converge on slightly different grain morphology-controlled equilibrium values (Fig. 3.3). Thus, this time-dependent α-recoil loss from freshly comminuted particles forms the theoretical foundation of U-series comminution dating (DePaolo et al., 2006).

The rate and degree of daughter nuclide depletion is dependent on a particle's physical properties, which dictate the proportion of decays that result in α-recoil ejection. Two simple approaches summarize these properties with a "fractional loss factor" f_m, where m denotes the mass of the radiogenic nuclide, e.g. 234 for ^{234}U. The first formulation, Equation 3.1a (after Semkow, 1991; DePaolo et al., 2006), calculates the fractional loss factor for a given radiogenic nuclide as a function of the effective recoil length (L_m), the sediment specific surface area (S), and the sediment density (ρ). The second formulation, Equation 3.1b (after Lee et al., 2010), replaces the S term with grain size parameters (Eq. 3.1c, after Anbeek et al., 1994): diameter (d), a dimensionless grain shape factor (K, after Cartwright, 1962), and a surface roughness factor (λ_r):

$$f_m = (L_m \cdot S \cdot \rho)/4 \tag{3.1a}$$

$$f_m = (L_m \cdot K \cdot \lambda_r)/(4d) \tag{3.1b}$$

$$S = (\lambda_r \cdot K)/(\rho \cdot d) \tag{3.1c}$$

The f parameter for some modeled silicate grain may then be combined with standard U-series decay series equations (e.g. Bateman, 1910), to model the grain's time-dependent radioisotopic evolution.

$$\frac{dN_{238}}{dt} = -\lambda_{238} N_{238} \tag{3.2a}$$

$$\frac{dN_{234}}{dt} = -\lambda_{234} N_{234} + (1 - f_{234}) \lambda_{238} N_{238} \tag{3.2b}$$

$$\frac{dN_{230}}{dt} = -\lambda_{230} N_{230} + (1 - f_{230}) \lambda_{234} N_{234} \tag{3.2c}$$

These equations may be solved numerically, assuming initial isotopic compositions, which for sediment freshly comminuted from an ancient bedrock source are expected to reflect SE, (^{234}U/^{238}U) =(^{230}Th/^{238}U)=1. In this idealized scenario, the activity ratios for the various grain sizes decrease from unity to a new, grain-size defined equilibrium composition (Fig. 3.3). With a well-constrained knowledge of f_{234}, one may calculate a "comminution age" from the measured (^{234}U/^{238}U).

Chemical weathering effects on the U-series system

Accurate and precise comminution dates have remained elusive because sedimentary systems are also characterized by chemical weathering and authigenic mineral forming processes that affect the U-series system. The most straightforward process of chemical weathering is dissolution of primary "detrital" material, which releases ions from the crystalline matrix of detrital minerals into the surrounding (typically aqueous) environment. Given the association of ^{234}U with damaged zones in mineral lattices, this isotope is preferentially leached compared to its parent ^{238}U (Andersen et al., 2009). In contrast, the typically lower solubility of Th predicts an excess of ^{230}Th relative to ^{234}U and ^{238}U following chemical weathering (Chabaux et al., 2003; Suresh et al., 2013; Menozzi et al., 2016; Cogez et al., 2018). To account for simple chemical weathering by dissolution and leaching of primary detrital mineral, an additional weathering rate term k may be incorporated into Equation 3.2 to capture the combined effects of silicate dissolution and α-recoil ejection of U-series nuclides, following the equations of Chabaux et al. (2003), Dosseto and Schaller (2016), and Cogez et al. (2018):

$$\frac{dN_{238}}{dt} = -k_{238}N_{238} - \lambda_{238}N_{238} \tag{3.3a}$$

$$\frac{dN_{234}}{dt} = -k_{234}N_{234} - \lambda_{234}N_{234} + (1 - f_{234})\lambda_{238}N_{238} \tag{3.3b}$$

$$\frac{dN_{230}}{dt} = -k_{230}N_{230} - \lambda_{230}N_{230} + (1 - f_{230})\lambda_{234}N_{234} \tag{3.3c}$$

where the value of k varies from isotope to isotope based on how readily it is weathered (e.g. $k_{234} > k_{238} > k_{230}$).

However, chemical weathering is a bidirectional process, comprised of both dissolution of detrital phases and precipitation of authigenic phases. Generally, authigenic phases are precipitated from aqueous solution and incorporate cations from the aqueous and sedimentary environment, including U and Th. Since surface waters are typically characterized by supra-SE (^{234}U/^{238}U) compositions (Andersen et al., 2009, and references therein), authigenic phases tend to increase the (^{234}U/^{238}U) of sediments (Martin et al., 2015). Martin et al. (2015) showed that sequential chemical extractions that dissolve specific authigenic phases such as oxide species, carbonates, and organic compounds each effectively remove U and change the (^{234}U/^{238}U) of the insoluble residues. In addition, non-silicate authigenic phases are complimented by authigenic silicate minerals, including “clay” minerals. While this term is also used to describe particle sizes <4 µm, we will use the term exclusively in a mineralogical sense to describe authigenic clay minerals. Like their non-silicate counterparts, authigenic clay minerals form by aqueous precipitation following dissolution of silicate minerals and therefore reflect $(^{234}U/^{238}U)>1$ parent-water compositions. Insoluble Th will preferentially leave the water column by adsorbing onto particle surfaces or partitioning into authigenic phases, resulting in elevated $(^{230}Th/^{238}U)$. Indeed, Menozzi et al. (2016) have shown that silicate clay minerals can persist through leaching techniques and impart elevated $(^{234}U/^{238}U)$ and $(^{230}Th/^{238}U)$. The degree of excess above SE scales with the U and Th content of authigenic phases well as the duration and extent of weathering (Fig. 3.3C,D).

Authigenic phases may also affect the U-series systems of adjacent detrital grains by implanting ^{234}U and ^{230}Th after α-recoil across the interface between the authigenic and detrital phases (Fig. 3.3A). As long as the adjacent authigenic phase is more uraniferous than the detrital phase, there will be a net positive flux of daughter isotopes to the detrital phase across the interface, enriching the detrital grain in ^{234}U and ^{230}Th (Fig. 3.3C,D). If this authigenic phase is soluble in any pretreatments or chemical extractions prior to final sediment digestion, the ^{234}U- and ^{230}Th-depleted authigenic phase is lost in these steps, leaving only the insoluble and ^{234}U-^{230}Th-enriched detrital phase. The longer this contact between the high-U soluble phase and lower-U insoluble phase persists, the higher the $(^{234}U/^{238}U)$ and $(^{230}Th/^{238}U)$ in the insoluble phase, until a new long-term equilibrium is reached (Fig. 3.3C,D). The process of α-recoil implantation has been observed between the high- and low-U phases of igneous rocks (Tanaka et al., 2015) and primary silicate phases of igneous regolith (Menozzi et al., 2016), but its role in sedimentary systems has only been speculated upon (Lee et al., 2010; Plater et al., 1992).

3.2.3 Exploring the timescales of physical and chemical weathering in Taylor Valley with U-series isotopes

This study expands on the aforementioned mathematical and theoretical models of sedimentary U-series geochemistry to predict the U-series evolutions of sediments subjected to α-recoil loss, chemical dissolution, authigenic mineral formation, and α-recoil implantation. We use these models to interpret the ^{230}Th-^{234}U-^{238}U systems of proglacial and englacial sediments from Taylor Valley in the context of chemical and physical weathering processes. Within this framework, we explore the potential of using U-series records of both physical fractionation and chemical alteration to discern the timescales of fine-particle production in Taylor Valley.

The physical weathering of Taylor Valley has been dominated by glacial wear processes. Beneath glaciers, mechanical crushing and abrasion readily comminute coarse material to sand- and silt-sized particles, respectively, that resist further comminution (Haldorsen, 1981). The chemical weathering environment of Taylor Valley and the greater MDV system is less straightforward and highly dependent on the availability of water. Outside of lakes and the hyporheic zones of streams, chemical weathering in the MDV occurs very slowly, limited largely to the oxidation of ferrous minerals and minor production of authigenic clays (Campbell and Claridge, 1981). Older soils at higher elevations in Taylor Valley are indurated with abundant soluble salts that refute any recent aqueous chemical alteration (Bockheim, 2002). However, at lower elevations of Taylor Valley, most salt accumulations reflect the evaporative residues of prior paleolake highstands, such as when the lake levels rose to >300 m elevations in western Taylor Valley during Marine Isotope Stage 2 (Toner et al., 2013; Hall et al., 2000). Contemporarily, areas of liquid water saturation, facilitated by high salinities that depress the freezing temperature, reflect far more active chemical weathering, evidenced by an increase in the clay fraction and sediment surface areas (Campbell and Claridge, 1981; Marra et al., 2017). Indeed, chemical alteration rates in saturated zones of Taylor Valley sediment indicate more efficient chemical weathering than previously thought for the MDVs (Lyons et al., 2021).

Given the heterogenous nature of chemical weathering in Taylor Valley, we take especial care to simplify our study of Taylor Valley sediment by limiting the myriad mechanisms of mechanical weathering. For each drift sample, we focus on two mineralogical groups: framework silicates (quartz and feldspars) and clays. Quartz and feldspar are generally more resilient to chemical weathering than phyllosilicates and mafic phases and offer an added benefit of a reasonably well-constrained and relatively consistent α-recoil length (Sun and Semkow, 1998). To further ensure the specificity of our study, we use chemical cleaning procedures that remove known non-silicate authigenic phases. We concurrently explore the U-series behavior of clay minerals to explore how these authigenic silicates are related to detrital materials. Finally, by examining the three-isotope ^{230}Th-^{234}U-^{238}U system, we gain the added insight of the integrated chemical and physical processes that fractionate ^{230}Th in addition to those physical processes involved in the fractionation of the two U isotopes. Within this framework, we test the hypothesis that the U-series systems of silts in Taylor Valley record the timeframes of physical comminution and authigenic chemical processes. We identify and explore the relevant weathering processes affecting U-series isotopes and use these to resolve whether efficient subglacial comminution beneath Taylor Glacier ceased after warmer Pliocene conditions or has continued throughout the Pleistocene.

3.3 Materials and Methods

3.3.1 Field methods and sample handling procedures

We collected drift sediment and debris-rich glacial ice from Taylor Valley during the austral spring of 2017 (Fig. 3.1). We sampled drift sediments from pits dug to ∼50 cm depth below the surface, taking care to sample beneath any apparent sedimentary fabrics and indurated salt crusts to ensure the samples represented original till deposits that had minimally interacted with surface snowmelt or running water. Debris-rich ice samples were chipped out of Taylor Glacier using a steel ice-chisel, targeting bands of sediment-laden basal ice. Ice samples were stored in plastic bags at −20 °C before melting under laboratory conditions.

3.3.2 Laboratory and analytical methods

Grain-size separation and mineralogical purification

This study targeted 10–45 and 75–125 µm diameter sediments of quartz-feldspar and clay mineralogy. We first separated silt-sized grains from bulk sediment by dry-sieving to grain diameters of <38 µm, 38–45 µm, and 75–125 µm (only the 90–125 µm fraction was recovered for sample Taylor-III). The <10 µm component was removed from the <38 µm aliquot by wet sieving. The 10–38 µm separates were dry-sieved to 10–20 µm and 20–38 µm diameter ranges with a Gilsonic UltraSiever sonic sieving device.

For each size range, we removed clay mineral phases with a Stokes settling hydraulic separation. We preferentially removed clay mineral phases by vigorously swirling sediments in water and allowing grains to settle for ≥10 minutes before pouring off suspended material and repeating the procedure $\geq$3 times. We recovered both the clay-rich components decanted with the supernatant (slow hydraulic settling), as well as the clay-poor "detrital" component (rapid hydraulic settling). The clay-rich components were leached without further purifications, whereas the settled, detrital components were further purified with magnetic and density separations.

We removed Fe-bearing phases with a Frantz magnetic separator (0.6 A magnetic field and 17 °C slope). We removed phosphate and zircon mineral phases by density separation in 2.85 g cm^{-3} LST heavy liquid. Purified quartz-feldspar mineralogies were recovered from the buoyant component. For samples Taylor-I, Taylor-II, and Taylor-IV, density separations lasted for 1 hour of settling time, whereas density separations for Taylor-III lasted for 10 minutes aided by low-speed centrifugation. These procedures yielded purified quartz-feldspar separates of three discrete "silt" grain size ranges, 10–20 µm, 20–38 µm, and 38–45 µm, as well as a "sand" grain size range of 75–125 µm. Mineralogical purity was confirmed by visual inspection under a binocular picking microscope.

For the englacial sediments of the Taylor-I sample, sediments were frozen within ice. Prior to mineralogical separations, we melted the ice in the presence of <0.05 M Ethylenediaminetetraacetic acid (EDTA) buffered with ammonia to pH>10 before sediments were dried and underwent mineralogic purification. This treatment had no discernible effect on U-series isotopics, as verified by an aliquot of Taylor-IV that was subjected to the same EDTA treatment (see sample TV-IV-R3L-5, Table S3.2, Supplementary Data).

Sequential chemical extraction or “leaching” methods

Prior to digestion and isotope dilution, some samples were chemically cleaned with a sequential extraction method, or “leaching” method for brevity, using reagents that preferentially dissolve specific secondary mineral phases, while leaving the silicate phases unperturbed. Leaching methods were modified from sequential extraction protocols that target various authigenic phases (Tessier et al., 1979; Poulton and Canfield, 2005; Lee et al., 2010), and each step is briefly outlined in Table 3.1. For each leach step, samples reacted with 50 ml of reagent.

Leaching procedures were performed in acid-cleaned (heated 7N HNO_3 bath for >12) PFA centrifuge tubes. All reactions were continuously agitated throughout the prescribed duration: room temperature reactions with a vertical rotation shaker and reactions held at 90 °C with an orbital shaker dry-bath. Following each step, the samples were centrifuged and the leachate decanted. The residue was rinsed and briefly agitated with 50 mL of ultra-pure water, centrifuged, and the rinse decanted. This rinsing procedure was repeated 3 times before advancing to the next leaching step. For all “leached” fractions reported herein, the 5-step procedure was repeated for a total of either 3 or 5 iterations.

Isotope dilution, digestion, elemental purification, and mass spectrometry

The following methods were performed in a class 1000 clean lab using triple-distilled or ultra-pure trace metal grade reagents. All beakers and digestion vessels were acid-cleaned. All PFA beakers fluxed a 14M HF - 3N HNO_3 solution followed by 6M HCl for $\geq$24 hours at 110 °C. Microwave digestion vessels underwent full digestion cycles (described below) with cleaning acid, followed by fluxing in 6M HCl.

Prior to digestion, sediment fractions were triple-rinsed with 50 ml of ultrapure water. After rinsing, the sediment was dried, massed, and added to a dissolution vessel and spiked with an in-house-calibrated $^{229}\mathrm{Th}-^{236}\mathrm{U}$ tracer prior to dissolution. Typical fraction masses were ∼250 mg for leached sediment and 50–100 mg for unleached sediment. Samples were digested one of two ways: 1. in a mixture of 6 ml concentrated HF and 200 µl concentrated HNO_3 for 15 minutes at 150 °C with an Anton Paar MultiWave Go microwave digestion system, or 2. in a mixture of 5 ml concentrated HF and 1 ml concentrated HNO_3 in a covered 15 ml PFA beaker on a 110 °C hotplate for 48 hours. No systematic difference in isotopic composition or blank were observed between these two methods. Microwave-digested solutions were transferred to 15 ml PFA beakers following dissolution.

Digested solutions were evaporated to dryness and redissolved in 5 ml 3M HCl with 250 µl 2.5M HCl saturated with H_3BO_3 to eliminate fluoride complexes. For this and all subsequent rehydration steps, samples were fluxed for several hours to allow complete dissolution and chemical equilibration. After elimination of fluoride complexes, we evaporated the solutions and rehydrated them with 5 ml 1M HCl. This process was repeated twice to evaporate residual H_3BO_3. To convert samples to nitrate salts for column chemistry, samples were twice evaporated and rehydrated with 5 ml of 7M HNO_3. Samples were finally evaporated and rehydrated in 3 ml 7M HNO_3 for introduction to column chemistry.

Th and U were purified from bulk solution with a two-column process. Primary separations were performed on a 2 ml resin bed of AG 1-X8 (200–400 µm mesh) resin. Samples were loaded onto cleaned and preconditioned resin in 3 ml of 7M HNO_3. We eluted matrix elements with 3 ml 7M HNO_3 followed by 0.5 ml 6M HCl. Then, Th was eluted in 4 ml 6M HCl, followed by U in 4 ml water. The eluted loading acid and 7M HNO_3 washes contained up to 50% of the total Th, so these elutions were reserved and reloaded onto the column (6 ml total) and washed with 3 ml 7M HNO_3 followed by 0.5 ml 6M HCl. The Th was eluted in 4 ml 6M HCl and combined with the initial Th elution. U and Th elutions were then evaporated, converted to nitrate salts by fluxing in 0.5 ml concentrated HNO_3, and then dried and rehydrated in 1 ml 7M HNO_3 for introduction to U and Th clean-up columns, following the methods of Blackburn et al. (2020). Purified U and Th elutions were evaporated to dryness and rehydrated in 250 µl 30% H_2O_2 and fluxed for $\geq$1 hour to eliminate any organic materials inherited from the resin. Finally, samples were evaporated just to dryness with trace H_3PO_4 for mass spectrometric analysis.

Isotopic compositions of U and Th were measured on the IsotopX X62 Phoenix Thermal Ionization Mass Spectrometer in the UC Santa Cruz W.M. Keck Isotope Laboratory. We loaded U onto Re ribbon (99.99% purity) with a Si gel-0.035M H_3PO_4 activator and measured isotopes as oxides using a dynamic Faraday-Daly method (Blackburn et al., 2020). Th was loaded with 1 µl 5% HNO_3 onto Re ribbon coated with graphite. Isotopes of Th were measured as a metal using a peak hopping method. Isotopes ^{230}Th and ^{229}Th were measured on the Daly-photomultiplier complex, while the high abundance of ^{232}Th required measurement by Faraday cup. A ^{230}Th-^{232}Th Faraday-Daly correction was calibrated from repeated measurements (n=30) of the standard UCSC ThA and the accepted composition of Rubin (2001). However, given Daly-Photomultiplier gain drift on the timescales of individual measurements, the Faraday-Daly Th ratios (i.e. ^{232}Th/^{229}Th and ^{232}Th/^{230}Th) are not consistently reproducible (Appendix Fig. C.1). Therefore, all ^{232}Th data are only semi-quantitative.

We corrected all measurements for instrument fractionation and tracer and blank contributions with an algorithm that fully propagates uncertainties. Concurrent total procedural blanks were measured throughout the study, confirming U and Th blanks reliably $\ll$1 ng, with typical blank amounts of both U and Th of $\sim$100 pg. We calculated model blank compositions from long-term means of total procedural blanks. Blank corrections did not significantly affect isotope ratios. The accuracy and reproducibility of ^{230}Th-^{234}U-^{238}U isotope measurements were verified by concurrent digestion, chemical purification, and measurement of USGS rock standard BCR-2 (Appendix Fig. C.1).

3.3.3 Major element compositions and chemical index of alteration

In addition to U-Th isotopes, we measured the major element compositions of several leached detrital (rapid hydraulic settling) aliquots. We digested $\sim$10 mg fractions using a scaled-down version of the digestion methods for isotopic analyses described above. Dissolved fractions were converted to nitrate salts, diluted, and atomic abundances measured via inductively-coupled plasma optical emission spectrometry (ICP-OES) at the University of California Santa Cruz Plasma Analytical Laboratory. Unknown major element abundances were calculated relative to a standard of concurrently prepared dissolutions of BCR-2. We validated the accuracy of these measurements by reproducing accepted major element compositions of the AThO rock standard. We use the accepted values from the GeoReM database for the major element compositions of both standards (Jochum et al., 2005).

In addition to reporting major element compositions, we calculate and report two forms of the chemical index of alteration (CIA). The CIA is calculated after Nesbitt and Young (1982), using oxide weight percentages: $CIA =$

$100 \times [Al_2O_3 \,/\, (Al_2O_3 + CaO^* + Na_2O + K_2O)]$, where CaO^* describes the weight percent CaO contained within the silicate fraction (i.e. carbonate has been removed). As all samples digested for major element analyses underwent the leaching procedures described above, all measured Ca can confidently be associated with only the silicate fraction. We also calculate the CIA (molar) from the molar oxide abundances (Goldberg and Humayun, 2010): $\mathrm{CIA\,(molar)} = Al_2O_{3(\mathrm{molar})} \,/\, (CaO^*_{(\mathrm{molar})} + Na_2O_{(\mathrm{molar})} + K_2O_{(\mathrm{molar})}\,)$.

3.3.4 Computational methods and U-series evolution codes

U-series isotopic evolution codes written in the Julia language numerically solve the equations outlined in the following section. The code is open-source and available at `https://github.com/grahamedwards/comminution`. Fractional loss factors (f_{230} and f_{234}) are calculated with Equation 3.1b from parameters summarized in Table 3.2 (after Lee et al., 2010).

3.4 Theory and Calculation

3.4.1 Interpreting weathering histories from ^{230}Th-^{234}U-^{238}U compositions of multiple sediment fractions

The dependency of the post-comminution U-series evolution of silts on the fractional loss factor (e.g. Fig. 3.3 and Eq. 3.2) highlights the importance of accurately constraining the f_m term (Equation 3.1) in order to accurately simulate and interpret sedimentary U-series behavior. Yet, neither theoretical estimations of f_m (Lee et al., 2010) nor direct measurements of grain morphological properties (Handley et al., 2013) accurately and precisely determine this value. In this section, we present a novel approach to account for variability in the f_m value with

^{230}Th-^{234}U-^{238}U systematics.

Assuming the idealized α-recoil only model of Equation 3.2, simulations of paired (^{230}Th/^{238}U)-(^{234}U/^{238}U) compositions array nearly linearly for grain diameters $\geq$10 µm and grain-shape parameters as in Table 3.2. While this relationship is not truly linear in a mathematical sense, it is effectively linear at the scale of analytical uncertainties (>0.1 %) for all f_m values representative of >1 µm diameter grains, yielding regressions with coefficients of determination of $r^2 > 0.999$ and modeled slopes varying by $< 1\%$. Thus, for a given comminution age, the (^{234}U/^{238}U) and (^{230}Th/^{238}U) values of chemically unaltered sediments should plot along isochrons, where older ages yield steeper slopes that converge on a maximal slope when grain size-controlled equilibrium is reached. For sediments of a single age, the position of each fraction on the isochron is a function of its effective f_m values: a small f_m (i.e. large grain diameter) results in activity ratios close to unity, and a large f_m (i.e. small grain diameter) result in highly depleted activity ratios. Therefore, any variations among the free parameters used in calculating these f_m values only move compositions along the slope of the array, eliminating the need for a precise f_m value by matching multiple isotopic measurements with an f_m-independent trend.

In Taylor Valley, however, chemical alteration processes may obscure pristine detrital signals and perturb this theoretical comminution isochron. Thus, this approach of interpreting the ^{230}Th-^{234}U-^{238}U systems of multiple sediment fractions with different grain sizes offers a new framework for interpreting the U-series evolutions of sediments in light of both physical and chemical weathering histories. While previous studies (Suresh et al., 2013; Cogez et al., 2018) have considered the role of ^{230}Th as a tracer of weathering processes in the interpretation of U-series α-recoil processes, our approach is more similar to that used in chronological models of regolith chemical weathering (Dosseto et al., 2012; Chabaux et al., 2013) that fit generalized weathering parameters to (^{234}U/^{238}U)-(^{230}Th/^{238}U) data. The present study unifies these two approaches to interpret (^{234}U/^{238}U)-(^{230}Th/^{238}U) data with coupled physical and chemical weathering models that correspond to specific weathering processes. In the following section we establish a quantitative model that explores dissolution-based weathering, authigenic effects, and α-recoil processes, providing a more nuanced approach to interpreting these U-series systematics.

3.4.2 Modeling ^{230}Th-^{234}U-^{238}U in fine particles in a physical and chemical framework

The following mathematical models build on equations for U-series comminution dating as well as regolith weathering models (Dosseto et al., 2012; Suresh et al., 2013; Chabaux et al., 2013). We assume that subglacial physical comminution is rapid and grain sizes are not further reduced (Haldorsen, 1981). We begin with the mathematical framework of Cogez et al. (2018), summarized in Equation 3.3, that models α-recoil ejection and loss to weathering. We treat chemical alteration of detrital silicate minerals as a bidirectional process, wherein U-series isotopes are not only removed by the dissolution of primary silicate phases (e.g. quartz and feldspar) but also added by authigenic mineral production. Our model tracks the evolution of the leach-insoluble sedimentary component, so meaningful authigenic replacement in this model is limited to silicate phases that are similarly leach-insoluble. Such authigenic silicates include amorphous silica, as observed in subglacial aqueous environments (Graly et al., 2020; Blackburn et al., 2019, 2020), and clay minerals such as illite, smectite, and kaolinite, each of which are observed as chemical weathering products in Taylor Valley sediments (Marra et al., 2017).

We assume a constant weathering rate and 1:1 (by mass) chemical replacement of detrital quartz-feldspar minerals with leach insoluble authigenic phases. This simplifying assumption likely overestimates the effect but is approximately consistent with evidence for significant chemical silicate weathering in water-saturated MDV sediments (Lyons et al., 2021), abundant clay production in Antarctic subglacial systems (Graly et al., 2020), and observations of the Greenland ice sheet subglacial system, where twice the amount of rock represented as dissolved solute is precipitated as clay minerals (Graly et al., 2016). Furthermore, the ^{230}Th-^{234}U-^{238}U measured herein require significant addition of supra-SE material, not merely loss of U-series isotopes (see Section 3.5.3), justifying a model of efficient authigenic addition of ^{230}Th-^{234}U-enriched material.

To model this chemical replacement, we replace the weathering rate $-kN_m$ terms in Equation 3.3 with $-k \cdot N_m^d + k \cdot N_m^a$ or $k(N_m^a - N_m^d)$, where the a and d superscripts respectively denote the authigenic and detrital phases of the simulated sediment. However, since chemical weathering occurs at the surface of particles, we scale k (in g m^{-2} a^{-1}) by the specific surface area S (in m^2 g^{-1}) calculated from Equation 3.1c for each modeled particle. While detrital material is being replaced by authigenic material within this model, we still consider this altered grain "detrital", in contrast to a soluble authigenic rind.

We also explore the effects of U-series radionuclide implantation by α-recoil from a high-U authigenic rind adjacent to the surface of the detrital grain. Prior studies have proposed the relevance of this α-recoil process in U-series systematics of sedimentary systems (Lee et al., 2010; Plater et al., 1992; Menozzi et al., 2016). Tanaka et al. (2015) have shown that α-recoil implantation of ^{230}Th and ^{234}U between phases in igneous rocks is common, and implanted nuclides are resilient to leaching with strong acid (6M HCl). On these grounds, we assert that this process is likely relevant in detrital-authigenic systems as well.

To quantitatively model implantation effects, we must first calculate an effective implantation factor for the authigenic rind that describes the fraction of α-decays that result in both ejection from the rind and implantation into the detrital material, analogous to the fractional loss terms (f_m) for α-recoil loss. To accomplish this, we relate the specific surface area of the detrital component (S^d) to the surface area of the authigenic rind (S^r, a specific surface area relative to the mass of the detrital component) scaled by the fraction of the sediment in contact with the rind (q).

$$S^r = qS^d \tag{3.4}$$

Since the product of specific surface area and density is equivalent to the quotient of absolute surface area (A_S) and volume (V), or volumetric surface area,

$$S\rho = \left(\frac{A_S}{V}\right), \tag{3.5}$$

we can approximate $S^r\rho^r$ using Equations 3.5 and 3.4 and a value z that represents the thickness of the authigenic rind.

$$S^r\rho^r = \frac{qS^d}{qS^d z} = \frac{1}{z} \tag{3.6}$$

By substituting Equation 3.6 into Equation 3.1a we calculate a fractional implantation factor (f_m^{impl}):

$$f_m^{impl} = \frac{L_m}{4z} \tag{3.7}$$

Thus, the rate of implantation of daughter nuclides (in moles) into the detrital component (N_D^d) may be calculated from the molar abundance of the parent isotope in the rind (N_P^r) and its decay constant (λ_P),

$$\frac{dN_D^d}{dt} = \frac{L_D}{4z}\lambda_P N_P^r, \tag{3.8}$$

And the evolution of the authigenic rind (dN_D^r) itself may be modeled with

$$\frac{dN_D^r}{dt} = \left(1 - \frac{L_D}{4z}\right)\lambda_P N_P^r \tag{3.9}$$

To simplify our calculations of the detrital grains, we use specific molar abundances (i.e. moles/gram) normalized to the mass of the detrital component. To convert specific molar abundance of the rind to a specific molar abundance relative to the mass of the detrital component we need the mass ratio of the authigenic (M^r) and detrital (M^d) components. Recalling that our parameters S^d and S^r are both normalized to the mass of the detrital component, we reformulate the mass-ratio with Equation 3.4 such that

$$\frac{M^r}{M^d} = S^r z\, \rho^r = q\, S^d z\, \rho^r \tag{3.10}$$

Hence, we can rewrite Equation 3.8 in terms of specific molar abundances (denoted with $\hat{N}$ to differentiate from the N for absolute abundances):

$$\frac{d\hat{N}_D^d}{dt} = \frac{L_D}{4}\lambda_P \hat{N}_P^r (q\, S^d \rho^r) \tag{3.11}$$

with S^d calculated from Equation 3.1c.

Including terms for chemical alteration and implantation, we rewrite Equations 3.3a–3.3c in terms of specific molar abundances:

$$\frac{d\hat{N}_{238}^d}{dt} = S^d k_{238}(\hat{N}_{238}^a - \hat{N}_{238}^d) - \lambda_{238}\hat{N}_{238} \tag{3.12a}$$

$$\begin{aligned}\frac{d\hat{N}^d_{234}}{dt} = \quad & S^d k_{234}(\hat{N}^a_{234} - \hat{N}^d_{234}) + \\ & \lambda_{234}\hat{N}_{234} + (1 - f_{234})\lambda_{238}\hat{N}_{238} + \\ & [(L_{234}/4)\, q\, S^d\, \rho^r]\lambda_{238}\hat{N}^r_{238}\end{aligned} \tag{3.12b}$$

$$\begin{aligned}\frac{d\hat{N}^d_{230}}{dt} = \quad & S^d k_{230}(\hat{N}^a_{230} - \hat{N}^d_{230}) + \\ & \lambda_{230}\hat{N}_{230} + (1 - f_{230})\lambda_{234}\hat{N}_{234} + \\ & [(L_{230}/4)\, q\, S^d\, \rho^r]\lambda_{234}\hat{N}^r_{234}\end{aligned} \tag{3.12c}$$

We numerically solve Equations 3.12a–3.12c to simulate the U-series evolutions of detrital particles that experience α-recoil loss, authigenic replacement, and α-recoil implantation. We explore the effects of these various processes on the U-Th isotopic compositions of silts from the Taylor-III drift in section 3.5.4. In conclusion of this discussion, we note that f_m values, as calculated here, implicitly assume homogenous distribution of parent radionuclide throughout the modeled grain. While this is almost certainly the case for decay of ^{238}U to ^{234}U, as time progresses, the distribution of ^{234}U becomes depleted in the outer ~35 nm of grain radii, violating this assumption for calculations of ^{234}U and ^{230}Th and potentially resulting in inaccuracies. However, overcoming this would require a geometrically complex model beyond the scope of the present study. We identify this as a key goal for future studies of sedimentary U-series systematics.

3.5 Results and Discussion

3.5.1 Major element compositions and weathering indices

We report the chemical index of alteration, or CIA, and molar chemical index of alteration, or CIA (molar), for leached detrital (rapid Stokes settling) separates of Taylor Valley sediments in Table 3.3 (raw major element data in Table S3.1, Supplementary Data). Traditional CIA values (after Nesbitt and Young, 1982) for detrital Taylor drift sediments are comparable to those calculated for bulk sediments (leached of carbonate and organic phases) of similar grain sizes (<63 µm) collected proximal to the terminus of Howard Glacier in central Taylor Valley (Marra et al., 2017). However, while the CIA>50 compositions ought to imply evidence of weathering, this index is developed for intermediate to felsic rocks (Nesbitt and Young, 1982; Marra et al., 2017). Since the nearby Ferrar dolerite is a sediment source rock, the observed CIA>50 values may instead reflect the incorporation of anorthitic plagioclase feldspar grains (CIA=64.5). We instead focus on the CIA (molar), which provides a more generalized and quantitative measure of the degree of alteration from primary feldspathic material to more aluminous authigenic clays, such that pristine feldspars exhibit a CIA (molar)=1 that increases with increasing degree of alteration to clay minerals (Goldberg and Humayun, 2010).

Within this framework, CIA (molar) compositions indicate 3 different weathering regimes reflected in the 3 Taylor drift units (Table 3.3). Taylor-I fractions are within uncertainty of unity, reflecting limited major element evidence of chemical alteration. With one exception, the Taylor-III fractions are significantly elevated above 1, with no significant relationship between grain-size and degree of alteration. The Taylor-IV 10–20 µm fraction exhibits a CIA (molar) composition significantly <1, while the 20–38 µm fraction is ≤ 1, indicating the presence of a subaluminous phase in the 10–20 µm fraction. A carbonate phase is improbable given the extensive low-pH leaching treatments used (Table 3.1). Instead, given the proximity of the Taylor-IV drift units to outcroppings of Ferrar dolerite sills, we favor pyroxene or another mafic or calcic phase to account for this chemistry. While a denser phase such as this ought to have been removed by mineral separation methods, these methods may have been less efficient for finer grained separates due to slow settling rates in LST or particle adhesion. Therefore, the relationship between grain size and CIA (molar) in Taylor-IV may represent one of two things: either a lesser abundance of a subaluminous phase among coarser grain sizes or a greater degree of feldspar alteration to aluminous clay minerals. Given our inspection of mineralogic separates, we favor the latter explanation of a greater authigenic clay component, though we cannot absolutely exclude the former. Finally, we acknowledge that clay minerals may also be inherited from the Beacon sandstones (Shaw, 1962), but collectively the CIA (molar) data show that little, if any, clay is incorporated into these "detrital" components of the Taylor drift sediments.

3.5.2 The effects of leaching

The leaching methods reduce U and Th concentrations of the residues relative to their unleached counterparts in all but two cases (Table S3.2): the U concentration (hereafter [U]) of the leached fraction was higher than the unleached fraction in the finest Taylor-I detrital grains (10–20 µm) and the leached and unleached fractions of Taylor-IV clays had similar [U]. The former observation seems most likely explained by sample heterogeneity in a small aliquot from which only two fractions were available. In terms of ^{230}Th-^{234}U-^{238}U data, leaching significantly altered the isotopic compositions of all detrital and clay size fractions with the exception of the 75–125 µm size fractions. However, the directionality and magnitude of these changes varied widely from sample to sample and even among grain-size fractions within a sample (Fig. 3.5), indicating a broadly heterogenous suite of leach-soluble phases that were effectively removed, leaving behind insoluble silicate residues. The notable exception to this is Taylor-IV, for which the (^{230}Th/^{238}U) and (^{234}U/^{238}U) of both leached and unleached fractions were similar for a given grain size. There was no significant effect on the composition of Taylor-I fractions leached 3 times vs. 5 times, whereas additional leach iterations resulted in slightly lower (^{234}U/^{238}U) compositions for Taylor-IV residues (Table S3.2) that do not affect the overall interpretation of these data.

3.5.3 Overview of Taylor drift ^{230}Th-^{234}U-^{238}U data

In the following sections, we explicitly discuss the compositions of leached residues, unless otherwise specified. Further, we follow the assumption that the hydraulic settling methods described in section 3.3.2 effectively separated predominantly detrital silicate grains from predominantly authigenic clay silicate grains. For the sake of brevity, we refer to sediment aliquots that settled rapidly in water as “detrital” and those that settled more gradually as “clay,” though we recognize that clay minerals may be incorporated into the detrital component and vice versa.

The U-series compositions of detrital silt fractions all array approximately linearly (Fig. 3.5). While regressions of Taylor-III and -IV silts exhibit slopes within uncertainty of the steepest slopes predicted by a strictly physical weathering (i.e. comminution only) model, Taylor-I and -II slopes are significantly shallower than any predicted slope (Fig. 3.4). Critically, all detrital fractions exhibit (^{230}Th/^{238}U)>1, except for the finest (10–20 µm) Taylor-I silts, and only the Taylor-I detrital fractions and finest (10–20 µm) Taylor-IV detrital fraction exhibit (^{234}U/^{238}U)<1. These observations stand in stark violation of an exclusively physical weathering history (Figs. 3.3,3.4) and require significant alteration by authigenic processes. We emphasize that while major element indices show limited evidence of chemical alteration, the ^{230}Th$-$^{234}U$-$^{238}U-system was strongly perturbed by these processes, underlining the impressive utility of U-series isotopes as tracers of chemical weathering in addition to physical weathering. The following sections interpret this U-Th data and infer the physical and chemical weathering histories for each Taylor drift unit.

3.5.4 Taylor III: combined weathering and implantation effects

Taylor-III exhibits a range of relatively low-U (0.13–0.3 µg g^{-1}) that is positively correlated with grain size (Fig 3.7, Table S3.2) and negatively correlated with (^{234}U/^{238}U) and (^{230}Th/^{238}U). The consistently low detrital [U] relative to clay and unleached fractions apparently allow grain-size dependent authigenic processes to become pronounced since the finest grains have the greatest enrichments in ^{234}U and ^{230}Th. Curiously, the array of detrtial Taylor-III fractions appears to bifurcate among the finer grain sizes (<38 µm) at high (^{234}U/^{238}U) and (^{230}Th/^{238}U), establishing a steeper-sloped subset and a shallower-sloped subset relative to the overall regression (Fig. 3.5). We explore these grain-size dependent processes and bimodal behavior using the mathematical framework of sediment U-series evolution from α-recoil and chemical weathering processes outlined in Section 3.4.2.

Model parameters

This section outlines and justifies the parameters chosen for the U-series physical-chemical weathering model, summarized in Table 3.4. In all simulations, we assume initial detrital (^{234}U/^{238}U) = (^{230}Th/^{238}U) = 1, constrained by the measured composition of Taylor-III sand-sized fractions (75–125 µm), which are expected to be generally insensitive to grain-size dependent processes due to their larger size. In all simulations we assume a leach-insoluble authigenic [U] of 1 µg g^{-1} based on the measured [U] of leached clay fractions (Table S3.2) and a 2 µg g^{-1} leach-soluble authigenic "rind" component that accounts for U-series radionuclide implantation. While we do not measure the [U] of the leach-soluble component directly, this estimate is reasonable in the context of the factor of 2–4 reduction in [U] after leaching, implying that the volumetrically small rind holds a large amount of U. Finally, we assume a 100 = nm rind thickness in all implantation simulations. Output results are insensitive to rind thicknesses equal to or greater than this.

We vary the following parameters among the simulated scenarios: detrital [U], the authigenic weathering rate k, the proportion of the detrital component covered by an authigenic rind, and the $^{230}\mathrm{Th}-^{234}\mathrm{U}-^{238}\mathrm{U}$ composition of the authigenic components. In each simulated scenario we select initial detrital [U] compositions so that concentrations approach the measured values within the modeled timeframes. In the higher weathering scenarios ($k > 1 \cdot 10^{-8}$), we use the same initial values for the sake of comparison, while in the case of nil authigenic weathering (implantation only), we simply use the measured [U] of Taylor-III detrital fractions as initial [U]. We select values for the authigenic weathering rate coefficient ranging $0 \leq k \leq 4 \cdot 10^{-8}$ (g m^{-2} a^{-1}). The upperbound is comparable to the long-term (10–10^3 ka) weathering rates applied to feldspars in Mediterranean climates (White et al., 1996). While this climate is warmer than that of Taylor Valley, these may be reasonable approximations for water-saturated environments (Lyons et al., 1998; Marra et al., 2017; Lyons et al., 2021). We lack observations to constrain the proportion of the detrital grains covered by the authigenic rind, so we assume a proportion of 0.4–0.5, though this parameter may vary interchangeably with rind [U].

Since authigenic clays form by precipitation or the aqueous alteration of primary silicates by hydrolysis, authigenic clays likely reflect the (^{234}U/^{238}U) composition of local waters. We estimate the (^{234}U/^{238}U) composition of the authigenic components from the aqueous compositions of Taylor Valley waters most likely to have interacted with these sediments. Given the elevation of Taylor-III at >700 m, this area has likely experienced little prolonged water residence since its deposition other than minor moisture from snowmelt (e.g. Campbell and Claridge, 1981), which is a poor source of solutes (Lyons et al., 1998) but may scavenge U from the abundant soluble salts. Alternative sources of water at this location are either streamflow or flooding in an ice-marginal pond. Care was taken to sample far from any apparently fluvial sedimentary features, and the distance of this site from any alpine glaciers (the primary sources of streams in Taylor Valley) contradicts significant streamflow in this area (Fig. 3.1). Therefore, water was likely delivered in small volumes by snowmelt or extended residence of an ice-marginal pond during a prior high-stand of Taylor Glacier.

To estimate the (^{234}U/^{238}U) composition of these salts and/or the theoretical ice-marginal pond, we infer what the major solute source to this pond would have been subglacial waters sourced from Taylor Glacier. These same fluids are observed today at Blood Falls and as groundwaters flowing into Lake Bonney bottomwaters (Mikucki et al., 2015), and an ice-marginal pond might similarly tap into subglacial groundwaters as Lake Bonney does contemporarily. Even without marginal ponding, Toner et al. (2013) showed that soil soluble salts in lower elevation Taylor Valley soils are the residues of evaporation at ancient paleolake highstands. Therefore, the most probable solute source for Taylor-III sediments are either saline groundwaters or nearby lakewater at the time of deposition.

Contemporary (^{234}U/^{238}U) compositions of Lake Bonney range from ∼3.0 in the surface waters to ∼4.5 in the stratified deep waters and Blood Falls (Henderson et al., 2006). Water-lain precipitates from Taylor Valley record comparable enrichments over at least the last 400 ka (Hendy et al., 1979; Higgins et al., 2000) These values may be upper estimates given that (^{234}U/^{238}U) decays with time, but this composition is bolstered bolstered by addition of ^{234}U ejected from sediments by α-recoil. After desiccation following drift deposition or evaporation of any ice-marginal waters, these salts might be routinely dissolved during snowmelt events and react with detrital material. Finally, since Th is insoluble, ^{230}Th is likely readily available on the surface of grains due to its preferential adsorption to sediment surfaces after α-recoil ejection or aqueous decay of ^{234}U. In the absence of any measurements of ^{230}Th in the Taylor Valley sedimentary environment, we assume (^{230}Th/^{238}U)=4.6 based off the value predicted from the Taylor-III regression for (^{234}U/^{238}U)=3.

Model results

The simulated ^{230}Th-^{234}U-^{238}U isotopic evolutions for physically and chemically weathered sediments are presented in Figure 3.6, while results for silicate-bound [U] and degree of authigenic replacement are summarized in Figure 3.7. Each simulation calculates the isotopic compositions of three model grain sizes (40, 30, 15 µm) though time, demarcating 400 ka and 1500 ka, at which point the system converges on an equilibrium state. The model simulates U-series response to α-recoil ejection from detrital sediments, authigenic replacement of detrital minerals, and α-recoil implantation into detrital material from a leach-soluble authigenic rind. This section outlines the latter two processes and compares the predicted effects to the measured U-series compositions of Taylor-III detrital fractions.

Panels A and D of Figure 3.6 show the combined effects of α-recoil ejection and authigenic replacement. As long as the rate of authigenic replacement exceeds the rate of α-recoil loss of ^{230}Th and ^{234}U, the bulk grain compositions climb to (^{234}U/^{238}U) and (^{230}Th/^{238}U) >1. Due to the grain-size dependence of chemical weathering, for sediments of similar [U], the smaller grains characterized by larger surface area-to-volume ratios, are more affected and record higher (^{234}U/^{238}U) and (^{230}Th/^{238}U) than larger grains. When only authigenic replacement occurs with α-recoil ejection, over the course of 1.5 Ma (^{234}U/^{238}U) and (^{230}Th/^{238}U) increase to supra-SE values along an approximately constant slope (Fig. 3.6), controlled by the relative compositions of the authigenic (^{234}U/^{238}U) and (^{230}Th/^{238}U) composition. In both scenarios the corresponding slope and modeled array is consistent with the upper-bound slopes of Taylor-III silts (Fig. 3.6). However, the slopes are insensitive to time at the level of analytical uncertainties and thus provide little insight into the age of the sediments, although the weathering rates require a $\ll$1.5 Ma age to accommodate the observed CIA (molar) and [U] (Fig. 3.7).

Panels B and E of Figure 3.6 explore the effects of only α-recoil processes: implantation and ejection. For the modeled authigenic rind compositions, the modeled grains evolve through a broader isotopic space than the “replacement only” scenario, settling on values consistent with the measured data close after nearly 1500 ka. While the replacement only scenario (Fig. 3.6A,D) appear to reproduce the steeper sloped array at all timeframes, the “implantation only” scenario (Fig. 3.6B,E) effectively reproduces the shallower sloped array for >400 ka timeframes. Since the two modeled authigenic rinds only differ in initial (^{234}U/^{238}U), they converge on identical long-term behavior. By definition, this α-recoil-only scenario includes no leach-insoluble (silicate) authigenic component and is inconsistent with the >1 CIA (molar) compositions of Taylor-III silts (Fig. 3.7, Table 3.3), unless these compositions reflect peraluminous detrital material or inherited clays from Beacon sandstone cements (Shaw, 1962).

Panels C and F of Figure 3.6 explore the combined effects of authigenic replacement, α-recoil implantation, and α-recoil ejection. The modeled arrays begin to intersect the measured values shortly after 400 ka and the long-term equilibria lie within the two endmember slopes. Thus, within 400–1500 ka the combined model reproduces observed isotopic compositions as well as [U] and CIA (molar) compositions (Fig. 3.7).

Preferred weathering history for Taylor-III sediments

In terms of $(^{230}\mathrm{Th}/^{238}\mathrm{U})$ and $(^{234}\mathrm{U}/^{238}\mathrm{U})$ compositions, the authigenic replacement-only endmember model satisfies the observed data that array a steeper slope after $\geq$400 ka, whereas the implantation-only endmember satisfies the shallower-sloped data for 400 to >1500 ka (Fig. 3.6). However, the twoendmember scenarios of chemical weathering respectively invoke exclusively leach-insoluble and leach-soluble chemical weathering products, resulting in predicted degrees of silicate chemical alteration that respectively overestimate and underestimate the CIA (molar) of the measured data (Fig. 3.7). While neither endmember scenario is able to independently satisfy the observed Taylor-III detrital sediment compositions, a combination of the two scenarios satisfies all of the observed data (Figs. 3.6,3.7).

While some degree of chemical alteration is implied by CIA (molar) values, we emphasize two key evidences for a significant role of α-recoil implantation from a high-U authigenic phase into the lower-[U] detrital phase. First, several <38 µm detrital grains exhibit more-enriched $(^{230}\mathrm{Th}/^{238}\mathrm{U})$ and $(^{234}\mathrm{U}/^{238}\mathrm{U})$

compositions than corresponding clay fractions, implying an additional ^{230}Th- and ^{234}U-enriching process beyond clay precipitation. Second, the (^{230}Th/^{238}U) and (^{234}U/^{238}U) compositions of unleached fractions are lower than their leached equivalents (Fig.3.5), while the unleached fractions all have at least twice the [U] of leached fractions, indicating complimentary reservoirs of high- and low-U that have exchanged ^{230}Th and ^{234}U (Tanaka et al., 2015; Menozzi et al., 2016). These observations indicate the removal of ^{230}Th- and ^{234}U-depleted, high-U authigenic rinds because very thin (e.g. <1 µm) rinds of authigenic material coating detrital grains have extremely high f_m values, resulting in efficient loss of ^{230}Th and ^{234}U to α-recoil on geologic timescales. Since a large proportion of the rind's α-recoil ejections are adjacent to the detrital grain surface, those implanted isotopes raise the (^{230}Th/^{238}U) and (^{234}U/^{238}U) of the detrital grain while lowering these compositions in the soluble rind.

At <38 µm grain sizes, Taylor III silts split into two separate into two groups of steeper and shallower slope. Histories dominated by authigenic clay formation favor the steeper slope, whereas implantation-dominated processes favor the shallower slope. We interpret this bifurcating array to reflect heterogeneity in the effective contribution of implantation and replacement at fine-grained sizes that are most sensitive to these processes: grains more affected by authigenic replacement trend to the steeper slope endmember, while those more affected by implantation trend toward the shallower slope. The combination of these two processes and the insensitivity of the arrays produced by authigenic replacement to time, obfuscate any temporal information about the physical or chemical weathering history other than an onset of weathering processes prior to 400 ka, consistent with the depositional age (Fig. 3.2). Similarly, we note that the preferred scenarios presented in this section do not uniquely explain the observed data, and minor adjustments to the chosen parameters can fine-tune a variety of weathering histories to match measured compositions. However, the model results do show conclusively that the U-series compositions of Taylor-III detrital silts require a combined authigenic alteration and α-recoil implantation history.

3.5.5 Taylor-II & Taylor-IV: mixing between detrital and authigenic endmembers

The line regressed to fit the detrital fractions of Taylor-IV intersects clay fractions at (^{234}U/^{238}U) and (^{230}Th/^{238}U) compositions ~5 times as enriched above SE, even though they were not included in the regression (Fig. 3.5). Extrapolating this line to lower values, it also intersects Taylor-I detrital grains, implying a plausible isotopic relationship among these three components. Indeed, a mixing envelope mapped between Taylor-I detrital and Taylor-IV clay components in the 10–38 µm grain diameter range, comfortably overlaps all other Taylor-IV fractions and the Taylor-I clay fraction (Fig. 3.8A,B). All >20 µm Taylor IV fractions also fall within the bounds of a mixing envelope bounded by the Taylor-I 38–45 µm fractions and the corresponding grain size of the Taylor-IV clay component (Fig. 3.8A,B).

This two-endmember mixing model is supported by the relationships between [U], grain size, and isotopic ratios: (^{234}U/^{238}U) and (^{230}Th/^{238}U) scale with grain size, while [U] is negatively correlated with each (Fig. 3.5, Table S3.2). Thus, the highest-[U] (~1.3 µg g^{-1}) 10–20 µm Taylor-IV fractions lie closest to the Taylor-I detrital endmember, while the lowest-[U] (<0.15 µg g^{-1}) 38–45 µm Taylor-IV fractions are more strongly leveraged by mixing with a high-(^{230}Th/^{238}U)-(^{234}U/^{238}U) clay-like endmember (Figs. 3.5,3.8). Incorporation of a clay-like endmember is also consistent with the higher CIA (molar) value for coarser Taylor-IV detrital grains, implying that these reflect a higher clay component than their finer-grained counterparts (Table 3.3). Curiously, Taylor-IV sands (75–125 µm) are decoupled from this trend with a [U] comparable to the 38–45 µm size fraction but (^{234}U/^{238}U)$\sim$(^{230}Th/^{238}U) ~ 1 (Fig. 3.5, Table S3.2), likely reflecting both a lesser clay contribution and relative insensitivity to grain-size dependent α-recoil processes at this size range.

This two-endmember mixing model coherently and parsimoniously explains the Taylor-IV data topology, though it does not explicitly identify the underlying mechanisms. The high-(^{234}U/^{238}U)-(^{230}Th/^{238}U) Taylor-IV clay endmember tempts the interpretation that efficient aqueous authigenic processes are contributing high-^{230}Th and -^{234}U phases (clay or amorphous silica) to detrital silicates. Yet, abundant authigenic mineral production seems improbable in the case of Taylor-IV. First, all simulations of authigenic replacement failed to reproduce the slope and topology of Taylor-IV data for any combination of input parameters. More importantly, given the ancient depositional age (>1.5 Ma; Wilch et al., 1993) of Taylor-IV, ancient products of chemical alteration would return to SE (or lower) unless routinely refreshed over this long timeframe. Therefore, sustaining the elevated (^{234}U/^{238}U) and (^{230}Th/^{238}U) compositions of Taylor-IV by authigenic replacement alone requires one of the following scenarios: frequent interaction with moderately high [U] and (^{234}U/^{238}U) waters or interaction within $\ll$1.5 Ma with very high [U] and/or (^{234}U/^{238}U) waters reminiscent of subglacial waters and groundwaters of Taylor and Wright Valleys (Henderson et al., 2006). The first scenario of frequent interaction with waters may be rejected due to the accumulation of abundant soluble salts in these sediments (Bockheim, 2002) that would be removed if the sediments were frequently flushed with water (e.g. Lyons et al., 2021). The second scenario is equally implausible, requiring transport of subglacial waters or lake bottom waters to heights of 1 km above where they are observed today. Expansions of lakes have not exceeded 400 m elevation in the last several hundred thousand years (Hall et al., 2000) and the nearby Taylor Glacier margin has not reached an elevation within 150 meters of the sample location in >450 ka (Fig. 3.1).

In the absence of significant authigenesis, the only viable mechanism to sustain the high-(^{234}U/^{238}U)-(^{230}Th/^{238}U) compositions of Taylor-IV sediments is α-recoil implantation of ^{230}Th and ^{234}U by an adjacent soluble and high-U phase. Indeed, a long-term implantation simulation approximately reproduces the trend of the Taylor-I–IV mixing envelope (Fig. 3.8). In Section 3.5.6 we show that Taylor-I sediments are recently comminuted, so we choose that composition as the initial composition, but the long-term (1500 ka) condition is independent of the chosen initial (^{234}U/^{238}U) and (^{230}Th/^{238}U) conditions. The extrapolated trend intersects the Taylor-IV (<38 µm) clay fraction and nearly intersects the highly-enriched 38–45 µm clay fraction. Although finer-grained Taylor-IV samples sit just below the modeled 1500 ka implantation line, this slight discordance may reflect minor leaching of implanted ^{234}U from damaged mineral lattice sites.

The overall concordance between the measured data and an α-recoil implantation model indicates that the mixing envelope reflects mixture between a detrital endmember, which may or may not be significantly affected by α-recoil implantation, and a clay endmember with U-series systematics dominated by α-recoil implantation due to the large surface area-to-volume ratios of clay minerals and weathered detrital silicates (e.g. Marra et al., 2017). As clays record implantation the most sensitively, an increasing clay component among lower-[U] and coarser-grained detrital fractions is consistent with both the mixing envelope and the CIA (molar) trend in Taylor-IV silts (Table 3.3). The model is further supported by the 38–45 μm Taylor-II fractions (detrital and clay) and the Taylor-I clay fraction that fall within the mixing envelope (Fig. 3.8D). This coherence implies physical mixing of ancient, high-(^{230}Th/^{238}U)-(^{234}U/^{238}U) Taylor-IV clays with these sediments found at >750 m lower elevations, caused by either by efficient down-valley aeolian transport (Diaz et al., 2018) from up-valley Taylor-IV deposits or by colluvial and downslope transport processes. Incorporating these clay materials into Taylor Glacier basal ice merely requires transport of the clay to the upper Taylor Valley floor during Marine Isotope Stage 2 when Taylor Glacier was at a reduced extent, after which Holocene advance overrode and entrained these inherited sediments. The inability of Stokes settling and aggressive leaching methods to separate clay materials from the Taylor-II and -IV detrital components indicates that these authigenic phases readily adhere to detrital quartz and/or feldspar surfaces, resisting removal by vigorous physical agitation as well as chemical attack (Cogez et al., 2018).

In contrast to the Taylor-II (38–45 μm) and Taylor-I clay fractions, Taylor-III fractions (detrital and clay) require an authigenic replacement component (Section 3.5.4) and are not satisfied by this mixing envelope and corresponding implantation history (Fig.3.8). Similarly, the 20–38 μm detrital fraction of Taylor-II does not fit this model, and we reject this single outlying measurement on the grounds that it may incorporate additional chemical weathering processes akin to those affecting Taylor-III silts.

We propose the abundant and widespread soluble salts found in Taylor-IV soils (Bockheim, 2002) as the most probable candidate for the high-U authigenic phase responsible for the α-recoil implantation histories recorded in Taylor-IV sediments. Unlike Taylor-III, the leached and unleached fractions of Taylor-IV sediments have comparable ^{230}Th-^{234}U-^{238}U compositions (Fig. 3.5), implying that these authigenic and detrital were both affected similarly by α-recoil implantation. Therefore, this adjacent high-U phase must have been removed before the sediments were exposed to leaching reagents. High salt contents have been observed in sediments collected near the Taylor-IV sample site and the high aqueous solubility of the soil salts in Taylor Valley ensure that they would have been efficiently removed during wet-sieving and Stokes settling procedures (Toner et al., 2013) . Indeed, we observed salt residues in the dehydrated supernatant waters of these experiments. Unfortunately, we did not preserve these salts and cannot directly test the hypothesis that these soil salts reflect a [U] in sufficient excess of the detrital fractions (i.e. >1 µg g^{-1}, Table S3.2) to account for the observed degree of α-recoil implantation. However, since these salts were likely sourced from subglacial or proglacial waters that later evaporated (Toner et al., 2013), this high-U hypothesis is supported by analogous salt material. Proglacial soluble salts (nahcolite, trona) from Lewis Cliff, Antarctica approach 1 µg g^{-1} U (Fitzpatrick et al., 1990). And Taylor Valley salts are likely even more uraniferous, given local gypsum precipitated from Holocene Lake Bonney with 2–3 µg g^{-1} U and Holocene to >400 ka carbonates that are typically > 10 µg g^{-1} U (Hendy et al., 1979).

3.5.6 A comminution age for Taylor I silts

The detrital fractions of Taylor-I reflect a narrow range of sub-SE (^{234}U/^{238}U) compositions (0.94 to 0.97) for all grain sizes, while (^{230}Th/^{238}U) vary more broadly from 0.9 to 1.1 (Fig. 3.5). These fractions lie along a shallow-sloped array that is not consistent with mixing with a Taylor-IV clay endmember (Fig. 3.8) but may reflect a mixture between a sub-SE (^{234}U/^{238}U) and ($^{230\text{Th}}$/^{238}U) detrital endmember and a higher-^{230}Th endmember. Because [U] varies from 0.2–

1.6 µg g^{-1} between the >20 µm and 10–20 µm fractions, respectively, the finest size fraction provides a best estimate for the U-series isotopic composition of the unaltered Taylor-I detrital component. This significantly sub-SE ^{230}Th-^{234}U-^{238}U composition independently suggests ancient physical comminution under the framework of U-series comminution dating (Fig. 3.4). However, the (^{234}U/^{238}U) is indistinguishable from the 75–125 µm fraction, which should be insensitive to grain-size-dependent α-recoil processes, suggesting that this sub-SE composition may instead be an inherited property from the source rock or a product of grain-size-independent weathering processes.

Two possible scenarios explain these universally sub-SE (^{234}U/^{238}U) compositions: 1. they reflect ancient comminution and a protracted history of α-recoil loss that is insensitive to grain size; or 2. the canonical assumption of initial SE in comminuted material is erroneous and Taylor-I silts reflect recent comminution from an effectively sub-SE bedrock source. We favor the second scenario of recent comminution from a sub-SE provenance for several reasons. First, the widely applied canonical assumption of initial SE has not been systematically confirmed with freshly comminuted sediments. Despite widespread observations of SE in $\geq$1.5 Ma rocks, the rapid release of release of U with (^{234}U/^{238}U)>1 from freshly comminuted granite to pore solutions implies that internal α-recoil damage to silicate matrices prior to comminution may leave atoms of radiogenic ^{234}U and ^{230}Th effectively labile when recoil-damaged zones are exposed to chemical weathering environments following comminution (Fig. 3.9; Andersen et al., 2009) Under such a model, grains comminuted from ancient bedrock rapidly converge on grain-size controlled sub-SE compositions as soon as they are exposed to conditions that support removal of labile U and Th (e.g. surface waters or leaching solutions; Fig. 3.9). Further, if we accept the sub-SE composition as an initial composition, the array of Taylor-I detrital grains is consistent with a <100 ka evolution controlled by α-recoil implantation (Fig. 3.8). However, this model still fails to explain why 75–125 µm fractions of Taylor-I (^{234}U/^{238}U) compositions do not exceed the <50 µm fractions. Under scenarios of both ancient and recent comminution this issue reflects grain shape parameters (e.g. K or λ_r; Table 3.2) that may account for lower-than-expected f_{234} values for sand-sized fractions. Additionally, the signals of α-recoil implantation in drifts Taylor-II–IV suggest that the radionuclides implanted in α-recoil damaged zones of those lithologies are resilient to leaching. Lithologic differences between the Taylor-I and Taylor drift sediments may account for different behavior in the damaged zones of these particles, supported by sand-sized grains with (^{234}U/^{238}U)$\sim$1 for all other Taylor drifts (II–IV). Altogether, the universally sub-SE compositions of Taylor-I detrital sediments fail to resolve the timescales of physical weathering beneath Taylor Glacier. Instead, these observations undermine one of the foundational assumptions of U-series comminution dating that pre-comminution α-recoil processes do not affect post-comminution α-recoil behavior.

The limited degree of chemical alteration observed in detrital Taylor-I sediments strongly support recent, rather than ancient, physical comminution. Given the various evidences for subglacial aquatic environments beneath Taylor Glacier (Hubbard et al., 2004; Mikucki et al., 2015), microbial activity in these waters (Mikucki et al., 2009) as well as basal ice (Montross et al., 2014), and the efficiency of aqueous chemical weathering in Taylor Valley groundwaters (Lyons et al., 2021), we predict efficient aqueous chemical alteration, likely enhanced by microbial activity (Montross et al., 2013), in the basal and subglacial environment of Taylor Glacier. Yet, with a CIA (molar) composition within $\leq 1\sigma$ of unity, the Taylor-I sediments extracted directly from this regime show no major-elemental evidence of primary silicate replacement with aluminous clay minerals like the Taylor-III and Taylor-IV silts do (Table 3.3). While amorphous SiO_2 coatings may contribute authigenic material without raising the CIA (molar), there is no reason to expect that the subglacial aqueous environment of Taylor Glacier would accommodate significant precipitation of amorphous SiO_2 without concomitant clay precipitation. U-series isotopes reinforce the limited extent of chemical alteration in Taylor-I sediments. Taylor-I clays fall on the mixing line between the detrital Taylor-I component and the high-($^{234}U/^{238}U$)-($^{230}Th/^{238}U$) clay component of Taylor-IV (Fig. 3.8A,B), suggesting that any extant clays were inherited from upslope Taylor-IV deposits (Section 3.5.5). Yet, the Taylor-I detrital components cannot be inherited or they would exhibit compositions of a Taylor-II–IV detrital silt. Rather they reflect an endmember composition within a relatively limited range of ($^{234}U/^{238}U$) and ($^{230}Th/^{238}U$), showing no evidence of appreciable U gain by authigenic processes and only limited ^{230}Th gain that varies distinctly from the more altered sediments of the drift sheets.

By all metrics, Taylor-I sediments reflect far less evidence of chemical weathering than any of the Taylor drift sheet sediments (II–IV). Yet, if all Taylor Valley sediments were comminuted before 1.5 Ma, then Taylor-I sediments, which have resided in reactive subglacial and proglacial waters, and Taylor-IV sediments, which are perched nearly 1 km above the modern valley floor in a hyperarid environment, should both exhibit at least a comparable degree of alteration. In the absence of any such evidence of weathering within the Taylor-I detrital fraction, we must accept a history of recent physical weathering and only brief chemical weathering.

3.5.7 The physical and chemical weathering history of Taylor Valley

While the chemical weathering signatures in sediments from Taylor Valley obfuscate any independent chronologic information about physical comminution, the apparently limited U-series evidence of chemical weathering in Taylor-I detrital sediments requires comminution more recent than all Taylor-II–IV drift sediments, i.e. within the last ∼100 ka. This age disparity between glacially entrained sediments and the sediments deposited by prior glacial advances provides robust support for the ongoing production of fine particles by mechanical wear processes beneath Taylor Glacier, likely facilitated by basal sliding in the sub-solidus zones observed beneath Taylor Glacier (e.g. Hubbard et al., 2004). Active mechanical wear processes, in turn, imply active glacial incision in Taylor Valley that continued through the Pleistocene and perhaps continues today. Although our results do not quantify the extent of Pleistocene incision, they contradict canonical models of stagnant MDV landscapes overs the last >15 Ma (Denton et al., 1993; Sugden and Denton, 2004). Rather, it appears that Taylor Glacier behaves more like warm-based outlet glaciers (e.g. Mackay Glacier) that actively denudate the valleys they occupy (Sugden and Denton, 2004) and contribute to the extreme relief within the Trans-Antarctic Mountains (Stern et al., 2005). While unglaciated high elevations likely reflect very ancient landscapes (Brook et al., 1995) our results emphasize that Antarctic glaciers with subglacial brine outlets like Taylor Glacier are likely candidates for lubricated basal conditions and contemporary valley incision.

Our results indicate chemical weathering histories no-less dynamic than those of physical weathering. The U-series systems of three drift deposits and sediments entrained in basal ice record a variety of chemical alteration processes that have varied as a function of both time and weathering environment. With the exception of freshly comminuted sediments (Taylor-I), enrichments of U-series intermediate daughter nuclides ^{230}Th and ^{234}U in silicate sediments are commonplace and comparable to many of the enrichments observed in surface waters (Henderson et al., 2006). These enrichments indicate that α-recoil processes have directly and indirectly influenced the isotopic evolutions of sediments in the various Taylor Glacier drift sheets. The ancient deposition, high elevation above the valley floor, and extensive salt accumulations of the Taylor-IV deposit refute any recent or routine aqueous alteration processes. U-series compositions instead indicate a >1 Ma duration of α-recoil implantation from an adjacent uraniferous phase that extremely affected clay fractions due to their very high surface areas (Fig. 3.8). The implanting phase was very likely the abundant water-soluble salts that cement many of these ancient drift deposits (Bockheim, 2002). In contrast, he U-series systematics of Taylor-III are most consistent with minor authigenic clay production in addition to α-recoil implantation, suggesting more recent/frequent contact with water than the higher elevation Taylor-IV deposits. Since the unleached fractions of Taylor-III reflect significantly lower (^{234}U/^{238}U) and (^{230}Th/^{238}U) compositions (Fig. 3.5), the leach-soluble phases represent reasonable candidates for the primary implanting phase, yet the supra-SE compositions of unleached fractions also imply a contribution from soluble salts. At lower elevations, chemical mixing of Taylor-I clays and Taylor-II silicates (clay and quartz-feldspar fractions) with Taylor-IV clays imply physical mixing of relatively freshly comminuted silicate material with ^{230}Th- and ^{234}U-enriched silicate material inherited from the higher elevation Taylor-IV drifts by colluvial processes or aeolian transport from up-valley Taylor-IV deposits (Diaz et al., 2018).

In the hyperarid high-elevation environments of Taylor Valley, α-recoil implantation processes exert a significant control on the U-series budgets of detrital silicate grains. This process may play a significant role in other hyperarid saline systems that facilitate the growth and preservation of soluble cements, perhaps even in Martian soils, for which MDV soils are considered analogous (Gibson et al., 1983). Given the time-dependence of this radiometric process, sedimentary α-recoil implantation may offer some chronometric potential in studies of pedogenic and regolith processes, so long as other authigenic processes are adequately accounted for.

Even at the low degrees of chemical alteration characteristic of the McMurdo Dry Valleys, the ^{230}Th-^{234}U-^{238}U systematics of fine sediments are highly sensitive to the processes of chemical weathering and alteration. U-series isotopics show extensive chemical mixing of several sediments with an endmember characterized by the so-called "clay" component of the Taylor-IV drift (Fig. 3.8). Its isotopic signature appears in clay fractions as well as detrital fractions (as separated by Stokes settling), implying either resilient adhesion to particles or *in situ* alteration of detrital silicate that is not removed by leaching methods. While we have referred to this endmember as a "clay," we did not ascertain its mineralogy, although its insolubility in leaching reagents suggests a silicate composition. It may be composed of true clay minerals: <63 µm sediments from Taylor Valley contain illite, kaolinite, smectite, vermiculite, and mixed layer clays (Marra et al., 2017). Another component may be an authigenic amorphous silicate phase such as those observed in Antarctic subglacial weathering products (Graly et al., 2020) and precipitate rocks (Blackburn et al., 2020). Indeed, amorphous SiO_2 saturation is found in Lake Bonney waters and may also occur in sediment porewaters supported by H_2SiO_4-rich shallow groundwaters (Lyons et al., 1998, 2021).

3.6 Conclusions

The U-series isotopics of glacigenic silts from Taylor Valley reflect complex weathering histories, with chemical weathering and physical fractionation processes occurring across different spatiotemporal regimes and a notable contribution from α-recoil implantation from high-U authigenic phases into lower-U detrital phases. In addition to evidence for this same process in fresh and highly weathered volcanic rocks (Tanaka et al., 2015; Menozzi et al., 2016), our results confirm that α-recoil implantation is a significant component of the U-series budget in sedimentary and pedogenic systems as well. The complex suite of chemical weathering and physical fractionation processes we observe, potentially including mineralogic memory of pre-comminution α-recoil damage, obfuscate the α-recoil ejection signatures that predicate comminution dating, undermining its applicability in this and other sedimentary systems. Nonetheless, the collective trends in U-series systematics reported here indicate contemporary subglacial comminution beneath Taylor Glacier, challenging canonical models of landscape evolution in Taylor Valley and implying a more geomorphologically dynamic Taylor Glacier over the Pleistocene than previously assumed.

U-series isotopes are remarkably sensitive to both chemical weathering and physical fractionation processes in detrital sediments, and record a wider range of these sedimentary weathering processes than oft-used major element indices of chemical weathering and alteration. In the context of ancient hyperarid regimes at high elevations in Taylor Valley, Antarctica, α-recoil implantation processes are a dominant process and MDV soils present a key environment to explore these systematics further. We propose these same implantation processes might dominate sedimentary U-series behavior on analogous arid planetary surfaces, such as Mars, and may even offer chronometric potential for regolith processes in terrestrial and extraterrestrial desert environments.

Acknowledgements

This chapter reflects a manuscript in preparation with the following coauthors: Terrence Blackburn, Gavin Piccione, and Slawek Tulaczyk.

Many thanks to Brian Dreyer for his essential input into method development. This study was funded under NSF Award 1644171.

3.7 Figures & Tables

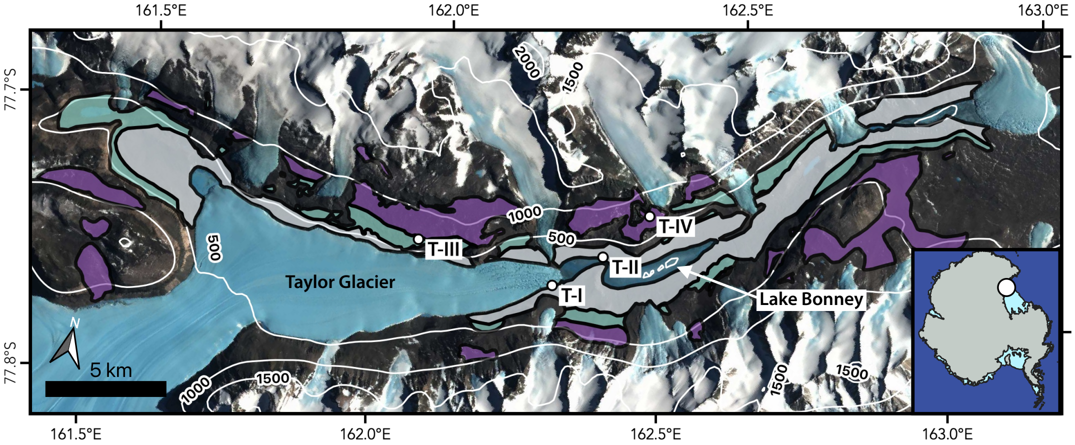

Figure 3.1: Map of Taylor Valley, Antarctica and glacial drift deposits (T). Colors code the drift units as described by Bockheim et al. (2008), where T-IV and T-III respectively correspond to their Taylor-IVb and Taylor-III, IVa units. White points identify sample sites from this study, labelled with the corresponding drift unit. Prepared with Quantarctica (Matsuoka et al., 2021).

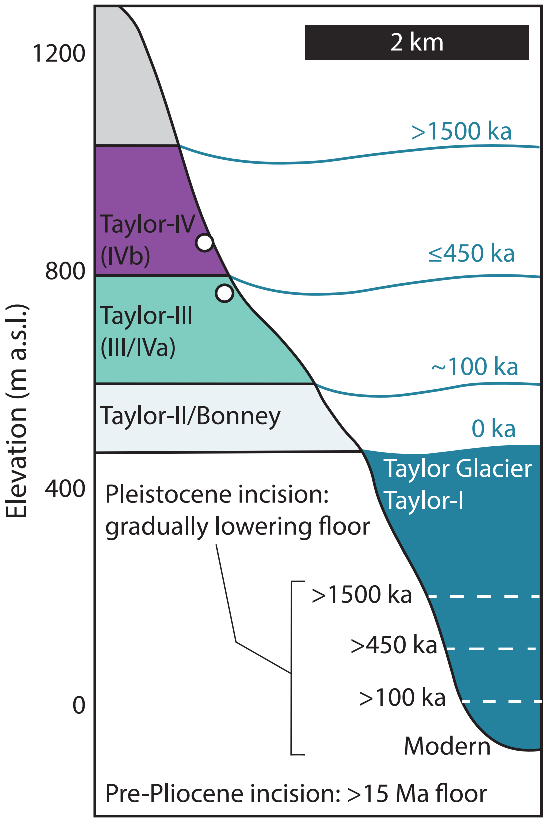

Figure 3.2: Generalized cross-section of upper Taylor Valley illustrating the depositional history of Taylor drift sheets and endmember erosional histories described in the text. Blue curves identify the age and elevation of prior ice highstands constrained by previous chronological work. Under the pre-Pliocene incision model, negligible subglacial mechanical weathering since >15 Ma has preserved the modern valley floor at the same elevation throughout the Pleistocene. Under the Pleistocene incision model, ongoing subglacial mechanical weathering has accommodated gradual valley incision up to the present. Circles demonstrate the elevations of Taylor-III (746 m) and Taylor-IV (878 m) drift samples. Taylor-I and Taylor-II sampling elevations (109 m and 113 m, respectively) are not included since these correspond to down-valley locations of thinned or terminated ice.

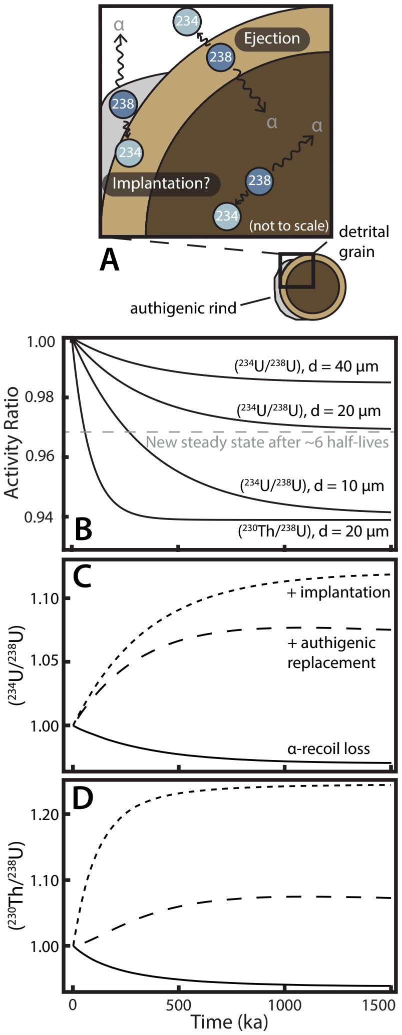

Figure 3.3: **(A)** Diagram of α-recoil processes that affect the U-series isotopic compositions of particles. For ancient particles in secular equilibrium, α-recoil within the grain interior does not affect the particle's isotopic composition. Within $\lesssim$40 nm of the grain surface, α-recoil ejection or implantation leads to isotopic disequilibrium in this zone that measurably affects the bulk-grain isotopic composition. **(B)** Simulated U-series isotope evolutions due to α-recoil ejection in idealized silt-sized particles. Curves are labelled with modeled activity ratios and particle diameter (d). Following comminution (time = 0 ka), activity ratios decrease at a rate controlled by grain morphology and the rate of radioactive decay, converging on a new grain-size-controlled equilibrium within six half-lives. **(C,D)** Modeled U-series isotope evolutions of a 20 μm diameter detrital grain affected by: only α-recoil loss (solid curves), α-recoil loss and authigenic replacement of primary material (dashed), and α-recoil loss and implantation from an adjacent high-U authigenic phase (dotted curves). Assumes authigenic phase $(^{230}\mathrm{Th}/^{238}\mathrm{U})=(^{234}\mathrm{U}/^{238}\mathrm{U})=3$.

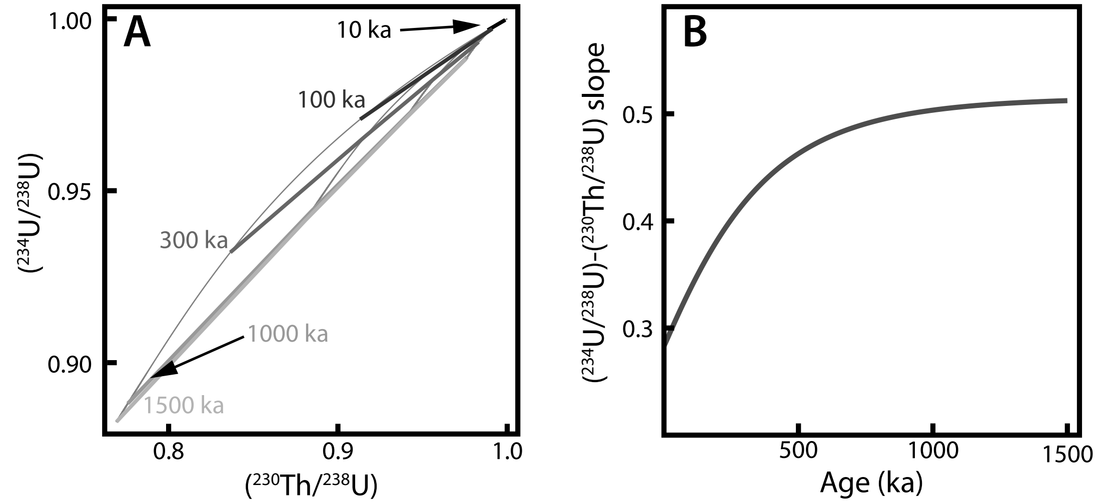

Figure 3.4: Simulations of paired (^{230}Th/^{238}U)-(^{234}U/^{238}U) systematics for chemically unaltered silt-sized particles following physical comminution. Numerical solutions to Equation 3.2 for a given time (t) produce a series of near-linear arrays for modeled grain diameters >1 µm **(A)**, each with a unique slope **(B)**. Thin grey curves in panel **A** trace evolutions of individual simulated grains through time.

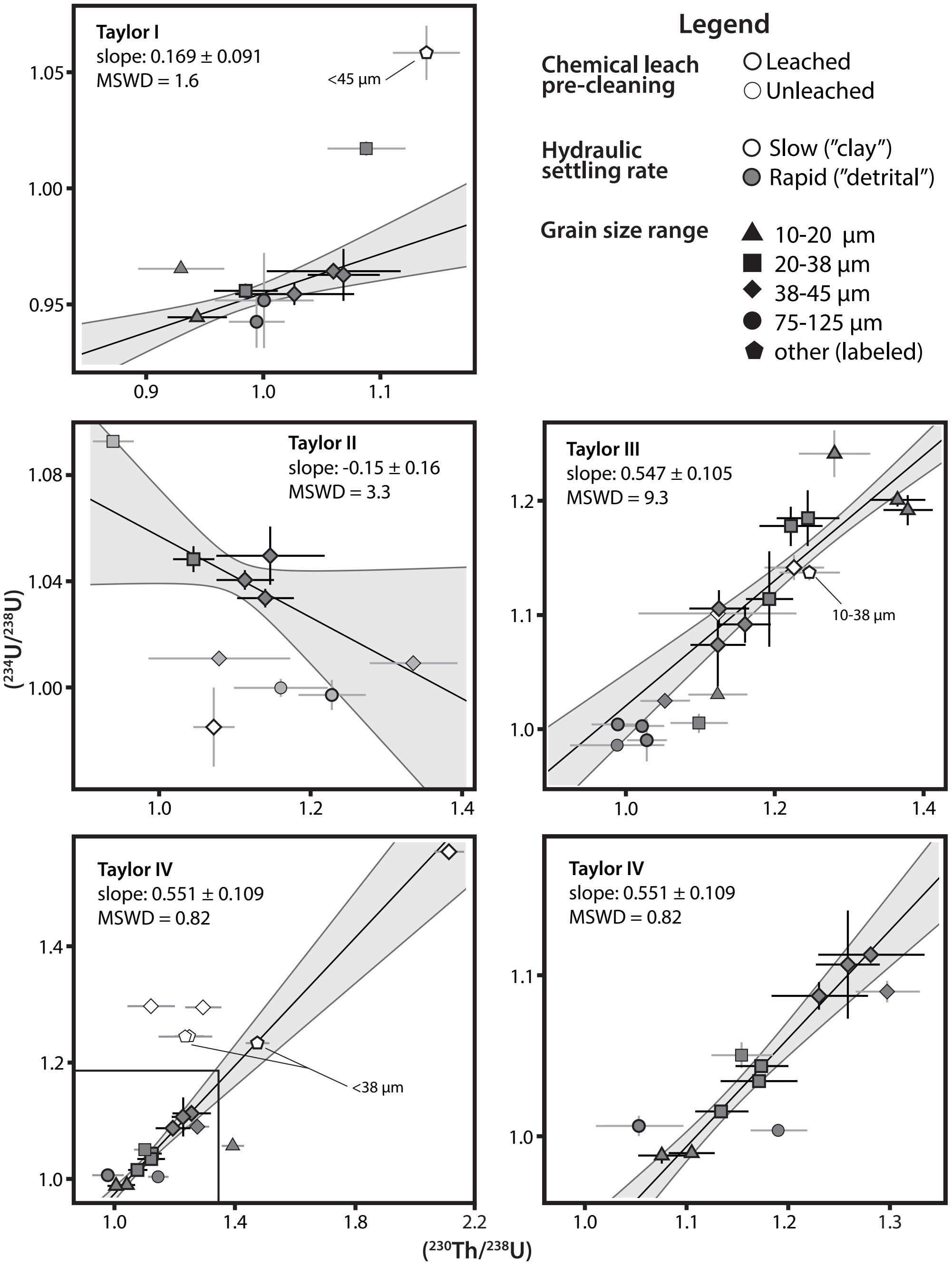

Figure 3.5: U-series compositions of sediments from each Taylor Valley drift deposit. Maximum likelihood estimation regressions are calculated for leached, <50 µm diameter fractions of "detrital" quartz-feldspar separates (black error bars indicate inclusion in regression) and slopes are reported with the 95% confidence interval (calculated with IsoplotR Vermeesch, 2018). Note that Taylor IV is plotted twice on two different scales, and the inset box bounds the enlarged area.

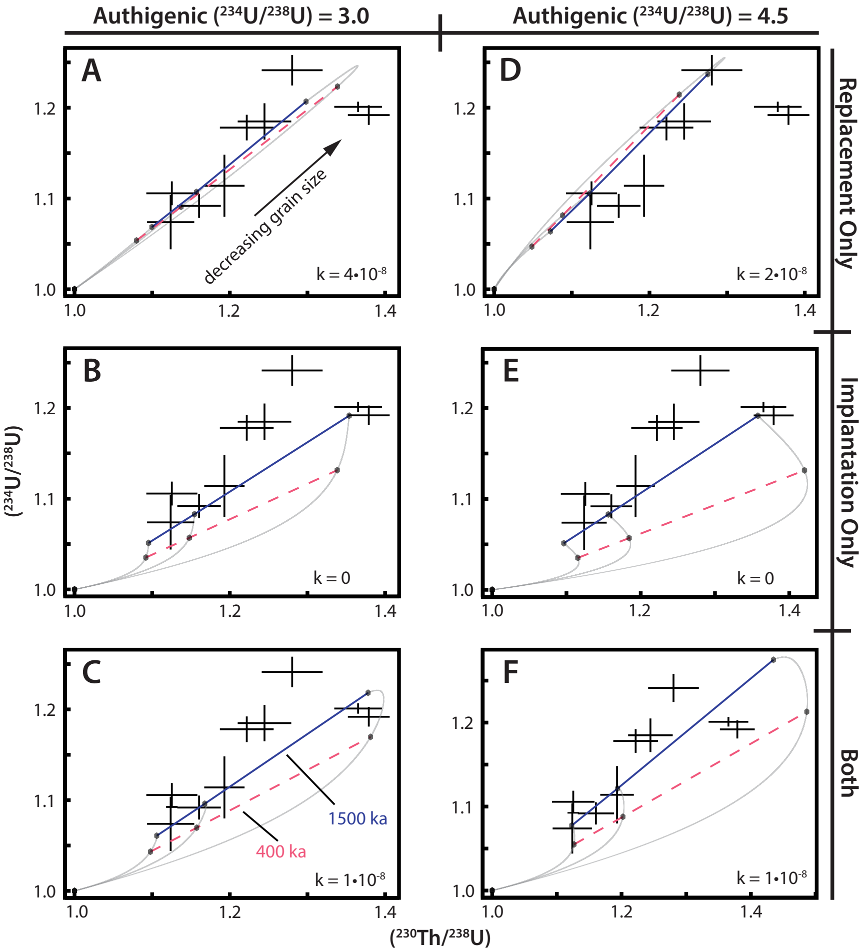

Figure 3.6: Simulated detrital sediment ^{230}Th-^{234}U-^{238}U systematics from a U-series chemical-physical weathering model compared to measured compositions of Taylor-III silts (black crosses trace 2σ standard error). The panels define a grid of model conditions: columns correspond to modeled authigenic (^{234}U/^{238}U) compositions while rows correspond to the modeled chemical alteration processes. Panels **A**–**C** reflect authigenic (^{234}U/^{238}U)=3.0. Panels **D**–**F** reflect authigenic (^{234}U/^{238}U)=4.5. Panels **A**,**D** model only chemical replacement of detrital silicate with authigenic silicate, panels **B**,**E** model only α-recoil implantation from a leach-soluble authigenic phase, and panels **C**,**F** incorporate both processes. Weathering rate coefficients (k, in g m^{-2} a^{-1}) are indicated in each panel. Additional parameters selected for each of these simulations are listed in Table 3.4. Gray curves trace the 1500 ka isotopic evolution of 15, 20, and 40 μm diameter grains with isochronous arrays drawn at 400 ka (pink/dashed) and 1500 ka (blue/solid). Note that measured and simulated data both reflect negative correlations between (^{230}Th/^{238}U) and grain-size.

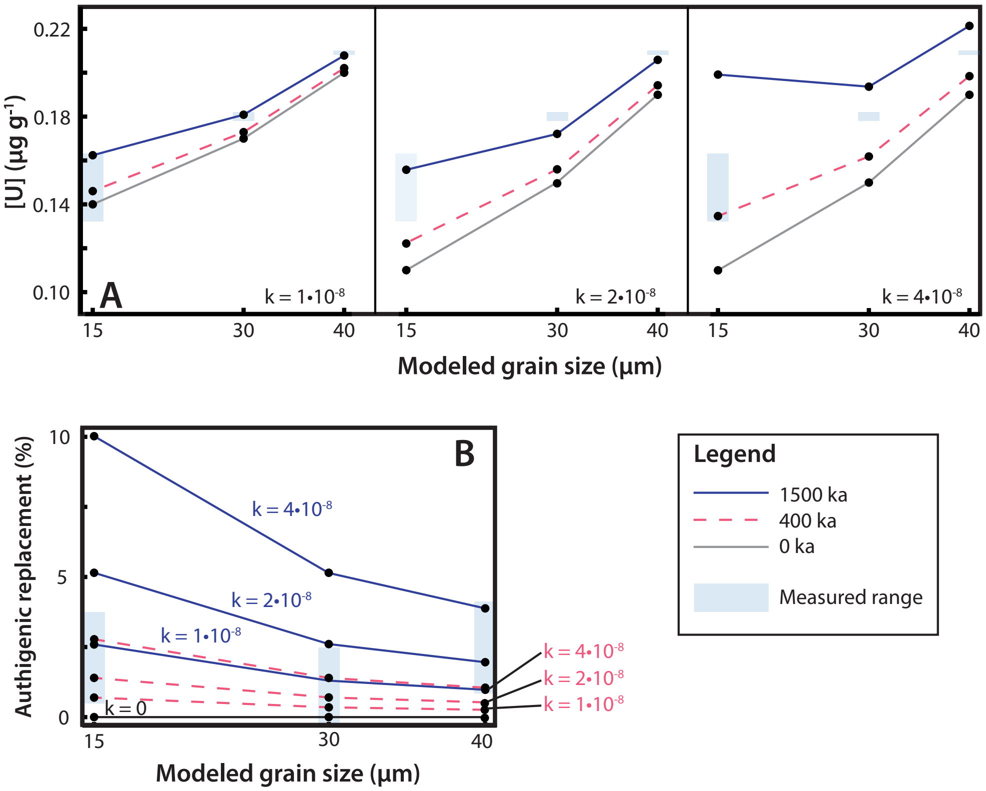

Figure 3.7: Simulated sediment chemistries from model results in Figure 3.6 compared to measured data from Taylor-III sediment fractions. **(A)** Modeled U concentrations at 0, 400, and 1500 ka for three different weathering coefficients (k, in g m^{-2} a^{-1}), corresponding to panels C and F ($k = 1 \cdot 10^{-8}$), D ($k = 2 \cdot 10^{-8}$), and A ($k = 4 \cdot 10^{-8}$) in Fig. 3.6. Initial U were selected to match simulation results with observed U compositions for the $k = 1 \cdot 10^{-8}$ and $k = 2 \cdot 10^{-8}$ conditions by 1500 ka. The same initial U concentrations were used for the $k = 2 \cdot 10^{-8}$ and $k = 4 \cdot 10^{-8}$ scenarios for comparison. **(B)** Curves showing the molar percent of replacement of primary detrital silicate material with authigenic silicate material for each weathering coefficient scenario at 400 and 1500 ka. Measured ranges are calculated from chemical index of alteration values in Table 3.3 assuming an authigenic composition of illite, CIA(molar)=4 . Note that any nil age condition or $k = 0$ weathering condiiton yields no authigenic replacement.

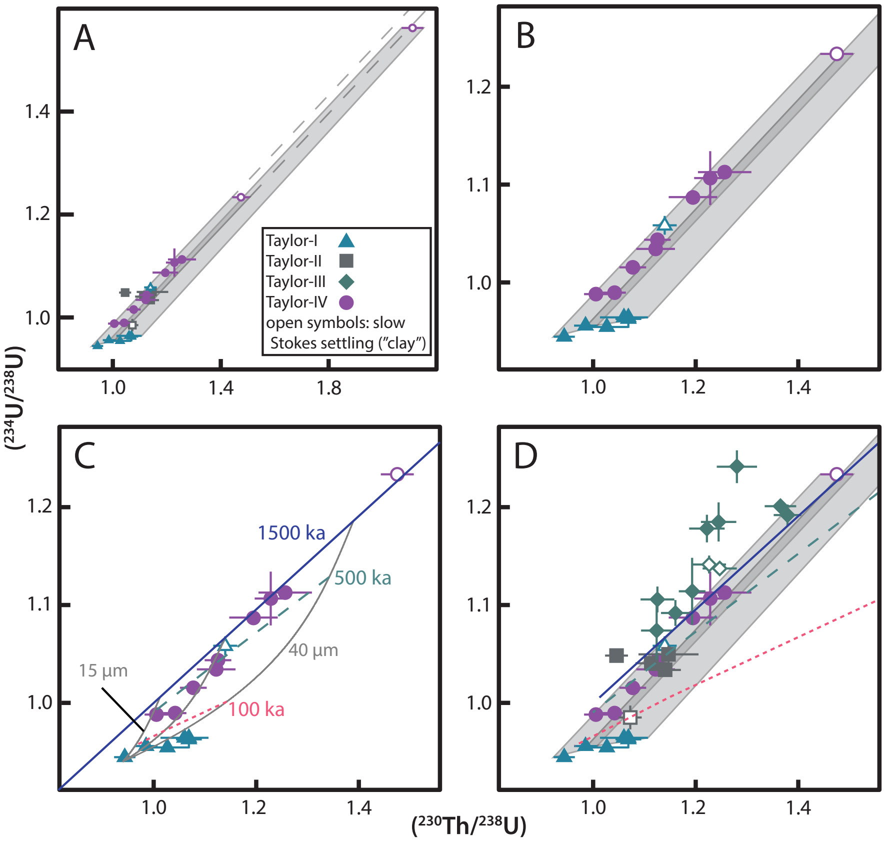

Figure 3.8: Mixing relationships among Taylor-I, -II, and -IV drifts in (^{230}Th/^{238}U)-(^{234}U/^{238}U) space, emphasizing mixing between a detrital Taylor-I endmember and clay Taylor-IV endmember. Filled symbols represent detrital quartz-feldspar fractions and open symbols represent clay fractions. **(A,B)** Mixing envelopes (gray) bounding the Taylor-I detrital endmember and Taylor-IV clay endmembers for 10–38 µm and 38–45 µm grain diameters. Dashed lines in **A** extrapolate the 10–38 µm grain size envelope. Taylor-IV detrital fractions and the T-I clay fraction overlap these envelopes. **(C)** Isotopic evolution curves (gray) and isochronous arrays (100, 500, 1500 ka) for a simulated history of α-recoil implantation from a soluble authigenic coating. The assumed model parameters are listed in Table 3.4. **(D)** Mixing envelopes from **A**-**B** and extrapolated arrays from **C**, including all leached detrital and authigenic silicate fractions from Taylor drifts I–IV.

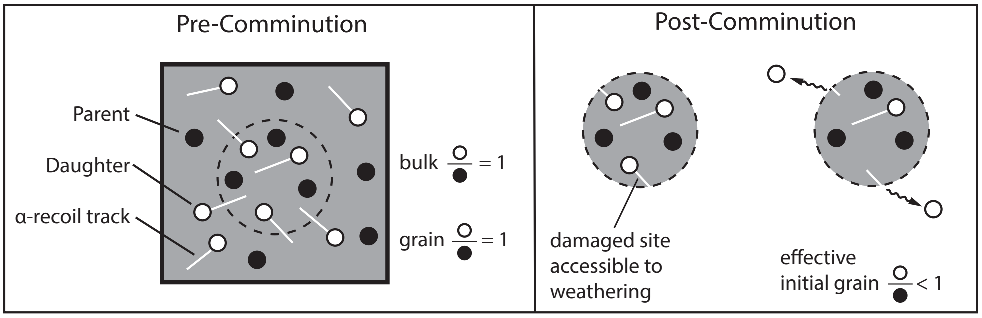

Figure 3.9: Diagram of the proposed process of rapid daughter (e.g. ^{234}U) loss following comminution. Prior to comminution, α-recoil events damage the mineral lattice around daughter isotopes, leaving "α-recoil tracks." Following comminution, those damaged zones are more susceptible to weathering, allowing for the rapid loss of daughter isotopes with α-recoil tracks intersecting the grain surface.

Table 3.1: Sequential extraction to remove soluble non-silicate authigenic phases.

Targeted Phase	**Procedure**
Amorphous Fe oxides	0.2 M ammonium oxalate + 0.2 M oxalic acid agitated at room temperature for $\geq$8 hours
Crystalline Fe oxides	0.2 M ammonium oxalate + 0.2 M oxalic acid + 114 mM ascorbic acid agitated at 90 °C for $\geq$8 hours
Mn oxides	25 % acetic acid + 0.04 M hydroxylammonium chloride agitated at 90 °C for $\geq$8 hours
Organic matter	30% H_2O_2 adjusted to pH 2 with 0.02 M HNO_3 agitated at 90 °C for $\geq$6 hours (additional 10 ml aliquots of reagent added at hours 4 and 5)
Carbonates	0.25 M HCl agitated at room temperature >4 hours

Table 3.2: Selected values for parameters used to calculate f_m values with Equation 3.1

Parameter	Description	Value	Reference	Notes
L_{234}	^{234}Th recoil distance	34 nm	(Sun and Semkow, 1998)	Mean simulated value.
L_{230}	^{230}Th recoil distance	37 nm	(Sun and Semkow, 1998)	Mean simulated value.
K	Grain shape factor	10	(Cartwright, 1962)	Oblate spheroid with 5:2 axial ratio
λ_r	Surface roughness factor	7	(White et al., 1996)	Freshly comminuted silicates
ρ	Density	2.65 g/cm^3	—	Denisty of quartz

Table 3.3: Chemical index of alteration (CIA) and CIA (molar) for fully leached sediments from Taylor Valley.

Drift	**Grain Size (μm)**	**CIA**	**±2σ**	**CIA (molar)**	**±2σ**
Taylor I (englacial)	20–38	59.8	2.4	0.98	0.04
Taylor I (englacial)	20–38	60.7	2.4	1.01	0.04
Taylor III	75–125	61.8	2.8	1.06	0.05
Taylor III	38–45	62.3	2.9	1.07	0.05
Taylor III	20–38	61.4	2.5	1.03	0.04
Taylor III	10–20	61.6	2.8	1.06	0.05
Taylor IV	20–38	59.4	2.4	0.96	0.04
Taylor IV	10–20	56.3	2.6	0.84	0.04

Table 3.4: Parameters used in simulations corresponding to each panel of Figures 3.6 and 3.8.

Parameter	**A**	**B**	**C**	**D**	**E**	**F**	**Fig. 3.8**
Initial detrital $(^{234}\mathrm{U}/^{238}\mathrm{U})$	1	1	1	1	1	1	0.94
Initial detrital $(^{230}\mathrm{Th}/^{238}\mathrm{U})$	1	1	1	1	1	1	0.94
Authigenic $(^{234}\mathrm{U}/^{238}\mathrm{U})$	3.0	3.0	3 .0	4.5	4.5	4.5	3.0
Authigenic $(^{230}\mathrm{Th}/^{238}\mathrm{U})$	4.6	4.6	4.6	4.6	4.6	4.6	—
Authigenic clay [U] (μg g^{-1})	1	1	1	1	1	1	—
Soluble rind [U] (μg g^{-1})	2	2	2	2	2	2	2
k (10^{-8} g m^{-2} a^{-1})	4	0	1	2	0	1	—
Proportion covered by rind	0	0.5	0.4	0	0.5	0.4	0.8
Rind thickness (nm)	0	100	100	0	100	100	≥1000

Chapter 4

Subglacial melting beneath the northern Laurentide Ice Sheet coincided with Heinrich events: terrestrial support for an ocean warming stimulus

4.1 Abstract

During the last glacial period, long-term expansion of the Laurentide Ice Sheet (LIS) was periodically perturbed by Heinrich events (HE): episodes of significant Hudson Strait Ice Stream acceleration and iceberg release, recorded by ice-rafted detritus in the North Atlantic sedimentary record. Proposed causal mechanisms of HEs include internal ice sheet dynamics as well as millennial-scale ocean-climate system oscillations, with more contemporary models invoking combinations of both, based on evidences in ocean sedimentary records, climate proxies, and physical simulations. Here, we present a terrestrial record of HEs from the northern LIS. Subglacial carbonate precipitates from central Baffin Island record episodes of subglacial melting in concert with HEs, spanning from before the last glacial maximum to the earliest phases of deglaciation. Given the relative stability of the Foxe Dome in LIS reconstructions of this timeframe, these subglacial melting events reflect neither transient thickening events, nor a dynamic response to ice streaming in the Hudson Strait. Rather, a more coherent explanation for the coincidence between HEs and subglacial melting on Baffin Island is shear heating of overlying ice in response to nearby ice stream acceleration in eastern Baffin Island following subsurface ocean warming and grounding line retreat. Concurrent ice streaming in Baffin Bay and the Hudson Strait supports a shared ocean-climate system stimulus for HE ice acceleration. In addition, our results implicate the presence of deeply sourced, ^{234}U-enriched groundwaters in subglacial aquifers near the LIS margin. Observations of other carbonate precipitate records encircling the LIS margin indicate widespread distribution of ^{234}U-enriched waters in LIS subglacial aquifers and permafrost environments. Enhanced basal melting and release of these fluids offer a likely mechanism for ocean U budget perturbations during early deglaciation.

4.2 Introduction

Over the course of the last glacial period, continental ice volumes crescendoed to their peak at the last glacial maximum (LGM), which was followed by collapse of the Eurasian ice sheets and the North American Laurentide Ice Sheet (LIS). Superimposed on these longer-term trends were millennial scale oscillations in climate and continental ice mass linked to interactions between the ice-ocean-atmospheric systems. The highest frequency oscillations are the so-called Dansgaard-Oeschger (D-O) events, originally observed in the oxygen isotope records of Greenland ice cores, that reflect episodes of significant local atmospheric warming (Menviel et al., 2020). D-O warm phases, or interstadials, are characterized by warm Greenland air temperatures, limited continental meltwater flux into the North Atlantic, and strong North Atlantic deepwater (NADW) formation and Atlantic meridional overturning circulation (AMOC). D-O cold phases, or stadials, are instead characterized by cooler Greenland air temperatures, enhanced continental meltwater flux to the North Atlantic, and dampened NADW formation and AMOC. Superimposed over some stadials, but not all, are Heinrich Events (HE): pulses of widespread iceberg discharge into the North Atlantic, predominantly from the LIS, that coincide with particularly fresh North Atlantic surface waters and especially weak NADW and AMOC (Hemming, 2004; Menviel et al., 2020). HEs seem to be importantly linked to stadial conditions, as they only occur during stadials and correlated climate proxies (e.g. Wang et al., 2001), and although the triggering mechanisms differ, the effects of HEs manifest much like enhanced stadial conditions (e.g. Menviel et al., 2020). For instance, Nordic sea ice varies with D-O cyclicity and HEs: sea ice extent is limited during interstadials and expands during stadials due to cooler temperatures and fresher surface waters, with North Atlantic sea ice maxima during HEs (Hoff et al., 2016).

Heinrich Events were first identified as cyclic intervals of increased lithic grain abundances in deep-sea sediment cores that reflect deposition of ice-rafted debris (IRD) born out to sea by icebergs (Heinrich, 1988). They recur quasiperiodically with a ∼7 ka frequency, and provenance studies have traced the bulk of HE-associated IRD to the Hudson Strait, implicating the Hudson Strait Ice Stream (HSIS; Fig. 4.1) as the source of much of HE iceberg discharge (Hemming, 2004).

Despite the unmistakable presence of HEs in ocean sedimentary archives and correlated climate proxies, the mechanisms initiating HSIS surging and iceberg swarms in the North Atlantic have remained a topic of debate. The quasiperiodicity and heterogenous behavior of HEs (e.g. Hemming, 2004) have motivated a longstanding effort to unravel their spatiotemporal complexity with a coherent mechanistic model. The onset of HEs depend on some combination of "internal" ice sheet dynamics and "external" ocean-climate forcings that enhanced ice streaming and iceberg production by the HSIS. MacAyeal (1993) proposed a model to describe HE cyclicity that is regulated entirely by internal ice sheet dynamics. Under this model, the LIS begins in a state of reduced thickness and cold basal temperatures that keeps the HSIS frozen at its base, resulting in slow ice velocities and inefficient transport from domes that cause the LIS to thicken. Eventually, the thickness provides enough weight and insulation to drive basal melting, which lubricates soft deformable sediments at the bed that allow rapid velocities and surging of the HSIS, thus generating icebergs with enough entrained sediment to satisfy the observed North Atlantic accumulations of IRD (Alley and MacAyeal, 1994).

While the internal model emphasizes the importance of HSIS basal conditions and ice streaming in facilitating rapid release of large ice volumes into the North Atlantic, the external ocean-climate forcing model underscores the coherence of HEs with fluctuations in the ocean-climate system. Zahn et al. (1997) observed that AMOC weakening not only overlaps HE-IRD layers, but it both precedes and follows them, indicating that HE iceberg surging is a response to an ocean-climate forcing, rather than an independent process. Marcott et al. (2011) showed that reduced AMOC circulation, as during a stadial, led to convective mixing of low-latitude warm waters that propagated subsurface ocean warming into the North

Atlantic, where intermediate-depth warming maxima coincided with HEs. By bringing warm waters into contact with marine-terminating ice and ice shelf loci of the LIS, this process heats an extremely vulnerable location for ice sheets where enhanced melting can lead to surging and rapid ice loss (Bassis et al., 2017; Noble et al., 2020; Wood et al., 2021). In the case of the LIS, Bassis et al. (2017) reconcile coordinated ice sheet dynamics and ocean forcings via the role of continental isostatic response. During periods of enhanced LIS thickness the HSIS advanced to a marine-terminating position, where isostatic adjustment lowered the HSIS grounding line to intermediate water depths ($\gtrsim$400 m). At this position, stadial subsurface warming melts the grounding line of the HSIS, which surges, thins, and retreats into the overdeepened Hudson Strait channel until centennial-scale isostatic rebound isolates the channel from intermediate water inflow and the HSIS re-stabilizes. As the HSIS begins to readvance, it is protected from subsequent stadial subsurface warming events in the uplifted channel, and will only collapse when it reaches a sufficiently advanced state that isostatic depression exposes its grounding line to intermediate-depth waters. This model is particularly attractive as it takes into account both ice sheet dynamics and ocean-climate forcings and, most importantly, coherently reproduces the differential tempos of HEs relative to D-O oscillations. Yet, this model remains theoretical and lacks observational evidence that corroborates the process of ice stream surging in response to grounding line melting by subsurface warming.

HEs reflected substantial mass loss events for the LIS where large volumes of continental ice were lost as meltwater and icebergs (Hemming, 2004; Ziemen et al., 2019). Of particular importance is the final HE (H1, with progressively earlier events increasing in number), which coincided with the termination of the last glacial period and LIS and Eurasian ice sheet collapse. H1 entailed multiple phases of complex ice-ocean interactions spanning as much as 4 ka: initial reduced NADW formation, extensive iceberg release accompanied by meltwater flux into the North Atlantic and IRD deposition, and finally recuperation of AMOC following a sustained reduced state (Stanford et al., 2011). The onset of stadial conditions preceding the H1 IRD events marks the onset of deglaciation and may have actively exacerbated terminal ice sheet collapse (Hodell et al., 2017). During the timeframe of H1 iceberg discharge and IRD deposition, the $\delta^{234}U$[1] composition of Atlantic surface waters rose by several per mille, indicating the influx of terrestrially sourced waters with particularly elevated $\delta^{234}U$ that implies provenance from subglacial reservoirs (Chen et al., 2016). The precise subglacial source of this high-$\delta^{234}U$ deglacial run-off is unclear, but its probable subglacial provenance temporally correlates the release of a significant subglacial aquatic reservoir in perfect coincidence with H1 iceberg surging during terminal LIS collapse. While this correlation implicates H1 iceberg surging in LIS deglaciation, a better understanding of the subglacial source of these distinct waters would clarify if these events are related and, if so, what glaciological mechanisms connected them.

To date, our current understanding of LIS dynamics over the course of HE and D-O cycles come from mathematical simulations, ocean sediment cores, and distal climate proxy records (Wang et al., 2001; Seierstad et al., 2014; Bassis et al., 2017). As is often the case in subglacial archives, the erosive efficiency and post-glacial flooding of the HSIS and other ice streams (e.g. Margold et al., 2015a) have overprinted or obscured *in situ* evidence of overlying ice behavior. On Baffin Island, however, the arid polar climate and persistence of cold-based ice caps have preserved subglacial $CaCO_3$ mineral precipitates that formed from subglacial LIS waters near the northern margin of the modern-day Barnes Ice Cap (BIC) and the Rimrock Hills region (Fig. 4.1). Prior studies of precipitates from these

---

[1] $\delta^{234}U = 1000 * [(^{234}U/^{238}U) - 1]$, where parentheses denote the activity ratio

sites verified their subglacial origin and dated their formation to approximately contemporaneous with the LGM (Refsnider et al., 2012, 2014). Here we expand on this prior work: we report U-Th dates of multiple episodes of aqueous carbonate precipitation in central Baffin Island and assess the provenance of the calcite-forming waters with several stable and radiogenic isotope proxies. The formation of these rocks requires the presence of liquid water beneath the LIS in a location that has historically been interpreted to be consistently cold-based (Marshall and Clark, 2002). Given the position of these subglacial precipitates between the LIS Foxe Dome and numerous marine-terminating ice streams (Fig. 4.1), ice flow acceleration and concomitant shear heating (e.g. Clarke et al., 1977; Ritz, 1987) in response to Baffin Bay ice stream surging may have driven the requisite basal melting at these locations. Herein we test the hypothesis that these subglacial precipitates record changes in the basal thermal regime due to HE-related ice streaming and contextualize these carbonate forming waters relative to potential subglacial aquifers of the LIS and their influence on global ocean chemistry.

4.3 Materials and Methods

We studied six subglacial carbonate precipitate rocks, including five samples from the northern BIC margin and one sample from the Rimrock Hills region (Figs. 4.1,4.2), originally reported by Refsnider et al. (2012, 2014). Each sample is detailed in Figure 4.2. Small "crust" samples (M09-B184R, M09-B152) were subsampled with steel hand tools, while larger samples were slabbed and subsampled with a rock saw before isolating individual fractions with hand tools.

4.3.1 Carbonate C and O isotope measurements

Isotopes of oxygen and carbon in carbonate phases were measured at the UC Santa Cruz Stable Isotopes Laboratory by acid digestion using an individual vial acid drop Themo Scientific Kiel IV carbonate device interfaced to a Thermo Scientific MAT 253 dual-inlet isotope ratio mass spectrometer (iRMS). We loaded ∼100 µg fractions into individual vials that were dried overnight in a 70 °C vacuum oven. Samples reacted at 75 °C in orthophosphoric acid (1.92 $g \cdot cm^{-3}$ specific gravity) to generate CO_2 and H_2O. The latter is cryogenically separated and noncondensible gases are pumped away prior to introduction of the CO_2 analyte into the iRMS. Samples are measured concurrently with replicates of NBS-18 limestone standard reference material and a Carrara Marble in-house standard (CM12, calibrated to NBS-18 and NBS-19). Carbonate $\delta^{18}O$ and $\delta^{13}C$ values are calculated relative to VPDB with a two-point calibration between CM12 and NBS-18 to correct for offset and linearity. Reproducibility and independent quality control are monitored with measurements of "Atlantis II" powdered coral. We convert $\delta^{18}O_{(VPDB)}$ to $\delta^{18}O_{(VSMOW)}$ via $\delta^{18}O_{(VSMOW)} = 1.03091 \times \delta^{18}O_{(VPDB)} + 30.91$ (Sharp, 2017).

4.3.2 Carbonate U, Th, and Sr isotope measurements

We measured U, Th, and Sr isotopes in the UC Santa Cruz Keck Isotope Laboratory. Individual carbonate precipitate fractions were each sonicated at room temperature in methanol for 30 minutes, triple-rinsed with ultra-pure water (deionized to 18 $M\Omega \cdot cm$), and transferred to an acid-cleaned PFA beaker. All reagents described hereafter are either triple-distilled or commercial trace-metal grade (except ultra-pure water). We submerged cleaned samples in approximately 1 ml ultra-pure water and gradually added 7 M HNO_3 dropwise to gently digest the carbonate minerals. When the reaction subsided, we brought the solution to 3 M HNO_3, spiked with a gravimetrically calibrated mixed ^{229}Th-^{236}U tracer, and warmed the solution for several hours to progress reactions to completion. We twice evaporated the fractions to dryness, rehydrated in 7 M HNO_3, and refluxed at 110 °C to ensure complete digestion and sample-spike equilibration.

We purified Th and U separates from each dissolved fraction using ion chromatography on a 1 ml bed of AG1-X8 anion-exchange resin (200–400 mesh). We introduced dissolved samples onto pre-cleaned resin in 1 ml 7 M HNO_3 and eluted matrix ions (including Sr) with 2 ml 7 M HNO_3 followed by 250 µl 6 M HCl. We eluted Th in 2 ml 6 M HCl followed by U in 3 ml water into a single beaker. We twice evaporated the U-Th separate to dryness and rehydrated with 7 M HNO_3 to ensure conversion from Cl^- to ${NO_3}^-$ salts. We then repeat the same ion chromatography procedure, collecting the Th and U elutions separately. We evaporated the elutions just to dryness, digested any residual resin by refluxing at 110 °C in 250 µl 30 % H_2O_2 for several hours, and finally dried the solutions with trace H_3PO_4. Total procedural blanks of Th and U were <50 pg and <80 pg, respectively, and negligible compared to sample sizes (100s of ng U, $\gg 10$ ng Th).

To obtain purified Sr, we evaporated the matrix elutions from the primary U-Th column to dryness, rehydrated in 0.5 ml 7 M HNO_3, and introduced this solution onto a 0.5 ml bed of pre-cleaned Sr-Spec resin. We eluted matrix with 3 ml 7 M HNO_3 and collected purified Sr in 4 ml 0.05 M HNO_3, which we dried with trace H_3PO_4.

We measured isotopes of U, Th, and Sr on the Isotopx X62 thermal ionization mass spectrometer at UC Santa Cruz. All samples were loaded onto degassed 99.99 % purity Re ribbons. We loaded U with a Si gel-0.035 M H_3PO_4 activator and measured UO_2 isotopologues using a dynamic Faraday-Daly method (Blackburn et al., 2020). We calculated U isotope compositions from UO_2 isotopologues by correcting for oxide isobaric interferences, although these corrections were negligible compared to analytical uncertainties. We corrected for mass-dependent fractionation with a linear model calibrated from long-term standard measurements and calibrated the photomultiplier deadtime from measurements of NBS SRM U-500 (as UO_2). The accuracy of U isotope measurements were validated over the course of this study with replicate measurements of NIST SRM 4321b (Appendix D, Fig. D.1). We loaded Th with 1 µl 5% HNO_3 onto Re filaments coated with graphite and measured isotopes of Th as a metal on the Daly-photomultiplier complex using a peak hopping method. Th isotope ratios were corrected for mass-dependent fractionation and photomultiplier deadtime using model values determined by measurements of SRM U-500 ionized as a metal.

U-Th isotope measurements were spike-subtracted with an algorithm that fully propagates analytical and tracer uncertainties, assuming uncorrelated uncertainties. We report and interpret measured isotopic data as activity ratios, denoted with parentheses. In the case of U isotopes, we report carbonate U compositions as $(^{234}U/^{238}U)$ ratios and report inferred calcite-forming water compositions in delta-notation: $\delta^{234}U = 1000*[(^{234}U/^{238}U)-1]$. To precisely calculate U-Th dates and initial $\delta^{234}U$ ($\delta^{234}U_o$), we used a Monte Carlo method algorithm (10^6 trials) that fully propagates the uncertainties of all input isotopic ratios, including corrections for detrital contributions where necessary (see Section 4.4.1). Dates are calculated relative to a 1950 CE “present” datum. The accuracy of U-Th dates and $\delta^{234}U_o$ were confirmed with concurrent measurement of an MIS 5e coral (Supplementary Data, Table S4.1; Hamelin et al., 1991; Chutcharavan and Dutton, 2021).

We loaded Sr with a $TaCl_5$ activator and measured Sr isotopes on Faraday cups with a static collection method. We correct for isobaric interference from ^{87}Rb on ^{87}Sr by concurrent measurement of ^{85}Rb and subtracting the intensity scaled by an assumed $^{87}\mathrm{Rb}/^{85}\mathrm{Rb} = 0.386$. We calculate a mass-dependent fractionation β factor from the measured $^{86}\mathrm{Sr}/^{88}\mathrm{Sr}$ with an exponential law, assuming a canonical $^{86}\mathrm{Sr}/^{88}\mathrm{Sr} = 0.11940$. We calculate fully corrected radiogenic $^{87}\mathrm{Sr}/^{86}\mathrm{Sr}$ compositions by applying this β factor to ^{87}Rb-corrected $^{87}\mathrm{Sr}/^{86}\mathrm{Sr}$ ratios. Before data collection, we confirmed reproduction of NIST SRM 987: $^{87}\mathrm{Sr}/^{86}\mathrm{Sr} = 0.710250 \pm 0.000011$ (1σ standard deviation, Ma et al., 2013). Over the course of this study, we report a mean SRM 987 $^{87}\mathrm{Sr}/^{86}\mathrm{Sr} = 0.710232 \pm 0.000027$ (2σ standard error, n=8), consistent with the accepted value.

4.3.3 Calculating accurate U-Th dates from detritus-rich carbonates

The accuracy of U-Th dates from aqueously formed precipitates is dependent on the effective exclusion of Th from aqueous solution (due to its insolubility), resulting in low initial Th/U ratios that do not convolute the ^{230}Th-^{234}U-^{238}U compositions used to calculate radiometric dates. Detritus-rich carbonates present a challenge to this assumption, given the propensity for adsorption of Th (and U to a lesser degree) on sediment surfaces. The acidic reagents used to digest carbonates for U-Th dating may dissolve this adsorbed Th and U as well as potentially leaching Th and U from the mineral matrices of acid-insoluble phases. Since ^{232}Th is effectively stable on the timescales of ^{230}Th and ^{234}U decay, it serves as a useful tracer of detrital Th in the acid-soluble fraction of a detritus-rich carbonate. When compared to the abundance of radiogenic ^{230}Th, ($^{230}\mathrm{Th}/^{232}\mathrm{Th}$) functionally measures the radiogenic signal-to-noise ratio. Canonically, a ($^{230}\mathrm{Th}/^{232}\mathrm{Th}$)>20 is sufficiently radiogenic to be insensitive to detrital ^{230}Th contributions.

In this study, we report U-Th dates and corresponding $\delta^{234}U_o$ without correction for all fractions with (^{230}Th/^{232}Th)≥20. In cases where (^{230}Th/^{232}Th)<20, we use isochron-based correction methods to account for detrital ^{230}Th and ^{234}U contributions. The U-Th isochron method assumes a two-component mixture between a thoraniferous detrital endmember and a uraniferous authigenic endmember. Given the four isotopes involved (^{230}Th, ^{232}Th, ^{234}U, ^{238}U), this requires a three-dimensional isochron diagram. The two forms are the "Osmond" diagram (axes normalized to ^{238}U; Osmond et al., 1970) and the "Rosholt" diagram (axes normalized to ^{232}Th; Rosholt, 1976). Although mathematically equivalent, these approaches visually depict radiogenic and detrital compositions differently: the (^{230}Th/^{238}U) and (^{234}U/^{238}U) intercepts of the Osmond isochron represent the ^{232}Th-free composition of the purely authigenic endmember, whereas the (^{230}Th/^{232}Th) and (^{234}U/^{232}Th) intercepts of the Rosholt diagram represent the composition of the thoraniferous detrital endmember. In this study, we plot three-dimensional U-Th isochrons with an Osmond type diagram since it better visualizes the scatter of data relative to analytical uncertainties (Ludwig and Titterington, 1994). In scenarios where we individually evaluate detrital (^{234}U/^{232}Th) and (^{230}Th/^{232}Th) compositions, we use two-dimensional Rosholt diagram projections to aid the visualization.

All regressions and isochron calculations were performed with a maximum likelihood estimation method in IsoplotR (Vermeesch, 2018). In cases where the isotopic data are sufficiently overdispersed relative to analytical uncertainties (we choose a threshold of MSWD>5), we use an overdispersion model (Vermeesch, 2018) that attributes all overdispersion to natural variability in one of the regressed variables. In the case of two-dimensional Rosholt-type regressions, this overdispersion is attributed to the y-variable, either (^{230}Th/^{232}Th) or (^{234}U/^{232}Th), reflecting heterogeneity in detrital U-Th compositions or calcite-forming water (^{234}U/^{238}U). In the case of three-dimensional isochron regressions, all overdispersion is attributed entirely to heterogeneity in the (^{234}U/^{238}U) composition. Since (^{234}U/^{238}U) consistently shows far greater dispersion relative to analytical uncertainties than (^{230}Th/^{238}U) when plotted against (^{232}Th/^{238}U) (Section 4.4.1), this approach provides a more accurate and precise calculation of U-Th dates than attributing overdispersion equally to all three isotope ratios. Where the overdispersion model is used, we report a dispersion term that quantifies the amount of dispersion in excess of analytical uncertainties.

All tabulated and reported U-Th dates incorporate systematic uncertainties stemming from uncertainties in isotope tracer composition (internally calibrated) and decay constants (Cheng et al., 2013). We calculate detrital (^{234}U/^{232}Th) and (^{230}Th/^{232}Th) corrections with only analytical uncertainties, excluding systematic tracer and decay constant uncertainties, to obtain a more precise internal correction.

4.4 Results

4.4.1 U-Th dates and subglacial calcite-forming events

U-Th isotope data for the six subglacial samples are summarized among Figures 4.3 to 4.7 and are tabulated in Table S4.1 (Supplementary Data). Samples range from highly radiogenic, with (^{230}Th/^{232}Th)$>$20, to relatively non-radiogenic (e.g. (^{230}Th/^{232}Th)$<$2) and (^{234}U/^{238}U) ranging from 1.7 to nearly 3.0. In this section, we use isochron-based methods to calculate accurate U-Th dates for each precipitate sample.

Samples M09-B177R and M09-B183R are both isochronous and array U-Th isochrons (Fig. 4.3), indicating that both samples formed rapidly, consistent with their massive textures (Fig. 4.2). The other four samples, however, do not array straightforward U-Th isochrons, with (^{234}U/^{238}U) being particularly heterogenous and poorly correlated with (^{232}Th/^{238}U). The isochron method assumes a simple two endmember mixture between a ^{232}Th-free authigenic endmember and a thoraniferous detrital endmember of homogenous U-Th isotope composition (Section 4.3.3). Therefore, the three-dimensional isochron can be perturbed by variability in both the isotopic composition of the detrital component as well as the (^{234}U/^{238}U) composition of the waters from which the authigenic carbonate phase precipitates. In the following discussions, we consider these scenarios and how to account for them in calculating U-Th dates of each remaining subglacial precipitate sample.

M09-B184R exhibits a correlation between (^{230}Th/^{238}U) and (^{232}Th/^{238}U), excluding a single high-^{87}Sr/^{86}Sr outlier, but no coherent correlation in the (^{234}U/^{238}U)-(^{232}Th/^{238}U) projection (Fig. 4.4). This implies a simple two endmember mixing model within respect to (^{230}Th/^{238}U), but substantial heterogeneity in (^{234}U/^{238}U) that is independent of ^{232}Th content and probably reflects (^{234}U/^{238}U) heterogeneity in the calcite-forming waters. Instead of attempting to constrain a single authigenic ^{230}Th-^{234}U-^{238}U composition, we individually assess the detrital endmember compositions of (^{230}Th/^{232}Th) and (^{234}U/^{232}Th). Figure 4.4B regresses the ^{238}U-free detrital endmember compositions of (^{230}Th/^{232}Th) and (^{234}U/^{232}Th), identifying a precise detrital (^{230}Th/^{232}Th) of 0.938 ± 0.132 and (^{234}U/^{232}Th) within uncertainty of zero (at 95 % confidence intervals). We thus interpret this to reflect a significant detrital ^{230}Th component but a negligible ^{234}U contribution. The (^{230}Th/^{232}Th)-dispersion ($0.059^{+0.080}_{-0.030}$) is minor relative to the calculated intercept, and we interpret it as a combination of minor detrital (^{230}Th/^{232}Th) heterogeneity and slight variations in radiogenic ^{230}Th production due to variable initial (^{234}U/^{238}U) in the different fractions. Since this latter contribution reflects a radiogenic component, we do not include the overdispersion in the uncertainty of our model detrital (^{230}Th/^{232}Th). By subtracting the calculated detrital (^{230}Th/^{232}Th) from the measured compositions, we recalculate Th-corrected U-Th dates of the five low-^{87}Sr/^{86}Sr M09-B184R fractions, which yield concordant ages (Table 4.1).

We interpret M09-B152R subsamples 1 and 2 (Fig. 4.2) separately since they exhibit different ^{87}Sr/^{86}Sr compositions and U-Th system behavior (Fig. 4.5). M09-B152R.2 arrays an isochron, which we regress with an overdispersion model to account for modest excess dispersion in (^{234}U/^{238}U). In contrast, the (^{234}U/^{238}U)-(^{232}Th/^{238}U) behavior of M09-B152R.1 is more erratic, reminiscent of the behavior observed in M09-B184R. In Figure 4.5B, we show that the two fractions of M09-B152R.1 regress a detrital (^{230}Th/^{232}Th) within uncertainty of zero, indicating that a detrital Th-correction is not necessary for this modestly radiogenic sample with (^{230}Th/^{232}Th)>8. As in the case of M09-B184R, we attribute the erratic (^{234}U/^{238}U) compositions of M09-B152R.1 to source water heterogeneity rather than the alternative interpretation that it formed from dramatically lower-(^{234}U/^{238}U) waters than its neighboring M09-B152R.2 counterpart. Therefore, we do not calculate or assume a (^{234}U/^{232}Th)-correction and instead accept the uncorrected U-Th dates of M09-B152R.1: 21.78 ± 0.45 and 22.34 ± 0.46 ka (relative to 1950 CE; Table S4.1). Since the M09-B152R.2 isochron date and uncorrected dates of M09-B152R.1 overlap, we consider these a single calcite-forming event, characterized by evolving waters or differing silicate detritus that account for the distinct carbonate textures and U and Sr isotope compositions.

M09-B176R exhibits two distinct layers, upper layer M09-B176R.a (subsampled at 5 intervals from a1 at the upper surface to a5 at the base) and lower layer M09-B176R.b, which exhibit distinct ^{87}Sr/^{86}Sr and U-Th isotope compositions (Figs. 4.2,4.6). We also measured the less coherent material between layers a and b, layer M09-B176R.ab, which exhibits ^{87}Sr/^{86}Sr and U-Th compositions intermediate between M09-B176R.a5 and M09-B176R.b, indicating mixture of the overlying and underlying components rather than a discreet calcite-forming event. We do not attribute a discrete date to this admixture, but rather its intermediate composition and unconsolidated texture indicate that the a-b contact is a disconformity and represents an erosive hiatus in calcite precipitation. The lower layer (b) arrays a U-Th isochron that imparts a very minor ^{230}Th-^{234}U-correction, despite the uniformly (^{230}Th/^{232}Th)<20 compositions, and yields an isochron date within uncertainty of the uncorrected U-Th dates of the constituent fractions (Fig. 4.6A,C). The upper layer (a) contains the most radiogenic material in this study with (^{230}Th/^{232}Th)>20 fractions observed at each subsampled layer, allowing us to confidently calculate independent U-Th dates without the need for a detrital correction. Overall, the U-Th dates young from the base of the layer (a5) to the top (a1; Fig. 4.6C), evidencing ongoing carbonate precipitation at the M09-B176R site from approximately 26–23 ka. The exception is layer a2, which has older U-Th dates than the underlying a3 layer, and differs texturally from surrounding layers by its coarser detritus and clasts of dark gray material similar to the matrix of layers a1 and a3–a5 (Fig. 4.6B,C). We conclude that a3 formed during a relatively erosive period that incorporated coarse detritus and rip-up clasts of older (a4, a5) material, resulting in the anomalously old U-Th dates. Thus, we exclude it as a carbonate precipitation event.

M09-B071R has mm-scale laminations that alternate between dark and light brown as a function of coarse detrital content (Fig. 4.2). We sampled these laminations at 8 intervals (Fig. 4.7). The uppermost interval M09-B071R.a1 has the lowest ^{87}Sr/^{86}Sr and the highest (^{232}Th/^{238}U) but arrays a U-Th isochron (Fig. 4.7A). In contrast, layers a2–a8 exhibit a relatively narrow range of ^{87}Sr/^{86}Sr and fairly uraniferous compositions of (^{232}Th/^{238}U)$<$0.04, comparable to the most radiogenic fractions of M09-B176R (Figs. 4.6,4.7). When regressed as a group, layers a2–a8 indicate ^{238}U-free detrital compositions of (^{234}U/^{232}Th) and (^{230}Th/^{232}Th) within uncertainty of zero (Fig. 4.7B), albeit with some scatter. While M09-B071R.a2–8 fractions all exhibit (^{230}Th/^{232}Th)$<$20, there is no correlation between the uncorrected U-Th date and (^{230}Th/^{232}Th), indicating a minor detrital ^{230}Th component that has negligible leverage on U-Th dates (Fig. 4.7). Therefore, these uncorrected U-Th dates are accurate estimations of the age of carbonate formation. When compared to their stratigraphic position, these dates span a $\sim$3 ka range and are not consistently correlated with stratigraphy. For example, the interior layers a3 and a5 exhibit the youngest dates. The relationship between U-Th dates and stratigraphy imply a complex history of minor open-system behavior and/or post-depositional calcite formation in interior layers a3–a5. Indeed the apparently younger interior ages may reflect continued fluid penetration into the pore-space of uncemented layers with more abundant coarse detrital grains (Fig. 4.7). Given the approximately normal distribution of dates centered about 18–19 ka, we conclude that M09-B071R likely underwent a protracted period of calcite formation that post-dated detrital sediment deposition with minor perturbations by open-system behavior, detrital contamination, and/or incorporation of detrital carbonate (Andrews et al., 1972).

With the exception of M09-B176R, all the samples described above reflect single episodes of subglacial calcite formation. M09-B176R records one episode of calcite formation in layer b, followed by a $>$4.66 ka hiatus in calcite formation and by four sequential episodes of calcite formation (a1 and a3–a5). The ages of these 10 Baffin Island subglacial calcite-forming events are summarized in Table 4.2 along with the corresponding calculated δ^{234}U of the formative waters at the time of calcite precipitation ($\delta^{234}\text{U}_\text{o}$). Isochron-calculated U-Th dates directly record the age of these calcite formation events and are reported without alteration. Similarly, the U-Th dates of M09-B176R layers with only one (^{230}Th/^{232}Th)>20 measurement are reported without alteration. For events with multiple U-Th dates for a single calcite-forming event (M09-B071R, M09-B184R, M09-B176R.a5), we calculate a single weighted mean date and $\delta^{234}\text{U}_\text{o}$ for the event (using a weighted mean with random effects model algorithm; Table 4.2). The more precise model ages (± <1 ka on each date) identify three episodes of subglacial carbonate formation on central Baffin Island: the first was at ∼31 ka (M09-B176R.b), the second phase spanned 25 to 23 ka (M09-B176R.a, consistent with the relatively imprecise dates of M09-B152R, M09-B183R, and M09-B177R), and the third phase at ∼18.5 ka (M09-B071R and M09-B184R, consistent with M09-B152R). BIC margin events span all three episodes, whereas Rimrock Hills carbonate formation only occurred during the most recent event. Corresponding $\delta^{234}\text{U}_\text{o}$ compositions are ∼798 ‰ at Rimrock Hills and range between 1200–2200 ‰ at the BIC margin, with no correlation between age and $\delta^{234}\text{U}_\text{o}$. These carbonate formation episodes and $\delta^{234}\text{U}_\text{o}$ are consistent with reliable U-Th dates measured by Refsnider et al. (2012): an isochron-derived U-Th date from the BIC margin of 21.0 ± 5.4 ka (overlaps both of the latter calcite-forming episodes) with $\delta^{234}\text{U}_\text{o} = 2170 \pm 260$ ‰ and a radiogenic single-fraction date of 19.1 ± 0.3 ka ($\delta^{234}\text{U}_\text{o} = 798 \pm 11$ ‰) from Rimrock Hills. We exclude a third date they calculated that uses ^{234}U- and ^{230}Th-corrections determined by an assumed mixing relationship between single measurements of separate samples.

4.4.2 Carbonate C, O, Sr, and U isotopes

We report stable and radiogenic isotope measurements of central Baffin Island carbonate precipitates, building on the work of Refsnider et al. (2014) with higher resolution sampling and the added dimensions of paired $^{87}Sr/^{86}Sr$-($^{234}U/^{238}U$) measurements and U-Th dates (Fig. 4.8). Paired $\delta^{18}O$-$\delta^{13}C$ data (Fig. 4.8A) reproduce previous observations (Refsnider et al., 2014). Precipitates at Rimrock Hills fall into two groups, the crack-fill conglomerates (heavier $\delta^{18}O$ and lighter $\delta^{13}C$) and the laminated M09-B071R (lighter $\delta^{18}O$ and heavier $\delta^{13}C$). BIC precipitates show a comparatively broad range of compositions both intermediate to the two Rimrock Hills groups and with heavier $\delta^{18}O$ and $\delta^{13}C$ compositions. This overall modest variability is consistent with O and C sourcing from slightly heterogenous mixtures of H_2O and dissolved inorganic carbon (DIC) from different reservoirs (Section 4.5.1) or varying degrees of local isotopic fractionation (e.g. regelation freezing). When compared against time, there is no systematic shift in $\delta^{13}C$ compositions of precipitates from the BIC margin, implying a relatively consistent C source to the calcite-forming waters (Fig. 4.8C). In contrast, preceding and during the LGM, all precipitates record carbonate $\delta^{18}O_{(VSMOW)}>5.9$ ‰ whereas the samples forming after the LGM (M09-B184 and M09-B071R) record $\delta^{18}O_{(VSMOW)}<5.8$ ‰(Fig. 4.8D).

Radiogenic isotopes, $^{87}Sr/^{86}Sr$ and ($^{234}U/^{238}U$), record the water-rock interaction histories of the calcite-forming fluids. In these discussions, we exclude the crack-fill carbonates from the Rimrock Hills site given their anomalously high $^{87}Sr/^{86}Sr$ compositions (>0.77) and distinct morphology that imply a distinct formation mechanism from M09-B071R and the BIC margin precipitates (Refsnider et al., 2014). Among the BIC margin samples and M09-B071R, $^{87}Sr/^{86}Sr$ ranges between 0.724 and 0.745. M09-B071R overlaps the upper range of most BIC margin precipitate ^{87}Sr/^{86}Sr compositions with the exception of the highly radiogenic sample M09-B177R (Fig. 4.8B). There is a slight positive trend in δ^{18}O-^{87}Sr/^{86}Sr space among the BIC margin samples (Fig. 4.8B) that is largely dependent on inclusion of the stratigraphically lower portion of M09-B177R (Table 4.3). There is no systematic change in ^{87}Sr/^{86}Sr with time among the Baffin Island precipitates, except among the layers of M09-B176R, which gradually evolve to less radiogenic ^{87}Sr/^{86}Sr compositions over the $\sim$1.5 ka duration of M09-B176R.a growth (Fig. 4.8E). This suggests a directionally evolving water composition for M09-B176R.a, rather than the more stochastic variability observed in M09-B071R over the duration of its formation.

In contrast to the stable isotopes, radiogenic ^{87}Sr/^{86}Sr and (^{234}U/^{238}U) define a distinctive trend among the BIC margin precipitates: an approximately hyperbolic path that implies isotopic mixing between $\geq$2 endmembers (Fig. 4.8F). The mixing trend is evident with or without M09-B177R, though inclusion of this high-^{87}Sr/^{86}Sr sample aids in constraining endmember compositions. The heterogeneity in compositions distributed through the generalized mixing envelope likely requires >2 endmembers, though at least one of these endmembers may be Sr and U leached out of the detrital component during carbonate digestion procedures. For instance, heterogenous distribution of Rb-rich minerals (e.g. biotite) may contribute to higher-^{87}Sr/^{86}Sr outliers. An additional source of heterogeneity in (^{234}U/^{238}U) is the time-dependent evolution from the original aqueous composition since the carbonate formed, which we do not correct for in the plotted compositions (consolidated δ^{234}U$_o$ compositions from isochrons would decouple the paired ^{87}Sr/^{86}Sr-(^{234}U/^{238}U) compositions we aim to investigate). However, this latter source of heterogeneity is minor as the age-correction between measured and initial (^{234}U/^{238}U) is <6 % for the timeframes of this study. Acknowledging these complexities, the $^{87}Sr/^{86}Sr$-($^{234}U/^{238}U$) data, though not broadly distributed enough to quantitatively identify endmember compositions, provide constraints on the isotopic compositions and concentrations of Sr and U in two endmembers, arbitrarily named endmembers I and II (Fig. 4.8F). Endmember I exhibits $^{87}Sr/^{86}Sr > 0.745$ and $(^{234}U/^{238}U) \leq 2$ ($\delta^{234}U \leq 1000$ ‰), whereas endmember II exhibits $^{87}Sr/^{86}Sr < 0.725$ and $(^{234}U/^{238}U) > 3$ ($\delta^{234}U > 2000$ ‰). Endmember I has a higher concentration of U and a lower concentration of Sr than endmember II.

4.5 Discussion

4.5.1 Provenance of subglacial calcite-forming waters

BIC margin and Rimrock Hills precipitates are restricted to the lee sides of bedrock undulations, bedrock fractures, and local depressions near summits, strongly supporting the conclusion that they form from the supersaturation of $CaCO_3$ in localized melt pockets cryoconcentrated by the process of basal freezing or regelation (Hallet, 1976; Refsnider et al., 2012, 2014). The extremely high U concentrations of these subglacial carbonates (40 to >100 $\mu g \cdot g^{-1}$) imply formation from a U-rich fluid, further supporting the role of cryoconcentration in increasing the ionic strength of the calcite-forming waters. Comparable calcite U concentrations are precedented in speleothems from permafrosted environments (e.g. Vaks et al., 2013), where cryoconcentration of source waters likely also occurs.

To form calcite ($CaCO_3$), Refsnider et al. (2014) inferred Ca provenance (via $^{87}Sr/^{86}Sr$) predominantly from local gneissic bedrock, O isotopically fractionated (during calcite precipitation) from H_2O in equilibrium with the overlying basal ice, and C isotopically fractionated from soil organic matter with minor contributions from bedrock calcite and atmospheric CO_2. Our results are consistent with their interpretations, affirming the preponderance of these two reservoirs as sources of H_2O and DIC in the system. Our additional chronologic work shows that by ∼19 ka carbonate $\delta^{18}O$ transitions from LGM values to compositions lighter than any observed in the prior 10 ka (Fig. 4.8D). This shift may reflect melting of isotopically lighter englacial ice (the debris-free ice above the basal ice layer; Refsnider et al., 2014) or delivery of isotopically lighter late Pleistocene ice (e.g. Mix and Ruddiman, 1984) to the bed.

While stable O and C isotopes indicate local provenance from nearly homogenous subglacial meltwater and soil organic matter reservoirs, radiogenic isotopes reveal that the dissolved cation component of the calcite-forming waters reflect a mixture of at least two distinct endmember waters (Fig. 4.8F). We propose that endmembers I and II respectively represent shallow, proximally sourced Baffin Island groundwaters and deep saline groundwaters sourced more distally from the Canadian interior.

The highly radiogenic $^{87}Sr/^{86}Sr$ signature of endmember I is consistent with local Baffin bedrock sources: glaciomarine sediments in the nearby Clyde Foreland, which received ice (and basal debris) from central Baffin Island during the LGM, range $0.74 \leq {}^{87}Sr/^{86}Sr \leq 0.76$, and Paleoproterozoic granites in southern Baffin Island with $^{87}Sr/^{86}Sr > 0.78$ are a reasonable analog for the felsic Paleoproterozoic and Archean basement rocks near the BIC margin and Rimrock Hills sites (Andrews et al., 1972; Lacelle et al., 2011; Refsnider et al., 2014). In contrast, deeply residing shield brines in Archaean to Proterozoic basement rocks of northern Canada and along the west coast of Hudson Bay range $0.710 < {}^{87}Sr/^{86}Sr \leq 0.728$ (McNutt et al., 1990). Rivers in the northern Hudson Bay region flow over glacial tills that likely reflect an integrated sample of regional bedrock compositions, and the dissolved $^{87}Sr/^{86}Sr$ of rivers from this region range from ∼0.72 to 0.73

(Wadleigh et al., 1985). These compositions overlap the required ^{87}Sr/^{86}Sr<0.725 of endmember II, qualifying groundwaters that have interacted extensively with basement rocks from central and northern Canada as plausible candidates for this endmember. Additionally, deep shield brines have higher total dissolved solids (TDS) than shallower groundwaters and have converged on $CaCl_2$ compositions (Bottomley, 1996), both of which may explain the higher Sr content of endmember II relative to the shallower-sourced endmember I.

We are not aware of any modern aqueous δ^{234}U measurements on Baffin Island, but the U isotopes measured herein provide robust evidence for the groundwater origins of both endmembers. Given the shape of the mixing relationship and accounting for the $\leq$6 % reduction in (^{234}U/^{238}U) since formation (see Section 4.4.2), the δ^{234}U of the endmember I water is slightly less than 1000 ‰, and the endmember II water substantially exceeds 2000 ‰ (at the time of calcite formation; Fig. 4.8F). Elevated aqueous δ^{234}U is associated with the time-dependent ejection of ^{234}Th, which rapidly decays to ^{234}U, from sediment surfaces following energetic α-decay (Kigoshi, 1971). Protracted residence in sediment and rock pore space allows for more production and injection of ^{234}U into waters, and ^{234}U enrichment is enhanced in systems where water volumes are very small compared to rock surface area, such as fractured bedrock (Méjean et al., 2016). While δ^{234}U>0 is typical among terrestrial waters, the largest enrichments are observed in groundwaters (e.g. Dunk et al., 2002). Aqueous δ^{234}U compositions in deep groundwaters are commonly several thousand per mille (Gascoyne, 1989). Waters with δ^{234}U>2000 ‰, as required by endmember II, are found in both bedrock aquifers (Gascoyne, 1989; Méjean et al., 2016) and groundwater-permafrost systems (Batchelor et al., 2019a; Vaks et al., 2013). We expect permafrost to have similar or elevated δ^{234}U compared to liquid groundwaters of similar depth, as permafrost waters can experience protracted residence frozen in contact with rock and sediment. Moreover, permafrost efficiently fractures rock (Murton et al., 2006), which increases surface area and enhances ^{234}U injection, a process that may have been augmented by subglacial hydraulic pressures from the LIS (Méjean et al., 2017).

Given the association of groundwaters with high δ^{234}U compositions, we identify groundwater provenance as the most defensible explanation for the elevated δ^{234}U compositions of the two endmember waters. Since deeper-residing groundwaters exhibit higher δ^{234}U than their shallower counterparts by as much as 1000 ‰ or more (Kraemer and Brabets, 2012; Méjean et al., 2016), we identify the lower-δ^{234}U endmember I as a relatively shallow groundwater, compared to the more deeply derived, higher-δ^{234}U endmember II. In addition to rock surface area and residence time, the degree of δ^{234}U enrichment in groundwaters scales with decreasing aqueous concentration of U (e.g. Méjean et al., 2016). Therefore, we expect high-δ^{234}U waters to reflect relatively lower U concentrations, consistent with predicted endmember compositions (Fig. 4.8F).

Mixing of these proposed groundwaters sources with subglacial meltwaters had no discernible effect on stable O and C isotope compositions. The most parsimonious explanation is that the local subglacial meltwater was initially well-mixed with shallow Baffin Island groundwater (endmember I), and this water source was the volumetrically dominant component of the mixture that formed BIC margin precipitates. Admixture of this endmember I water with small volumes of high-TDS groundwaters (endmember II) significantly affected the Sr and U isotope systems without measurably perturbing the isotopic composition of the H_2O or DIC. And even if larger volumes were incorporated, this would have a minor effect on both C and O compositions: deep saline and brine groundwaters have low DIC contents (Frape et al., 1984) and O isotope compositions similar to or lighter than local meteoric water, such that saline groundwaters in northern central Canada approach the same composition as BIC basal ice compositions (Frape and Fritz, 1982; Refsnider et al., 2012). If the elevated $\delta^{18}O$ and $^{87}Sr/^{86}Sr$ compositions of M09-B177R (Fig. 4.8B) reflect lighter O isotopes affiliated with endmember I, this would imply that shallow Baffin groundwaters are modestly heavier than deep Canadian groundwaters. However, the tenuous correlation between $\delta^{18}O$ and $^{87}Sr/^{86}Sr$ among BIC margin precipitates fail to conclusively support or refute this hypothesis.

Thus, between 31 and 18 ka, Baffin Island shallow groundwaters were well mixed with LIS basal meltwater (in equilibrium with the basal ice) and had DIC predominantly derived from oxidized soil organic matter. These shallow groundwaters mixed with small volumes of saline or briny groundwaters distally sourced from deep bedrock aquifers toward the continental interior, altering cation compositions but having no measurable effect on the isotopic composition of H_2O or DIC. Apparently, deep groundwaters did not reach the Rimrock Hills location, where U did not vary from a $\delta^{234}U_o$ of $\sim$800 ‰ (Table 4.2; Refsnider et al., 2012). In terms of $^{87}Sr/^{86}Sr$, M09-B071R does not fall on the BIC mixing trend and fracture-filling Rimrock Hills precipitates are highly radiogenic ($^{87}Sr/^{86}Sr>0.77$; Refsnider et al., 2014). While fracture-filling Rimrock Hills precipitates may present a viable endmember I composition ($^{87}Sr/^{86}Sr\sim0.78$, $\delta^{234}U\sim800$ ‰), U and Sr isotopes from the Rimrock Hills site indicate no evidence of deep groundwater incorporation and we conclude that these samples likely precipitated from uncontaminated local waters with a broad range of $^{87}Sr/^{86}Sr$ compositions dependent on varied local lithology or the heterogenous incorporation of minerals with readily leachable radiogenic Sr (e.g. biotite). Thus, unlike the modern BIC margin, the Rimrock Hills sites were isolated from distally sourced groundwaters, perhaps due to their locations at local summits (Andrews et al., 1972; Refsnider et al., 2012) or other regional factors that limited groundwater flow to the region.

4.5.2 Mechanisms of groundwater transport toward the LIS margin

While calcite-forming sites of the Rimrock Hills region remained isolated from non-local groundwaters during the early deglacial period (∼20–17 ka), precipitates at the modern-day BIC margin record the presence of waters from 31–18 ka that are compositionally consistent with high salinity groundwaters found at several hundreds of meters depth in crystalline basement rocks of the Canadian shield (Frape et al., 1984; McNutt et al., 1990). The presence of these high-density shield brines at the base of the LIS requires a powerful physical mechanism to pump them to the surface at this location. Such a pump was likely achieved by glaciohydraulic reorganization of groundwater flow beneath the LIS. The overlying weight of ice sheets drive downward infiltration of basal meltwaters beneath the ice sheet interior, pressurizing subglacial aquifers and generating a steep hydraulic gradient between the ice sheet interior and margin (Boulton et al., 1993; Clark et al., 2000). As fresh meltwaters are driven deep into subsurface, they both mobilize and mix with high-salinity shield brines. Geochemical observations evidence LIS-related cryogenic effects on saline Canadian groundwaters at depths up to 1300 m (Clark et al., 2000; Stotler et al., 2012), an observation matched by numerical simulations of LIS groundwater recharge (Lemieux and Sudicky, 2010). As these waters flow along hydraulic gradients to the thinner ice sheet margin, their flow paths shallow, bringing deeply sourced shield brines, diluted to varying degrees with meltwater, toward the surface. Simulations of sub-LIS groundwater flow predict upwelling of ancient, deeply sourced groundwater extending ∼100 km interior from the northeastern LIS margin (Lemieux and Sudicky, 2010). Although these simulations predict that the BIC margin region was underlain by permafrost over this timeframe (Lemieux et al., 2008; Lemieux and Sudicky, 2010), the presence of carbonate precipitates formed during this timeframe require at least intermittent subsolidus conditions at this site, and the evidence of aqueous mixtures implies that melting accommodated connectivity with deeper groundwaters. Upwelling may have been facilitated by rock fracture networks and high-salinity brines may have helped lower the melting point of overlying permafrost to penetrate the surface.

4.5.3 Synchrony of Heinrich events and subglacial calcite formation on Baffin Island

Figure 4.9 compares the ages of central Baffin Island calcite-forming events with several paleoclimate proxies spanning the interval 12 to 35 ka. Subglacial calcite-forming events occurred during a state of ice thicknesses above pre-30 ka levels, indicating the clustering of these events around LGM ice sheet conditions (Fig. 4.9D). Precise U-Th ages align closely with HEs, as recorded by several proxies: HE-associated stadials in the NGRIP $\delta^{18}O$ record (Fig. 4.9A; Seierstad et al., 2014); HE-associated positive excursions of the chronologically well-constrained Hulu cave record (Fig. 4.9B; Wang et al., 2001); and enhanced surface freshening in the North Atlantic recorded by $\delta^{18}O$ of sinistral *Neogloboquadrina pachyderma* (Fig. 4.9C; Hillaire-Marcel and Bilodeau, 2000; Lynch-Stieglitz et al., 2014). Central Baffin Island carbonate precipitation also coincides with IRD peaks during H2 and H3 and North Atlantic intermediate-depth warming, a hypothesized HE stimulus, during H1 and H3 (Fig. 4.9F,G; Marcott et al., 2011).

Although the North Atlantic subsurface temperature record is absent during H2, local $\delta^{18}O$ maxima in the Western Antarctic Ice Sheet (WAIS) Divide ice core, which reflect Southern Ocean warming, lag North Atlantic subsurface warming peaks by ~300 to 900 years, and a WAIS $\delta^{18}O$ peak at ~23.7 ka implies a 24.0–24.6 ka North Atlantic subsurface temperature peak that coincides with the H2 carbonate precipitation event (Fig. 4.9E,G,H). Since North Atlantic subsurface warming is directly related to stadial conditions (Marcott et al., 2011), this behavior is fully consistent with "polar seesaw" models of inter-hemispheric heat redistribution over D-O cycles, whereby Southern Ocean warming occurs during cool North Atlantic surface conditions of stadials (e.g. EPICA Community Members, 2006). The observed time lag may be related to inter-hemispheric lags between the WAIS and northern hemisphere records of up to 300 years (WAIS Divide Project Members, 2015) or age-depth model uncertainties for core EW9302-2JPC ($2\sigma = 200$ to 600 years at each dated horizon; Marcott et al., 2011).

In concert, these records indicate perfect concordance between Baffin Island carbonate precipitation events and typical (non-terminal) HEs, implying a relationship between HE processes and basal ice sheet processes over central Baffin Island. Cold-based conditions at the BIC margin and across much of Baffin Island margin during the last glacial period are supported by ice sheet reconstructions (Marshall and Clark, 2002) and the preservation of >40 ka plants in growth position within the modern Penny Ice Cap (Pendleton et al., 2019). However, the requirement of liquid water for $CaCO_3$ precipitation indicates that LIS processes during HEs accommodated basal melting at the modern BIC margin by either thickening the overlying ice mass or by shear heating resulting from accelerated ice flow. The stability of reconstructed ice thickness over Baffin Island during the interval from 30–15 ka contradicts a cyclic thickening (i.e. binge-purge) mechanism driving subglacial melting at this location (Fig. 4.9D; Gowan et al., 2021).

Therefore, melting at this site requires ice acceleration and concomitant shear-heating, which could be achieved by enhanced ice streaming in the numerous ice streams on the eastern coast of Baffin Island (Fig. 4.1). Baffin Island ice streams that formerly occupied the Scott and Buchanan Troughs adjacent to the BIC, reached LGM extents that positioned their grounding lines in excess of 1000 m below modern day sea-level (Brouard and Lajeunesse, 2017), the same intermediate water depths that record benthic warming correlated with HEs (Fig. 4.9G; Marcott et al., 2011). Models relating HEs to subsurface warming invoke HSIS surging in response to grounding line melting and retreat (Bassis et al., 2017) or collapse of ice-stream-buttressing ice shelves (Marcott et al., 2011). We propose that the same process(es) occurred for ice streams along the Baffin Island coast, resulting in ice stream surging that accelerated inland ice velocities and elevated basal temperatures via shear heating (e.g. Clarke et al., 1977; Ritz, 1987) to accommodate basal melting and carbonate precipitation at the BIC margin. The enhanced ice flow velocity must be connected to Baffin Island ice stream surging rather than HSIS surging given the relative stability of the Foxe Dome during widespread LIS thinning associated with HSIS surges. For instance, the early deglacial period (20–15 ka) saw significant thinning of the Keewatin and Quebec-Labrador domes, whereas the Foxe Dome elevation remained essentially unchanged (Fig. 4.1; Gowan et al., 2021). Thus, the formation of subglacial precipitates at the BIC margin was a consequence of local ice stream responses to ocean subsurface warming and implicates subsurface North Atlantic warming as a causal mechanism of HEs, independent of traditional HSIS evidences. The similar pacing of these Baffin Island HE responses imply that the recovery time of Baffin Island ice streams were similar to the HSIS (Bassis et al., 2017) or that HE-inducing ocean warming events were especially pronounced or modulated by ice shelf and sea ice processes (Marcott et al., 2011; Hoff et al., 2016).

Despite ongoing subsurface ocean warming during H1, subglacial calcite precipitation stopped by ∼18 ka, prior to the onset of H1 IRD deposition (Fig. 4.9E–G). The abrupt cessation may suggest a shift in LIS dynamics and associated basal conditions following the progression of glacial termination that began between 18–20 ka (Denton et al., 2010). Alternatively, this may be an artifact of a small number of samples (two at the Rimrock Hills site and one at the BIC margin) that fail to capture the true duration of subglacial calcite precipitation across the H1 interval. Moreover, the concordance of the two Rimrock Hills samples may indicate that calcite precipitation at the Rimrock Hills site was not sensitive to HE fluctuations over the course of Marine Isotope Stage (MIS) 2, but rather was sensitive to basal melting only during the LGM. The distinct morphological character of the Rimrock Hills sample suite and their formation at summit locations (Refsnider et al., 2012) imply that their formation mechanism may be decoupled from the BIC margin precipitates. Further collection and analysis of subglacial precipitates from central Baffin Island will be crucial to sufficiently evaluate the duration of subglacial calcite precipitation at the onset of H1.

Conversely, our findings and those of Refsnider et al. (2012) do not identify any subglacial carbonate precipitation on Baffin Island preceding H3, which reflects either inhibited basal melting or poor precipitate preservation prior to ∼30 ka. The reduced thickness of the LIS during MIS 3 (Dalton et al., 2019; Gowan et al., 2021) may have prevented basal melting and calcite formation even during periods of ice acceleration. Indeed, the first carbonate precipitate appears when local ice recovers to its thickest since MIS 3 (Fig. 4.9D). The recuperated ice thickness (>1400 m at BIC margin by 30 ka) may have been necessary to sufficiently insulate the bed to accommodate melting during HE-associated ice stream acceleration and shear heating. In addition, MIS 2 expansion of the LIS may have taken until ~30 ka to advance the grounding lines of Baffin Island ice streams into intermediate-depth ocean water (or establish a large enough ice shelf) and become sufficiently sensitive to subsurface warming events. Alternatively, limited preservation of pre-H3 carbonate precipitates may also account for their absence in the present dataset. The disconformity between the layers M09-B176R.a and M09-B176R.b (Fig. 4.6B,C) confirms erosion of early-formed carbonate precipitates between episodes of formation. However, preservation of M09-B176R.b, albeit partially eroded, implies that more ancient samples may be found near the BIC margin if they were adequately protected from these erosive episodes. Further collection and analysis of BIC margin carbonate precipitates will provide important tests of this hypothesis and evaluate whether significant basal melting in central Baffin Island occurred prior to ~30 ka.

4.5.4 A source for elevated ocean δ^{234}U during early deglaciation

The elevated $\delta^{234}U_o$ compositions of calcite-forming subglacial waters on Baffin Island are consistent with the subglacially derived high-δ^{234}U waters invoked to explain the rise in North Atlantic δ^{234}U during H1 (Fig. 4.9K; Chen et al., 2016). In addition, seafloor sediments from Baffin Bay record a release of high-δ^{234}U waters into Baffin Bay shortly after lower latitude Atlantic δ^{234}U reaches its peak. In Baffin Bay, sedimentation rate and the flux of unsupported ^{230}Th to sediments increase in unison during H2 and H3 (Fig. 4.9I,J), consistent with enhanced transport of scavenged ^{230}Th to the seafloor during increased sedimentation (Simon et al., 2012; Nuttin and Hillaire-Marcel, 2015). Yet, the sedimentation rate remains conspicuously unchanged during a surge of ^{230}Th flux to values

4–5 times higher than background conditions, beginning immediately following final subglacial carbonate formation on Baffin Island and peak $\delta^{234}U$ in the low-latitude Atlantic (Fig. 4.9E,I–K). Since ^{230}Th flux to the seafloor scales with the amount of parent ^{234}U in the water column, increased marine ^{234}U will enhance ^{230}Th production rates and lead to an enhanced sedimentary flux of unsupported ^{230}Th. Therefore, the elevated ^{230}Th flux to Baffin Bay sediments without a corresponding sedimentation rate increase implies the release of high [U] and $\delta^{234}U$ waters into Baffin Bay. The deglacial ^{230}Th flux is nearly 5 times greater than the background flux, an enrichment almost 2 orders of magnitude greater than the 6 % increase in $\delta^{234}U$ observed in lower latitude Atlantic waters (Chen et al., 2016). Thus, we infer a localized high-$\delta^{234}U$ perturbation in Baffin Bay, implicating $\delta^{234}U > 1000$ ‰ waters, such as those recorded by subglacial carbonates in central Baffin Island for 15 ka prior to this event. Before ∼17 ka, high-$\delta^{234}U$ subglacial groundwater aquifers were likely restrained by permafrost conditions at the LIS margin that persisted during HEs. During the extended H1-deglacial conditions, we propose this water was instead routed to the ice sheet margin, perhaps due to protracted subsurface ocean warming or more extensive LIS basal melting than during previous HEs (Marshall and Clark, 2002).

Elevated $\delta^{234}U$ compositions are found widely in marginal zones of the LGM LIS (Fig. 4.1A). Speleothems just beyond the southern LIS margin and within 20–50 m of the modern surface record $\delta^{234}U_o$ ranging from 800 to 8000 ‰, with the majority >2000 ‰, spanning the last 250 ka (Batchelor et al., 2019a). Late Pleistocene speleothems from caves near the southeastern LIS margin record some $\delta^{234}U_o$ compositions in excess of 1000 ‰ (Lauritzen and Mylroie, 2000). Cryogenically precipitated carbonates in an aufeis frozen from LIS basal waters near the LGM northwestern margin at ∼19 ka record $\delta^{234}U_o \sim 800$ ‰ (Lacelle et al., 2013).

In the southern Canadian Rockies, near the southwestern margin of the LIS, some high-elevation (2500 m above modern sea level) speleothems record $\delta^{234}U_o$ in excess of 1000 ‰ (Biller-Celander et al., 2021). We acknowledge that the above-mentioned elevated $\delta^{234}U$ compositions are not necessarily an artifact of glacio-hydraulic pumping of deep shield groundwaters to the surface and may instead reflect protracted residence of porewater in permafrost environments (e.g. Ewing et al., 2015). For example, long-lived permafrost systems in Siberia have maintained $\delta^{234}U > 1000$ ‰ over million-year timeframes without the presence of an ice sheet (Vaks et al., 2013, 2020). Southern and southeastern LIS permafrost environments were flushed by groundwater discharge during glacial terminations (if not more frequently; Lemieux et al., 2008), making the protracted ($10^5 - 10^6$ years) porewater residence necessary for substantial *in situ* ^{234}U-enrichment improbable (Ewing et al., 2015; Vaks et al., 2020). Nonetheless, the groundwater-permafrost distinction is functionally unimportant: the mechanisms of ^{234}U-enrichment by α-recoil injection are identical in bedrock aquifer, subglacial groundwater, and permafrost settings (Ewing et al., 2015; Méjean et al., 2016; Blackburn et al., 2020) and all produce high-$\delta^{234}U$ subglacial and periglacial groundwaters. Collectively, records of high-$\delta^{234}U$ shallow and surfacing groundwaters ringing the LIS margin imply that such waters were commonplace, constituting a significant reservoir of continental waters with elevated $\delta^{234}U$ stored in permafrost and (potentially pressurized) subglacial aquifers (Boulton et al., 1993).

We identify LIS groundwaters, broadly encompassing liquid porewaters in subglacial tills as well as permafrost in sub- and proglacial settings, as a compelling candidate for the subglacial reservoir responsible for 6 ‰ enrichment of Atlantic Ocean $\delta^{234}U$ during early deglaciation (Chen et al., 2016). As discussed above, these waters both occurred widely around the LIS margin and, in Baffin Bay, appear to have been responsible for locally elevated seawater δ^{234}U (evidenced by elevated sedimentary ^{230}Th flux). Therefore, LIS groundwaters represent a sizable reservoir of relatively high-δ^{234}U waters that may be readily released into marine environments during deglacial processes. Chen et al. (2016) simulated the upper North Atlantic record by reducing a simplified model AMOC by 50 % and enhancing the δ^{234}U of modern riverine and groundwater inputs into the upper Atlantic from 339 to 800 ‰. In comparison, LIS-associated groundwater δ^{234}U are often ≥800 ‰. In terms of the total flux, subglacial precipitates are poor records of the quantitative U content of parental subglacial groundwaters, given their proposed formation from cryoconcentrated residues of groundwaters (periglacial speleothems and concretions may be similarly concentrated or diluted with meltwater). However, deep groundwaters with elevated δ^{234}U are typically >10 µg U·l^{-1} (e.g. Gascoyne, 1989), and Arctic permafrosts with δ^{234}U approaching 1000 ‰ range from ∼1–50 µg·l^{-1} (Ewing et al., 2015). These compositions exceed the U content of seawater (∼3 µg·l^{-1}; Chen et al., 1986), indicating that subglacial waters and melted permafrost may serve as powerful levers on ocean δ^{234}U at lesser volumes than riverine input (typically ≪3 µg·l^{-1}; Dunk et al., 2002). Thus, melted permafrosts and deeply sourced groundwaters can approximate the U fluxes identified by Chen et al. (2016) to adequately reproduce North Atlantic δ^{234}U enrichment at 20–15 ka.

The likely role of LIS permafrosts and groundwaters in the deglacial Atlantic U budget is further supported by the sensitivity of these two reservoirs to basal melting. The areal extent of the LIS remained stable from the LGM until about 15 ka (Dyke et al., 2002), indicating that ice margin retreat and subaerial exposure of subglacial waters are not tenable mechanisms for subglacial water release. LIS models predict that LGM-like ice volumes similarly persisted to ∼15 ka, but basal melt increased from <40 % at 25 ka to >50–60 % between 20 and 15 ka (Marshall and Clark, 2002), in large part due to sustained LGM ice thickness. The early deglacial progression of subglacial melting provided an efficient mechanism to mobilize high-δ^{234}U waters sealed in permafrost and sub-permafrost marginal aquifers and enhance hydrologic connectivity to deliver interior groundwaters to the ice sheet margin.

4.6 Conclusions & Future Work

Subglacially formed carbonate precipitates from the northern BIC margin and Rimrock Hills region of Baffin Island provide a terrestrial record of changing LIS dynamics and subglacial melting during HEs. Since reconstructed ice thickness remains fairly stable at the BIC margin spanning several episodes of subglacial melting, enhanced thickness during HEs is an unlikely impetus for subglacial melting, instead requiring a dynamic heat source. However, the Foxe Dome and northward ice drainage over central Baffin Island are relatively insensitive to southerly ice thinning and require local changes in ice dynamics to generate basal warming. Collectively, observations and predictions are most consistent with basal shear heating caused by Baffin Bay ice stream surging in response to subsurface ocean warming, which also triggers HSIS surging (Marcott et al., 2011; Bassis et al., 2017). While internal ice sheet dynamics may play a modulating role in the process, our terrestrial record of ice acceleration supports an ocean warming stimulus for HEs.

Stable and radiogenic isotope compositions of the carbonate precipitates identify local provenance of C and O, whereas dissolved cations indicate mixture of local waters with deep groundwaters derived from the continental interior. The elevated δ^{234}U compositions of groundwaters on Baffin Island are comparable to records of other sub- and peri-glacial groundwaters found widely along the LIS margin, indicating that high δ^{234}U subglacial groundwaters and permafrosts were widespread beneath the marginal LIS. Basal melting of the LIS during early deglaciation would have melted, mixed, and released these waters at the ice sheet margin and may have caused the rise in Atlantic intermediate-surface water δ^{234}U observed during this timeframe (Chen et al., 2016). Ongoing work in this study will more quantitatively explore how model LIS groundwaters may have contributed to the Atlantic Ocean U budget during the latest Pleistocene, building on pre-existing ocean mixing model frameworks.

Acknowledgements

This chapter reflects a manuscript in preparation with the following coauthors: Terrence Blackburn, Slawek Tulaczyk, Gavin Piccione, Gifford Miller, and Cosmo Varah-Sikes.

We thank E. Troy Rasbury and Sidney Hemming for thoughtful insights and discussions. We are indebted to Colin Carney of the UCSC Stable Isotope Laboratory for his wisdom and expertise. We thank Jean Lynch-Stieglitz for sharing recalibrated sediment core data.

4.7 Figures & Tables

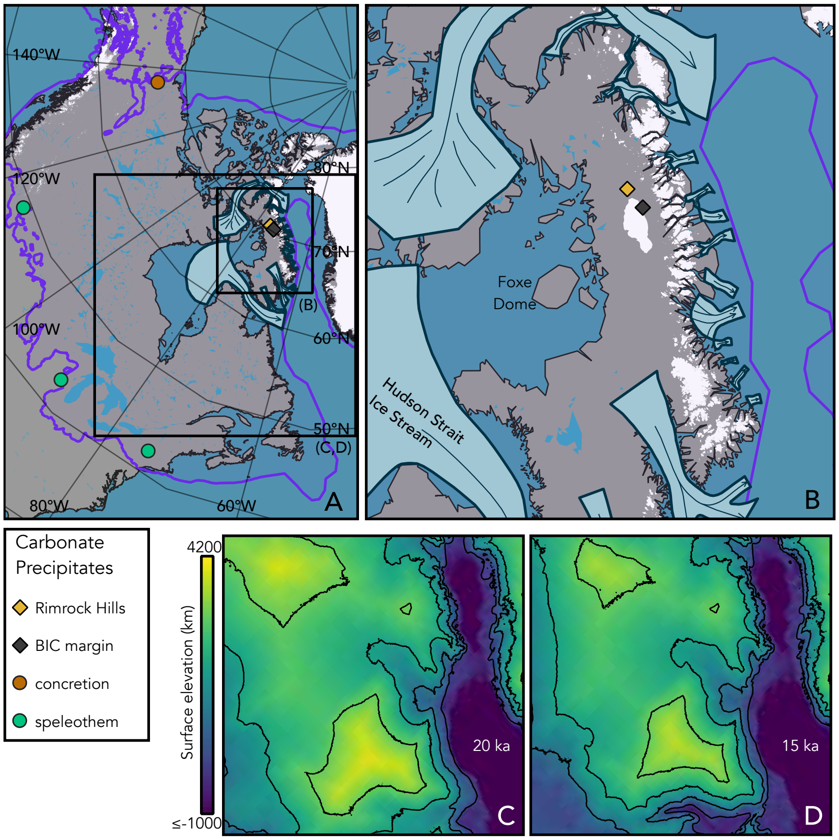

Figure 4.1: **A,B.** Maps of the Laurentide ice sheet (LIS) extent (A) and Baffin Island (B). Modern sea level and land ice distribution (white) are overlain by LIS extent at the last glacial maximum (purple border; Batchelor et al., 2019b), paleo-ice streams draining the Foxe Dome (pale blue with dark borders; Margold et al., 2015b), subglacial carbonate precipitates measured in this study (diamonds), and groundwater-fed periglacial carbonate precipitates with $\delta^{234}U_o > 500$ ‰ (circles; Lauritzen and Mylroie, 2000; Lacelle et al., 2013; Batchelor et al., 2019a; Biller-Celander et al., 2021). Black boxes in A indicate extents in B–D. **C,D.** Surface elevation of LIS and surrounding land and bathymetry (relative to modern sea level) at 20 and 15 ka (Gowan et al., 2021) with contours at 1000 m intervals (starting at 0 m).

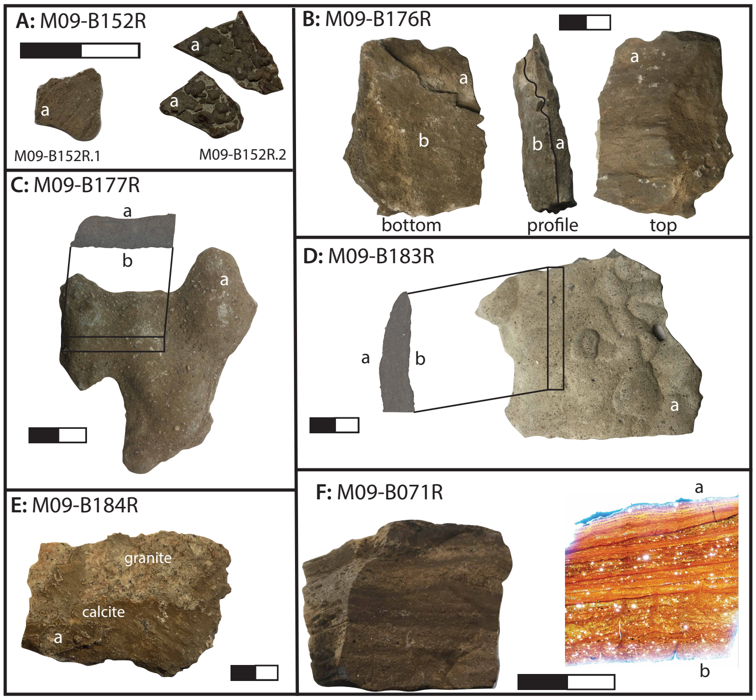

Figure 4.2: Subglacial carbonate precipitates analyzed in this study. Scale bars represent 2 cm and "a" and "b" labels respectively indicate upper and lower surfaces and layers. **A.** M09-B152R fragments are mm-scale veneers formed on rock surfaces, exhibiting two different lithologies. M09-B152R.1: light-brown carbonate-cemented clastics with linear grooves parallel to the direction of ice flow. M09-B152R.2: dark brown, mm-scale nodules with less detrital content. **B.** M09-B176R has two distinct layers (a and b), separated by a sharp contact (traced in "profile" perspective). **C.** M09-B177R is gray-brown with a globular surface morphology and a massive interior texture of calcite-cemented sand-to-silt detritus. Black box outlines location of cross-section. **D.** M09-B183R is pale grey to beige with a globular surface morphology and a massive calcite-cemented interior texture similar to M09-B177R. Cross-section outlined as in D. This rock was sampled within 60 m of the BIC edge, suggesting very recent exposure, which may account for its lighter surface color compared to the morphologically similar M09-B177R. **E.** M09-B184R is a thin, light brown veneer of calcite on a granite clast, with delicate fluted lineations parallel to local ice flow. **F.** M09-B071R, sampled from the Rimrock Hills region, is a calcite-cemented siltstone with alternating dark and light brown laminations. Light layers correspond to increased detrital sand content (visible in transmitted light photomicrograph).

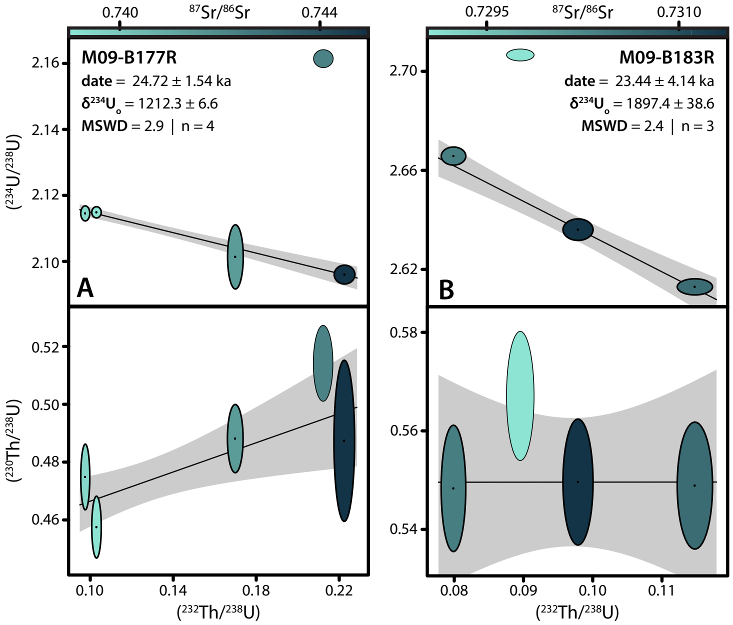

Figure 4.3: Two-dimensional projections of three-dimensional U-Th isochrons for M09-B177R (**A**) and M09-B183R (**B**). Color denotes ^{87}Sr/^{86}Sr. All reported and plotted uncertainties (ellipses and gray regression envelopes) reflect 95 % confidence intervals and include decay constant and tracer uncertainties. Fractions included in the regressions are indicated with black dots and thick borders.

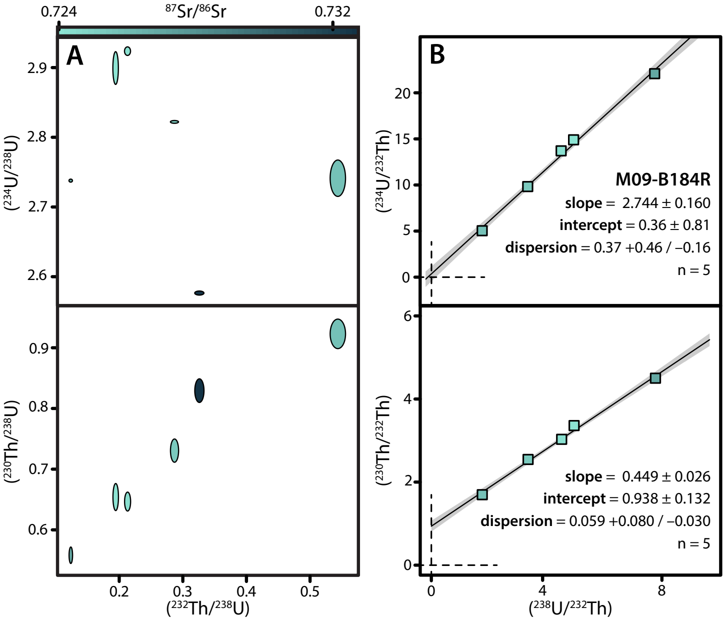

Figure 4.4: U-Th isotope and ^{87}Sr/^{86}Sr compositions of M09-B184R fractions. **A.** Low ^{87}Sr/^{86}Sr fractions are apparently correlated with respect to (^{230}Th/^{238}U)-(^{232}Th/^{238}U) but not (^{234}U/^{238}U)-(^{232}Th/^{238}U). Ellipses reflect 95 % confidence intervals, including decay constant and tracer uncertainties. **B.** Regressions of ^{232}Th-normalized ^{230}Th-^{234}U-^{238}U data identify a significantly non-zero (^{230}Th/^{232}Th) intercept and an (^{234}U/^{232}Th) intercept within uncertainty of zero (dashed lines). Regressions incorporate analytical uncertainties only (smaller than symbols) and were calculated with a maximum likelihood estimation method that attributes over-dispersion to geologic variation in (^{234}U/^{232}Th) or (^{230}Th/^{232}Th), summarized in the reported "dispersion" terms (Vermeesch, 2018). Plotted and reported uncertainties are 95 % confidence intervals.

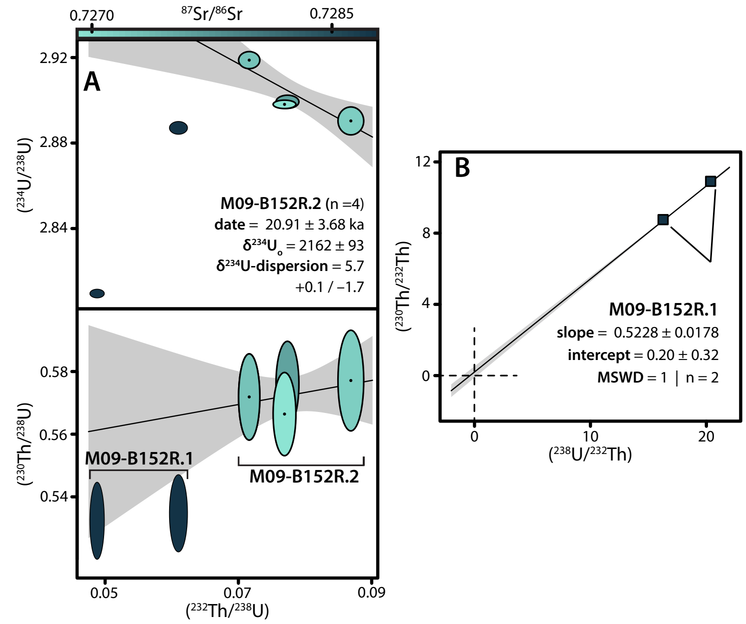

Figure 4.5: U-Th isotope and ^{87}Sr/^{86}Sr compositions of M09-B152R fractions. **A.** M09-B152R.1 and M09-B152R.2 exhibit distinct Sr isotope compositions and U-Th behavior. All plotted uncertainties (ellipses and gray regression envelopes) and reported uncertainties reflect 95 % confidence intervals and include tracer and decay constant uncertainties. Regression was calculated by a maximum likelihood estimation method that attributes over-dispersion to geologic variability in (^{234}U/^{238}U) (Vermeesch, 2018). **B.** Regression of (^{230}Th/^{232}Th)-(^{238}U/^{232}Th) data intersect the origin (dashed lines) within a 95 % confidence interval (gray envelope) for M09-B152R.1. Regressions incorporate analytical uncertainties only (smaller than symbols).

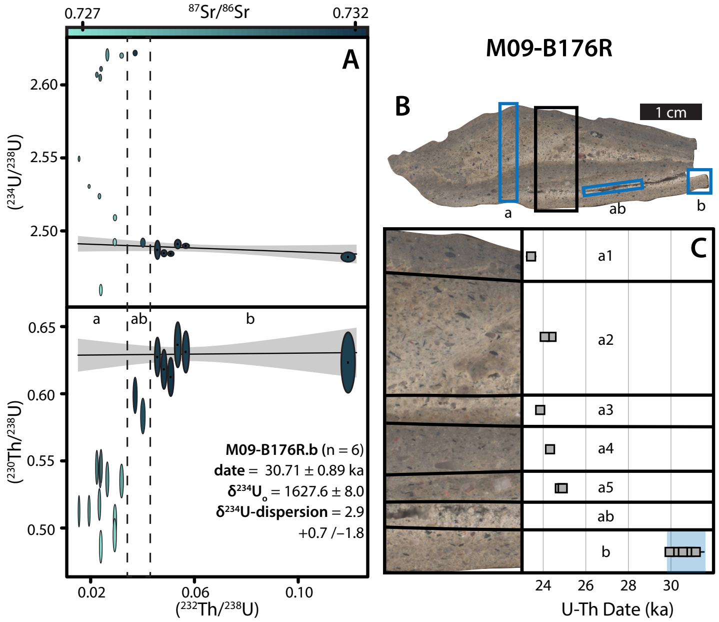

Figure 4.6: A. Two-dimensional projections of three-dimensional U-Th isotope plots and $^{87}Sr/^{86}Sr$ compositions of M09-B176R fractions. Subsample groups a, ab, and b (panel B) are separated by vertical dashed lines. Fractions of subsample M09-B176R.b exhibit similarly elevated $^{87}Sr/^{86}Sr$ compositions and array a U-Th isochron (included fractions have black central dots and thick ellipse borders). All reported and plotted uncertainties (ellipses and gray regression envelopes) reflect 95 % confidence intervals and include tracer and decay constant uncertainties. Regression was calculated by a maximum likelihood estimation method that attributes over-dispersion to geologic variability in ($^{234}U/^{238}U$) (Vermeesch, 2018). **B.** Cross-section of M09-B176R. Blue boxes indicate sampling locations of upper unit (a), lower unit (b), and less coherent material between those units (ab). Black box bounds enlarged region in panel C. **C.** Uncorrected U-Th dates of stratigraphic layers of M09-B176R, plotted with analytical uncertainties (2σ standard error, typically smaller than symbols). Black lines demarcate layer divisions. M09-B176R.b U-Th dates are within uncertainty of the isochron date (blue). All plotted M09-B176R.a dates reflect fractions with ($^{230}Th/^{232}Th$)>20.

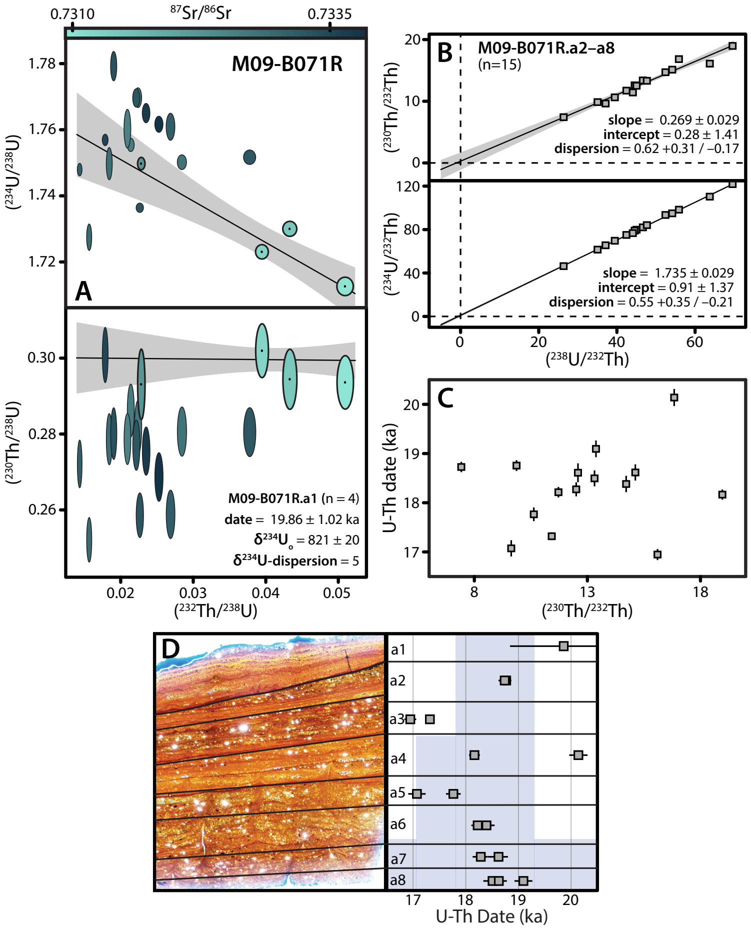
0.7310
$^{87}Sr/^{86}Sr$
0.7335
M09-B071R
A
$(^{234}U/^{238}U)$
1.78
1.76
1.74
1.72
$(^{230}Th/^{238}U)$
0.30
0.28
0.26
M09-B071R.a1 (n = 4)
date = 19.86 ± 1.02 ka
$\delta^{234}U_o$ = 821 ± 20
δ^{234}U-dispersion = 5
0.02
0.03
0.04
0.05
$(^{232}Th/^{238}U)$
B
M09-B071R.a2–a8
(n=15)
$(^{230}Th/^{232}Th)$
20
10
0
slope = 0.269 ± 0.029
intercept = 0.28 ± 1.41
dispersion = 0.62 +0.31 / −0.17
$(^{234}U/^{232}Th)$
120
80
40
0
slope = 1.735 ± 0.029
intercept = 0.91 ± 1.37
dispersion = 0.55 +0.35 / −0.21
0
20
40
60
$(^{238}U/^{232}Th)$
C
U-Th date (ka)
20
19
18
17
8
13
18
$(^{230}Th/^{232}Th)$
D
a1
a2
a3
a4
a5
a6
a7
a8
17
18
19
20
U-Th Date (ka)

Figure 4.7: **A.** Two-dimensional projections of three-dimensional U-Th isotope plots and ^{87}Sr/^{86}Sr compositions of M09-B071R fractions. M09-B071R.a1 (see panel D) exhibits the four lowest ^{87}Sr/^{86}Sr compositions and arrays a U-Th isochron (fractions identified with black center dots and thick ellipse borders). Remaining fractions show no apparent trend in U-Th isotopes or ^{87}Sr/^{86}Sr. Reported and plotted uncertainties (ellipses and gray regression envelopes) reflect 95 % confidence intervals that include tracer and decay constant uncertainties. Regression was calculated by a maximum likelihood estimation method that attributes over-dispersion to geologic variability in (^{234}U/^{238}U) (Vermeesch, 2018). Uncertainty on δ^{234}U dispersion is smaller than the reported significant figures on $\delta^{234}U_o$. **B.** Regressions of ^{232}Th-normalized ^{230}Th-^{234}U-^{238}U data of the remaining M09-B071R layers (a2–a8) identify detrital (^{234}U/^{232}Th) and (^{230}Th/^{232}Th) contributions within uncertainty of zero (dashed lines). Regressions incorporate analytical uncertainties only (smaller than symbols) and were calculated with a maximum likelihood estimation method that attributes over-dispersion to geologic variation in (^{234}U/^{232}Th) or (^{230}Th/^{232}Th), summarized in the reported "dispersion" terms (Vermeesch, 2018). Gray envelopes and reported uncertainties are 95 % confidence intervals. **C.** Uncorrected U-Th dates of fractions from layers a2–a8 exhibit no dependency on (^{230}Th/^{232}Th), indicating a negligible detrital ^{230}Th contribution. Dates plotted with 2σ (standard error) analytical uncertainties. **D.** U-Th dates relative to stratigraphic position. Layer a1 date from isochron (A). Layers a2–a8 are uncorrected single-fraction dates ($\pm 2\sigma$ standard error analytical uncertainty). Black lines demarcate layer divisions. Pale blue bars reflect histogram distribution of mean values (bin width=0.75 ka; panel height=5 counts).

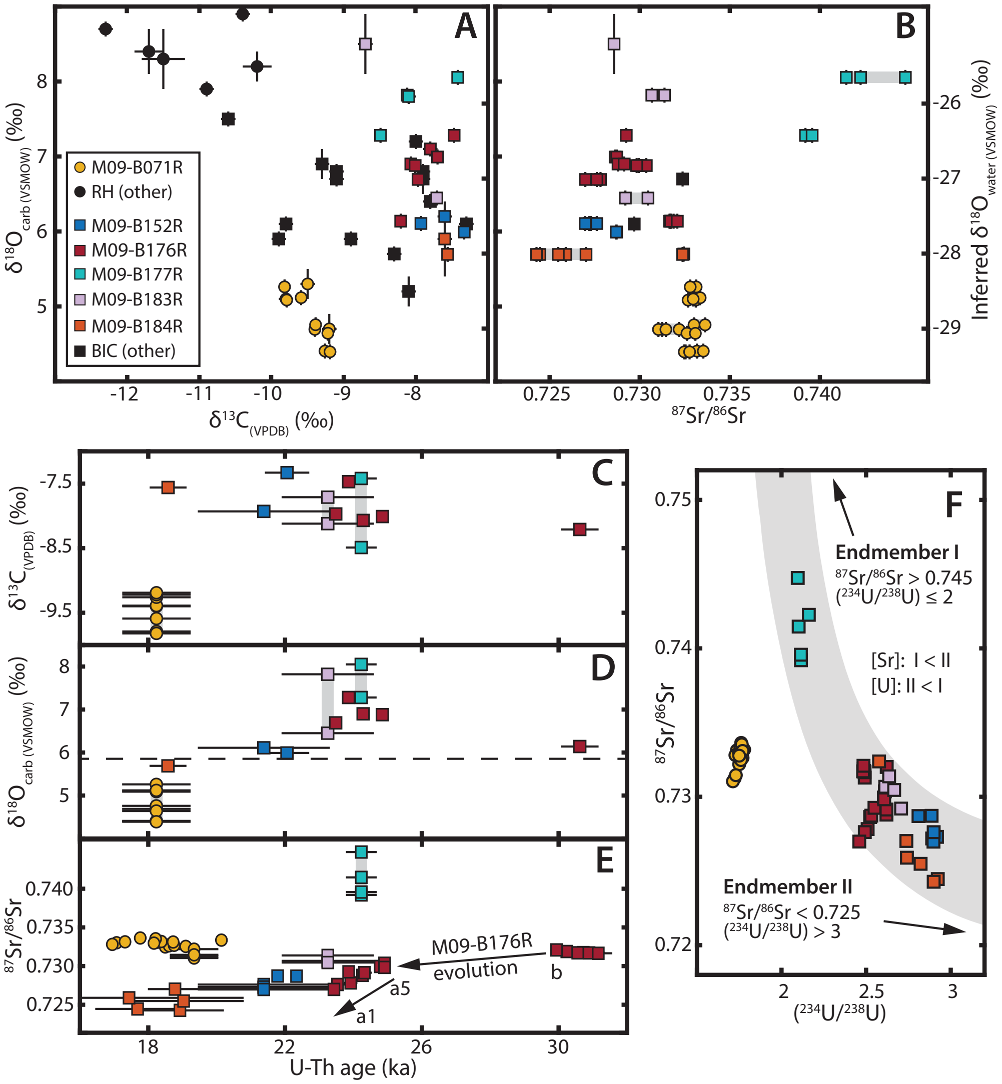
A
B
C
D
E
F
M09-B071R
RH (other)
M09-B152R
M09-B176R
M09-B177R
M09-B183R
M09-B184R
BIC (other)
$\delta^{18}O_{carb\ (VSMOW)}$ (‰)
$\delta^{13}C_{(VPDB)}$ (‰)
-12
-11
-10
-9
-8
5
6
7
8
$^{87}Sr/^{86}Sr$
0.725
0.730
0.735
0.740
Inferred $\delta^{18}O_{water\ (VSMOW)}$ (‰)
-26
-27
-28
-29
-7.5
-8.5
-9.5
0.740
0.735
0.730
0.725
M09-B176R evolution
a5
a1
b
18
22
26
30
U-Th age (ka)
0.75
0.74
0.73
0.72
2
2.5
3
$(^{234}U/^{238}U)$
Endmember I
$^{87}Sr/^{86}Sr > 0.745$
$(^{234}U/^{238}U) \leq 2$
[Sr]: I < II
[U]: II < I
Endmember II
$^{87}Sr/^{86}Sr < 0.725$
$(^{234}U/^{238}U) > 3$

Figure 4.8: **A,B.** Carbonate δ^{18}O, δ^{13}C, ^{87}Sr/^{86}Sr, and (^{234}U/^{238}U) of Baffin Island subglacial precipitates from Rimrock Hills (RH, circles) and Barnes Ice Cap (BIC, squares) margin (data from this study and Refsnider et al., 2014). Left and right y-axis units respectively represent measured carbonate δ^{18}O compositions ($\delta^{18}\mathrm{O}_{\mathrm{carb\ (VSMOW)}}$) and calculated calcite-forming water δ^{18}O compositions ($\delta^{18}\mathrm{O}_{\mathrm{water\ (VSMOW)}}$), assuming a water-carbonate fractionation of 33.6 ‰ at 0°C (after Refsnider et al., 2012). RH samples other than M09-B071R plot beyond the bounds of B due to high ^{87}Sr/^{86}Sr (>0.77). ^{87}Sr/^{86}Sr uncertainties are 2σ standard error (smaller than symbols). δ^{13}C and δ^{18}O uncertainties are 2σ standard error of individual fractions (this study) or 1σ standard deviation of replicate means (Refsnider et al., 2014). **C–E.** Carbonate δ^{13}C, δ^{18}O, and ^{87}Sr/^{86}Sr vs. U-Th ages of carbonate formation from Table 4.2. Ages incorporate only analytical uncertainties (95 % confidence intervals) to allow more precise internal comparison. Dashed line in D represents the threshold of post-LGM δ^{18}O compositions. Arrows in E indicate the stratigraphic progression of ^{87}Sr/^{86}Sr evolution in M09-B176R (labels correspond to Fig. 4.6). In panels B–E gray bars indicate affiliation among samples that use a redundant age or isotopic ratio due to consolidation with a model age or lower resolution sampling for δ^{18}O-δ^{13}C measurements. **F.** Paired ^{87}Sr/^{86}Sr-(^{234}U/^{238}U) compositions ($\pm 2\sigma$ standard error) from BIC and RH precipitates. The topology of BIC precipitates are plausibly explained by a ≥ 2 endmember hyperbolic mixing model (gray envelope shows a reasonable range). Arrows indicate relative endmembers, accompanied by constraints on isotopic compositions and relative elemental concentrations based on the implied mixing relationship.

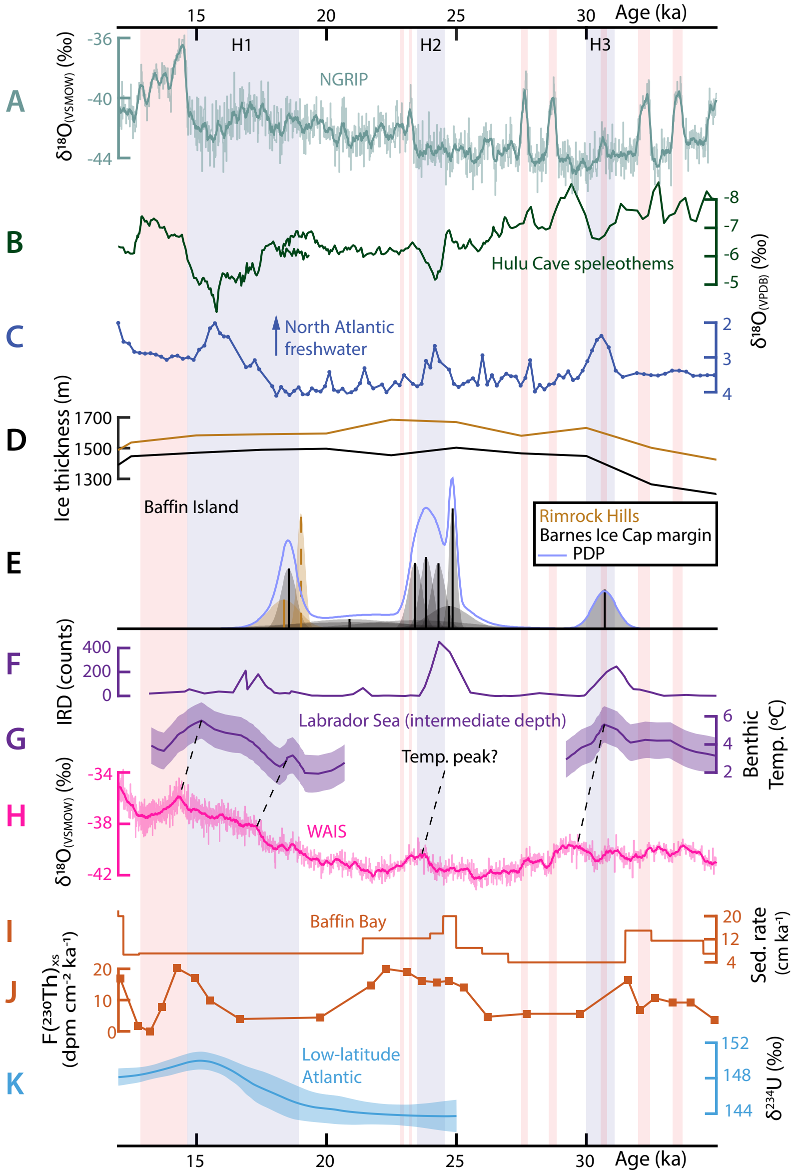

15
20
25
30
Age (ka)
H1
H2
H3
A
$\delta^{18}O_{(VSMOW)}$ (‰)
-36
-40
-44
NGRIP
B
Hulu Cave speleothems
-8
-7
-6
-5
$\delta^{18}O_{(VPDB)}$ (‰)
C
North Atlantic freshwater
2
3
4
D
Ice thickness (m)
1700
1500
1300
Baffin Island
E
Rimrock Hills
Barnes Ice Cap margin
PDP
F
IRD (counts)
400
200
0
G
Labrador Sea (intermediate depth)
Temp. peak?
6
4
2
Benthic Temp. (ºC)
H
$\delta^{18}O_{(VSMOW)}$ (‰)
-34
-38
-42
WAIS
I
Baffin Bay
20
12
4
Sed. rate (cm ka⁻¹)
J
F(²³⁰Th)xs (dpm cm⁻² ka⁻¹)
20
10
0
K
Low-latitude Atlantic
152
148
144
$\delta^{234}U$ (‰)
15
20
25
30
Age (ka)

Figure 4.9: Chronologic comparison of Baffin Island subglacial calcite-forming events with various climate, ocean, and ice sheet records (datum: 1950 CE). Multiple proxies from the same record are plotted in the same color (F/G and I/J). Red bars indicate "Greenland Interstadial" events of Rasmussen et al. (2014). Blue bars indicate Heinrich events: H1 spans the comprehensive timeframe of Stanford et al. (2011); and H2 and H3 are constrained from HE-associated excursions in the Hulu Cave speleothem record (B). **A.** NGRIP δ^{18}O record of Greenland temperature variation (GICC05 timescale, adjusted to 1950 CE datum; Rasmussen et al., 2014). **B.** Hulu cave δ^{13}C from stalagmites PD and MSD records Asian monsoon precipitation changes that vary synchronously with Greenland temperature changes (Wang et al., 2001). **C.** Sinistral *Neogloboquadrina pachyderma* δ^{18}O record at Orphan Knoll (core MD95-2024P), a proxy for freshwater flux into the North Atlantic. Recalibrated from the original record (Hillaire-Marcel and Bilodeau, 2000) by Lynch-Stieglitz et al. (2014). **D.** Simulated ice thickness over the Rimrock Hills (bronze) and Barnes Ice Cap margin (black; Gowan et al., 2021). **E.** Baffin Island calcite-forming events from individual samples and subsamples dated in this study and Refsnider et al. (2012, indicated with dashed lines), traced with a probability density plot (PDP; Vermeesch, 2012). Bells indicate uncertainty distributions about mean dates (vertical lines). **F,G.** Carbonate ice-rafted detritus (IRD, panel F) and water temperatures calculated from benthic foraminifera Mg/Ca at an intermediate-depth site in the Labrador Sea (Marcott et al., 2011). **H.** West Antarctic Ice Sheet (WAIS) divide ice core δ^{18}O (WD2014 chronology; WAIS Divide Project Members, 2015). Local maxima in WAIS δ^{18}O lag Labrador Sea subsurface warming by 300–900 years (dashed lines). A $\sim$24 ka WAIS δ^{18}O peak implies a Labrador Sea subsurface warming event shortly after 25 ka within a gap in the benthic temperature record in G. **I,J.** Sedimentation rate (I; Simon et al., 2012) and flux of unsupported ^{230}Th (F(^{230}Th)$_{xs}$) to seafloor sediments (J; Nuttin and Hillaire-Marcel, 2015) in Baffin Bay. **K.** Seawater δ^{234}U ($\pm 2\sigma$ uncertainty) in the upper (<1.5 km-depth) low-latitude North Atlantic Ocean, reconstructed from deep-sea corals (Chen et al., 2016).

Table 4.1: Detrital Th-corrected U-Th dates and initial δ^{234}U ($\delta^{234}U_o$) for sample M09-B184R, calculated by subtracting the detrital (^{230}Th/^{232}Th) composition regressed in Figure 4.4. Uncertainties are absolute 2σ standard error and include systematic (i.e. tracer, decay-constant) uncertainties.

	U-Th date (ka)[a]	**$\delta^{234}U_o$**
M09-B184R-2	17.69 ± 1.29	2022.4 ± 8.9
M09-B184R-3	17.44 ± 3.37	1829.5 ± 27.8
M09-B184R-4	18.92 ± 1.34	2004.0 ± 20.9
M09-B184R-5	18.78 ± 0.87	1832.8 ± 4.9
M09-B184R-6	19.03 ± 1.80	1923.0 ± 9.9

---

[a] Dates calculated relative to 1950 CE.

Table 4.2: Representative model ages and initial δ^{234}U ($\delta^{234}U_o$) compositions of central Baffin Island subglacial calcite-forming events, calculated from isochron regressions, individual fractions, or weighted means (with a random effects model) of individual fractions. Means are calculated from uncorrected U-Th dates and $\delta^{234}U_o$ of fractions unless otherwise stated. In cases where the MSWD>5, we report the calculated dispersion (with uncertainties) of the random effects model in lieu of the discreet MSWD value. All uncertainties reflect 95 % confidence intervals.

Formation Event	**Method**	**n**	**Model age (ka)**[a]	**MSWD or dispersion** $(^{+}_{-})$	$\delta^{234}U_o$ **(‰)**	**MSWD or dispersion** $(^{+}_{-})$
M09-B071R	mean[b]	16	18.38 ± 0.40	$0.80^{+0.41}_{-0.24}$	797.5 ± 7.1	$14.3^{+7.1}_{-4.0}$
M09-B184R	mean[c]	5	18.56 ± 0.58	0.78	1923 ± 71	81^{+96}_{-33}
M09-B152R	isochron	4	20.91 ± 3.68	—	2162 ± 93	$5.7^{+0.1}_{-1.7}$
M09-B183R	isochron	3	23.44 ± 4.14	2.4	1897.4 ± 38.6	—
M09-B177R	isochron	4	24.72 ± 1.54	2.9	1212.3 ± 6.6	—
M09-B176R.a1	—	1	23.43 ± 0.53	—	1559.6 ± 4.0	—
M09-B176R.a3	—	1	23.86 ± 0.49	—	1657.6 ± 2.8	—
M09-B176R.a4	—	1	24.32 ± 0.53	—	1736.0 ± 4.4	—
M09-B176R.a5	mean	3	24.87 ± 0.29	0.085	1724.8 ± 3.3	$2.5^{+6.0}_{-2.1}$
M09-B176R.b	isochron	6	30.71 ± 0.89	—	1627.6 ± 8.0	$2.9^{+0.7}_{-1.8}$

---

[a] Dates calculated relative to 1950 CE datum.

[b] Mean calculated from n=15 individual fraction dates and n=1 isochron date (B071R.a1, Fig. 4.7)

[c] Mean calculated from dates in Table 4.1

Table 4.3: Carbonate C and O isotope compositions of Baffin Island subglacial precipitates. Subsample labels follow the labelling schemes of Figures 4.2,4.6,4.7 for U-Th-Sr. Uncertainties of δ^{13}C and δ^{18}O measurements are <0.05 and <0.10 ‰, respectively.

Sample.Subsample	**Weight % $CaCO_3$**	δ^{13}**C$_{(VPDB)}$ (‰)**	δ^{18}**O$_{(VSMOW)}$ (‰)**	δ^{18}**O$_{(VPDB)}$ (‰)**
M09-B071R.a1	69.1	-9.40	4.69	-25.43
M09-B071R.a2	66.3	-9.79	5.09	-25.05
M09-B071R.a3	56.5	-9.82	5.26	-24.88
M09-B071R.a4	73.0	-9.59	5.12	-25.02
M09-B071R.a5	65.2	-9.39	4.76	-25.37
M09-B071R.a6	62.6	-9.26	4.41	-25.71
M09-B071R.a7	67.3	-9.22	4.64	-25.48
M09-B071R.a8	65.1	-9.19	4.39	-25.72
M09-B15R2.1	75.2	-7.33	5.99	-24.17
M09-B152R.2	85.1	-7.93	6.11	-24.06
M09-B176R.a1	71.7	-7.97	6.69	-23.49
M09-B176R.a2	52.9	-7.70	6.99	-23.20
M09-B176R.a3	72.4	-7.47	7.28	-22.92
M09-B176R.a4	64.3	-8.07	6.90	-23.29
M09-B176R.a5	57.9	-8.01	6.88	-23.31
M09-B176R.b	59.8	-8.21	6.14	-24.03
M09-B177R.a	53.4	-8.49	7.28	-22.92
M09-B177R.b	33.1	-7.42	8.05	-22.17
M09-B183R.a	47.8	-8.12	7.82	-22.40
M09-B183R.b	46.3	-7.71	6.45	-23.73
M09-B184R	80.0	-7.56	5.69	-24.46

Appendix A

Data Repository Content for "Detecting the extent of ca. 1.1 Ga Midcontinent Rift plume heating using U-Pb thermochronology of the lower crust"

Reprinted from:

Edwards & Blackburn, 2018. "Detecting the extent of ca. 1.1 Ga Midcontinent Rift plume heating using U-Pb thermochronology of the lower crust," *Geology* 46, 911–914. DOI: 10.1130/G45150.1

Appendix DR1. Sample Preparation, U-Pb Measurement, and Data Reduction

Xenolith samples from the Victor North kimberlite (Fig. 1) were supplied by De Beers Group with assistance of Karen Smit. Twenty-two of the larger samples that appeared to represent a range of lithologies were selected for study. Lithologies and accessory mineral presence/absence were identified by petrographic microscopy of thin-sections made by Wagner Petrographic Inc. (Fig. DR1.1; Table DR1.1). For those samples containing rutile and/or apatite, accessory mineral fractions were extracted from xenoliths by standard crushing, followed by magnetic and heavy liquid (LMT) separations. Single crystal fractions of rutile and single and multi-grain fractions of apatite were selected for analysis based on grain size, morphology, and color. Minimum grain diameters (Table DR1.1) were measured from digital photomicrographs using Leica Application Suite (Version 4.5.0) software.

Rutile fractions were heated at 90 ºC for 30 minutes in concentrated nitric acid, and apatite fractions were sonicated at room temperature for 30 minutes in 5% acetic acid. Following these treatments, fractions were rinsed 3x with 18 MΩ·cm deionized ultrapure water, loaded into Savillex fluoropolymer (PFA) microcapsules, and spiked with an in-house mixed ^{205}Pb-^{233}U-^{235}U tracer. Samples were dissolved within PARR digestion vessels. Rutile was dissolved in concentrated HF for 48 hours at 210 ºC and converted to chlorides in 6N HCl for 12 hours at 180 ºC. Apatite was dissolved in 6N HCl for 12 hours at 180 ºC. All samples were then converted to 1.1 N HBr for column introduction, and U and Pb were separated from other elements using an HBr/HCl anion exchange recipe after Schmitz and Bowring (2003) with a 50 µL micro-column.

Reported U and Pb isotopic data are whole crystal analyses measured with Isotope Dilution-Thermal Ionization Mass Spectrometry (ID-TIMS) conducted on the UCSC IsotopX X62 Thermal Ionization Mass Spectrometer. U and Pb separates were loaded onto zone-refined (99.999%) Re ribbon with a Si gel-0.035 M H_3PO_4 activator. Pb was measured with a peak jumping method on a single collector Daly-photomultiplier ion counting system, and U was measured using either peak jumping methods on the Daly-photomultiplier system or static collection on Faraday cup detectors connected to 10^{12} Ω resistance amplifier cards.

Model U-Pb dates were calculated using U-Pb Redux (McLean et al., 2011). General constants used in model U-Pb date calculations are tabulated in Table DR1.2. Total procedural blanks ranged between 0.5-0.9pg, as did the common Pb amounts of many rutile analyses (Table DR1.1). Those samples with common Pb amounts exceeding these laboratory blank levels were assigned an initial Pb composition for 2.7 Ga (Stacey and Kramers, 1975). The exception to this was sample 14-VK-02, from which rutile fractions exhibited modest discordance inconsistent with the much more radiogenic fractions from sample 14-VK-22, which were insensitive to the assumed initial Pb composition. Samples 14-VK-02 and 14-VK-22 produced similar apparent ^{206}Pb/^{238}U dates that indicate a similar or even greater depth of residence for sample 14-VK-02 (Appendix DR3). If we assume 14-VK-02 rutile remained open to Pb-diffusion during its high temperature history and use a Stacey and Kramers (1975) initial Pb composition for any time between 160-1100 Ma, the U-Pb model dates are consistent with both the data from 14-VK-22 and the results of the coupled thermal and U-Pb diffusion model.

The interpretation of apparent ages determined from mixed crystal domains (e.g. a large crystal with a crack that serves as a fast diffusion pathway) is not straightforward. Based on model U/Pb dates, age-grain size correlations were used to identify fractions exhibiting multi-domain Pb diffusion behavior following the methods of Blackburn and others (2012). Those grains failing to plot consistently with a positive correlation between ^{206}Pb/^{238}U date and measured grain size likely represent multi- or partial crystal domains and were subsequently rejected from the dataset. Additionally, measurements with ratios of radiogenic Pb (Pb*) to common Pb (Pb_c) that were less than unity were rejected due to the necessarily large Pb_c corrections and corresponding uncertainties. Such uncertainty ranges, typically in excess of 100 My, provide inadequate resolution for assessing thermochronologic histories. Exceptions to these criteria were applied to samples 14-VK-02 and 14-VK-11, given the narrow ^{206}Pb/^{238}U age ranges represented by both samples and the negligible effect that the inclusion of those fractions with non-positive age-grain size correlations and/or $Pb^*/Pb_c<1$ had on interpretation of thermochronologic histories. All other measurements presented in this study represent fractions exhibiting apparently single-domain grain behavior based on age-grain size correlations and Pb^*/Pb_c values exceeding unity.

Sample 14-VK-03 represents a special case in which only one fraction (r8; Table DR1.1) from this sample exhibits a value of $Pb^*/Pb_c>1$. Since only this measurement is included, the sample cannot be rigorously tested for an age-grain size correlation. However, it is bracketed with respect to its ^{206}Pb/^{238}U date by samples of similar, garnet-bearing petrology (14-VK-17, 14-VK-08, 14-VK-06) that have ΔU-Pb values within uncertainty of 14-VK-03 (Figure 3). The bracketing among these samples with respect to ^{206}Pb/^{238}U and general agreement among ΔU-Pb values validate the inclusion of 14-VK-03 (fraction r8).

In addition to rutile, sample 14-VK-02 yielded an aliquant of apatite that we measured by ID-TIMS. After correction for fractionation, tracer, and laboratory blank contributions, 14-VK-02 apatite Pb compositions (Table DR1.3) are significantly less radiogenic than contemporary terrestrial Pb compositions and approximately consistent with modeled Neoarchean compositions (Stacey and Kramers, 1975). We interpret these primitive Pb compositions as maximum estimates of the nonradiogenic, common Pb composition of 14-VK-02, supporting an Archean origin for 14-VK-02.

References

Blackburn, T.J., Bowring, S.A., Perron, J.T., Mahan, K.H., Dudas, F.O., and Barnhart, K.R., 2012, An exhumation history of continents over billion-year time scales: Science, v. 335, p. 73–76, doi: 10.1126/science.1213496.

Hiess, J., Condon, D.J., McLean, N., and Noble, S.R., 2012, ^{238}U/^{235}U systematics in terrestrial uranium-bearing minerals: Science, v. 335, p. 1610-1614, doi: 10.1126/science.1215507.

Jaffey, A.H., Flynn, K.F., Glendenin, L.E., Bentley, W.C., and Essling, A.M., 1971, Precision measurement of half-lives and specific activities of ^{235}U and ^{238}U: Physical Review C, v. 4, p. 1889–1906, doi: 10.1103/PhysRevC.4.1889.

McLean, N.M., Bowring, J.F., and Bowring, S.A., 2011, An algorithm for U-Pb isotope dilution data reduction and uncertainty propagation: Geochemistry, Geophysics, Geosystems, v. 12, no. 6, p. 1–26, doi: 10.1029/2010GC003478.

Schmitz, M.D., and Bowring, S.A., 2003, Constraints on the thermal evolution of continental lithosphere from U-Pb accessory mineral thermochronometry of lower crustal xenoliths, southern Africa: Contributions to Mineralogy and Petrology, v. 144, p. 592–618, doi: 10.1007/s00410-002-0419-9.

Stacey, J.S., and Kramers, J.D., 1975, Approximation of terrestrial lead isotope evolution by a two-stage model: Earth and Planetary Science Letters, v. 26, p. 207–221, doi: 10.1016/0012-821X(75)90088-6.

Appendix DR2. Numerical Modeling and Statistical Methods

Thermal and U-Pb Diffusion Models

This study employs the methods of Blackburn and others (2012) in the application of a lithosphere-scale transient thermal model, the results of which (time-temperature paths for crustal rocks) are used as an input for a U-Pb diffusion model. The same discussions of model structure, inputs, and constants therein apply here, excepting differences to account for the geologic setting (i.e. crust and lithosphere thickness) and the exploration of a reheating event. All thermal model simulations were run using a 180 km initial lithosphere thickness, the Moho initially at 45 km depth, and an initial geothermal gradient characterized by a 70 mW/m^2 surface heat flux. As shown in Blackburn and others (2012), model U-Pb results are insensitive to the assumed initial geothermal gradient due to early, fast cooling. Reheating events were simulated by interrupting the otherwise continuous cooling history at specified times with 1) an instantaneous geotherm adjustment (Figs. 4, DR2.1A, DR2.1B), 2) simulation of basal lithospheric thinning (i.e. shallowing of the lithospheric thermal boundary layer; Figs. 5, DR2.1C, DR2.1D), and/or 3) simulation of a mantle plume (i.e. heating at the base of the lithosphere; Figs. 5, DR2.1E, DR2.1F). In cases of instantaneous geothermal gradient adjustment, the new geotherm was set, held for a duration of 10 My and permitted to relax. This was explored for a range of geothermal gradients characterized by surface heat fluxes of 50, 60, 70, and 80 mW/m^2 (Fig. 4; 70mW/m^2 shown in Fig. DR2.1). Thinning of the basal lithosphere and replacement by mantle of some temperature is simulated within the numerical model by fixing a temperature for some specified depth down to the original lithosphere depth (Fig. DR2.1C). In the example shown in Figure DR2.1C, the temperatures from 180 km to 125 km depth are replaced with ambient mantle temperature (1400 ºC), representing a “thinning only” end-member whereby no increase in model asthenospheric mantle temperature occurs. A mantle plume heating end-member is simulated by an increase of the lithosphere basal temperature. In the example shown in Figure DR2.1E, the base of the lithosphere is fixed to 1800 ºC, resulting in reshaping of the geotherm from the bottom-up with time. For both end-member heating scenarios explored in this appendix, a 200 My duration of heating is used to provide ample time for heat to propagate through the lithosphere to crustal levels. The goodness of fit between measured thermochronologic data and model simulations that explore these two end members of reheating (basal lithosphere thinning and plume heating) as well as hybrid space are presented in Figure 5 and discussed below.

Pearson Chi-Squared Test Methods to Compare Measured and Modeled U-Pb Data

We utilize a Pearson chi-squared (χ^2) test to assess goodness of fit between measured data and model outputs exploring various reheating scenarios. For each model reheating scenario, a χ^2 value is calculated for the pairing of a given measured data point with every modeled data point. The χ^2 calculation incorporates uncertainties of measured ^{206}Pb/^{238}U and ^{207}Pb/^{235}U (1σ standard error values and covariance). To accommodate the range of observed grain sizes and probable partial and/or multi-domain behavior, these calculations are repeated for model results representing a range of grain sizes (25, 50, 100, and 150 μm radius). The minimum of these χ^2 values is selected as the sole χ^2 value for that measured data point, representing its variance from the model prediction that best represents the measured value. This is repeated for each measured data point, applying modeled data for apatite and rutile appropriately to the respective measured data. The minimum χ^2 values for each measured data point are then summed for that model reheating scenario. We identify the summation as *S*. This process is repeated for each model reheating scenario, and the "best-fit" scenario is identified as the one with the minimum *S* value (S_o). To compare the goodness of fit among the various scenarios, the differences between each *S* and S_o are plotted over a two-dimensional space defined by the model parameters of the reheating scenario (e.g. Fig. 5). Contours are interpolated among these $S\text{-}S_o$ values using either a cubic spline with not-a-knot end conditions or a linear interpolation. Those *S* values falling within 1σ of S_o are identified such that $S \leq S_o + 1$. The goodness of fit for any given *S* may be independently evaluated by dividing *S* by the degrees of freedom, yielding a reduced χ^2 value, analogous to a "mean square of weighted deviates" (MSWD; Wendt and Carl, 1991; McLean et al., 2011).

Given the modeled data's demonstrated sensitivity to diffusion kinetics on timescales between 1.1 and 2.5 Ga (Appendix DR3), the χ^2 test is only applied to measured data with $^{206}Pb/^{238}U$ dates <1.1 Ga, where modeled data is insensitive to these parameters. Indeed, this constraint results in the exclusion of all the measured apatite data, which exclusively exhibit $^{206}Pb/^{238}U$ dates greater than 1.1 Ga. However, the high uncertainties of the measured apatite data cause them to minimally affect results from Pearson tests of the entire modeled 2.7 Ga date range (Fig. DR2.2). Though not used in the Pearson tests, the apatite data do inform of a continuous slow cooling history between >2.5 and 1.1 Ga.

Constraining an Accurate 1σ Ellipse Within Chi-Squared Tests

To produce Figure 5, we ran simulations with the coupled lithosphere thermal-Pb diffusion model for a mesh of conditions constructed from the complete set of combinations of 9 basal lithosphere temperature conditions (1400–1800 ºC) and 7 lithosphere thinning depths (120–180 km), run at 4 grain sizes (25, 50, 100, 150 µm), a total of 252 simulations. To model the S–S_o value for intervening space among simulated mesh points (identified in Figs. 5, DR2.3 with black dots), we apply a cubic spline interpolation with not-a-knot end conditions. The interpolation is applied to 100 x 100 node matrices over the spaces within each group of 4 adjacent mesh points (i.e. each group of mesh points that form a 1 x 1 square). We are confident that this node resolution is adequate based on the observation that results for 100 x 100 node matrices and 1000 x 1000 node matrices are visually indistinguishable. As shown in Figure DR2.3, the interpolation yields three 1σ ellipse-bounded areas within the model parameter space, a result inconsistent with the expectation of a single 1σ ellipse enveloping some best-fit S_o coordinate. Furthermore, the only truly accurate S value (mesh point) falling within the ellipse is the S_o value, also calling into question the accuracy of the interpolated ellipse boundaries. To assess whether this result was accurate or an artifact of model mesh spacing and interpolation, we ran additional model simulations at a higher resolution over a reduced parameter area that contains interpolated ellipse space within our geologically permissible range (Fig. DR2.3, inset). We ran an additional 360 simulations within this area: the complete set of combinations of 10 basal lithosphere temperatures (1610 – 1700 ºC) and 9 thinned lithosphere depths (125 km to 133 km) run at 4 grain sizes. We calculate contour values from the Pearson χ^2 test results (mesh points) using a more conservative linear interpolation that is less prone to underestimating S-S_o values near unity than a cubic interpolation technique. The results (DR2.3 inset) reveal a continuous ellipse area within this space, containing a contiguous array of model output conditions (black dots) and a lower S_o, further confirming the accuracy of the ellipse (Figs. 5, DR2.3). The coarser grid likely hindered the ability of the interpolation to accurately model subtle variations in S-S_o at magnitudes of 10^{-1}. Given the continuity of the ellipse within the high-resolution space and its abutment with the boundaries of the space, we conclude that it likely continues beyond into the impermissible regions, supporting the statistical validity of a continuous 1σ ellipse surrounding some S_o.

Reference

Blackburn, T.J., Bowring, S.A., Perron, J.T., Mahan, K.H., Dudas, F.O., and Barnhart, K.R., 2012, An exhumation history of continents over billion-year time scales: Science, v. 335, p. 73–76, doi: 10.1126/science.1213496.

McLean, N.M., Bowring, J.F., and Bowring, S.A., 2011, An algorithm for U-Pb isotope dilution data reduction and uncertainty propagation: Geochemistry, Geophysics, Geosystems, v. 12, p. 1–26, doi: 10.1029/2010GC003478.

Wendt, I., and Carl, C., 1991, The statistical distribution of the mean squared weighted deviation: Chemical Geology: Isotope Geoscience section, v. 86, p. 275–285, doi: 10.1016/0168-9622(91)90010-T.

Appendix DR3. Reconstructing Lower Crustal Thermal Histories Despite Uncertainties in Model Parameters, Sample Depth, and Timescales of ~1.1 Ga Heating

Some of the parameters utilized in the thermal and Pb diffusion models employed include uncertainties and perhaps inaccuracies. Here we show how the interpretation of measured data may be judged reliable through the identification of aspects of the modeled data that are insensitive to changes in model parameters. These aspects include 1) the ΔU-Pb topology and values for the deepest, most isotopically reset samples (<1.1 Ga U-Pb dates); 2) the position and ΔU-Pb values of the concave-up inflection (hereafter referred to simply as "inflection") in ΔU-Pb space; and 3) the topology, but not absolute values, of ΔU-Pb data predicted for shallow samples recording slow cooling between 2.5 and 1.1 Ga. The sections below explore how our conclusions remain unaffected by uncertainties in Pb-mineral diffusion kinetics, thermal diffusivity, surface erosion rate, and absolute sample depth. Finally, we utilize Pearson χ^2 tests of modeled data to constrain the timescales of both onset and duration for Mesoproterozoic Attawapiskat heating.

Uncertainties in Model Parameters: Diffusion Kinetics, Thermal Diffusivity, and Erosion Rate

Diffusion Kinetics

The diffusion of Pb in apatite and rutile is strongly temperature dependent and characterized by an Arrhenius relationship that requires input of a diffusion coefficient, D_0 (m^2/s) and activation energy, E_a (J/mol). These are experimentally determined values (e.g. Cherniak et al., 2000). Successful characterization of lower crustal thermal histories would seem to require well-constrained Pb diffusion kinetics for accessory phases. Problematically, the geochronologic dataset presented here, as well as several others (summarized in Blackburn et al., 2011), require that apatite begins to retain Pb at higher temperatures than rutile (e.g. 14-VK-11), a relationship in conflict with predictions of closure temperatures from Pb-diffusion kinetics (Fig. 3; Cherniak, et al., 1991; Cherniak, 2000, 2010). Figure DR3.1 systematically explores how aspects of the model results ($^{206}Pb/^{238}U$ age, ΔU-Pb values) respond to variations in diffusion kinetics over a wide range of values well beyond the uncertainties of those published for rutile and apatite (Ea = 250 kJ/mol and D_0 = 3.9e-10 m^2/s for rutile, 223 kJ/mol and 1.27e-8 m^2/s for apatite; Cherniak, et al., 1991; Cherniak, 2000, 2010). The goal of this exercise is to clarify what aspects of the data can be reliably interpreted even if the accuracy of diffusion kinetics is in question.

Kinetics primarily control the temperature, and therefore the depth, of Pb retention. In DR3.1A, we demonstrate the effect of changing E_a and D_0 on the absolute $^{206}Pb/^{238}U$ age determined for a 30km deep sample. For a sample at a fixed depth, a higher E_a or lower D_0 increases the temperature of Pb retention, resulting in an older date (DR3.1A). Yet, this increase in the temperature of Pb-retention correspondingly increases the depth of the Pb Partial Retention Zone (PRZ). A sample positioned within this deeper PRZ experiences a slower cooling rate (due to higher insulation) and thus a longer duration of PRZ residence. As a result of this longer PRZ residence, increases in E_a and decreases in D_0 correspond with an increase in maximum ΔU-Pb values, as observed in the "right-side" hump of data in ΔU-Pb space (Fig. DR 3.1B).

While the maximum ΔU-Pb value and corresponding absolute $^{206}Pb/^{238}U$ age is sensitive to diffusion kinetics, the timing and ΔU-Pb magnitude of the inflection are not (Fig. DR3.1C). This insensitivity stems from how the lithosphere is heated from its base during a thinning and/or plume-heating event. In both end-member scenarios, the intensity of heating scales with depth, so that if minerals had retained Pb at higher temperatures (high E_a and/or low D_0) and therefore greater depths, they lie closer to the heat source and experience a proportionally larger heating intensity than in a system where shallower samples retained Pb at lower temperatures due to low E_a and/or high D_0. In result, the effects of reheating on Pb retention are largely preserved for samples that experience near-complete resetting of the Pb isotopic system. Consequently, the subtle dependence of inflection ΔU-Pb values on diffusion kinetics (<10My) is too small for the measured data to resolve. Furthermore, we find that samples with U-Pb dates < 1.1 Ga (i.e. the "left-side" hump) have ΔU-Pb values within <10 My of each other, independent of the diffusion kinetics used (Fig. DR3.1C).

These observations collectively allow us to conclude that any potential uncertainties in diffusion kinetics will negligibly influence the overall topology of modeled data, the ΔU-Pb values of the inflection, and all the ΔU-Pb values with U-Pb dates <1.1 Ga. Therefore, uncertainties in diffusion kinetics do not affect any conclusions that relate to: 1) the timing of lithosphere reheating; 2) the timing of continuous cooling of the lithosphere; and 3) the intensity of heating and the model-inferred temperature for the mantle beneath the Attawapiskat region at 1.1 Ga. Thus, only the abovementioned three aspects of the data (overall topology, inflection of ΔU-Pb values, and ΔU-Pb values with U-Pb dates <1.1 Ga) are used to evaluate the best fit data in Figure 5 and the other Pearson χ^2 tests applied in this study.

Thermal Diffusivity & Surface Erosion Rate

In addition to kinetics of accessory phase Pb-diffusion, we explore two other parameters that may control the topology of model curves and the goodness of fit between modeled and measured data: assumed lithosphere thermal diffusivity and long-term surface erosion rate. With regards to thermal diffusivity, a 25% change in thermal diffusivity has very little effect on the overall topology of a modeled curve, instead scaling the degree of discordance and subtly shifting the inflection point, but not to an extent that would alter the interpretation of the data (Fig. DR3.2).

The absence of a known long-term (billion-year) erosion rate for the Superior Province and Attawapiskat region presents challenges in assigning an appropriate exhumation rate to the thermal model simulations. Given the contemporary presence of Phanerozoic sediments overlying the Attawapiskat region (Fig. 1) and a regional record of oscillating burial and exhumation through the Phanerozoic (e.g. Lorencak et al., 2004), we assign a 0 m/Ma exhumation rate post-1.1 Ga. Under this condition, the results of Pearson chi-squared (χ^2) tests of modeled and measured data with $^{206}Pb/^{238}U$ dates <1.1 Ga are insensitive to variations in erosion rates (1-5 m/Ma) for the period between 2.7 Ga (model start) and 1.1 Ga: S_o values occur under the same paired lithosphere depth and temperature conditions, and S_o MSWDs vary negligibly (<2%; Fig. DR3.3). Therefore, we assign a rate of 1 m/Ma, a value consistent with the low long-term erosion rates observed by Blackburn and others (2012) but also accommodating modest erosion averaged across the history of the Superior Province.

Uncertainties in Sample Depth

The precise xenolith residence depth is not necessary information for the conclusions drawn by the present study. We do not claim to know the residence depths of xenolith samples and the decision to not make geobarometric determinations was largely driven by the fact that such measurements are difficult for non-garnet bearing samples. We instead assume that shallow samples cool first and deeper samples later. Further, we point to similar arguments made for uncertainties in the diffusion kinetics, namely that the timing of inflections, the magnitude and topology of ΔU-Pb values <1.1 Ga, and the timing of periods of cooling are insensitive to the depth at which Pb retention occurs. We do note that, given the reasonable assumption that shallow samples cool first and deep samples last, the sample petrology-age relationships in the measured data are generally consistent with a crustal stratigraphy whereby garnet bearing samples underlie non-garnet bearing samples (Jagoutz and Schmidt, 2012; Jull and Kelemen, 2001; Schulte-Pelkum et al., 2017).

Constraining Timescales of Mesoproterozoic Attawapiskat Heating

Two aspects of model lithosphere basal heating, duration and timing of onset, are particularly important to consider because they both affect the position of ΔU-Pb inflection. Although the timescales of MCR volcanism are well characterized (e.g. Davis and Green, 1997), the timescales of heating are not.

To ascertain the most appropriate duration of reheating in our simulations, we apply a Pearson χ^2 test (Appendix DR2) to thermal model simulations of various heating durations (Fig. DR3.4) with an onset date of 1135 Ma (see below) and compare these results to independent geological constraints. Thinning of the basal lithosphere may have occurred to no deeper than 125 km as evidenced by depleted compositions and Archaean Re-Os dates in mantle xenoliths from Jurassic Attawapiskat kimberlites (Smit et al., 2014). Albers and Christensen (1996) limit the temperature of an ascending plume to ~300 K in excess of ambient mantle, a value consistent with the observations of Herzberg et al. (2007). Based on this estimate, we limit the permissible basal lithosphere temperature to a maximum possible impinged plume temperature of 1700 ºC.

Over shorter durations (ex. 25 My – 75 My), the temperatures and thinning depths required to adequately reproduce the data (blue contours) fall outside of the geologically permissible area (Fig. DR3.4). Therefore, the measured data require a long-lived heating feature, persisting on timescales exceeding 50-75 My, with a 100 My duration yielding a broad area of "good fit" modeled scenarios within the geologically permissible region (Fig. DR3.4). This evidence for a long-lived heating event is consistent with the long "holding times" required to conduct heat through the lithosphere to the lower crust (Appendix DR2). Nonetheless, plume durations exceeding 100 My are rejected for two reasons. 1) As durations exceed 100 My, the goodness of fit degrades (S_o MSWD increases; Fig. DR3.4). This is controlled by the high precision measured data with $^{206}Pb/^{238}U$ ages ≤500 Ma (Fig. 3), whereby prolonged heating times do not allow the modeled data to recover to these lower ΔU-Pb values soon enough. 2) Mantle plumes persisting for durations approaching 200 My require unreasonably high mantle viscosities, while plumes existing for <100 My may be modeled under more typical calculated mantle viscosities (King, 1995; Davaille and Vatteville, 2005). Thus, we conclude that a 100 My heating duration most accurately represents the duration of ~1.1 Ga plume heating experienced beneath the Attawapiskat region and use this value in our simulations.

To ascertain the most appropriate duration of reheating, we apply a Pearson χ^2 test to thermal models with 100 My lithosphere heating/thinning beginning at a range of dates (800-1200 Ma; Fig DR3.5). For onset times >1.2 Ga and <1 Ga Ma, S_o MSWD values exceed 10 and are rejected on the grounds of poor statistical fit. For onset times between 1 Ga and 1.2 Ga S_o MSWD values of ~7 are achieved (Figs. DR3.5, DR2.3), supporting a model of heating onset beneath the Attawapiskat region between 1 and 1.2 Ga. An apparently unperturbed mantle xenolith reconstructed geotherm from a Mesoproterozoic Kyle Lake kimberlite pipe (Smit et al., 2014) suggests that the timing of reheating was either approximately concurrent with or after this event. Although the slightly elevated Kyle Lake geotherm may reflect some reheating, any significant heating event in advance of the eruption would have already destroyed the diamond stability field. A Rb-Sr phlogopite age of ~1135 Ma provides a maximum plausible age for eruptions of the Kyle Lake cluster (Heaman et al., 2004). Given the onset of Keweenawan volcanism at 1108 Ma (Davis and Green, 1997), and the association between Keweenawan volcanism with concurrent carbonaceous volcanism (Ernst and Bell, 2010), we use this date of 1135 Ma in our models for the onset of basal lithosphere "plume" heating. Such a model is consistent with the findings of Kent et al. (1992) that mantle plumes likely experience a period of incubation beneath continental crust before the onset of significant magmatism (e.g. large igneous province eruptions).

References

Albers, M., and Christensen, U.R., 1996, The excess temperature of plumes rising from the core-mantle boundary: Geophysical Research Letters, v. 23, p. 3567–3570, doi: 10.1029/96GL03311.

Blackburn, T., Bowring, S.A., Schoene, B., Mahan, K., and Dudas, F., 2011, U-Pb thermochronology: Creating a temporal record of lithosphere thermal evolution: Contributions to Mineralogy and Petrology, v. 162, no. 3, p. 479–500, doi: 10.1007/s00410-011-0607-6.

Blackburn, T.J., Bowring, S.A., Perron, J.T., Mahan, K.H., Dudas, F.O., and Barnhart, K.R., 2012, An exhumation history of continents over billion-year time scales: Science, v. 335, p. 73–76, doi: 10.1126/science.1213496.

Cherniak, D.J., 2000, Pb diffusion in rutile: Contributions to Mineralogy and Petrology, v. 139, p. 198–207, doi: 10.1007/PL00007671.

Cherniak, D.J., 2010, Diffusion in accessory minerals: Zircon, titanite, apatite, monazite and xenotime: Reviews in Mineralogy and Geochemistry, v. 72, p. 827–869, doi: 10.2138/rmg.2010.72.18.

Cherniak, D.., Lanford, W.., and Ryerson, F.., 1991, Lead diffusion in apatite and zircon using ion implantation and Rutherford Backscattering techniques: Geochimica et Cosmochimica Acta, v. 55, no. 6, p. 1663–1673, doi: 10.1016/0016-7037(91)90137-T.

Davaille, A., and Vatteville, J., 2005, On the transient nature of mantle plumes: Geophysical Research Letters, v. 32, no. 14, p. 1–4, doi: 10.1029/2005GL023029.

Davis, D.W., and Green, J.C., 1997, Geochronology of the North American Midcontinent rift in western Lake Superior and implications for its geodynamic evolution: Canadian Journal of Earth Sciences, v. 34, p. 476-488.

Ernst, R.E., and Bell, K., 2010, Large igneous provinces (LIPs) and carbonatites: Mineralogy and Petrology, v. 98, no. 1, p. 55–76, doi: 10.1007/s00710-009-0074-1.

Heaman, L.M., Kjarsgaard, B.A., and Creaser, R.A., 2004, The temporal evolution of North American kimberlites: Lithos, v. 76, p. 377–397, doi: 10.1016/j.lithos.2004.03.047.

Herzberg, C., Asimow, P.D., Arndt, N., Niu, Y., Lesher, C.M., Fitton, J.G., Cheadle, M.J., and Saunders, A.D., 2007, Temperatures in ambient mantle and plumes: Constraints from basalts, picrites, and komatiites: Geochemistry, Geophysics, Geosystems, v. 8, no. 2, p. 1–34, doi: 10.1029/2006GC001390.

Jagoutz, O., and Schmidt, M.W., 2012, The formation and bulk composition of modern juvenile continental crust: The Kohistan arc: Chemical Geology, v. 298–299, p. 79–96, doi: 10.1016/j.chemgeo.2011.10.022.

Jull, M., and Kelemen, P.B., 2001, On the conditions for lower crustal convective instability: Journal of Geophysical Research: Solid Earth, v. 106, p. 6423–6446, doi: 10.1029/2000JB900357.

Kent, R.W., Storey, M., and Saunders, A.D., 1992, Large igneous provinces: Sites of plume impact or plume incubation? Geology, v. 20, p. 891–894, doi: 10.1130/0091-7613(1992)020<0891:LIPSOP>2.3.CO;2.

King, S.D., 1995, Models of Mantle Viscosity, in Mineral Physics & Crystallography: A Handbook of Physical Constants, American Geophysical Union, p. 227–236.

Lorencak, M., Kohn, B.P., Osadetz, K.G., and Gleadow, A.J.W., 2004, Combined apatite fission track and (U–Th)/He thermochronometry in a slowly cooled terrane: results from a 3440-m-deep drill hole in the southern Canadian Shield: Earth and Planetary Science Letters, v. 227, p. 87–104, doi: 10.1016/J.EPSL.2004.08.015.

Schulte-Pelkum, V., Mahan, K.H., Shen, W., and Stachnik, J.C., 2017, The distribution and composition of high-velocity lower crust across the continental U.S.: Comparison of seismic and xenolith data and implications for lithospheric dynamics and history: Tectonics, v. 36, p. 1455–1496, doi: 10.1002/2017TC004480.

Smit, K. V, Pearson, D.G., Stachel, T., and Seller, M., 2014, Peridotites from Attawapiskat, Canada: Mesoproterozoic reworking of Palaeoarchaean lithospheric mantle beneath the Northern Superior Superterrane: Journal of Petrology, v. 55, p. 1829–1863, doi: 10.1093/petrology/egu043.

Appendix DR4: Modeling a Crustal Intrusive Heat Source

The duration and heating required to reset or partially reset U-Pb thermochronometers is substantial (Fig. 4), and any plausible heat source must be long-lived and therefore large. Here we test whether the measured U-Pb thermal history in this study may record an intrusive heat source at crustal depths rather than a heat source at the base of the lithosphere. We adapt the transient thermal model to simulate intrusive events with a range of thicknesses (5-25 km) and temperatures (800-1200 ºC). The intrusion is modeled by adjusting the temperature between the base of the crust (45 km depth) and the prescribed intrusion thickness below the crust (50-70 km depth). To prevent erratic behavior of the thermal model in response to the perturbation and more accurately model an igneous intrusion's thermal structure, a curve is interpolated to set the temperature at the intrusion boundaries to the averages of the wall rock (base of crust/roof of mantle) and intrusion center temperatures. The temperature perturbation is allowed to relax immediately, simulating a single, transient intrusive event.

Figure DR4.1 presents the results of Pearson χ^2 tests comparing modeled U-Pb data from the intrusive heat source simulations to measured U-Pb data, following the methods outlined in Appendix DR2. Within the parameter space, the best fit (S_o) condition occurs for the thickest and hottest intrusion model, with an MSWD nearly an order of magnitude greater than those obtained for plume heating scenarios (Figs. DR4.1, DR2.3), suggesting that even hotter and/or thicker intrusions are required to comparably replicate the measured data.

Table DR1.1. Lithology, mineralogy, and U-Pb thermochronologic data of xenoliths collected from Victor kimberlite (52.82º N, 83.88º W; Fig. 1).

		Dates (Ma)										Composition				Isotopic Ratios						
	Min. Grain Diameter (µm)	206Pb/ 238U a	±2σ abs	207Pb/ 235U a	±2σ abs	207Pb/ 206Pb a	±2σ abs	ΔU-Pb (Ma)	±2σ abs	Corr. coef.	% disc b	Th/ U c	Pb* (pg) d	Pbc (pg) e	Pb*/ Pbc f	206Pb/ 204Pb g	206Pb/ 238U h	±2σ %	207Pb/ 235U h	±2σ %	207Pb/ 206Pb h	±2σ %
Sample number, Mineral dated, Lithology: Mineralogy																						
14-VK-02: rutile, Granulite: plag, grt, cpx, opx, rt																						
r8	231	159.549	3.031	167.281	13.824	278.118	199.930	7.7	14.2	0.226	43	0.1	1.4	1.6	0.9	76.6662	0.0251	1.9232	0.1791	8.9632	0.0519	8.7320
r9	267	169.337	0.980	175.013	9.262	252.404	130.472	5.7	9.3	0.202	33	0.1	2.5	1.9	1.4	107.7695	0.0266	0.5866	0.1881	5.7611	0.0513	5.6720
r13	175	177.462	2.948	184.210	30.271	271.653	404.537	6.7	30.4	0.236	35	0.1	0.9	2.1	0.4	45.6889	0.0279	1.6840	0.1989	17.9685	0.0517	17.6479
14-VK-03: rutile,Granulite: grt, cpx, plag, opx, rt																						
r8	135	1044.059	10.061	1116.625	25.715	1260.734	66.185	72.6	27.6	0.509	17	0.3	3.3	2.0	1.7	108.8578	0.1758	1.0438	2.0033	3.7967	0.0827	3.3866
14-VK-06: rutile, Gabbro: cpx, opx, plag, grt, rt																						
r6	131	1182.030	2.945	1296.806	5.454	1492.172	11.917	114.8	6.2	0.573	21	0.0	11.4	1.6	7.3	452.9397	0.2012	0.2726	2.5864	0.7448	0.0933	0.6288
r13	209	1154.018	27.677	1254.336	18.907	1430.867	2.927	100.3	33.5	0.998	19	0.0	69.5	2.0	35.4	2139.4650	0.1960	2.6193	2.4395	2.6253	0.0903	0.1499
r18	114	1185.613	12.469	1274.297	8.491	1427.185	4.632	88.7	15.1	0.978	17	0.0	17.6	0.5	38.6	2572.6191	0.2019	1.1513	2.5078	1.1697	0.0901	0.2404
14-VK-07: apatite, Amphibolite: amp, cpx, opx, plag, bio, ap																						
170705-1	147	1845.677	16.403	1931.634	33.084	2025.151	62.248	86.0	36.9	0.429	9	3.3	19.4	9.7	2.0	74.0655	0.3315	1.0220	5.7018	3.8297	0.1248	3.5142
170705-2	multi-grain	1392.436	7.593	1488.010	41.520	1627.000	94.338	95.6	42.2	0.450	14	2.8	230.8	135.7	1.7	68.8760	0.2411	0.6063	3.3296	5.3172	0.1002	5.0734
a3	109	1272.458	13.199	1287.779	45.071	1313.424	113.415	15.3	47.0	0.373	3	1.0	10.0	8.5	1.2	67.6627	0.2182	1.1430	2.5547	6.1763	0.0849	5.8470
14-VK-08: rutile, Granulite: plag, cpx, grt, opx, rt, bio																						
r8	185	1025.630	7.650	1050.189	31.558	1101.624	91.377	24.6	32.5	0.389	7	0.2	4.9	3.2	1.5	101.1005	0.1725	0.8068	1.8131	4.8222	0.0763	4.5687
r13	151	722.134	17.614	742.739	40.702	805.362	133.769	20.6	44.3	0.640	10	0.0	1.2	0.9	1.3	104.8920	0.1185	2.5783	1.0782	7.7264	0.0660	6.3897
14-VK-11: rutile, Amphibole gabbro, plag, cpx, opx, amp, rt																						
r5	88	1323.427	3.422	1418.773	6.475	1564.943	14.021	95.3	7.3	0.495	15	0.0	17.0	2.9	5.9	356.3490	0.2279	0.2860	3.0442	0.8472	0.0969	0.7473
r6	103	1277.124	2.191	1365.530	2.671	1506.699	4.944	88.4	3.5	0.697	15	0.0	29.9	1.8	16.6	1013.3498	0.2191	0.1891	2.8376	0.3557	0.0940	0.2597
r7	164	1303.144	2.102	1354.630	1.843	1436.855	2.742	51.5	2.8	0.817	9	0.0	59.3	1.3	44.1	2733.3325	0.2240	0.1781	2.7966	0.2464	0.0906	0.1401
r8	198	1278.626	6.620	1356.825	4.358	1482.277	1.757	78.2	7.9	0.987	14	0.0	193.2	3.1	62.8	3708.7581	0.2194	0.5708	2.8048	0.5822	0.0928	0.0869
14-VK-11: apatite																						
a1	61	2000.756	37.135	2137.021	28.046	2270.740	39.480	136.3	46.5	0.685	12	2.7	3.1	1.4	2.3	96.0153	0.3639	2.1590	7.2042	3.1455	0.1436	2.2903
a3	82	2499.043	11.375	2516.299	12.572	2530.248	19.984	17.3	17.0	0.479	1	1.7	11.2	3.4	3.3	142.2554	0.4735	0.5491	10.9195	1.3516	0.1673	1.1903
14-VK-13: apatite, Amphibolite, plag, amph, cpx, bio, opx																						
170705-1	140	2032.870	6.395	2124.305	19.259	2214.001	35.083	91.4	20.3	0.456	8	1.7	52.0	20.8	2.5	109.9182	0.3707	0.3668	7.1021	2.1638	0.1390	2.0227
170705-2	multi-grain	1978.979	4.134	2056.361	13.281	2134.853	24.701	77.4	13.9	0.459	7	1.7	137.3	36.4	3.8	159.9928	0.3593	0.2426	6.5777	1.5068	0.1328	1.4116
a1	68	1605.098	21.890	1663.453	24.858	1737.920	44.087	58.4	33.1	0.622	8	1.6	3.6	1.5	2.4	116.0583	0.2827	1.5406	4.1462	3.0386	0.1064	2.4045
a5	383	2169.229	3.057	2222.595	10.566	2272.148	18.908	53.4	11.0	0.507	5	2.2	1294.9	261.2	5.0	189.3111	0.4000	0.1660	7.9256	1.1719	0.1438	1.0967
14-VK-17: rutile, Granulite: plag, cpx, opx, grt, bio, rt																						
r1	84	1523.304	36.575	1590.602	28.655	1680.980	38.914	67.3	46.5	0.809	9	0.1	2.6	1.2	2.1	144.4539	0.2666	2.6959	3.7899	3.5667	0.1032	2.1071
r2	137	1599.796	10.737	1671.941	12.453	1763.735	22.811	72.1	16.4	0.575	9	0.1	12.2	3.7	3.3	200.6780	0.2817	0.7578	4.1894	1.5192	0.1079	1.2478
14-VK-22: rutile, Granulite: grt, plag, cpx, rt																						
r4	288	545.124	0.463	563.299	0.930	637.399	3.796	18.2	1.0	0.603	14	0.0	62.3	0.9	66.8	4409.8695	0.0882	0.0886	0.7415	0.2150	0.0610	0.1734
r5	235	498.672	0.617	517.878	1.047	603.530	4.223	19.2	1.2	0.679	17	0.0	48.8	0.8	63.6	4318.5436	0.0804	0.1285	0.6653	0.2580	0.0600	0.1925
r6	228	298.346	1.191	302.980	1.580	338.827	9.343	4.6	2.0	0.732	12	0.0	26.0	0.8	31.3	2116.7886	0.0474	0.4085	0.3477	0.6033	0.0533	0.4112
r9	167	226.971	0.705	237.228	3.600	340.066	37.283	10.3	3.7	0.265	33	0.0	3.8	0.5	7.6	538.5812	0.0358	0.3159	0.2632	1.7019	0.0533	1.6462
r10	203	217.627	0.724	219.249	1.288	236.696	10.846	1.6	1.5	0.724	8	0.0	17.0	0.5	33.1	2308.4463	0.0343	0.3385	0.2410	0.6530	0.0509	0.4690
r14	256	278.257	0.735	289.776	1.440	383.714	10.296	11.5	1.6	0.613	27	0.0	23.7	1.2	19.2	1248.3625	0.0441	0.2699	0.3303	0.5711	0.0543	0.4571
r15	243	304.846	2.759	314.916	3.185	390.124	14.604	10.1	4.2	0.834	22	0.0	16.0	1.1	14.1	926.3715	0.0484	0.9265	0.3636	1.1763	0.0545	0.6498
r16	360	380.265	0.933	390.954	1.163	454.685	5.129	10.7	1.5	0.767	16	0.0	58.5	1.5	38.3	2426.1216	0.0608	0.2527	0.4697	0.3584	0.0561	0.2288

a Isotopic dates calculated using λ238 = 1.55125E-10 (Jaffey et al. 1971) and λ235 = 9.8485E-10 (Jaffey et al. 1971).
b % discordance = 100 - (100 * (206Pb/238U date) / (207Pb/206Pb date))
c Th contents calculated from radiogenic 208Pb and 230Th-corrected 206Pb/238U date of the sample, assuming concordance between U-Pb Th-Pb systems.
d Total mass of radiogenic Pb.
e Total mass of common Pb.
f Ratio of radiogenic Pb (including 208Pb) to common Pb.
g Measured ratio corrected for fractionation and spike contribution only.
h Measured ratios corrected for fractionation, tracer, blank and, where applicable, initial common Pb.

Table DR1.2. Constants used in measured U/Pb date calculations with 1σ absolute uncertainties

Pb fractionation model (α)	0.23 ± 0.02 %/amu
Pb blank mass	0.7 ± 0.2 pg
Blank $^{206}Pb/^{204}Pb$	18.416 ± 0.349
Blank $^{207}Pb/^{204}Pb$	15.358 ± 0.226
Blank $^{208}Pb/^{204}Pb$	37.461 ± 0.735
Sample and blank $^{238}U/^{235}U$ composition	137.8185 ± 0.0223[1]
$(^{18}O/^{16}O)_{U\text{-}oxide}$	0.00205 ± 0.00002
U blank mass	0.1 ± 0.01 pg
Tracer mass uncertainty	± 0.0001 g

[1] Adapted from Hiess et al. (2012).

Table DR1.3. Pb compositions of single grain apatite fractions of 14-VK-02, measured by ID-TIMS and corrected for fractionation, tracer, and blank contributions. Uncertainties represent 2σ absolute standard error of measurement, without fractionation, tracer, or blank uncertainties incorporated.

Fraction	**Pb Mass (pg)**	**$^{206}Pb/^{204}Pb$**	**$^{207}Pb/^{204}Pb$**	**$^{208}Pb/^{204}Pb$**
a1	11.8	13.957 ± 0.043	14.787 ± 0.049	33.594 ± 0.109
a2	34.7	14.266 ± 0.047	14.722 ± 0.041	33.628 ± 0.114
a3	60.7	13.705 ± 0.045	14.506 ± 0.052	32.753 ± 0.114

Figure DR1.1

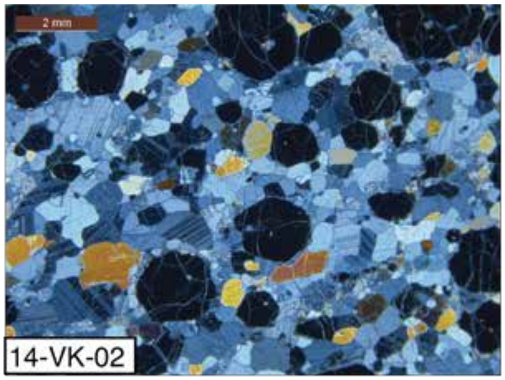

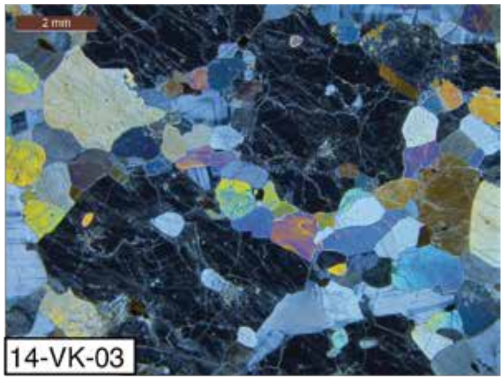

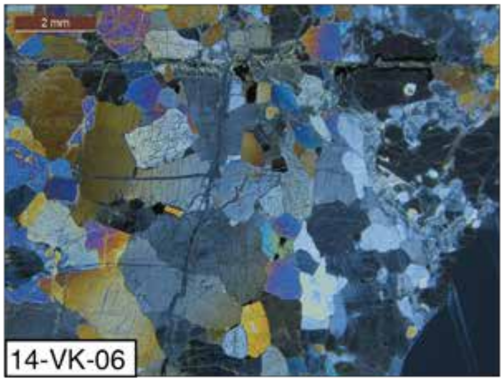

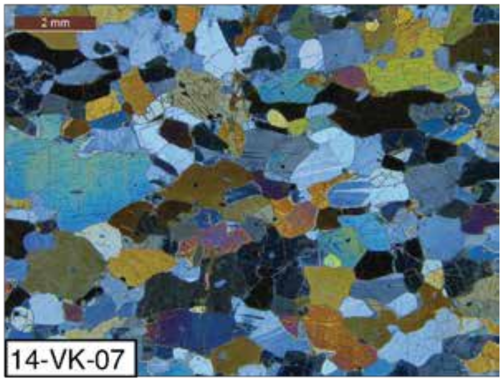

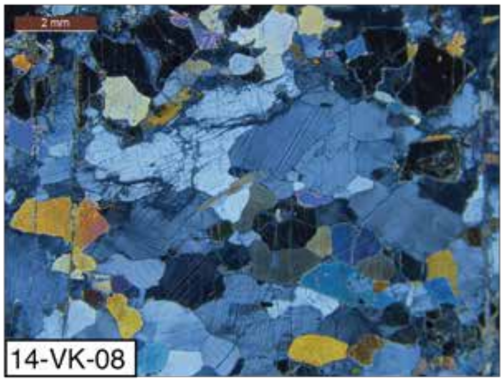

Figure DR1.1. Representative photomicrographs of the Victor kimberlite xenoliths measured in this study (n=9, continued on next page), taken under cross-polarized light. Brown bars in the upper left corners of each image indicate 2mm scale. Mineralogy and lithology are tabulated with U-Pb thermochronologic data in Table DR1.1.

Figure DR1.1, cont…

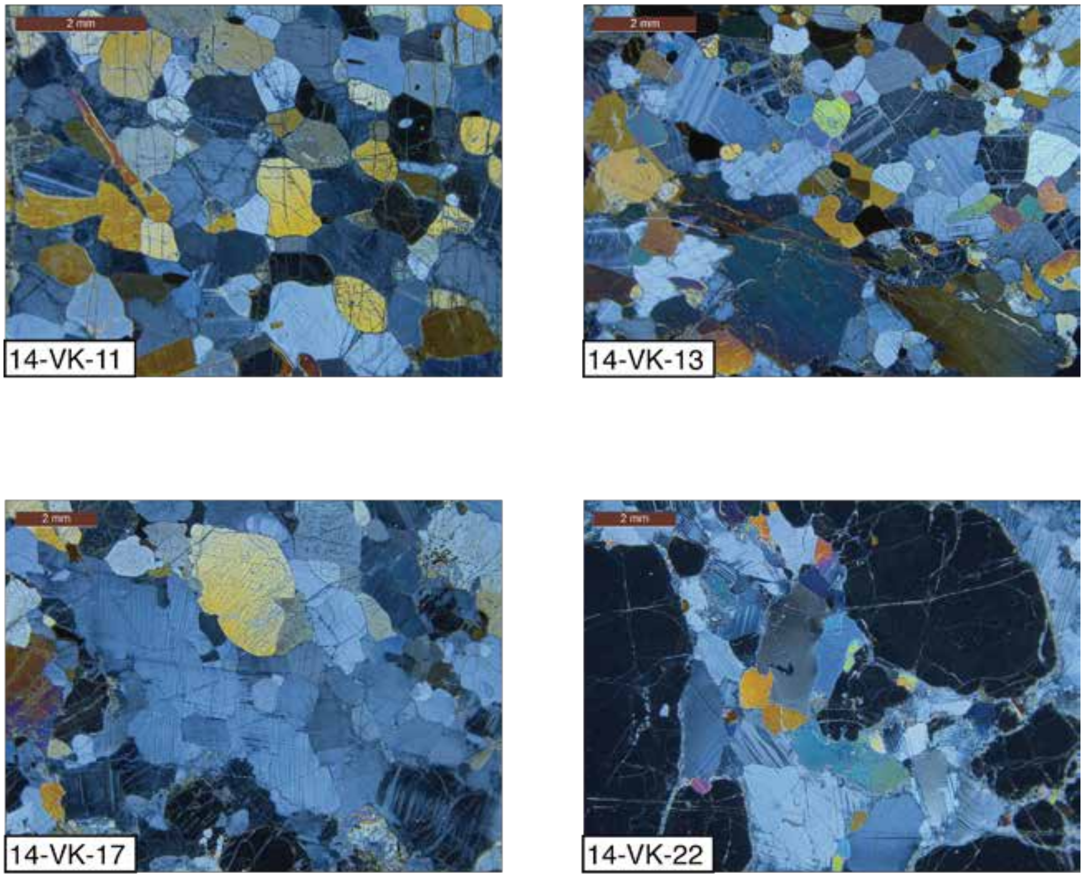

Figure DR2.1

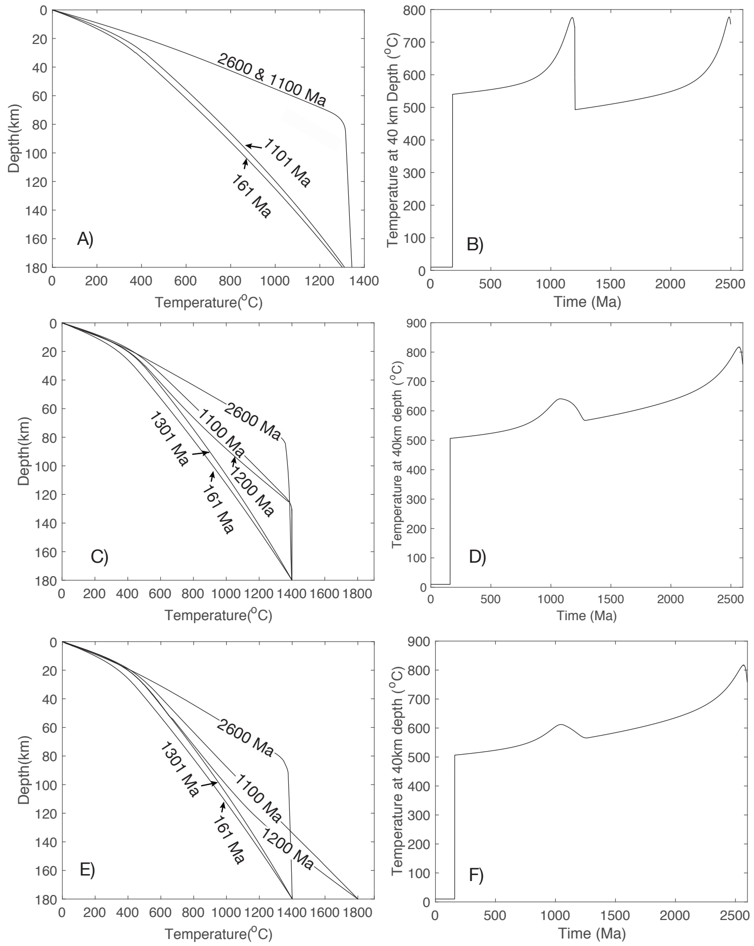

Figure DR2.1. A,C,E) Results of thermal models presented as depth vs. temperature plots at selected time intervals for each of 3 scenarios simulating lithosphere reheating: **A)** generalized reheating model simulated by arbitrarily raising the geothermal gradient (characterized by a surface heat flux of 70 mW/m^2) for 10 My at 1100 Ma; **C)** lithosphere thinning, simulated by the fixture of depths ranging from 125-180 km to ambient mantle temperatures (1400ºC) and held for 200 My; and **E)** basal lithosphere heating simulated by the fixture of 180 km depths to 1800ºC for 200 My. Panels **B, C,** and **F** present time-temperature (t-T) paths at 45 km depth, the model crust-mantle boundary, for corresponding geotherm evolutions shown in **A**, **C**, and **E**, respectively. All scenarios begin with gradual cooling from a geotherm characterized by 70 mW/m^2 surface heat flux at 2600 Ma (**A**, **C, E**). In panel **A**, the curve at 1101 Ma represents the geotherm prior to the geotherm adjustment illustrated by the curve at 1100 Ma. In panel **C** and **E**, the curve labeled 1301 Ma shows the geotherm prior to sublithospheric heating. The "1200 Ma" curves show pronounced mantle lithosphere heating and the "1100 Ma" curves show peak heating conditions propagating well into crustal depths. The "161 Ma" curves (**A**, **C, E**) represent the geotherms just prior to the time of kimberlite eruption, at which point the xenolith population experiences a drop to 10ºC as shown in the t-T paths in panels **B**, **D, F**.

Figure DR2.2

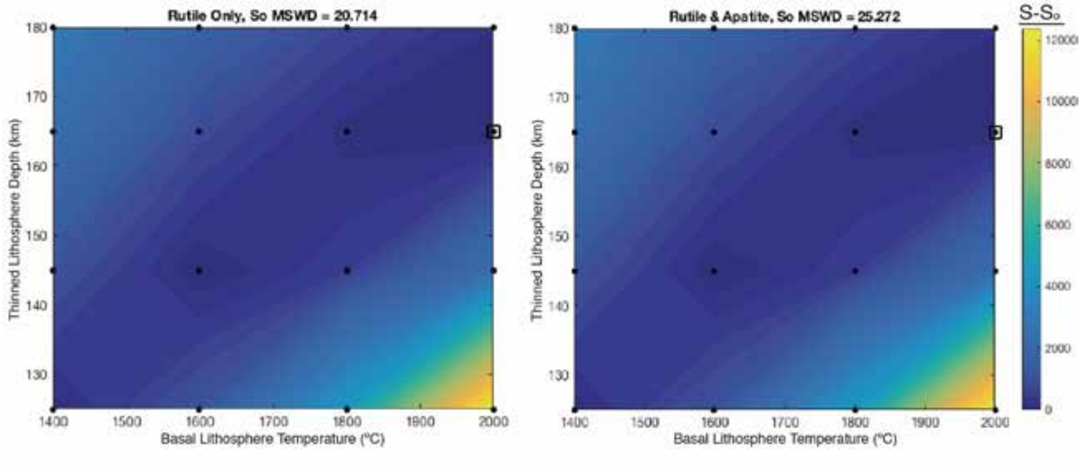

Figure DR2.2. Pearson χ^2 test results comparing the goodness of fit between model results for a single suite of reheating scenarios and measured data excluding (left) and including (right) apatite U-Pb measurements. To accommodate the inclusion of measured apatite data with U-Pb ages exceeding 1.1 Ga, the Pearson test is applied to all measured and modeled U-Pb ages. The visually identical results and comparable S_o values between the conditions illustrate the insensitivity of Pearson χ^2 test results to the large uncertainties of the measured apatite U-Pb data. Black dots represent paired model parameters of thinned lithosphere depth and basal lithosphere temperature. Contour values are calculated by a linear interpolation method and represent the difference between the sum of χ^2 values for a given modeled condition (S) and the minimum χ^2 summation (S_o, identified with a black square).

Figure DR2.3

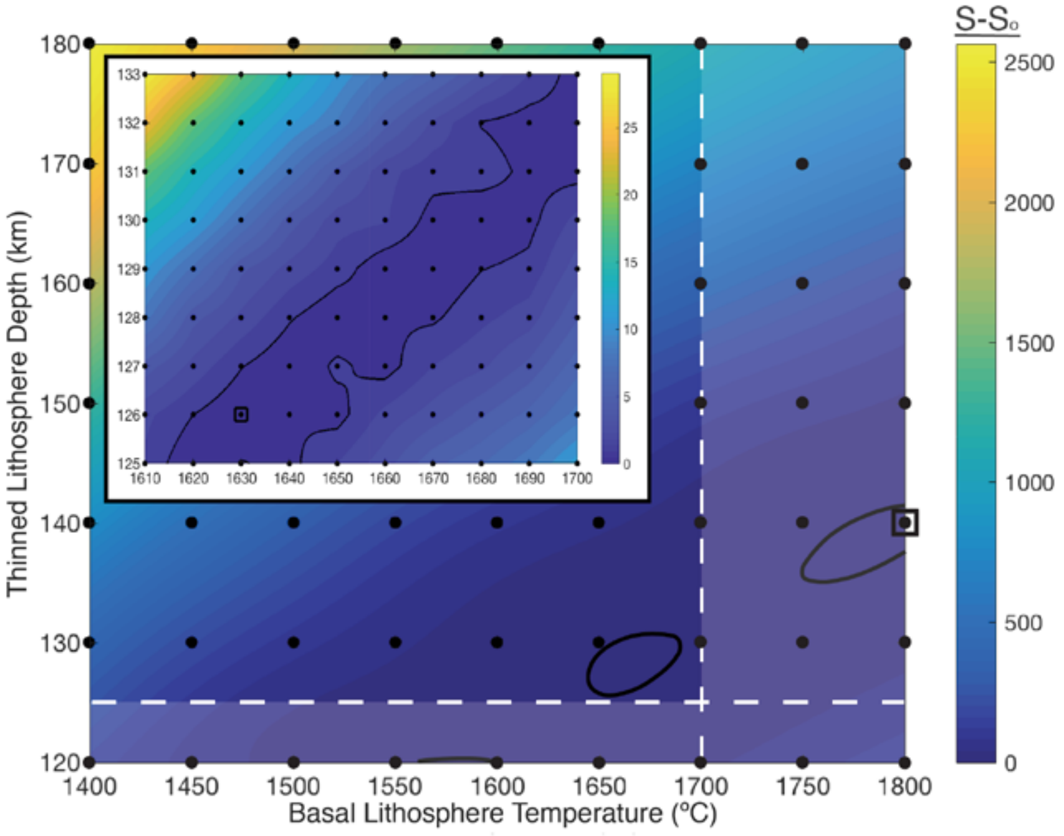

Figure DR2.3. Results of Pearson chi-squared (χ^2) tests comparing measured data with model results for a range of simulated conditions of basal lithosphere reheating and removal. The two plots shown here represent the same datasets used to construct Figure 5. Black dots represent paired model parameters of thinned lithosphere depth and basal lithosphere temperature. Simulations were run at steps of 10 km and 50 ºC in the "coarse" mesh of the main panel and at steps of 1 km and 10 ºC over a reduced area (125-133 km and 1610-1700 ºC) in the "high resolution" mesh of the inset. Contour values, calculated using a cubic spline interpolation with not-a-knot end conditions (main panel) or a linear interpolation (inset), represent the difference between the sum of χ^2 values for a given modeled condition (S) and the minimum χ^2 summation (S_o, identified with a black square). For the main panel S_o MSWD=6.927. The results shown in the inset identify a slightly improved S_o MSWD of 6.925. The black contours demarcate those conditions with interpolated S values within 1σ of S_o. The dashed white lines indicate the minimum depth of the lithosphere constrained by Jurassic xenoliths and a maximum plausible mantle plume temperature. Geologically impermissible conditions are faded.

Figure DR3.1

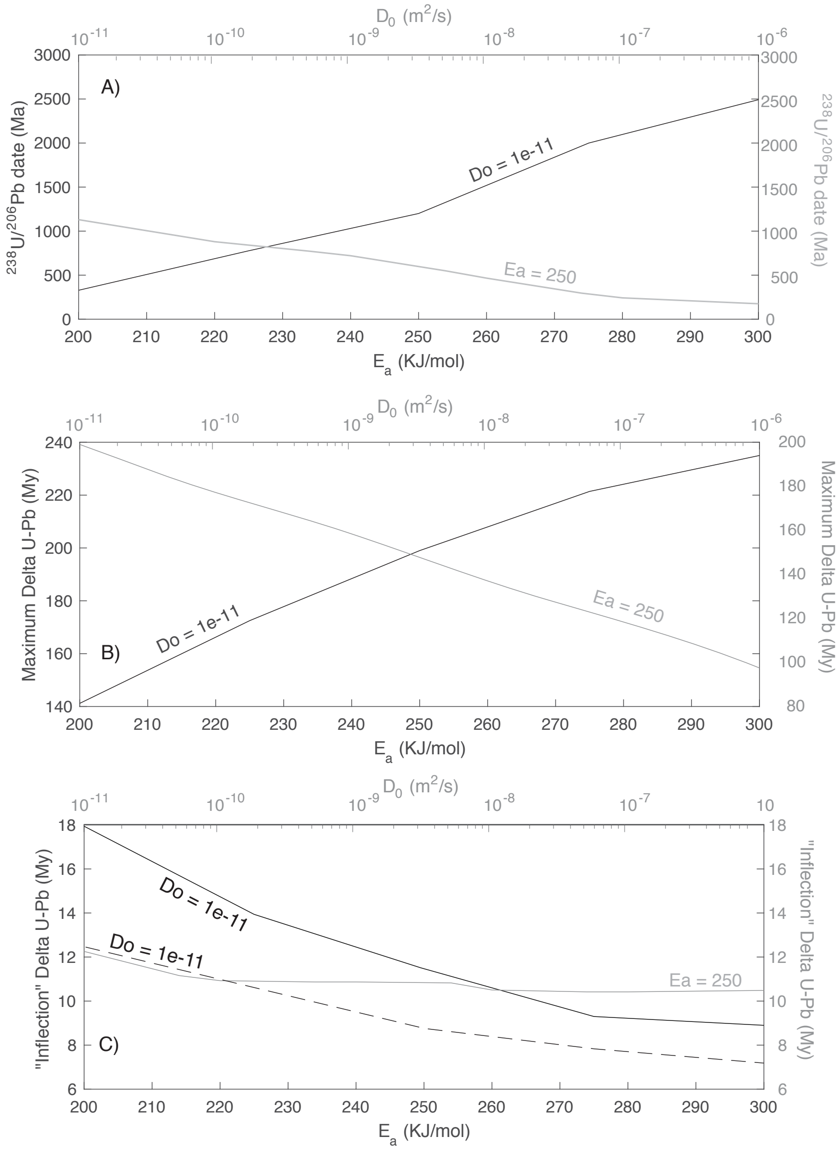

Figure DR3.1. Output of coupled thermal and Pb-diffusion model runs exploring the effects of diffusion kinetics (E_a—black, lower x-axis and D_0, grey, upper x-axis) on different aspects of the U-Pb data. **A)** Predicted $^{238}U/^{206}Pb$ date for a 30 km depth sample for a range of diffusion kinetics. **B)** Predicted maximum ΔU-Pb values for a range of diffusion kinetics. **C)** Predicted inflection ΔU-Pb values for a range of diffusion kinetics. In **C)** Dashed line marks a longer heating holding time. The observed suppression of inflection ΔU-Pb values with longer heating supports our interpretation that minor differences in inflection ΔU-Pb values are the result of differences in post-heating cooling rate: higher E_a results in PRZ residence for deeper samples that experience slower cooling rates following the simulated 1.1 Ga heating.

Figure DR3.2

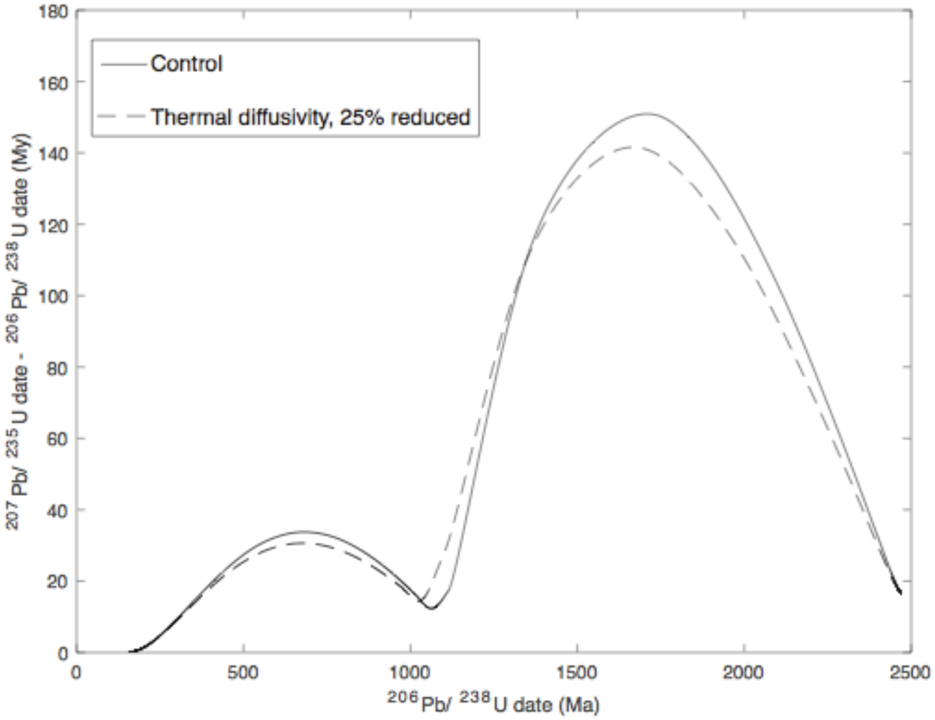

Figure DR3.2. Coupled thermal and Pb-diffusion model runs exploring the effects of lithosphere diffusivity on output U-Pb data topology. All curves trace simulated data from time-temperature histories of cooling since 2.5 Ga and peak reheating conditions at 1.1 Ga for a single grain size at closely spaced depths.

Figure DR3.3

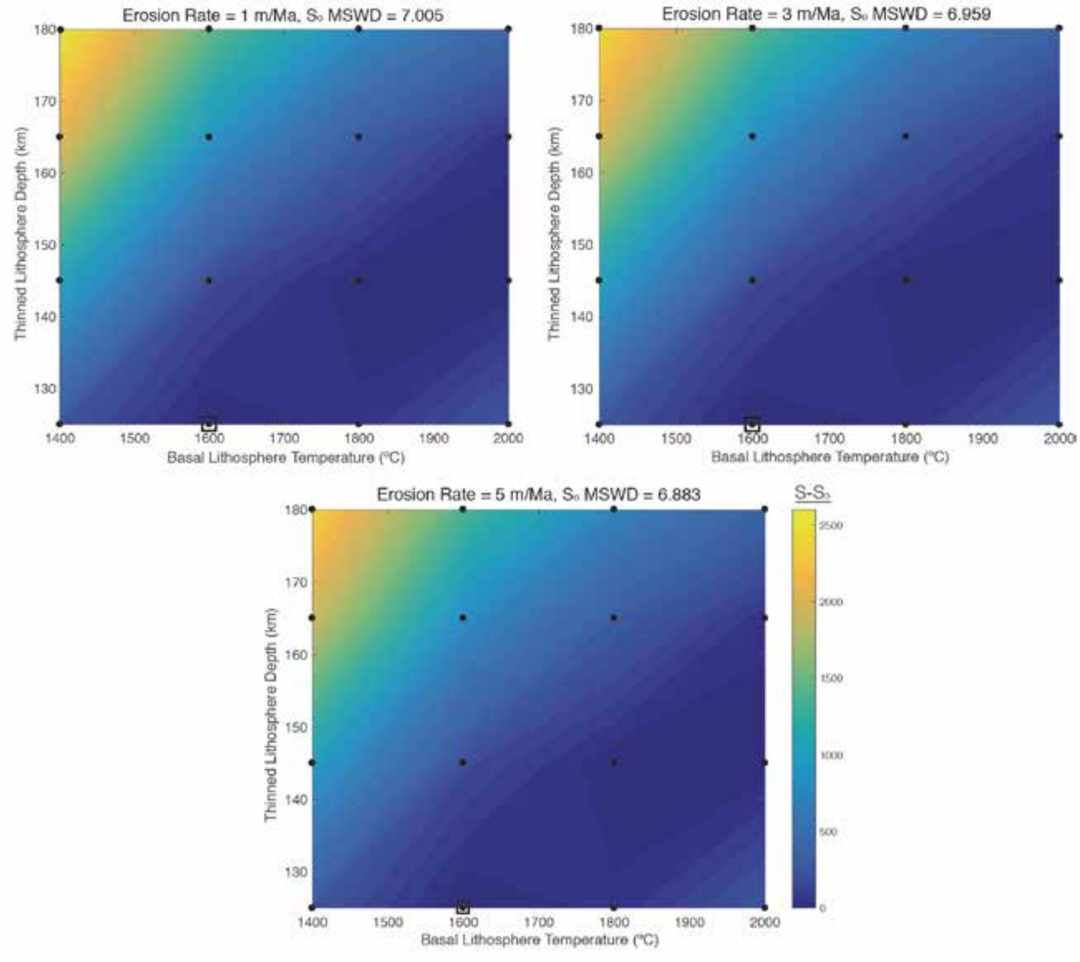

Figure DR3.3. Pearson χ^2 test results exploring the effects of simulated erosion rate on the goodness of fit between measured and modeled U-Pb data. Black dots represent paired model parameters of thinned lithosphere depth and basal lithosphere temperature, from which contours are calculated. Contour values are calculated by a linear interpolation method and represent the difference between the sum of χ^2 values for a given modeled condition (S) and the minimum χ^2 summation (S_o, identified with a black square). S_o MSWD values vary by less than 2% among the three erosion rate scenarios.

Figure DR3.4 (continued on next page)

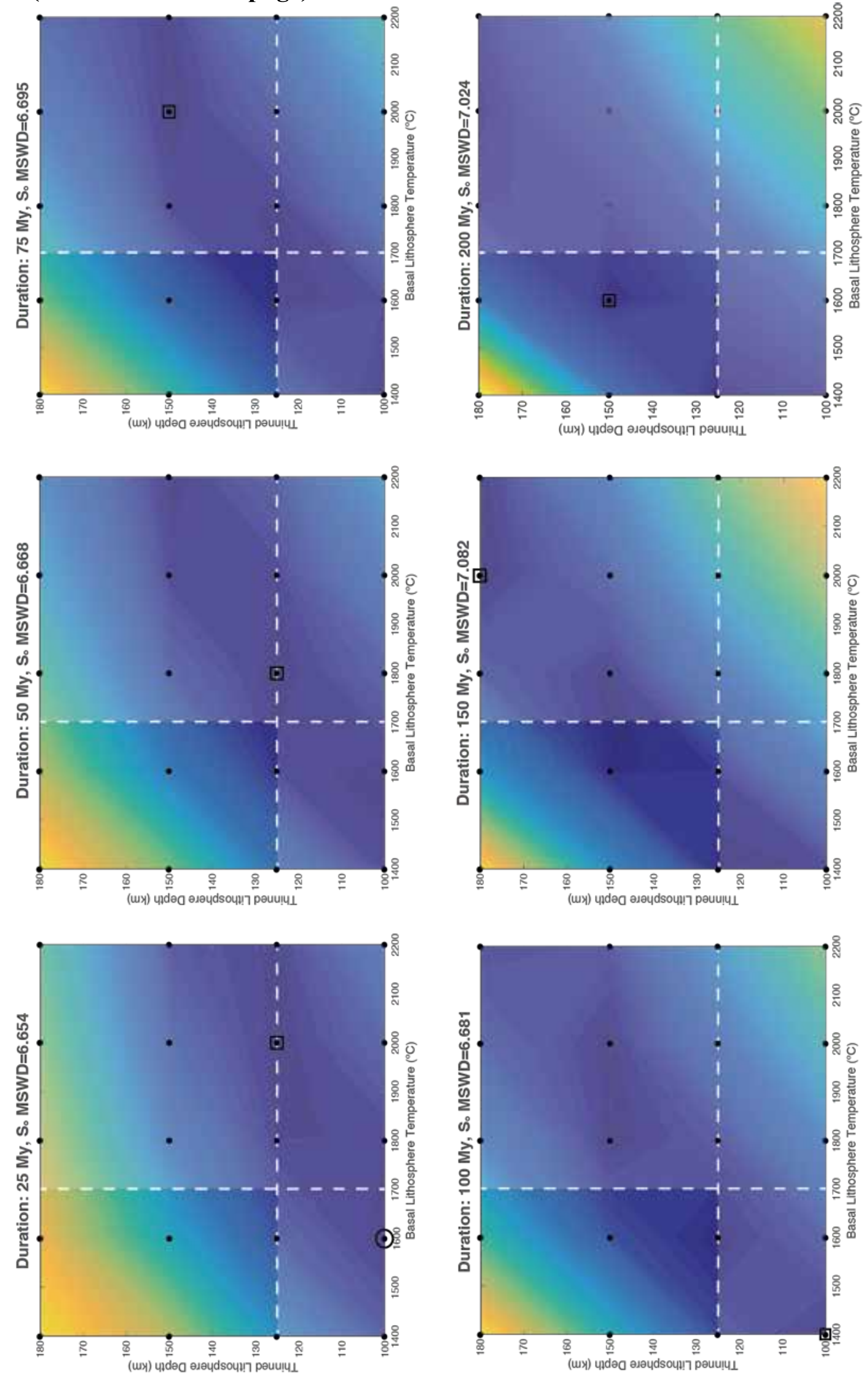

Figure DR3.4 (continued from previous page)

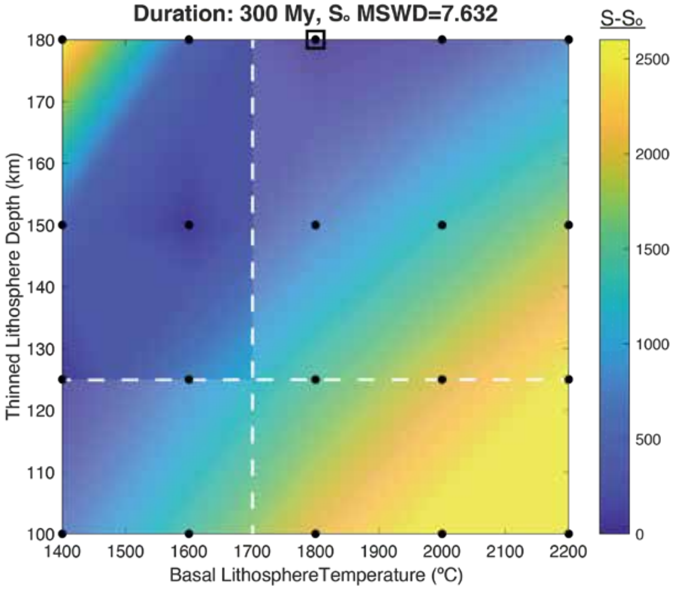

Figure DR3.4. Pearson χ^2 test results exploring the effects of simulated basal lithosphere heating duration on the goodness of fit between measured and modeled U-Pb data. Black dots represent paired model parameters of thinned lithosphere depth and basal lithosphere temperature. Contour values are calculated by a linear interpolation method and represent the difference between the sum of χ^2 values for the given modeled condition (S) and the minimum χ^2 summation (S_o, identified with a black square). Circled grid points are within 1σ of S_o. Dashed white lines indicate the minimum depth of the lithosphere as constrained by Archaen Re-Os ages from Jurassic xenoliths (Smit et al., 2014) and maximum mantle plume temperature as constrained by theory (Albers and Christensen, 1996) and observations (Herzberg et al., 2007; faded region is forbidden).

Figure DR3.5

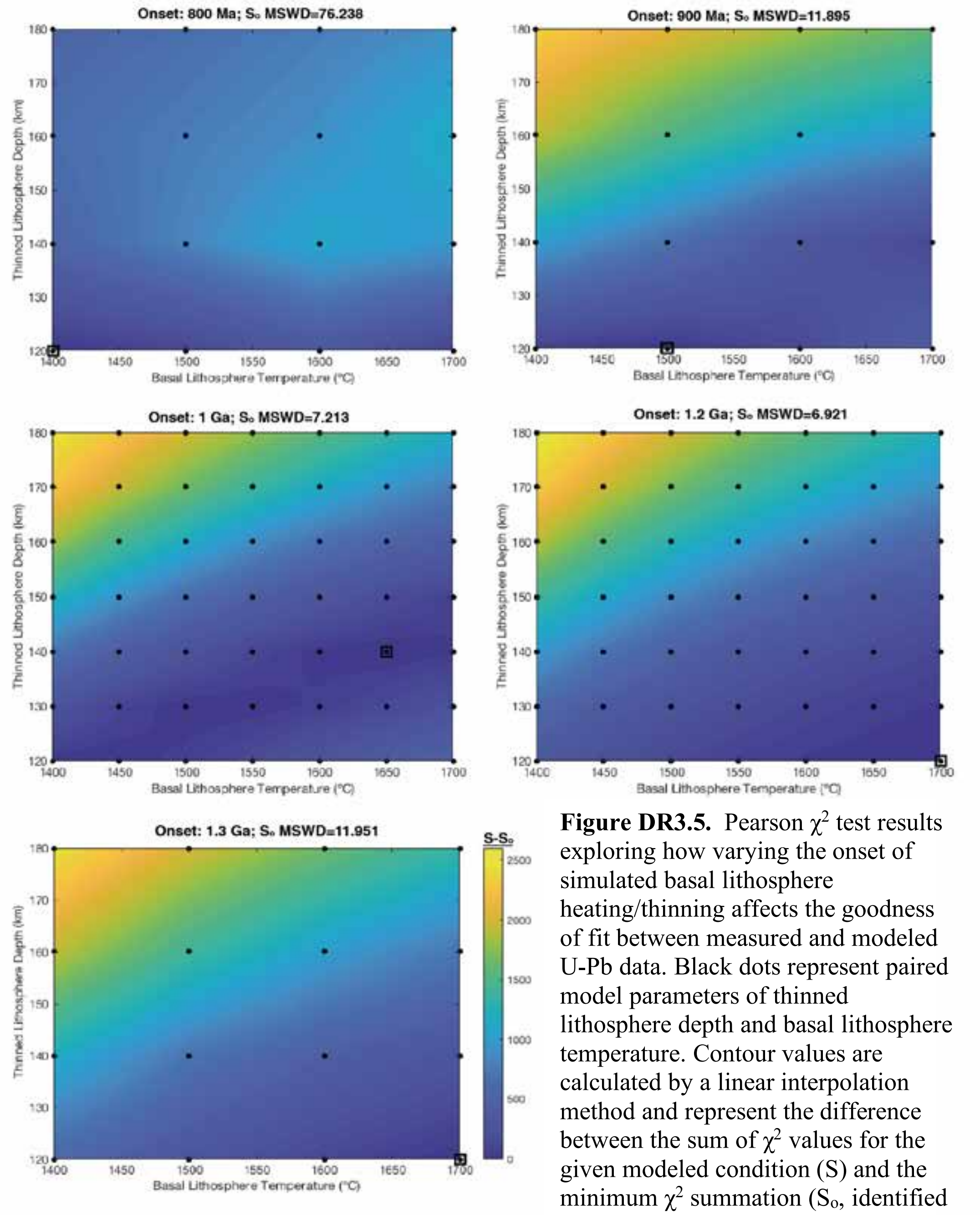

Figure DR3.5. Pearson χ^2 test results exploring how varying the onset of simulated basal lithosphere heating/thinning affects the goodness of fit between measured and modeled U-Pb data. Black dots represent paired model parameters of thinned lithosphere depth and basal lithosphere temperature. Contour values are calculated by a linear interpolation method and represent the difference between the sum of χ^2 values for the given modeled condition (S) and the minimum χ^2 summation (S_o, identified with a black square). Adequately good fits are found for onsets between 1 and 1.2 Ga (also see Fig. DR2.3) but degrade beyond this range.

Figure DR4.1

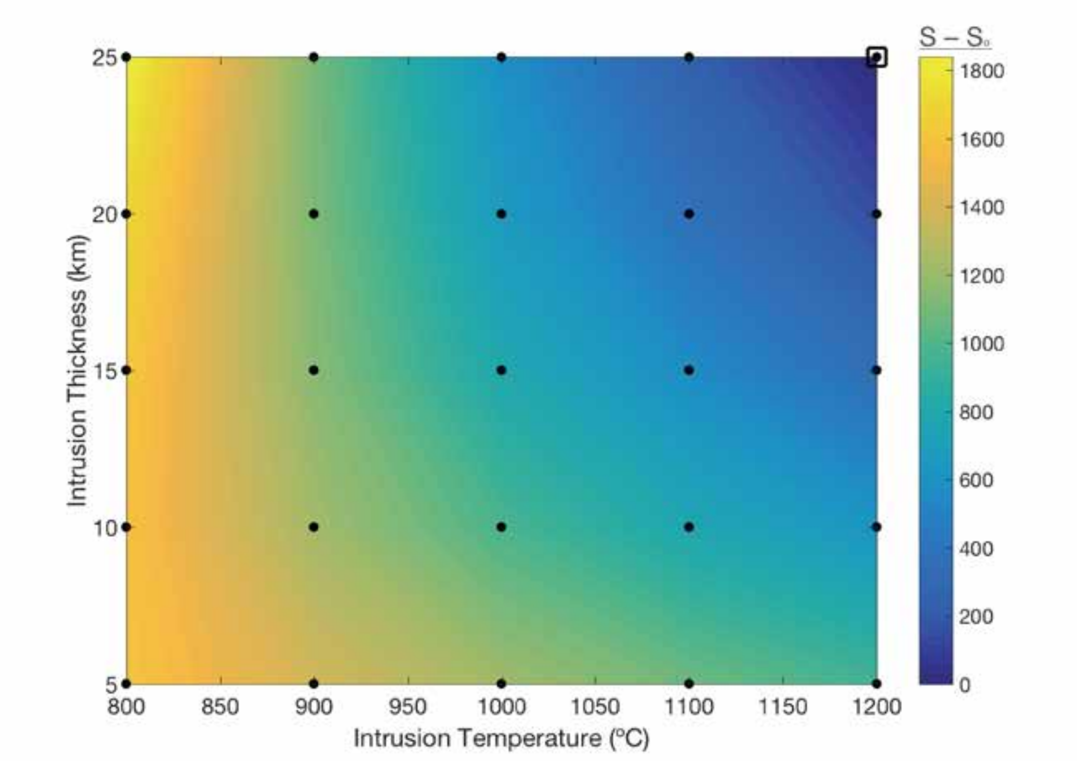

Figure DR4.1. Pearson χ^2 test results comparing measured U-Pb data and coupled thermal and Pb-diffusion model simulations of an intrusion reheating event for a range of intrusion thicknesses and temperatures. Intrusion thickness values represent depth below the base of the crust (45 km depth) within which reheating is simulated. Black dots represent modeled thickness-temperature pairs. Contour values are calculated by a linear interpolation method and represent the difference between the sum of χ^2 values for the given modeled condition (S) and the minimum χ^2 summation (S_o, identified with the black square). The calculated MSWD for S_o is 41.4770.

Appendix B

Supplementary Information to "Accretion of a large LL parent planetesimal from a recently formed chondrule population"

Reprinted from:

Edwards & Blackburn, 2020. "Accretion of a large LL parent planetesimal from a recently formed chondrule population," *Science Advances* 6, eaay8641. DOI: 10.1126/sciadv.aay8641

Science Advances
AAAS

advances.sciencemag.org/cgi/content/full/6/16/eaay8641/DC1

Supplementary Materials for

Accretion of a large LL parent planetesimal from a recently formed chondrule population

Graham H. Edwards* and Terrence Blackburn

*Corresponding author. Email: ghedwards@ucsc.edu

Published 15 April 2020, *Sci. Adv.* **6**, eaay8641 (2020)
DOI: 10.1126/sciadv.aay8641

The PDF file includes:

- Supplementary Methods
- Supplementary Text
- Figs. S1 to S7
- Tables S1 to S4
- References

Other Supplementary Material for this manuscript includes the following:

(available at advances.sciencemag.org/cgi/content/full/6/16/eaay8641/DC1)

- Data file S1

Supplementary Methods

Construction of Figure 2

Fig. 2 is constructed by simulating planetesimal thermal histories and corresponding Pb-phosphate ages for a grid of paired parameters of initial body $^{26}Al/^{27}Al$ composition and body radius. Body radii are simulated between 25 and 400 km at 25 km increments. Initial $^{26}Al/^{27}Al$ compositions are simulated at the values 11.44, 9.46, 8.60, 7.82, 7.11, 6.78, 6.47, 6.17, 6.02, 5.88, 5.74, 5.61, and 5.35 ($\times 10^{-6}$), which respectively correspond to formation ages of 1.6, 1.8, 1.9, 2.0, 2.10, 2.15, 2.20, 2.25, 2.275, 2.3, 2.325, 2.35, and 2.4 Ma after CAIs, assuming $(^{26}Al/^{27}Al)_o = 5.23\times10^{-5}$ (*9*). For each paired parameter simulation, the peak planetesimal temperatures are recorded, and Pb-production-diffusion in phosphate codes are calculated for the output thermal histories from the simulated planetesimal center and top of the type 6 region. The type 6 region "top" is identified as the shallowest depth that reaches a peak temperature of 875 ºC, the minimum peak metamorphic temperature recorded by LL6 thermometry (*51*). The Pb-phosphate model assumes a representative effective phosphate grain radius of 50 μm (Fig. S1). The LL6 age range (ΔLL6-age) is calculated for each paired parameter simulation by taking the difference between the output Pb-phosphate ages from the center and top of the type 6 region. Using the minimum peak metamorphic temperature affords a maximum ΔLL6-age estimate for a given thermal history and thus a minimum estimate of the initial $^{26}Al/^{27}Al$ ratio and planetesimal size required to achieve such a ΔLL6-age value, since ΔLL6-age scales with $^{26}Al/^{27}Al$ ratio and planetesimal size (Figs. 2,4).

The results of peak planetesimal temperature, central Pb-phosphate age, and ΔLL6-age are interpolated between the paired initial $^{26}Al/^{27}Al$-radius grid points using a two-dimensional modified Akima cubic Hermite interpolation technique in MATLAB. Interpolated grids have 100 times the resolution of the original parameter grid. Interpolated values of ΔLL6-age are contoured over the parameter space, with the contour of ΔLL6-age=30 Ma highlighted (see following paragraph). Additional contours are traced for those parameters yielding peak planetesimal temperatures of the LL chondrite solidus of 1140 ºC (*32*) and the absolute minimum possible LL6 peak metamorphic temperature (accommodated by measurement and calibration uncertainties) of 800 ºC (*51*). The final contour traces those parameter conditions yielding a central Pb-phosphate age overlapping the upperbound of the youngest Pb-phosphate date (ALH 83070, ~4485 Ma). The central Pb-phosphate date is fairly insensitive to modeled phosphate grain size: assuming a minimum grain radius of 10 μm only reduces this minimum estimate to ~140 km.

For large (≥100 km radius) model planetesimals, interiors experience gradual cooling recorded by the Pb-phosphate systems over timescales in excess of 30 Ma, even if the planetesimal does not reach a temperature of 875 ºC. In such cases with temperatures <875 ºC, a nil ΔLL6-age is calculated since an LL6 ceiling cannot be identified, even though a ≥30 Ma Pb-phosphate cooling history is recorded. We assume that the minimum LL6 thermometric condition of metamorphic temperatures ≥875 ºC must be met, and so for adequately large bodies, the ΔLL6-age=30 Ma contour will trace the 875 ºC maximum temperature contour. However, ΔLL6-age interpolations underestimate this step-change contour (Figs. S5, S6). In Fig. 4, for circumstances where the interpolated contour underestimates the corresponding initial $^{26}Al/^{27}Al$ ratio of the ΔLL6-age=30 Ma contour, we align the gray ΔLL6-age=30 Ma contour with the appropriate 875 ºC maximum temperature contour.

With respect to Semarkona chondrule Al-Mg systematics, we include only ferromagnesian chondrule Al-Mg data. We exclude Al-rich chondrules on the basis of evidence for partial derivation from CAI material (*55*), which can result in an apparently higher initial $^{26}Al/^{27}Al$ ratio (older date) that does not reflect the actual chondrule formation time. The kernel density estimation in Fig. 2 was calculated using DensityPlotter (v. 8.5) software (*56*).

Supplementary Text

An improved radiogenic Pb signal with acetic acid leaching treatment

We use a dilute acetic acid leaching treatment that targets labile Pb on phosphate grains to minimize terrestrial Pb contamination. The measurements of ALH 83070 bulk phosphate fractions 180701-1, -2, -3, and -4 (Tables S1, S2) illustrate the effects of leaching phosphate grains with 5% acetic acid in an ultrasonic bath (fractions 180701-3 and -4) relative to sonicating grains in ultra-pure water (fractions 180701-1 and -2). Dilute acid treatment significantly reduces the contribution of Pb_c, apparent in the order of magnitude decreases in $^{204}Pb/^{206}Pb$ values. These changes correspond with a decrease in the $^{207}Pb/^{206}Pb$ values of dilute acid-leached fractions, which necessarily leads to a decreased $^{207}Pb^*/^{206}Pb^*$ value and younger apparent age. We conclude that the leaching treatment effectively attacks and removes labile Pb from the surface of grains, reduces effects of terrestrial Pb contamination, and minimizes the transmission of labile initial Pb_c inherited from the bulk chondrite sample.

The leaching method results in removal of non-trivial amounts of apparent Pb*: water-cleaned fractions have ~2-5 times more apparent Pb* (after Pb_c-correction) than acid-leached fractions, despite all four fractions being of similar size. This raises the concern that acid-leaching is attacking surficial portions of the phosphate grains, since phosphate minerals are soluble in concentrated acetic acid solutions. In the case of phosphate grains where the outermost portions of the grain profile retain the youngest $^{207}Pb/^{206}Pb$ compositions (*18*), the effect of surficial dissolution would cause measured fractions to yield an apparently older age. Yet, age inaccuracies resulting from this process may be disregarded based on the following evidences. In the case of ALH 83070, the $^{207}Pb/^{206}Pb$ compositions (and apparent ages) are significantly less radiogenic (i.e. younger) for acid-leached fractions than water-cleaned fractions, and thus significant surficial dissolution is unlikely. Measurements of Ladder Creek bulk phosphate fractions with different leaching times (170608-1 and -3 experienced a 15-minute leach time, 170608-2 experienced a 30-minute leach time) indicate that variations in dilute acid exposure times have no discernible effect on the subsequent model Pb-phosphate dates. Additionally, Pb-phosphate dates for acetic-treated Ladder Creek fractions are similarly indistinguishable from or within <1 Ma of model Pb-phosphate dates for water-sonicated fractions of Ladder Creek (*18*). Finally, the cooling histories experienced by OC phosphates are likely too rapid to develop significant diffusion profiles that would be perturbed by minor surficial dissolution (*18*).

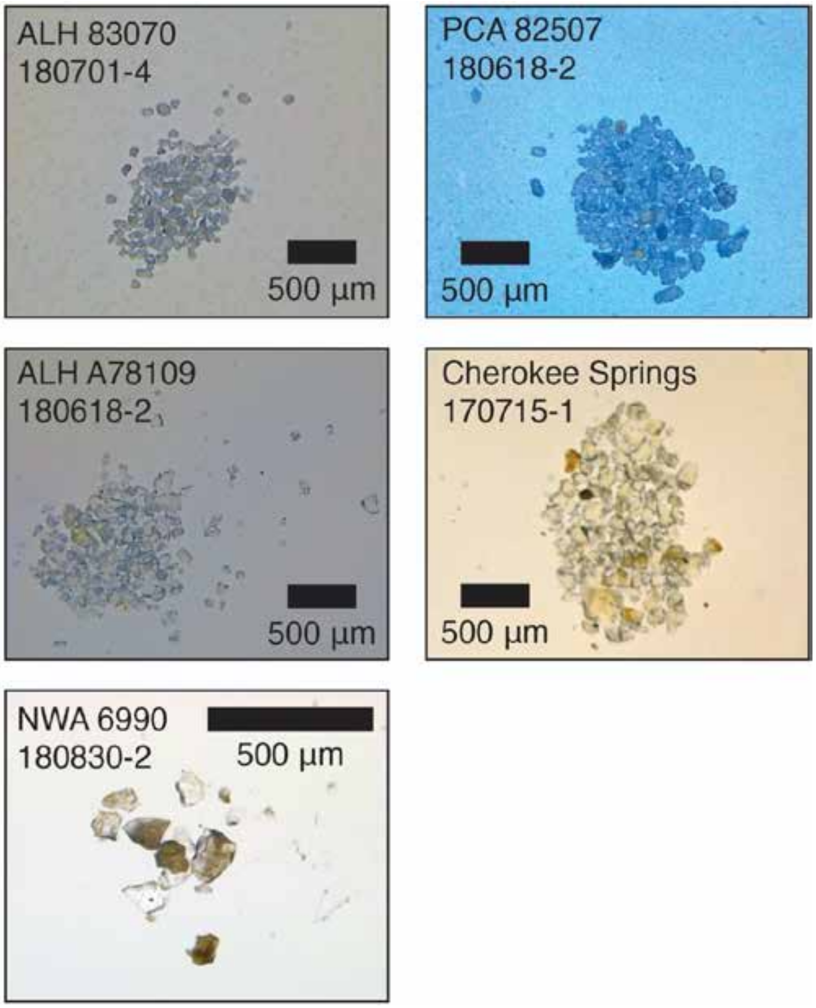

Fig. S1.

Representative photomicrographs of bulk phosphate fractions measured in this study. Photomicrographs were taken prior to leaching treatments.

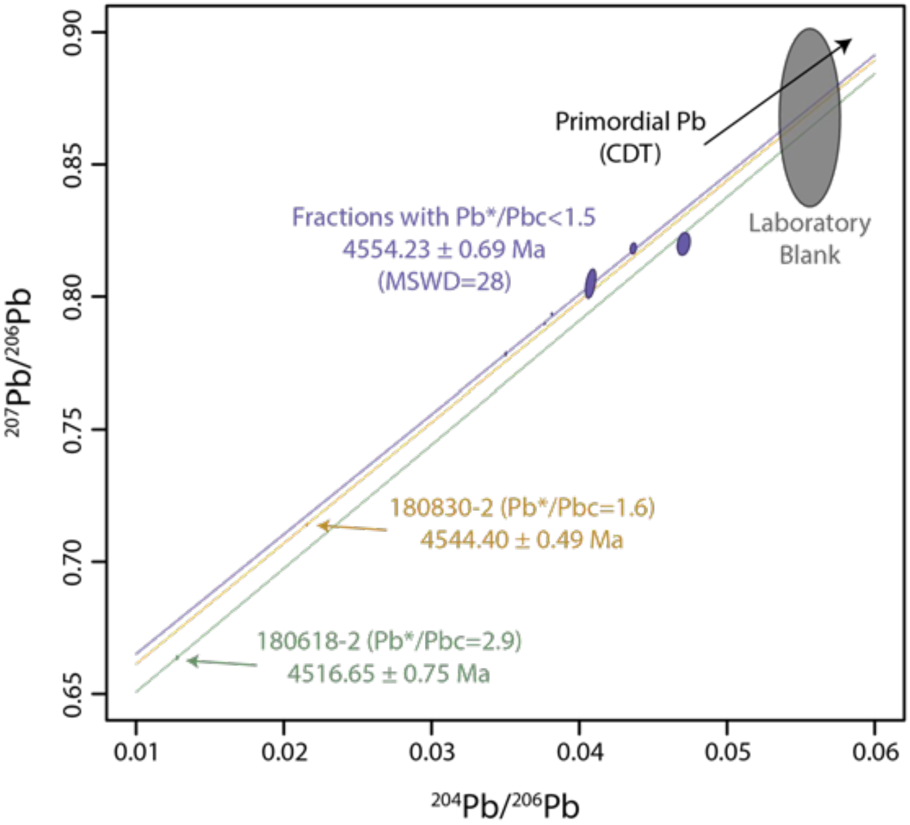

Fig. S2.

Inverse isochron of PCA 82507 phosphate fractions illustrating how confidence in the accuracy of ^{207}Pb*/^{206}Pb* scales with Pb*/Pb$_c$. Due to the magnitude of Pb$_c$-correction required for high ^{204}Pb/^{206}Pb compositions, ^{207}Pb*/^{206}Pb* ratios calculated from fractions with lower Pb*/Pb$_c$ are highly sensitive to minor variations in the measured ^{207}Pb/^{206}Pb, including effects on this value stemming from terrestrial Pb$_c$ contamination (we provide our laboratory blank composition as an arbitrary terrestrial Pb composition) or inaccuracies in the assumed primordial Pb$_c$ composition. In the case of PCA 82507, this results in substantially older dates calculated for fractions with Pb*/Pb$_c$<1.5. As ^{204}Pb/^{206}Pb is reduced (higher Pb*/Pb$_c$), the y-intercept from which the ^{207}Pb/^{206}Pb date is calculated is more reliable because it is less dependent on minor Pb composition variations. Isochrons were calculated and plotted with IsoplotR (*57*). Dates are calculated assuming a primordial composition of Canyon Diablo Troilite (CDT) (*43*). When these regressions are calculated using the primordial Pb composition advised by (*44*) the resultant ^{207}Pb/^{206}Pb dates are 4516.17 ± 0.73 Ma for 180618-2, 4543.39 ± 0.49 Ma for 180830-2, and 4552.34 ±0.28 Ma for fractions with Pb*/Pb$_c$<1.5. Only for the fraction with Pb*/Pb$_c$>2 are these two dates indistinguishable within uncertainties. The data do not discern whether the errors in the Pb$_c$ correction for low Pb*/Pb$_c$ fractions stem from terrestrial contamination or inaccurately estimated primordial Pb$_c$ composition, so a revised Pb$_c$ composition cannot be calculated with confidence.

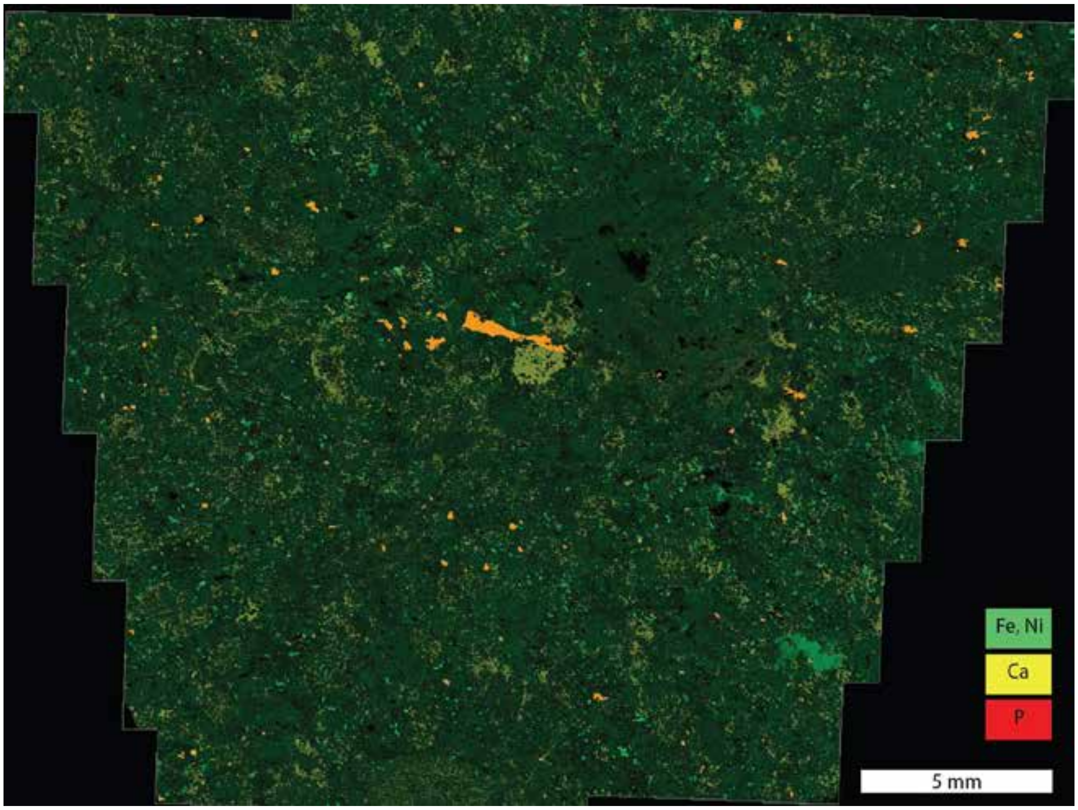

Fig. S3.
Energy-dispersive X-ray spectroscopy elemental map of NWA 6990. The heterogenous distribution of coarse-textured and vein-like phosphate minerals (these appear orange from color mix of Ca and P) is comparable to that observed in Portales Valley (H7), which is interpreted to have developed these distinctive properties in response to partial melting caused by a shock-heating event (*27*).

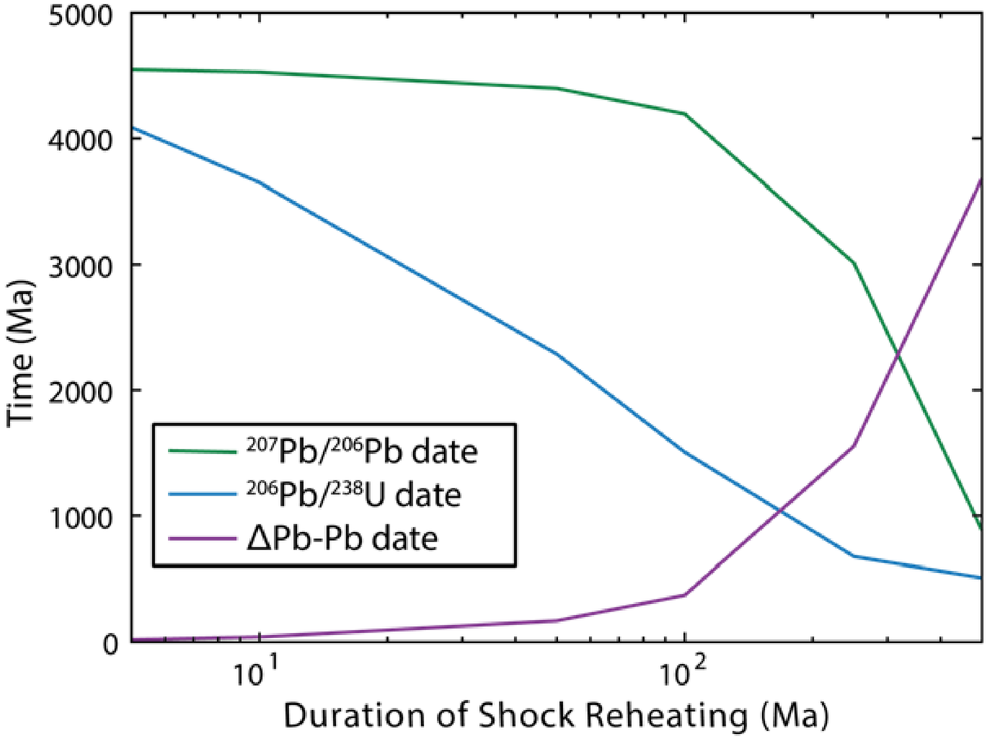

Fig. S4.

Relative sensitivities of the ^{238}U-^{206}Pb and ^{207}Pb-^{206}Pb systems in model phosphate grains experiencing reheating events of varying duration (5-500 Ma) after early cooling. Coupled thermal-Pb-production-diffusion codes simulate initial cooling rates of 1000 ºC/Ma from temperatures of 1000 ºC to model rapid early cooling. Shock reheating events were simulated by raising the temperature to 800 ºC at 500 Ma and holding for a specified duration before allowing a post-shock cooling rate of 100 ºC/Ma. The purple curve (ΔPb-Pb date) plots the difference between initial Pb-phosphate date and the partially reset date. The result is insensitive to initial cooling rates, whereas slow post-shock cooling rates exacerbate the change in Pb-phosphate date. Notably, the ^{238}U-^{206}Pb system is markedly more sensitive to heat-induced resetting than the ^{207}Pb-^{206}Pb system.

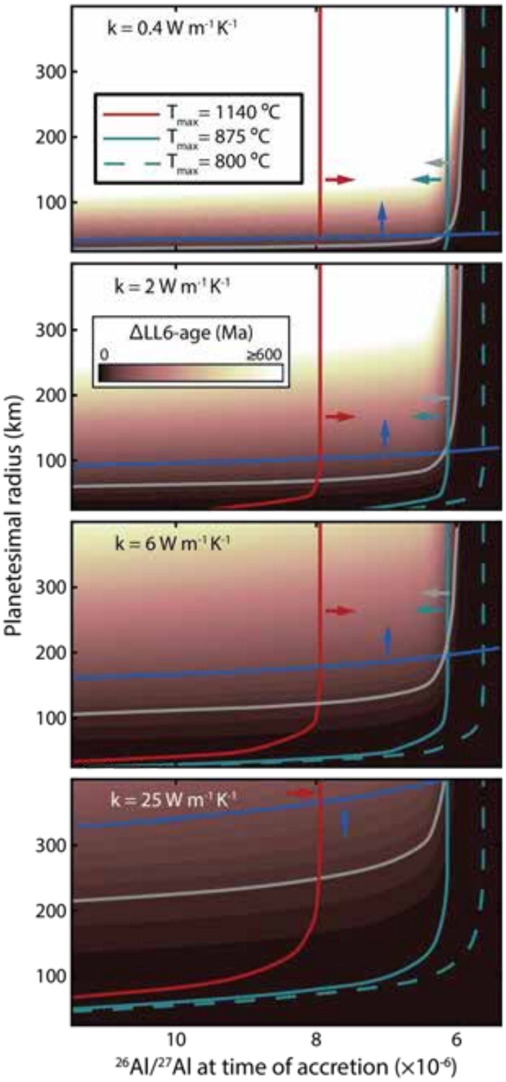

Fig. S5.

Modeled relationships between planetesimal radius, initial ^{26}Al/^{27}Al, peak metamorphic temperature (T_{max}), and Pb-phosphate systematics for simulated bodies with a range of thermal diffusivities. We scale thermal diffusivity (κ) by varying the least-well constrained term, thermal conductivity (*k*). The blue curves identify conditions that produce the required earliest central cooling age of 4485 Ma, the gray curves identify a ΔLL6-age of 30 Ma, red curves define maximum permissible T_{max} conditions (solidus), and teal curves identify minimum T_{max} conditions required by two-pyroxene thermometry (*51*). Although the gray ΔLL6-age curves extend to initial ^{26}Al/^{27}Al ratios less than the minima required by a T_{max} value of ≥875 ºC, this is an artifact of contour interpolation between modeled parameter conditions (Fig. S6). For these circumstances, the appropriate initial ^{26}Al/^{27}Al ratio is defined by the adjacent solid teal curve. Colored arrows point to permissible regions relative to contours, as in Fig. 4. For *k* values ranging from the minimum measured in highly porous chondrites (k=0.4 W m^{-1} K^{-1}) (*50*) to a pure Ni-Fe alloy at 1000 K (k=25 W m^{-1} K^{-1}) (*58*), combined metamorphic thermal requirements and measured Pb-phosphate systematics define a consistent permissible range of initial ^{26}Al/^{27}Al.

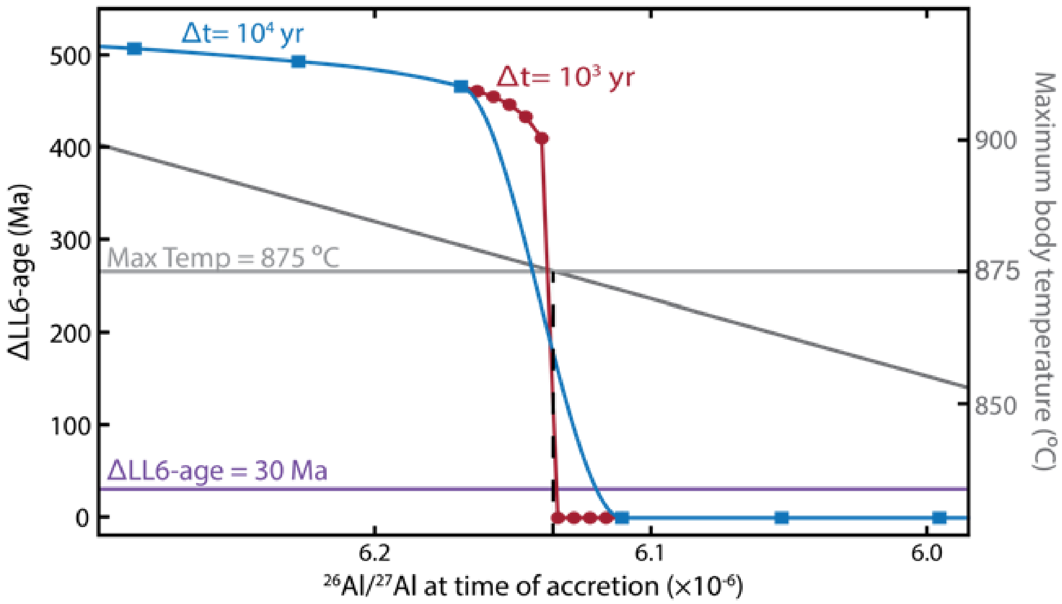

Fig. S6.

Interpolating ^{26}Al/^{27}Al at time of accretion from discrete model results for a large (400 km radius) model planetesimal that establishes a ΔLL6-age of 30 Ma. Blue squares and red circles correspond to values on the left-axis (ΔLL6-age) and respectively reflect the results for modeled initial ^{26}Al/^{27}Al conditions that are simulated at coarse (Δt=10^4 yr between each modeled accretion time) and fine (Δt=10^3 yr) resolutions. Interpolations between modeled data points (red and blue curves) are calculated with a one-dimensional cubic interpolation method comparable to the two-dimensional method used in Fig. 4. The purple line identifies the ΔLL6-age=30 Ma contour of interest. Gray lines correspond to the right axis (Maximum body temperature). The dark gray line reflects modeled peak temperatures, the results of which are insensitive to changes in simulation resolution. The light gray line highlights the 875 ºC peak temperature that is selected to identify the upper boundary of the LL6 region in ΔLL6-age calculations (e.g. Fig. S5). In large planetesimals such as the one modeled here, achieving ΔLL6-age=30 Ma is contingent on the body heating to the specified peak temperature of ≥875 ºC. For any simulation where the maximum temperature is <875 ºC, ΔLL6-age=0 Ma. However, for ^{26}Al/^{27}Al slightly above 6.1×10^{-6}, the ≥875 ºC temperature condition is met and cooling across this large isothermal LL6 yields ΔLL6>>30 Ma. Interpolations underestimate the corresponding ^{26}Al/^{27}Al of this discrete threshold. Subsequently, for those bodies where obtaining ΔLL6-age=30 Ma is contingent on reaching an internal temperature of ≥875 ºC, the ΔLL6-age=30 Ma contour overlaps the contour that demarcates the specified minimum interior temperature.

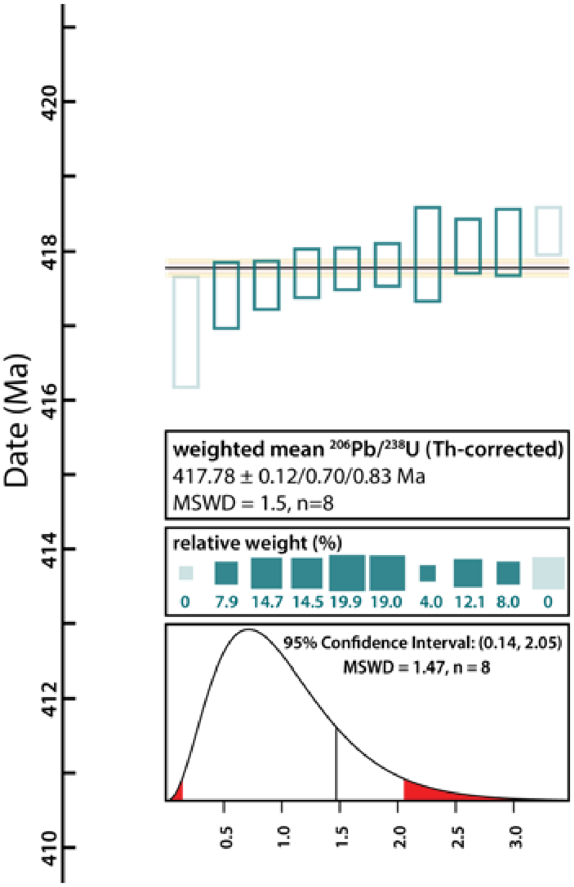

Fig. S7.

Laboratory U-Pb date reproducibility as evidenced with the Temora zircon standard. ID-TIMS measurements were conducted in 2017 and dates calculated from raw data using U-Pb Redux software (*42*). Two outlying measurements are rejected. Th-corrected error-weighted mean date is presented with uncertainties propagated respectively from analytical uncertainties only; analytical and tracer uncertainties; and analytical, tracer, and decay constant uncertainties. Analytical uncertainties alone reveal reproducibility within 0.03%.

Table S1.

Chondrite phosphate Pb-Pb and U-Pb dates and elemental compositions.
Also tabulated in Data file S1.

	Dates (Ma), Absolute Uncertainties [a]					Masses (pg)			
	^{207}Pb/^{206}Pb	±2σ	^{206}Pb/^{238}U	±2σ	% disc[b]	U	Pb* [c]	Pb_c [d]	Pb*/ Pb_c [e]
Cherokee Springs, LL5									
170628-2	4540.67	0.20	4564.3	5.0	-1	270	490	3.5	140
170703-1	4540.8	1.6	4142	57	9	7.8	26	1.1	23
170703-2	4536.7	1.2	5031	67	-11	7.2	23	1.5	16
170703-3	4540.65	0.48	4667	14	-3	33	120	2.3	51
170703-4	4540.62	0.90	4702	41	-4	11	41	1.2	34
170715-1	4541.62	0.94	4342	31	4	45	140	4.6	30
170715-2	4544.36	0.27	4600.6	6.3	-1	69	270	5.2	52
ALH A78109, LL5									
180420-1	4537.92	0.65	4885	34	-8	13	35	4.8	7
180420-2	4538.26	0.54	4979	21	-10	21	63	7.9	8
180618-1	4537.21	0.51	5077	15	-12	34	87	11	8
180618-2	4541.12	0.87	-	-	-	-	43	2.0	22
PCA 82507, LL6									
180420-1	-	-	-	-	-	-	17	27	0.6
180420-2	-	-	-	-	-	54	180	200	0.9
180531-1	-	-	-	-	-	80	240	240	1.0
180618-1	-	-	-	-	-	1.0	2.3	3.0	0.8
180618-2	4516.65	0.77	5228	45	-16	10	24	8.5	2.9
180830-1	-	-	-	-	-	44	120	140	0.9
180830-2	-	-	-	-	-	53	110	65	1.6
180830-3	-	-	-	-	-	20	30	43	0.7
ALH 83070, LL6									
180420-1	4479.93	0.36	4818.6	9.7	-8	47	100	9.8	10
180420-2	4479.40	0.30	4922.8	5.2	-10	87	190	13	15
180618-1	4485.20	0.67	5022	13	-12	38	95	5.0	19
180618-2	4481.35	0.46	5165	10	-15	48	120	7.0	17
180701-1	-	-	-	-	-	130	380	340	1
180701-2	-	-	-	-	-	110	360	370	1
180701-3	4485.97	0.39	4801	16	-7	32	70	9.0	8
180701-4	4485.58	0.38	4920	15	-10	31	74	10	7
ALH 83070 (Leachates)									
180701-1 (L)	-	-	-	-	-	14	0.8	4.7	0.2
180701-2 (L)	-	-	-	-	-	13	9.1	23	0.4
180701-3 (L)	-	-	-	-	-	38	160	230	0.7
180701-4 (L)	-	-	-	-	-	49	1400	3500	0.4
ALH 84081, LL6									
180531-1	-	-	-	-	-	-	1.9	5.1	0.4
180531-2	-	-	-	-	-	-	2.2	5.9	0.4
NWA 6990, LL7									
180830-2	4546.55	0.59	2335	12	49	35	27	5.0	5
180830-3	4540.6	9.3	2460	240	46	1.5	3.6	0.6	6
Ladder Creek, L6									
170608-1	4514.3	2.1	798.8	9.7	82	55	13	2.1	6
170608-2	4512.65	0.83	4761	18	-5	16	33	1.7	20
170608-3	4513.07	0.90	4953	32	-10	16	36	3.3	11

[a] Isotopic dates calculated using λ_{238} = 1.55125E-10 and λ_{235} = 9.8485E-10 (*59*).

[b] % Discordance = 100 - (100 * (^{206}Pb/^{238}U date) / (^{207}Pb/^{206}Pb date))

[c] Total mass of radiogenic Pb.

[d] Total mass of common Pb.

[e] Ratio of radiogenic Pb (including ^{208}Pb) to common Pb.

Table S2.

Chondrite phosphate Pb and U-Pb isotopic ratios.
Also tabulated in Data file S1.

	^{207}Pb/ ^{235}U^{a}	±2σ (%)	^{206}Pb/ ^{238}U^{a}	±2σ (%)	U-Pb ϱ	^{207}Pb/ ^{206}Pb ^{a}	±2σ (%)	^{204}Pb/ ^{206}Pb ^{b}	±2σ (%)	^{207}Pb/ ^{206}Pb ^{b}	±2σ (%)	Pb-Pb ϱ
Cherokee Springs, LL5												
170628-2	1.03	0.15	87.2	0.15	0.996	0.614	0.01	2.10 E-04	1.2	0.615	0.04	0.029
170703-1	0.901	1.9	76.3	1.9	0.998	0.614	0.11	1.43 E-03	5.7	0.621	0.26	0.073
170703-2	1.18	1.9	99.8	1.9	0.999	0.612	0.08	2.10 E-03	2.5	0.622	0.17	0.117
170703-3	1.06	0.41	89.9	0.41	0.997	0.614	0.03	1.06 E-03	1.7	0.619	0.07	0.053
170703-4	1.07	1.2	90.9	1.2	0.999	0.614	0.06	9.47 E-04	5.0	0.618	0.15	0.068
170715-1	0.961	0.98	81.4	0.98	0.998	0.614	0.06	2.16 E-03	1.1	0.624	0.14	0.049
170715-2	1.04	0.19	88.3	0.19	0.995	0.616	0.02	1.48 E-03	0.63	0.622	0.04	0.041
ALH A78109, LL5												
180420-1	1.13	0.99	95.7	0.99	0.999	0.613	0.04	6.11 E-03	0.42	0.641	0.08	0.165
180420-2	1.16	0.61	98.4	0.61	0.998	0.613	0.04	6.40 E-03	0.42	0.642	0.08	0.106
180618-1	1.20	0.42	101	0.42	0.996	0.613	0.03	5.73 E-03	0.29	0.639	0.07	0.093
180618-2	-	-	-	-	-	0.614	0.06	2.12 E-03	1.7	0.624	0.14	0.037
PCA 82507, LL6												
180420-1	-	-	-	-	-	0.597	0.92	4.71 E-02	0.73	0.820	0.42	0.231
180420-2	1.47	0.23	126	0.23	0.971	0.619	0.05	3.76 E-02	0.03	0.790	0.03	0.356
180531-1	1.34	0.18	114	0.20	0.939	0.620	0.07	3.50 E-02	0.05	0.778	0.07	0.446
180618-1	0.898	14	76.8	14	1.00	0.621	0.42	4.08 E-02	0.68	0.805	0.55	0.453
180618-2	1.25	1.3	104	1.3	0.999	0.604	0.05	1.28 E-02	0.19	0.664	0.08	0.201
180830-1	1.22	0.29	104	0.30	0.980	0.621	0.06	3.81 E-02	0.05	0.793	0.04	0.322
180830-2	1.06	0.25	89.8	0.25	0.993	0.616	0.03	2.16 E-02	0.06	0.714	0.04	0.278
180830-3	0.677	12	58.0	12	1.00	0.621	0.31	4.37 E-02	0.36	0.818	0.20	0.200
ALH 83070, LL6												
180420-1	1.11	0.29	90.21	0.29	0.996	0.589	0.02	3.98 E-03	0.21	0.608	0.05	0.129
180420-2	1.15	0.15	93.0	0.15	0.991	0.589	0.02	2.88 E-03	0.28	0.603	0.04	0.067
180618-1	1.18	0.36	96.0	0.37	0.993	0.591	0.04	2.38 E-03	0.57	0.602	0.09	0.051
180618-2	1.23	0.28	99.8	0.29	0.994	0.590	0.03	2.58 E-03	0.26	0.602	0.05	0.081
180701-1	1.43	0.12	119	0.13	0.932	0.605	0.05	3.07 E-02	0.04	0.748	0.04	0.377
180701-2	1.64	0.15	137	0.21	0.846	0.609	0.12	3.38 E-02	0.08	0.765	0.11	0.445
180701-3	1.11	0.47	90.1	0.47	0.998	0.591	0.02	5.33 E-03	0.36	0.617	0.06	0.081
180701-4	1.15	0.43	93.3	0.43	0.998	0.591	0.02	6.00 E-03	0.30	0.620	0.06	0.087
ALH 83070 (Leachates)												
180701-1 (L)	-	-	-	-	-	-	-	5.84 E-02	2.8	0.904	2.9	0.915
180701-2 (L)	-	-	-	-	-	-	-	5.56 E-02	0.52	0.883	0.36	0.476
180701-3 (L)	-	-	-	-	-	-	-	4.16 E-02	0.39	0.810	0.45	0.374
180701-4 (L)	-	-	-	-	-	-	-	5.97 E-02	0.13	0.947	0.11	0.124
ALH 84081, LL6												
180531-1	-	-	-	-	-	0.621	1.1	5.52 E-02	0.81	0.870	0.78	0.589
180531-2	-	-	-	-	-	0.628	0.96	5.69 E-02	0.54	0.881	0.49	0.672
NWA 6990, LL7												
180830-2	0.437	0.61	37.1	0.60	0.998	0.617	0.04	6.51 E-03	0.35	0.646	0.07	0.126
180830-3	0.465	12	39.3	12	0.999	0.614	0.64	3.96 E-03	8.5	0.632	1.1	0.144
Ladder Creek, L6												
170608-1	0.132	1.3	11.0	1.3	0.994	0.603	0.15	3.51 E-03	3.3	0.619	0.37	0.094
170608-2	1.09	0.54	90.7	0.55	0.995	0.602	0.06	8.84 E-04	5.8	0.606	0.16	0.059
170608-3	1.16	0.91	96.0	0.91	0.998	0.603	0.06	2.78 E-03	1.5	0.616	0.14	0.093

[a] Measured ratios corrected for fractionation, tracer, blank, and initial common Pb.

[b] Measured ratios corrected for fractionation, tracer, and blank only.

Table S3. Results from energy-dispersive X-ray spectroscopy elemental maps for individual phosphate grains from PCA 82507. Elemental amounts are given in weight % with 1σ errors, as measured from K lines. Grain p2 reflects evidence of merrillite composition, whereas grains p1, p3, and p4 are apatite.

	P	**Na**	**Mg**	**Ca**	**Fe**	**F**	**Cl**
p1	17.23 ± 0.08	0.41 ± 0.04	0.00 ± 0.03	38.46 ±0.11	0.00 ± 0.07	0.00 ± 0.11	5.62± 0.05
p2	17.05 ± 0.06	0.44 ± 0.03	0.19 ± 0.02	37.84 ± 0.09	0.18 ± 0.05	0.25 ± 0.08	5.54 ± 0.04
p3	16.27 ± 0.08	0.43 ± 0.04	0.00 ± 0.02	39.90 ± 0.12	0.00 ± 0.07	0.35 ± 0.10	5.47 ± 0.05
p4	17.36 ± 0.10	0.56 ± 0.05	0.00 ± 0.03	38.16 ± 0.14	0.00 ± 0.09	0.45 ± 0.13	5.17 ± 0.06

Table S4.

Constants used in U-Pb and Pb-Pb calculations. Uncertainties given as 1σ absolute.

Constants		**Reference**
Initial common Pb model – Canyon Diablo Troilite (CDT)		(*43*)
$^{206}Pb/^{204}Pb$	9.307 ± 0.003	
$^{207}Pb/^{204}Pb$	10.294 ± 0.003	
$^{208}Pb/^{204}Pb$	29.476 ± 0.009	
Pb blank model		
$^{206}Pb/^{204}Pb$	17.985 ± 0.272	
$^{207}Pb/^{204}Pb$	15.605 ±0.075	
$^{208}Pb/^{204}Pb$	37.809 ± 0.325	
Contemporary sample $^{238}U/^{235}U$	137.786 ± 0.0065	(*14*)
Blank $^{238}U/^{235}U$	137.8185 ± 0.0223	(*60*)
$(^{18}O/^{16}O)_{U\text{-}oxide}$	0.00205 ± 0.00002	
Tracer mass uncertainty	± 0.0001 g	
Pb fractionation model (α)	0.23 ± 0.02 %/amu	
Pb blank uncertainty	± 0.3 pg	
U blank uncertainty	± 0.05 pg	

REFERENCES AND NOTES

1. P. Vernazza, B. Zanda, R. P. Binzel, T. Hiroi, F. E. DeMeo, M. Birlan, R. Hewins, L. Ricci, P. Barge, M. Lockhart, Multiple and fast: The accretion of ordinary chondrite parent bodies. *Astrophys. J.* **791**, 120 (2014).

2. A. Johansen, J. S. Oishi, M.-M. Mac Low, H. Klahr, T. Henning, A. Youdin, Rapid planetesimal formation in turbulent circumstellar disks. *Nature* **448**, 1022–1025 (2007).

3. S. J. Weidenschilling, Initial sizes of planetesimals and accretion of the asteroids. *Icarus* **214**, 671–684 (2011).

4. S. Henke, H.-P. Gail, M. Trieloff, W. H. Schwarz, Thermal evolution model for the H chondrite asteroid-instantaneous formation versus protracted accretion. *Icarus* **226**, 212–228 (2013).

5. N. Sugiura, W. Fujiya, Correlated accretion ages and ε^{54}Cr of meteorite parent bodies and the evolution of the solar nebula. *Meteorit. Planet. Sci.* **49**, 772–787 (2014).

6. J. Pape, K. Mezger, A.-S. Bouvier, L. P. Baumgartner, Time and duration of chondrule formation: Constraints from ^{26}Al-^{26}Mg ages of individual chondrules. *Geochim. Cosmochim. Acta* **244**, 416–436 (2019).

7. M. Miyamoto, N. Fujii, H. Takeda, Ordinary chondrite parent body: An internal heating model. *Lunar Planet. Sci. Conf.* **12B**, 1145–1152 (1981).

8. A. Ghosh, S. J. Weidenschilling, H. Y. McSween, A. Rubin, Asteroidal heating and thermal stratification of the asteriod belt, in *Meteorites and the Early Solar System II*, D. S. Lauretta, H. Y. McSween, Eds. (University of Arizona Press, 2006), pp. 555–566.

9. B. Jacobsen, Q.-z. Yin, F. Moynier, Y. Amelin, A. N. Krot, K. Nagashima, I. D. Hutcheon, H. Palme, ^{26}Al–^{26}Mg and ^{207}Pb–^{206}Pb systematics of Allende CAIs: Canonical solar initial ^{26}Al/^{27}Al ratio reinstated. *Earth Planet. Sci. Lett.* **272**, 353–364 (2008).

10 J. Villeneuve, M. Chaussidon, G. Libourel, Homogeneous distribution of ^{26}Al in the Solar System from the Mg isotopic composition of chondrules. *Science* **325**, 985–988 (2009).

11. G. Budde, T. S. Kruijer, T. Kleine, Hf-W chronology of CR chondrites: Implications for the timescales of chondrule formation and the distribution of ^{26}Al in the solar nebula. *Geochim. Cosmochim. Acta* **222**, 284–304 (2018).

12. A. P. Boss, Mixing in the solar nebula: Implications for isotopic heterogeneity and large-scale transport of refractory grains. *Earth Planet. Sci. Lett.* **268**, 102–109 (2008).

13. J. L. Hellmann, T. S. Kruijer, J. A. Van Orman, K. Metzler, T. Kleine, Hf-W chronology of ordinary chondrites. *Geochim. Cosmochim. Acta* **258**, 290–309 (2019).

14. J. N. Connelly, M. Bizzarro, A. N. Krot, Å. Nordlund, D. Wielandt, M. A. Ivanova, The absolute chronology and thermal processing of solids in the solar protoplanetary disk. *Science* **338**, 651–655 (2012).

15. J. Bollard, J. N. Connelly, M. J. Whitehouse, E. A. Pringle, L. Bonal, J. K. Jørgensen, Å. Nordlund, F. Moynier, M. Bizzarro, Early formation of planetary building blocks inferred from Pb isotopic ages of chondrules. *Sci. Adv.* **3**, e1700407 (2017).

16. G. Budde, T. Kleine, T. S. Kruijer, C. Burkhardt, K. Metzler, Tungsten isotopic constraints on the age and origin of chondrules. *Proc. Natl. Acad. Sci. U.S.A.* **113**, 2886–2891 (2016).

17. C. M. O. Alexander, J. N. Grossman, D. S. Ebel, F. J. Ciesla, The formation conditions of chondrules and chondrites. *Science* **320**, 1617–1619 (2008).

18. T. Blackburn, C. M. O. Alexander, R. Carlson, L. T. Elkins-Tanton, The accretion and impact history of the ordinary chondrite parent bodies. *Geochim. Cosmochim. Acta* **200**, 201–217 (2017).

19. C. Göpel, G. Manhès, C. J. Allègre, U-Pb systematics of phosphates from equilibrated ordinary chondrites. *Earth Planet. Sci. Lett.* **121**, 153–171 (1994).

20. M. Trieloff, E. K. Jessberger, I. Herrwerth, J. Hopp, C. Fiéni, M. Ghélis, M. Bourot-Denise, P. Pellas, Structure and thermal history of the H-chondrite parent asteroid revealed by thermochronometry. *Nature* **422**, 502–506 (2003).

21. A. W. Tait, A. G. Tomkins, B. M. Godel, S. A. Wilson, P. Hasalova, Investigation of the H7 ordinary chondrite, Watson 012: Implications for recognition and classification of Type 7 meteorites. *Geochim. Cosmochim. Acta* **134**, 175–196 (2014).

22. H. Takeda, T. J. Huston, M. E. Lipschutz, On the chondrite-achondrite transition: Mineralogy and chemistry of Yamato 74160 (LL7). *Earth Planet. Sci. Lett.* **71**, 329–339 (1984).

23. A. Bouvier, J. Blichert-Toft, F. Moynier, J. D. Vervoort, F. Albarède, Pb-Pb dating constraints on the accretion and cooling history of chondrites. *Geochim. Cosmochim. Acta* **71**, 1583–1604 (2007).

24. J. H. Chen, G. J. Wasserburg, The isotopic composition of uranium and lead in Allende inclusions and meteoritic phosphates. *Earth Planet. Sci. Lett.* **52**, 1–15 (1981).

25. D. J. Cherniak, Diffusion in accessory minerals: Zircon, titanite, apatite, monazite and xenotime. *Rev. Mineral. Geochemistry*. **72**, 827–869 (2010).

26. E. Jarosewich, M. Brian, Chemical analyses with notes on one mesosiderite and seven chondrites. *Geochim. Cosmochim. Acta* **33**, 411–416 (1969).

27. A. Ruzicka, M. Killgore, D. W. Mittlefehldt, M. D. Fries, Portales Valley: Petrology of a metallic-melt meteorite breccia. *Meteorit. Planet. Sci.* **40**, 261–295 (2005).

28. A. Ruzicka, J. M. Friedrich, R. Hugo, M. Hutson, Macro- and microstructures in ordinary chondrites: Implcations for impact deformation and annealing processes, in *46th Lunar and Planetary Science Conference*, Woodlands, Texas, 16 to 20 March 2015, pp. 1544.

29. S. Li, W. Hsu, The nature of the L chondrite parent body's disruption as deduced from high-pressure phases in the Sixiangkou L6 chondrite. *Meteorit. Planet. Sci.* **53**, 2107–2122 (2018).

30. A. Blinova, Y. Amelin, C. Samson, Constraints on the cooling history of the H-chondrite parent body from phosphate and chondrule Pb-isotopic dates from Estacado. *Meteorit. Planet. Sci.* **42**, 1337–1350 (2007).

31. G. Crozaz, C. Floss, M. Wadhwa, Chemical alteration and REE mobilization in meteorites from hot and cold deserts. *Geochim. Cosmochim. Acta* **67**, 4727–4741 (2003).

32. T. E. Johnson, G. K. Benedix, P. A. Bland, Metamorphism and partial melting of ordinary chondrites: Calculated phase equilibria. *Earth Planet. Sci. Lett.* **433**, 21–30 (2016).

33. K. J. Walsh, A. Morbidelli, S. N. Raymond, D. P. O'Brien, A. M. Mandell, A low mass for Mars from Jupiter's early gas-driven migration. *Nature* **475**, 206–209 (2011).

34. J. N. Cuzzi, R. C. Hogan, W. F. Bottke, Towards initial mass functions for asteroids and Kuiper belt objects. *Icarus* **208**, 518–538 (2010).

35. J. E. Chambers, Planetary accretion in the inner Solar System. *Earth Planet. Sci. Lett.* **223**, 241–252 (2004).

36. A. Morbidelli, W. F. Bottke, D. Nesvorný, H. F. Levison, Asteroids were born big. *Icarus* **204**, 558–573 (2009).

37. J. D. Gilmour, M. J. Filtness, Dissipation of the Solar System's debris disk recorded in primitive meteorites. *Nat. Astron.* **3**, 326–331 (2019).

38. A. S. G. Roth, K. Metzler, L. P. Baumgartner, I. Leya, Cosmic-ray exposure ages of chondrules. *Meteorit. Planet. Sci.* **51**, 1256–1267 (2016).

39. J. A. Lewis, R. H. Jones, Primary feldspar in the Semarkona LL3.00 chondrite: Constraints on chondrule formation and secondary alteration. *Meteorit. Planet. Sci.* **54**, 72–89 (2019).

40. M. A. Morris, A. C. Boley, in *Chondrules*, S. S. Russell, H. C. Connolly, A. N. Krot, Eds. (Cambridge Univ. Press, 2018), pp. 375–399.

41. D. J. Condon, B. Schoene, N. M. McLean, S. A. Bowring, R. R. Parrish, Metrology and traceability of U-Pb isotope dilution geochronology (EARTHTIME Tracer Calibration Part I). *Geochim. Cosmochim. Acta* **164**, 464–480 (2015).

42. N. M. McLean, J. F. Bowring, S. A. Bowring, An algorithm for U-Pb isotope dilution data reduction and uncertainty propagation. *Geochem. Geophys. Geosyst*. **12**, Q0AA18(2011).

43. M. Tatsumoto, R. J. Knight, C. J. Allegre, Time differences in the formation of meteorites as determined from the ratio of lead-207 to lead-206. *Science* **180**, 1279–1283 (1973).

44. J. Blichert-Toft, B. Zanda, D. S. Ebel, F. Albaràde, The Solar System primordial lead. *Earth Planet. Sci. Lett.* **300**, 152–163 (2010).

45. J. Castillo-Rogez, T. V. Johnson, M. H. Lee, N. J. Turner, D. L. Matson, J. Lunine, ^{26}Al decay: Heat production and a revised age for Iapetus. *Icarus* **204**, 658–662 (2009).

46. K. Lodders, B. Fegley, in *Planetary Scientist's Companion* (Oxford Univ. Press, 1998), pp. 290–331.

47. D. T. Britt, S. J. G. J. Consolmagno, Stony meteorite porosities and densities: A review of the data through 2001. *Meteorit. Planet. Sci.* **38**, 1161–1180 (2003).

48. T. L. Dunn, G. Cressey, H. Y. McSween, T. J. McCoy, Analysis of ordinary chondrites using powder X-ray diffraction: 1. Modal mineral abundances. *Meteorit. Planet. Sci.* **45**, 123–134 (2010).

49. K. Yomogida, T. Matsui, Physical properties of ordinary chondrites. *J. Geophys. Res.* **88**, 9513–9533 (1983).

50. C. P. Opeil, G. J. Consolmagno, D. J. Safarik, D. T. Britt, Stony meteorite thermal properties and their relationship with meteorite chemical and physical states. *Meteorit. Planet. Sci.* **47**, 319–329 (2012).

51. V. Slater-Reynolds, H. Y. McSween Jr, Peak metamorphic temperatures in type 6 ordinary chondrites: An evaluation of pyroxene and plagioclase geothermometry. *Meteorit. Planet. Sci.* **40**, 745–754 (2005).

52. N. T. Kita, H. Nagahara, S. Togashi, Y. Morishita, A short duration of chondrule formation in the solar nebula: Evidence from ^{26}Al in Semarkona ferromagnesian chondrules. *Geochim. Cosmochim. Acta* **64**, 3913–3922 (2000).

53. N. G. Rudraswami, J. N. Goswami, B. Chattopadhyay, S. K. Sengupta, A. P. Thapliyal, ^{26}Al records in chondrules from unequilibrated ordinary chondrites: II. Duration of chondrule formation and parent body thermal metamorphism. *Earth Planet. Sci. Lett.* **274**, 93–102 (2008).

54. I. D. Hutcheon, R. Hutchison, Evidence from the Semarkona ordinary chondrite for ^{26}Al heating of small planets. *Nature* **337**, 238–241 (1989).

55. G. J. MacPherson, G. R. Huss, Petrogenesis of Al-rich chondrules: Evidence from bulk compositions and phase equilibria. *Geochim. Cosmochim. Acta* **69**, 3099–3127 (2005).

56. P. Vermeesch, On the visualisation of detrital age distributions. *Chem. Geol.* **312**–**313**, 190–194 (2012).

57. P. Vermeesch, IsoplotR: A free and open toolbox for geochronology. *Geosci. Front.* **9**, 1479–1493 (2018).

58. C. Y. Ho, M. W. Ackerman, K. Y. Wu, S. G. Oh, T. N. Havill, Thermal conductivity of ten selected binary alloy systems. *J. Phys. Chem. Ref. Data Monogr.* **7**, 959–1178 (1978).

59. A. H. Jaffey, K. F. Flynn, L. E. Glendenin, W. C. Bentley, A. M. Essling, Precision measurement of half-lives and specific activities of ^{235}U and ^{238}U. *Phys. Rev. C* **4**, 1889–1906 (1971).

60. J. Hiess, D. J. Condon, N. McLean, S. R. Noble, ^{238}U/^{235}U systematics in terrestrial uranium-bearing minerals. *Science* **335**, 1610–1614 (2012).

Appendix C

Appendix to "Uranium-series isotopes as tracers of physical and chemical weathering in glacial sediments from Taylor Valley, Antarctica"

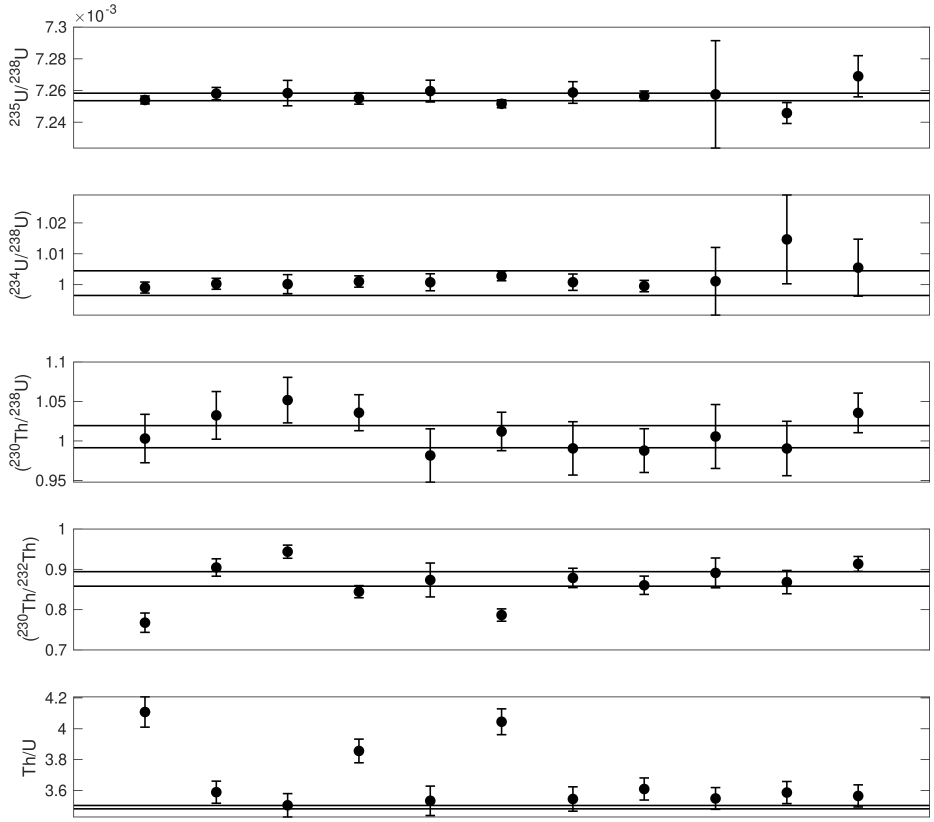

Figure C.1: Measured U-Th isotope compositions of USGS rock standard BCR-2, compared to published values (range demarcated with black lines; Koornneef et al., 2010). ^{230}Th-^{234}U-^{238}U data consistently fall within the range of published compositions. All uncertainties are 2σ standard error.

Appendix D

Appendix to “Subglacial melting beneath the northern Laurentide Ice Sheet coincided with Heinrich events: terrestrial support for an ocean warming stimulus”

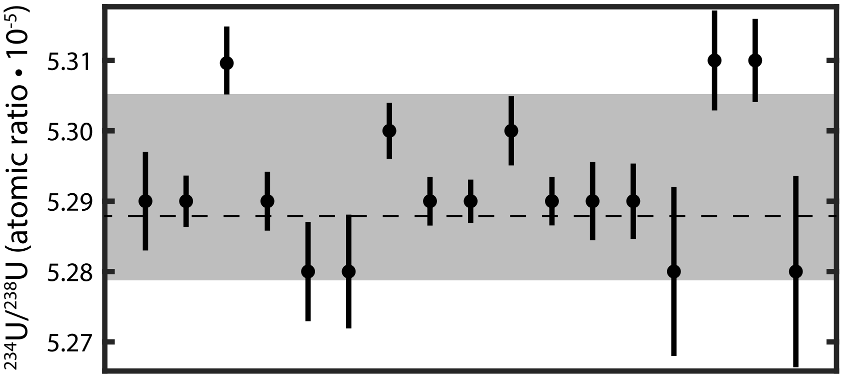

Figure D.1: Measurements of standard reference material (SRM) 4321b collected over the course of this study confirm U isotope reproducibility. Gray bar represents the 1 standard deviation (~0.25 %) envelope about the long-term laboratory mean ($^{234}U/^{238}U = 5.29195 \cdot 10^{-5}$, n=72), which overlaps the reported mean of SRM 4321b mean of Neymark and Paces (2006, dashed line, $^{234}U/^{238}U = 5.2879 \cdot 10^{-5}$, n=135).

References

Alley, R.B., MacAyeal, D.R., 1994. Ice-rafted debris associated with binge/purge oscillations of the Laurentide Ice Sheet. Paleoceanography 9, 503–511. doi:`10.1029/94PA01008`.

Anbeek, C., Van Breemen, N., Meijer, E.L., Van Der Plas, L., 1994. The dissolution of naturally weathered feldspar and quartz. Geochimica et Cosmochimica Acta 58, 4601–4613. doi:`10.1016/0016-7037(94)90194-5`.

Andersen, M.B., Erel, Y., Bourdon, B., 2009. Experimental evidence for ^{234}U-^{238}U fractionation during granite weathering with implications for ^{234}U/^{238}U in natural waters. Geochimica et Cosmochimica Acta doi:`10.1016/j.gca.2009.04.020`.

Andrews, J.T., Ives, J.D., Guennel, G.K., Wray, J.L., 1972. An Early Tertiary outcrop in North-Central Baffin Island, Northwest Territories, Canada: Environment and significance. Canadian Journal of Earth Sciences 9, 233–238. doi:`10.1139/e72-019`.

Arendt, C.A., Aciego, S.M., Sims, K.W., Das, S.B., Sheik, C., Stevenson, E.I., 2018. Influence of glacial meltwater on global seawater δ^{234}U. Geochimica et Cosmochimica Acta 225, 102–115. doi:`10.1016/j.gca.2018.01.007`.

Badgeley, J.A., Pettit, E.C., Carr, C.G., Tulaczyk, S., Mikucki, J.A., Lyons, W.B., 2017. An englacial hydrologic system of brine within a cold glacier: Blood Falls, McMurdo Dry Valleys, Antarctica. Journal of Glaciology 63, 387–400. doi:`10.1017/jog.2017.16`.

Barboni, M., Boehnke, P., Keller, B., Kohl, I.E., Schoene, B., Young, E.D., McKeegan, K.D., 2017. Early formation of the Moon 4.51 billion years ago. Science Advances 3, e1602365. doi:`10.1126/sciadv.1602365`.

Bassis, J.N., Petersen, S.V., Mac Cathles, L., 2017. Heinrich events triggered by ocean forcing and modulated by isostatic adjustment. Nature 542, 332–334. doi:`10.1038/nature21069`.

Batchelor, C.J., Orland, I.J., Marcott, S.A., Slaughter, R., Edwards, R.L., Zhang, P., Li, X., Cheng, H., 2019a. Distinct permafrost conditions across the last two glacial periods in midlatitude North America. Geophysical Research Letters 46, 13318–13326. doi:`10.1029/2019GL083951`.

Batchelor, C.L., Margold, M., Krapp, M., Murton, D.K., Dalton, A.S., Gibbard, P.L., Stokes, C.R., Murton, J.B., Manica, A., 2019b. The configuration of Northern Hemisphere ice sheets through the Quaternary. Nature Communications 10, 3713. doi:`10.1038/s41467-019-11601-2`.

Bateman, H., 1910. Solution of a system of differential equations occurring in the theory of radioactive transformations. Proceedings of the Cambridge Philosophical Society 15, 423–427.

Becquerel, H., 1896. Sur diverses propriétés des rayons uraniques. Comptes rendus hebdomadaires des séances de l'Académie des sciences 123, 855–858.

Biller-Celander, N., Shakun, J.D., McGee, D., Wong, C.I., Reyes, A.V., Hardt, B., Tal, I., Ford, D.C., Lauriol, B., 2021. Increasing Pleistocene permafrost persistence and carbon cycle conundrums inferred from Canadian speleothems. Science Advances 7, eabe5799. doi:`10.1126/sciadv.abe5799`.

Blackburn, T., Edwards, G.H., Tulaczyk, S., Scudder, M., Piccione, G., Hallet, B., McLean, N., Zachos, J.C., Cheney, B., Babbe, J.T., 2020. Ice retreat in Wilkes Basin of East Antarctica during a warm interglacial. Nature 583, 554–559. doi:`10.1038/s41586-020-2484-5`.

Blackburn, T., Siman-Tov, S., Coble, M.A., Stock, G.M., Brodsky, E.E., Hallet, B., 2019. Composition and formation age of amorphous silica coating glacially polished surfaces. Geology 47, 347–350. doi:`10.1130/G45737.1`.

Bockheim, J.G., 1997. Properties and classification of cold desert soils from Antarctica. Soil Science Society of America Journal 61, 224–231. doi:`10.2136/sssaj1997.03615995006100010031x`.

Bockheim, J.G., 2002. Landform and soil development in the McMurdo Dry Valleys, Antarctica: A regional synthesis. Arctic, Antarctic, and Alpine Research 34, 308–317.

Bockheim, J.G., Prentice, M.L., McLeod, M., 2008. Distribution of glacial deposits, soils, and permafrost in Taylor Valley, Antarctica. Arctic, Antarctic, and Alpine Research 40, 279–286. doi:`10.1657/1523-0430(06-057)`.

Bottomley, D., 1996. A Review of Theories on the Origins of Saline Waters and Brines in the Canadian Precambrian Shield. Technical Report 17. Atomic Energy Control Board. Ottawa, Canada.

Boulton, G.S., Slot, T., Blessing, K., Glasbergen, P., Leijnse, T., van Gijssel, K., 1993. Deep circulation of groundwater in overpressured subglacial aquifers and its geological consequences. Quaternary Science Reviews 12, 739–745. doi:`10.1016/0277-3791(93)90014-D`.

Brook, E.J., Brown, E.T., Kurz, M.D., Ackert, R.P., Raisbeck, G.M., Yiou, F., 1995. Constraints on age, erosion, and uplift of Neogene glacial deposits in the Transantarctic Mountains determined from in situ cosmogenic ^{10}Be and ^{26}Al. Geology 23, 1063. doi:`10.1130/0091-7613(1995)023<1063:COAEAU>2.3.CO;2`.

Brook, E.J., Kurz, M.D., Ackert, R.P., Denton, G.H., Brown, E.T., Raisbeck, G.M., Yiou, F., 1993. Chronology of Taylor Glacier advances in Arena Valley, Antarctica, using in situ cosmogenic ^{3}He and ^{10}Be. Quaternary Research 39, 11–23. doi:`10.1006/QRES.1993.1002`.

Brouard, E., Lajeunesse, P., 2017. Maximum extent and decay of the Laurentide Ice Sheet in Western Baffin Bay during the Last glacial episode. Scientific Reports 7, 10711. doi:`10.1038/s41598-017-11010-9`.

Burgess, S.D., Muirhead, J.D., Bowring, S.A., 2017. Initial pulse of Siberian Traps sills as the trigger of the end-Permian mass extinction. Nature Communications 8, 164. doi:`10.1038/s41467-017-00083-9`.

Campbell, I.B., Claridge, G.G.C., 1981. Soil research in the Ross Sea region of Antarctica. Journal of the Royal Society of New Zealand 11, 401–410. doi:`10.1080/03036758.1981.10423330`.

Cartwright, J., 1962. Particle shape factors. The Annals of Occupational Hygiene 5, 163–171. doi:`10.1093/annhyg/5.3.163`.

Chabaux, F., Blaes, E., Stille, P., di Chiara Roupert, R., Pelt, E., Dosseto, A., Ma, L., Buss, H.L., Brantley, S.L., 2013. Regolith formation rate from U-series nuclides: Implications from the study of a spheroidal weathering profile in the Rio Icacos watershed (Puerto Rico). Geochimica et Cosmochimica Acta 100, 73–95. doi:`10.1016/j.gca.2012.09.037`.

Chabaux, F., Riotte, J., Dequincey, O., 2003. U-Th-Ra fractionation during weathering and river transport. Reviews in Mineralogy and Geochemistry 52, 533–576. doi:`10.2113/0520533`.

Chen, J.H., Lawrence Edwards, R., Wasserburg, G.J., 1986. ^{238}U, ^{234}U and ^{232}Th in seawater. Earth and Planetary Science Letters 80, 241–251. doi:`10.1016/0012-821X(86)90108-1`.

Chen, T., Robinson, L.F., Beasley, M.P., Claxton, L.M., Andersen, M.B., Gregoire, L.J., Wadham, J., Fornari, D.J., Harpp, K.S., 2016. Ocean mixing and ice-sheet control of seawater ^{234}U/^{238}U during the last deglaciation. Science 354, 626–629. doi:`10.1126/science.aag1015`.

Cheng, H., Lawrence Edwards, R., Shen, C.C., Polyak, V.J., Asmerom, Y., Woodhead, J., Hellstrom, J., Wang, Y., Kong, X., Spötl, C., Wang, X., Calvin Alexander, E., 2013. Improvements in ^{230}Th dating, ^{230}Th and ^{234}U half-life values, and U-Th isotopic measurements by multi-collector inductively coupled plasma mass spectrometry. Earth and Planetary Science Letters 371-372, 82–91. doi:`10.1016/j.epsl.2013.04.006`.

Chutcharavan, P.M., Dutton, A., 2021. A global compilation of U-series-dated fossil coral sea-level indicators for the Last Interglacial period (Marine Isotope Stage 5e). Earth System Science Data 13, 3155–3178. doi:`10.5194/essd-13-3155-2021`.

Clark, I.D., Douglas, M., Raven, K., Bottomley, D., 2000. Recharge and preservation of Laurentide glacial melt water in the Canadian shield. Ground Water 38, 735–742. doi:`10.1111/j.1745-6584.2000.tb02709.x`.

Clarke, G.K.C., Nitsan, U., Paterson, W.S.B., 1977. Strain heating and creep instability in glaciers and ice sheets. Reviews of Geophysics 15, 235–247. doi:`10.1029/RG015i002p00235`.

Cogez, A., Herman, F., Pelt, É., Reuschlé, T., Morvan, G., Darvill, C.M., Norton, K.P., Christl, M., Märki, L., Chabaux, F., 2018. U–Th and ^{10} Be constraints on sediment recycling in proglacial settings, Lago Buenos Aires, Patagonia. Earth Surface Dynamics 6, 121–140. doi:`10.5194/esurf-6-121-2018`.

Cuffey, K.M., Conway, H., Gades, A.M., Hallet, B., Lorrain, R., Severinghaus, J.P., Steig, E.J., Vaughn, B., White, J.W., 2000. Entrainment at cold glacier beds. Geology 28, 351–354. doi:`10.1130/0091-7613(2000)028<0351:EACGB>2.3.CO;2`.

Dalton, A.S., Finkelstein, S.A., Forman, S.L., Barnett, P.J., Pico, T., Mitrovica, J.X., 2019. Was the Laurentide Ice Sheet significantly reduced during Marine Isotope Stage 3? Geology 47, 111–114. doi:`10.1130/G45335.1`.

Denton, G.H., Anderson, R.F., Toggweiler, J.R., Edwards, R.L., Schaefer, J.M., Putnam, A.E., 2010. The last glacial termination. Science 328, 1652–1656. doi:`10.1126/science.1184119`.

Denton, G.H., Armstrong, R.L., Stuiver, M., 1970. Late Cenozoic glaciation in Antarctica: The record in the McMurdo Sound region. Antarctic Journal of the United States 5, 15–21.

Denton, G.H., Bockheim, J.G., Wilson, S.C., Stuiver, M., 1989. Late Wisconsin and early Holocene glacial history, inner Ross Embayment, Antarctica. Quaternary Research 31, 151–182. doi:`10.1016/0033-5894(89)90004-5`.

Denton, G.H., Sugden, D.E., Marchant, D.R., Hall, B.L., Wilch, T.I., 1993. East Antarctic Ice Sheet sensitivity to Pliocene climatic change from a Dry Valleys perspective. Geografiska Annaler. Series A, Physical Geography 75, 155. doi:`10.2307/521200`.

DePaolo, D.J., Maher, K., Christensen, J.N., McManus, J., 2006. Sediment transport time measured with U-series isotopes: Results from ODP North Atlantic drift site 984. Earth and Planetary Science Letters 248, 379–395. doi:`10.1016/j.epsl.2006.06.004`.

Diaz, M.A., Adams, B.J., Welch, K.A., Welch, S.A., Opiyo, S.O., Khan, A.L., McKnight, D.M., Cary, S.C., Lyons, W.B., 2018. Aeolian material transport and its role in landscape connectivity in the McMurdo Dry Valleys, Antarctica. Journal of Geophysical Research: Earth Surface 123, 3323–3337. doi:`10.1029/2017JF004589`.

Doran, P.T., McKay, C.P., Clow, G.D., Dana, G.L., Fountain, A.G., Nylen, T., Lyons, W.B., 2002. Valley floor climate observations from the McMurdo dry valleys, Antarctica, 1986-2000. Journal of Geophysical Research Atmospheres 107, 4772. doi:`10.1029/2001JD002045`.

Dosseto, A., Buss, H.L., Suresh, P.O., 2012. Rapid regolith formation over volcanic bedrock and implications for landscape evolution. Earth and Planetary Science Letters 337-338, 47–55. doi:`10.1016/j.epsl.2012.05.008`.

Dosseto, A., Schaller, M., 2016. The erosion response to Quaternary climate change quantified using uranium isotopes and in situ-produced cosmogenic nuclides. Earth-Science Reviews 155, 60–81. doi:`10.1016/j.earscirev.2016.01.015`.

Dunk, R.M., Mills, R.A., Jenkins, W.J., 2002. A reevaluation of the oceanic uranium budget for the Holocene. Chemical Geology 190, 45–67. doi:`10.1016/S0009-2541(02)00110-9`.

Dyke, A.S., Andrews, J.T., Clark, P.U., England, J.H., Miller, G.H., Shaw, J., Veillette, J.J., 2002. The Laurentide and Innuitian ice sheets during the Last Glacial Maximum. Quaternary Science Reviews 21, 9–31. doi:`10.1016/S0277-3791(01)00095-6`.

EPICA Community Members, 2006. One-to-one coupling of glacial climate variability in Greenland and Antarctica. Nature 444, 195–198. doi:`10.1038/nature05301`.

Esat, T.M., Yokoyama, Y., 2006. Variability in the uranium isotopic composition of the oceans over glacial-interglacial timescales. Geochimica et Cosmochimica Acta 70, 4140–4150. doi:`10.1016/j.gca.2006.06.013`.

Ewing, S.A., Paces, J.B., O'Donnell, J.A., Jorgenson, M.T., Kanevskiy, M.Z., Aiken, G.R., Shur, Y., Harden, J.W., Striegl, R., 2015. Uranium isotopes and dissolved organic carbon in loess permafrost: Modeling the age of ancient ice. Geochimica et Cosmochimica Acta 152, 143–165. doi:`10.1016/j.gca.2014.11.008`.

Fitzpatrick, J.J., Muhs, D.R., Jull, A.J.T., 1990. Saline minerals in the Lewis Cliff ice tongue, Buckley Island Quadrangle, Antarctica, in: Contributions to Antarctic Research I. American Geophysical Union. volume 50 of *Antarctic Research Series*, pp. 57–69. doi:`10.1029/ar050p0057`.

Fountain, A.G., Nylen, T.H., MacClune, K.L., Dana, G.L., 2006. Glacier mass balances (1993-2001), Taylor Valley, McMurdo Dry Valleys, Antarctica. Journal of Glaciology 52, 451–462. doi:`10.3189/172756506781828511`.

Frape, S., Fritz, P., McNutt, R., 1984. Water-rock interaction and chemistry of groundwaters from the Canadian Shield. Geochimica et Cosmochimica Acta 48, 1617–1627. doi:`10.1016/0016-7037(84)90331-4`.

Frape, S.K., Fritz, P., 1982. The chemistry and isotopic composition of saline groundwaters from the Sudbury Basin, Ontario. Canadian Journal of Earth Sciences 19, 645–661. doi:`10.1139/e82-053`.

Gascoyne, M., 1989. High levels of uranium and radium in groundwaters at Canada's Underground Research Laboratory, Lac du Bonnet, Manitoba, Canada. Applied Geochemistry 4, 577–591. doi:`10.1016/0883-2927(89)90068-1`.

Gibson, E.K., Wentworth, S.J., McKay, D.S., 1983. Chemical weathering and diagenesis of a cold desert soil from Wright Valley, Antarctica: An analog of Martian weathering processes. Journal of Geophysical Research 88, A912–A928. doi:`10.1029/jb088is02p0a912`.

Goldberg, K., Humayun, M., 2010. The applicability of the Chemical Index of Alteration as a paleoclimatic indicator: An example from the Permian of the Paraná Basin, Brazil. Palaeogeography, Palaeoclimatology, Palaeoecology 293, 175–183. doi:`10.1016/j.palaeo.2010.05.015`.

Gowan, E.J., Zhang, X., Khosravi, S., Rovere, A., Stocchi, P., Hughes, A.L.C., Gyllencreutz, R., Mangerud, J., Svendsen, J.I., Lohmann, G., 2021. A new global ice sheet reconstruction for the past 80 000 years. Nature Communications 12, 1199. doi:`10.1038/s41467-021-21469-w`.

Graly, J.A., Humphrey, N.F., Harper, J.T., 2016. Chemical depletion of sediment under the Greenland Ice Sheet. Earth Surface Processes and Landforms 41, 1922–1936. doi:`10.1002/esp.3960`.

Graly, J.A., Licht, K.J., Bader, N.A., Bish, D.L., 2020. Chemical weathering signatures from Mt. Achernar Moraine, Central Transantarctic Mountains I: Subglacial sediments compared with underlying rock. Geochimica et Cosmochimica Acta doi:`10.1016/j.gca.2020.06.005`.

Haldorsen, S., 1981. Grain-size distribution of subglacial till and its realtion to glacial crushing and abrasion. Boreas 10, 91–105. doi:`10.1111/j.1502-3885.1981.tb00472.x`.

Hall, B.L., Denton, G.H., Hendy, C.H., 2000. Evidence from Taylor Valley for a grounded ice sheet in the Ross Sea, Antarctica. Geografiska Annaler, Series A: Physical Geography 82, 275–303. doi:`10.1111/j.0435-3676.2000.00126.x`.

Hallet, B., 1976. Deposits formed by subglacial precipitation of $CaCO_3$. GSA Bulletin 87, 1003–1015. doi:`10.1130/0016-7606(1976)87<1003:DFBSPO>2.0.CO;2`.

Hallet, B., Hunter, L., Bogen, J., 1996. Rates of erosion and sediment evacuation by glaciers: A review of field data and their implications. Global and Planetary Change 12, 213–235. doi:`10.1016/0921-8181(95)00021-6`.

Hamelin, B., Bard, E., Zindler, A., Fairbanks, R.G., 1991. $^{234}U/^{238}U$ mass spectrometry of corals: How accurate is the U-Th age of the last interglacial period? Earth and Planetary Science Letters 106, 169–180. doi:`10.1016/0012-821X(91)90070-X`.

Handley, H.K., Turner, S., Afonso, J.C., Dosseto, A., Cohen, T., 2013. Sediment residence times constrained by uranium-series isotopes: A critical appraisal of the comminution approach. Geochimica et Cosmochimica Acta 103, 245–262. doi:`10.1016/j.gca.2012.10.047`.

Heinrich, H., 1988. Origin and consequences of cyclic ice rafting in the Northeast Atlantic Ocean during the past 130,000 years. Quaternary Research 29, 142–152. doi:`10.1016/0033-5894(88)90057-9`.

Hemming, S.R., 2004. Heinrich events: Massive late Pleistocene detritus layers of the North Atlantic and their global climate imprint. Reviews of Geophysics 42, RG1005. doi:`10.1029/2003RG000128`.

Henderson, G.M., Hall, B.L., Smith, A., Robinson, L.F., 2006. Control on $(^{234}U/^{238}U)$ in lake water: A study in the Dry Valleys of Antarctica. Chemical Geology 226, 298–308. doi:`10.1016/j.chemgeo.2005.09.026`.

Hendy, C.H., Healy, T.R., Rayner, E.M., Shaw, J., Wilson, A.T., 1979. Late Pleistocene glacial chronology of the Taylor Valley, Antarctica, and the global climate. Quaternary Research 11, 172–184. doi:`10.1016/0033-5894(79)90002-4`.

Higgins, S.M., Hendy, C.H., Denton, G.H., 2000. Geochronology of Bonney Drift, Taylor Valley, Antarctica: Evidence for interglacial expansions of Taylor Glacier. Geografiska Annaler. Series A, Physical Geography 82, 391–409. doi:`10.1111/j.0435-3676.2000.00130.x`.

Hillaire-Marcel, C., Bilodeau, G., 2000. Instabilities in the Labrador Sea water mass structure during the last climatic cycle. Canadian Journal of Earth Sciences doi:`10.1139/e99-108`.

Hodell, D.A., Nicholl, J.A., Bontognali, T.R.R., Danino, S., Dorador, J., Dowdeswell, J.A., Einsle, J., Kuhlmann, H., Martrat, B., Mleneck-Vautravers, M.J., Rodríguez-Tovar, F.J., Röhl, U., 2017. Anatomy of Heinrich Layer 1 and its role in the last deglaciation. Paleoceanography 32, 284–303. doi:`10.1002/2016PA003028`.

Hoff, U., Rasmussen, T.L., Stein, R., Ezat, M.M., Fahl, K., 2016. Sea ice and millennial-scale climate variability in the Nordic seas 90 kyr ago to present. Nature Communications 7, 12247. doi:`10.1038/ncomms12247`.

Holen, S.R., Deméré, T.A., Fisher, D.C., Fullagar, R., Paces, J.B., Jefferson, G.T., Beeton, J.M., Cerutti, R.A., Rountrey, A.N., Vescera, L., Holen, K.A., 2017. A 130,000-year-old archaeological site in southern California, USA. Nature 544, 479–483. doi:`10.1038/nature22065`.

Holmes, A., 1911. The Association of Lead with Uranium in Rock-Minerals, and Its Application to the Measurement of Geological Time. Proceedings of the Royal Society A: Mathematical, Physical and Engineering Sciences 85, 248–256. doi:`10.1098/rspa.1911.0036`.

Hubbard, A., Lawson, W., Anderson, B., Hubbard, B., Blatter, H., 2004. Evidence for subglacial ponding across Taylor Glacier, Dry Valleys, Antarctica. Annals of Glaciology 39, 79–84. doi:`10.3189/172756404781813970`.

Jochum, K.P., Nohl, U., Herwig, K., Lammel, E., Stoll, B., Hofmann, A.W., 2005. GeoReM: A new geochemical database for reference materials and isotopic standards. Geostandards and Geoanalytical Research 29, 333–338. doi:`10.1111/j.1751-908X.2005.tb00904.x`.

Kigoshi, K., 1971. Alpha-recoil Thorium-234 : Dissolution into water and the uranium-234 / uranium-238 disequilibrium in nature. Science 173, 47–48.

Koornneef, J.M., Stracke, A., Aciego, S., Reubi, O., Bourdon, B., 2010. A new method for U-Th-Pa-Ra separation and accurate measurement of ^{234}U-^{230}Th-^{231}Pa-^{226}Ra disequilibria in volcanic rocks by MC-ICPMS. Chemical Geology 277, 30–41. doi:`10.1016/j.chemgeo.2010.07.007`.

Kraemer, T.F., Brabets, T.P., 2012. Uranium isotopes (^{234}U/ ^{238}U) in rivers of the Yukon Basin (Alaska and Canada) as an aid in identifying water sources, with implications for monitoring hydrologic change in arctic regions. Hydrogeology Journal 20, 469–481. doi:`10.1007/s10040-012-0829-3`.

Ku, T.L., 1965. An evaluation of the U ^{234} /U ^{238} method as a tool for dating pelagic sediments. Journal of Geophysical Research 70, 3457–3474. doi:`10.1029/JZ070i014p03457`.

Lacelle, D., Lauriol, B., Clark, I.D., 2011. Origin, age, and paleoenvironmental significance of carbonate precipitates from a granitic environment, Akshayuk Pass, southern Baffin Island, Canada. Canadian Journal of Earth Sciences 44, 61–79. doi:`10.1139/e06-088`.

Lacelle, D., Lauriol, B., Zazula, G., Ghaleb, B., Utting, N., Clark, I.D., 2013. Timing of advance and basal condition of the Laurentide Ice Sheet during the last glacial maximum in the Richardson Mountains, NWT. Quaternary Research 80, 274–283. doi:`10.1016/j.yqres.2013.06.001`.

Lauritzen, S.E., Mylroie, J.E., 2000. Results of a speleothem U/Th dating reconnaissance from the Helderberg Plateau, New York. Journal of Cave and Karst Studies 62, 20–26.

Lee, V.E., DePaolo, D.J., Christensen, J.N., 2010. Uranium-series comminution ages of continental sediments: Case study of a Pleistocene alluvial fan. Earth and Planetary Science Letters 296, 244–254. doi:`10.1016/j.epsl.2010.05.005`.

Lemieux, J.M., Sudicky, E.A., 2010. Simulation of groundwater age evolution during the Wisconsinian glaciation over the Canadian landscape. Environmental Fluid Mechanics 10, 91–102. doi:`10.1007/s10652-009-9142-7`.

Lemieux, J.M., Sudicky, E.A., Peltier, W.R., Tarasov, L., 2008. Dynamics of groundwater recharge and seepage over the Canadian landscape during the Wisconsinian glaciation. Journal of Geophysical Research: Earth Surface 113, F01011. doi:`10.1029/2007JF000838`.

Ludwig, K.R., Titterington, D.M., 1994. Calculation of ^{230}Th/U isochrons, ages, and errors. Geochimica et Cosmochimica Acta 58, 5031–5042. doi:`10.1016/0016-7037(94)90229-1`.

Lynch-Stieglitz, J., Schmidt, M.W., Gene Henry, L., Curry, W.B., Skinner, L.C., Mulitza, S., Zhang, R., Chang, P., 2014. Muted change in Atlantic overturning circulation over some glacial-aged Heinrich events. Nature Geoscience 7, 144–150. doi:`10.1038/ngeo2045`.

Lyons, W.B., Leslie, D.L., Gooseff, M.N., 2021. Chemical Weathering in the McMurdo Dry Valleys, Antarctica, in: Hydrogeology, Chemical Weathering, and Soil Formation. American Geophysical Union (AGU). chapter 11, pp. 205–216. doi:`10.1002/9781119563952.ch11`.

Lyons, W.B., Welch, K.A., Neumann, K., Toxey, J.K., McArthur, R., Williams, C., McKnight, D.M., Moorhead, D.L., 1998. Geochemical linkages among glaciers, streams and lakes within the Taylor Valley, Antarctica. Ecosystem dynamics in a polar desert; the McMurdo dry valleys, Antarctica 72, 77–92. doi:`10.1029/AR072p0077`.

Ma, J., Wei, G., Liu, Y., Ren, Z., Xu, Y., Yang, Y., 2013. Precise measurement of stable ($\delta^{88/86}$Sr) and radiogenic (^{87}Sr/^{86}Sr) strontium isotope ratios in geological standard reference materials using MC-ICP-MS. Chinese Science Bulletin 58, 3111–3118. doi:`10.1007/s11434-013-5803-5`.

MacAyeal, D.R., 1993. Binge/purge oscillations of the Laurentide Ice Sheet as a cause of the North Atlantic's Heinrich events. Paleoceanography 8, 775–784. doi:`10.1029/93PA02200`.

Mager, S., Fitzsimons, S., Frew, R., 2007. Stable isotope composition of the basal ice from Taylor Glacier, Southern Victoria Land, Antarctica, in: 10th International Symposium on Antarctic Earth Sciences, pp. 1–4.

Marcott, S.A., Clark, P.U., Padman, L., Klinkhammer, G.P., Springer, S.R., Liu, Z., Otto-Bliesner, B.L., Carlson, A.E., Ungerer, A., Padman, J., He, F., Cheng, J., Schmittner, A., 2011. Ice-shelf collapse from subsurface warming as a trigger for Heinrich events. Proceedings of the National Academy of Sciences 108, 13415–13419. doi:`10.1073/pnas.1104772108`.

Margold, M., Stokes, C.R., Clark, C.D., 2015a. Ice streams in the Laurentide Ice Sheet: Identification, characteristics and comparison to modern ice sheets. Earth-Science Reviews 143, 117–146. doi:`10.1016/j.earscirev.2015.01.011`.

Margold, M., Stokes, C.R., Clark, C.D., Kleman, J., 2015b. Ice streams in the Laurentide Ice Sheet: A new mapping inventory. Journal of Maps 11, 380–395. doi:`10.1080/17445647.2014.912036`.

Marra, K.R., Elwood Madden, M.E., Soreghan, G.S., Hall, B.L., 2017. Chemical weathering trends in fine-grained ephemeral stream sediments of the McMurdo Dry Valleys, Antarctica. Geomorphology 281, 13–30. doi:`10.1016/j.geomorph.2016.12.016`.

Marshall, S.J., Clark, P.U., 2002. Basal temperature evolution of North American ice sheets and implications for the 100-kyr cycle. Geophysical Research Letters 29, 67–1–67–4. doi:`10.1029/2002GL015192`.

Martin, A.N., Dosseto, A., Kinsley, L.P., 2015. Evaluating the removal of non-detrital matter from soils and sediment using uranium isotopes. Chemical Geology 396, 124–133. doi:`10.1016/j.chemgeo.2014.12.016`.

Matsuoka, K., Skoglund, A., Roth, G., de Pomereu, J., Griffiths, H., Headland, R., Herried, B., Katsumata, K., Le Brocq, A., Licht, K., Morgan, F., Neff, P.D., Ritz, C., Scheinert, M., Tamura, T., Van de Putte, A., van den Broeke, M., von Deschwanden, A., Deschamps-Berger, C., Van Liefferinge, B., Tronstad, S., Melvær, Y., 2021. Quantarctica, an integrated mapping environment for Antarctica, the Southern Ocean, and sub-Antarctic islands. Environmental Modelling & Software 140, 105015. doi:`10.1016/j.envsoft.2021.105015`.

McNutt, R.H., Frape, S.K., Fritz, P., Jones, M.G., MacDonald, I.M., 1990. The ^{87}Sr/^{86}Sr values of Canadian Shield brines and fracture minerals with applications to groundwater mixing, fracture history, and geochronology. Geochimica et Cosmochimica Acta 54, 205–215. doi:`10.1016/0016-7037(90)90208-3`.

Méjean, P., Pinti, D.L., Ghaleb, B., Larocque, M., 2017. Fracturing-induced release of radiogenic ^{4}He and ^{234}U into groundwater during the last deglaciation: An alternative source to crustal helium fluxes in periglacial aquifers. Water Resources Research 53, 5677–5689. doi:`10.1002/2016WR020014`.

Méjean, P., Pinti, D.L., Larocque, M., Ghaleb, B., Meyzonnat, G., Gagné, S., 2016. Processes controlling ^{234}U and ^{238}U isotope fractionation and helium in the groundwater of the St. Lawrence Lowlands, Quebec: The potential role of natural rock fracturing. Applied Geochemistry 66, 198–209. doi:`10.1016/J.APGEOCHEM.2015.12.015`.

Menozzi, D., Dosseto, A., Kinsley, L.P., 2016. Assessing the effect of sequential extraction on the uranium-series isotopic composition of a basaltic weathering profile. Chemical Geology 446, 126–137. doi:`10.1016/j.chemgeo.2016.05.031`.

Menviel, L.C., Skinner, L.C., Tarasov, L., Tzedakis, P.C., 2020. An ice–climate oscillatory framework for Dansgaard–Oeschger cycles. Nature Reviews Earth & Environment 1, 677–693. doi:`10.1038/s43017-020-00106-y`.

Mikucki, J.A., Auken, E., Tulaczyk, S., Virginia, R.A., Schamper, C., Sørensen, K.I., Doran, P.T., Dugan, H., Foley, N., 2015. Deep groundwater and potential subsurface habitats beneath an Antarctic dry valley. Nature Communications 6, 6831. doi:`10.1038/ncomms7831`.

Mikucki, J.A., Pearson, A., Johnston, D.T., Turchyn, A.V., Farquhar, J., Anbar, A.D., Schrag, D.P., Priscu, J.C., Lee, P.A., 2009. A Contemporary Microbially Maintained Subglacial Ferrous "Ocean". Science 324, 397–400. doi:`10.1126/science.1167350`.

Mix, A.C., Ruddiman, W.F., 1984. Oxygen-isotope analyses and Pleistocene ice volumes. Quaternary Research 21, 1–20. doi:`10.1016/0033-5894(84)90085-1`.

Montross, S., Skidmore, M., Christner, B., Samyn, D., Tison, J.L., Lorrain, R., Doyle, S., Fitzsimons, S., 2014. Debris-rich basal ice as a microbial habitat. Geomicrobiology Journal 31, 76–81. doi:`10.1080/01490451.2013.811316`.

Montross, S.N., Skidmore, M., Tranter, M., Kivimäki, A.L., Parkes, R.J., 2013. A microbial driver of chemical weathering in glaciated systems. Geology 41, 215–218. doi:`10.1130/G33572.1`.

Murton, J.B., Peterson, R., Ozouf, J.C., 2006. Bedrock fracture by ice segregation in cold regions. Science 314, 1127–1129. doi:`10.1126/science.1132127`.

Nesbitt, H.W., Young, G.M., 1982. Early Proterozoic climates and plate motions inferred from major element chemistry of lutites. Nature 299, 715–717. doi:`10.1038/299715a0`.

Neymark, L.A., Paces, J.B., 2006. High-Precision Isotope Analysis of Uranium and Thorium by TIMS. AGU Fall Meeting Abstracts 11, V11E–04.

Noble, T.L., Rohling, E.J., Aitken, A.R.A., Bostock, H.C., Chase, Z., Gomez, N., Jong, L.M., King, M.A., Mackintosh, A.N., McCormack, F.S., McKay, R.M., Menviel, L., Phipps, S.J., Weber, M.E., Fogwill, C.J., Gayen, B., Golledge, N.R., Gwyther, D.E., Hogg, A.M., Martos, Y.M., Pena-Molino, B., Roberts, J., van de Flierdt, T., Williams, T., 2020. The sensitivity of the Antarctic Ice Sheet to a changing climate: Past, present, and future. Reviews of Geophysics 58, e2019RG000663. doi:`10.1029/2019RG000663`.

Nuttin, L., Hillaire-Marcel, C., 2015. U- and Th-series isotopes in deep Baffin Bay sediments: Tracers of detrital sources and of contrasted glacial/interglacial sedimentary processes. Marine Geology 361, 1–10. doi:`10.1016/j.margeo.2015.01.003`.

Osmond, J., May, J.P., Tanner, W.F., 1970. Age of the Cape Kennedy Barrier-and-Lagoon Complex. Journal of Geophysical Research 75, 469–479. doi:`10.1029/JB075I002P00469`.

Pendleton, S.L., Miller, G.H., Lifton, N., Lehman, S.J., Southon, J., Crump, S.E., Anderson, R.S., 2019. Rapidly receding Arctic Canada glaciers revealing landscapes continuously ice-covered for more than 40,000 years. Nature Communications 10, 445. doi:`10.1038/s41467-019-08307-w`.

Plater, A.J., Ivanovich, M., Dugdale, R.E., 1992. Uranium series disequilibrium in river sediments and waters: The significance of anomalous activity ratios. Applied Geochemistry 7, 101–110. doi:`10.1016/0883-2927(92)90029-3`.

Poulton, S.W., Canfield, D.E., 2005. Development of a sequential extraction procedure for iron: Implications for iron partitioning in continentally derived particulates. Chemical Geology 214, 209–221. doi:`10.1016/j.chemgeo.2004.09.003`.

Rasmussen, S.O., Bigler, M., Blockley, S.P., Blunier, T., Buchardt, S.L., Clausen, H.B., Cvijanovic, I., Dahl-Jensen, D., Johnsen, S.J., Fischer, H., Gkinis, V., Guillevic, M., Hoek, W.Z., Lowe, J.J., Pedro, J.B., Popp, T., Seierstad, I.K., Steffensen, J.P., Svensson, A.M., Vallelonga, P., Vinther, B.M., Walker, M.J.C., Wheatley, J.J., Winstrup, M., 2014. A stratigraphic framework for abrupt climatic changes during the Last Glacial period based on three synchronized Greenland ice-core records: Refining and extending the INTIMATE event stratigraphy. Quaternary Science Reviews 106, 14–28. doi:`10.1016/j.quascirev.2014.09.007`.

Refsnider, K.A., Miller, G.H., Fogel, M.L., Fréchette, B., Bowden, R., Andrews, J.T., Farmer, G.L., 2014. Subglacially precipitated carbonates record geochemical interactions and pollen preservation at the base of the Laurentide Ice Sheet on central Baffin Island, eastern Canadian Arctic. Quaternary Research 81, 94–105. doi:`10.1016/j.yqres.2013.10.014`.

Refsnider, K.A., Miller, G.H., Hillaire-Marcel, C., Fogel, M.L., Ghaleb, B., Bowden, R., 2012. Subglacial carbonates constrain basal conditions and oxygen isotopic composition of the Laurentide Ice Sheet over Arctic Canada. Geology 40, 135–138. doi:`10.1130/G32335.1`.

Ritz, C., 1987. Time dependent boundary conditions for calculating of temperature fields in ice sheets, in: The Physical Basis of Ice Sheet Modeling. International Association of Hydrological Sciences, Wallingford, UK, pp. 207–216.

Rosholt, J., 1976. ^{230}Th/^{234}U dating of travertine and caliche rinds. Abstracts with Programs–Geological Society of America 6, 1076.

Rubin, K.H., 2001. Analysis of ^{232}Th/^{230}Th in volcanic rocks: A comparison of thermal ionization mass spectrometry and other methodologies. Chemical Geology 175, 723–750. doi:`10.1016/S0009-2541(00)00340-5`.

Rutherford, E., 1906. Radioactive Transformations. Mrs. Hepsa Ely Silliman Memorial Lectures, C. Scribner's Sons, New York.

Schoene, B., 2013. U-Th-Pb Geochronology, in: Treatise on Geochemistry: Second Edition. Elsevier. volume 4, pp. 341–378. doi:`10.1016/B978-0-08-095975-7.00310-7`.

Seierstad, I.K., Abbott, P.M., Bigler, M., Blunier, T., Bourne, A.J., Brook, E., Buchardt, S.L., Buizert, C., Clausen, H.B., Cook, E., Dahl-Jensen, D., Davies, S.M., Guillevic, M., Johnsen, S.J., Pedersen, D.S., Popp, T.J., Rasmussen, S.O., Severinghaus, J.P., Svensson, A., Vinther, B.M., 2014. Consistently dated records from the Greenland GRIP, GISP2 and NGRIP ice cores for the past 104 ka reveal regional millennial-scale δ^{18}O gradients with possible Heinrich event imprint. Quaternary Science Reviews 106, 29–46. doi:`10.1016/j.quascirev.2014.10.032`.

Semkow, T.M., 1991. Fractal model of radon emanation from solids. Physical Review Letters 66, 3012–3015. doi:`10.1103/PhysRevLett.66.3012`.

Sharp, Z.D., 2017. Principles of Stable Isotope Geochemistry. Second ed. doi:`10.25844/h9q1-0p82`.

Shaw, S.E., 1962. Petrography of Beacon Sandstone samples from Beacon Height West, Upper Taylor Glacier, Antarctica. New Zealand Journal of Geology and Geophysics 5, 733–739. doi:`10.1080/00288306.1962.10417634`.

Simon, Q., St-Onge, G., Hillaire-Marcel, C., 2012. Late Quaternary chronostratigraphic framework of deep Baffin Bay glaciomarine sediments from high-resolution paleomagnetic data. Geochemistry, Geophysics, Geosystems 13. doi:`10.1029/2012GC004272`.

Soddy, F., 1913. Intra-atomic charge. Nature 92, 399–400. doi:`10.1038/092399c0`.

Stanford, J.D., Rohling, E.J., Bacon, S., Roberts, A.P., Grousset, F.E., Bolshaw, M., 2011. A new concept for the paleoceanographic evolution of Heinrich event 1 in the North Atlantic. Quaternary Science Reviews 30, 1047–1066. doi:`10.1016/j.quascirev.2011.02.003`.

Stern, T.A., Baxter, A.K., Barrett, P.J., 2005. Isostatic rebound due to glacial erosion within the Transantarctic Mountains. Geology 33, 221–224. doi:`10.1130/G21068.1`.

Stotler, R.L., Frape, S.K., Ruskeeniemi, T., Pitkänen, P., Blowes, D.W., 2012. The interglacial-glacial cycle and geochemical evolution of Canadian and Fennoscandian Shield groundwaters. Geochimica et Cosmochimica Acta 76, 45–67. doi:`10.1016/j.gca.2011.10.006`.

Strutt, R.J., 1908. On the accumulation of helium in geological time. Proceedings of the Royal Society of London. Series A, Containing Papers of a Mathematical and Physical Character 81, 272–277. doi:`10.1098/rspa.1908.0079`.

Sugden, D., Denton, G., 2004. Cenozoic landscape evolution of the Convoy Range to Mackay Glacier area, Transantartic Mountains: Onshore to offshore synthesis. Bulletin of the Geological Society of America 116, 840–857. doi:`10.1130/B25356.1`.

Sun, H., Semkow, T.M., 1998. Mobilization of thorium, radium and radon radionuclides in ground water by successive alpha-recoils. Journal of Hydrology 205, 126–136. doi:`10.1016/S0022-1694(97)00154-6`.

Suresh, P., Dosseto, A., Hesse, P., Handley, H., 2013. Soil formation rates determined from Uranium-series isotope disequilibria in soil profiles from the southeastern Australian highlands. Earth and Planetary Science Letters 379, 26–37. doi:`10.1016/j.epsl.2013.08.004`.

Tanaka, R., Yokoyama, T., Kitagawa, H., Tesfaye, D.B., Nakamura, E., 2015. Evaluation of the applicability of acid leaching for the ^{238}U–^{230}Th internal isochron method. Chemical Geology 396, 255–264. doi:`10.1016/j.chemgeo.2014.12.025`.

Tessier, A., Campbell, P.G., Bisson, M., 1979. Sequential extraction procedure for the speciation of particulate trace metals. Analytical Chemistry 51, 844–851. doi:`10.1021/ac50043a017`.

Toner, J.D., Sletten, R.S., Prentice, M.L., 2013. Soluble salt accumulations in Taylor Valley, Antarctica: Implications for paleolakes and Ross Sea Ice Sheet dynamics. Journal of Geophysical Research: Earth Surface 118, 198–215. doi:`10.1029/2012JF002467`.

Vaks, A., Gutareva, O.S., Breitenbach, S.F.M., Avirmed, E., Mason, A.J., Thomas, A.L., Osinzev, A.V., Kononov, A.M., Henderson, G.M., 2013. Speleothems reveal 500,000-year history of Siberian permafrost. Science 340, 183–6. doi:`10.1126/science.1228729`.

Vaks, A., Mason, A.J., Breitenbach, S.F.M., Kononov, A.M., Osinzev, A.V., Rosensaft, M., Borshevsky, A., Gutareva, O.S., Henderson, G.M., 2020. Palaeoclimate evidence of vulnerable permafrost during times of low sea ice. Nature 577, 221–225. doi:`10.1038/s41586-019-1880-1`.

Vermeesch, P., 2012. On the visualisation of detrital age distributions. Chemical Geology 312-313, 190–194. doi:`10.1016/J.CHEMGEO.2012.04.021`.

Vermeesch, P., 2018. IsoplotR: A free and open toolbox for geochronology. Geoscience Frontiers 9, 1479–1493. doi:`10.1016/j.gsf.2018.04.001`.

Wadleigh, M.A., Veizer, J., Brooks, C., 1985. Strontium and its isotopes in Canadian rivers: Fluxes and global implications. Geochimica et Cosmochimica Acta 49, 1727–1736. doi:`10.1016/0016-7037(85)90143-7`.

WAIS Divide Project Members, 2015. Precise interpolar phasing of abrupt climate change during the last ice age. Nature 520, 661–665. doi:`10.1038/nature14401`.

Wang, Y.J., Cheng, H., Edwards, R.L., An, Z.S., Wu, J.Y., Shen, C.C., Dorale, J.A., 2001. A high-resolution absolute-dated Late Pleistocene monsoon record from Hulu Cave, China. Science 294, 2345–2348. doi:`10.1126/science.1064618`.

White, A.F., Blum, A.E., Schulz, M.S., Bullen, T.D., Harden, J.W., Peterson, M.L., 1996. Chemical weathering rates of a soil chronosequence on granitic alluvium: I. Quantification of mineralogical and surface area changes and calculation of primary silicate reaction rates. Geochimica et Cosmochimica Acta doi:`10.1016/0016-7037(96)00106-8`.

Wilch, T.I., Denton, G.H., Lux, D.R., McIntosh, W.C., 1993. Limited Pliocene glacier extent and surface uplift in Middle Taylor Valley, Antarctica. Geografiska Annaler. Series A, Physical Geography 75, 331. doi:`10.2307/521206`.

Wood, M., Rignot, E., Fenty, I., An, L., Bjørk, A., van den Broeke, M., Cai, C., Kane, E., Menemenlis, D., Millan, R., Morlighem, M., Mouginot, J., Noël, B., Scheuchl, B., Velicogna, I., Willis, J.K., Zhang, H., 2021. Ocean forcing drives glacier retreat in Greenland. Science Advances 7, eaba7282. doi:`10.1126/sciadv.aba7282`.

Zahn, R., Schönfeld, J., Kudrass, H.R., Park, M.H., Erlenkeuser, H., Grootes, P., 1997. Thermohaline instability in the North Atlantic during meltwater events: Stable isotope and ice-rafted detritus records from Core SO75-26KL, Portuguese Margin. Paleoceanography 12, 696–710. doi:`10.1029/97PA00581`.

Ziemen, F.A., Kapsch, M.L., Klockmann, M., Mikolajewicz, U., 2019. Heinrich events show two-stage climate response in transient glacial simulations. Climate of the Past 15, 153–168. doi:`10.5194/cp-15-153-2019`.